University of Basel

Swiss Nanoscience Institute

SNI SWISS NANOSCIENCE INSTITUTE
EINE INITIATIVE DER UNIVERSITÄT BASEL UND DES KANTONS AARGAU

Annual Report 2017 Supplement

Swiss Nanoscience Institute
University of Basel

The Swiss Nanoscience Institute (SNI) is a research initiative of the Canton of Aargau and the University of Basel.

This report summarizes work conducted at the Swiss Nanoscience Institute (SNI) in 2017.

Swiss Nanoscience Institute
Klingelbergstrasse 82
4056 Basel
Switzerland
www.nanoscience.ch

Cover illustration: The beauty of foam, REM-image taken during the block course at the Nano Imaging Lab (Corinne Mattle).

Contents

Miniaturizing sample preparation for protein structure analysis by EM and X-FEL

Project P1201 Microfluidics to study nano-crystallization of proteins
Project Leader: T. Braun and H. Stahlberg
Collaborators: S. Arnold (SNI PhD Student), N. Opara, C. Padeste, K. Goldie, A. Syntychaki, S. Albiez, A. Bieri, M. Chami, M.-A. Mahi, and T. Schwede

Introduction

Two recent developments have caused fast and lasting changes to the field of structural biology: the advent of X-ray free electron lasers (X-FEL), and the introduction of direct electron detector (DED) cameras now used in electron microscopy (EM). While the X-FEL promises to solve the structure of proteins assembled in nanometer-sized 3D/2D crystals, cryo-electron microscopy (cryo-EM) allows the structural investigation of protein complexes without crystallization by a so called “single particle approach”.
However, state-of-the-art sample preparation techniques suffer, amongst others, from high sample consumption, such as the liquid-jet injectors commonly used to deliver protein crystals to the X-FEL beam. Similarly, techniques for single particle EM still depend on filter paper blotting, a method used to remove excess sample during preparation. Blotting consumes high amounts of sample, can cause reproducibility issues, and loss or degradation of sample.
Analogous to electron microscopy, where specimens are deposited on an electron transparent EM grid, protein crystals can be introduced into the X-FEL beam on an X-ray transparent support [1]. In this case, the same constraints as for EM apply, *i.e.*, the biological specimens must be prepared in a way that preserves their native structure. This can be achieved by cryo-preservation or sugar embedding with trehalose. For EM, a third alternative is the embedding of specimens in a layer of amorphous heavy metal salt (negative stain EM). The latter exhibits a high signal-to-noise ratio, but lacks the high resolution of cryo-EM.
Here, we report on new sample conditioning and preparation methods using nanoliter-sized samples of 3D nanocrystals or single protein particles for diffraction experiments and single particle EM, respectively. In addition, these methods further enable a technique named “visual proteomics”, which is used to study the protein content of individual mammalian cells.

Nanoliter sample conditioning

In the classical EM negative stain or trehalose embedding preparation, the sample is first adsorbed on a thin carbon layer and excess sample is blotted away with a filter paper. Before everything dries, the conditioning solution (negative stain or trehalose) is applied. Eventually, the conditioning solution is blotted away as well and the grid is air-dried.
We have developed a method for negative stain sample preparation or trehalose embedding of protein particles and nanocrystals that only consumes 5 nL or less of biological material [2]. To this end, a few nanoliter of sample are aspirated in the tip of a microcapillary (Fig. 1a). The loaded tip is immersed into a reservoir of negative stain or trehalose; the conditioning is driven by diffusion, exploiting the different diffusion constants of salt molecules and larger protein particles/nanocrystals (Fig. 1b). Subsequently, the sample is spread on a support, here a glow-discharged carbon surface of an EM grid (Fig. 1c). The results show that trehalose embedding protects crystals from the ultrahigh vacuum in the EM. Figure 2a shows an image of a sugar-embedded nanocrystal. Figure 2b shows the corresponding diffraction pattern with diffraction spots below 1/(1 Å) (arrows).

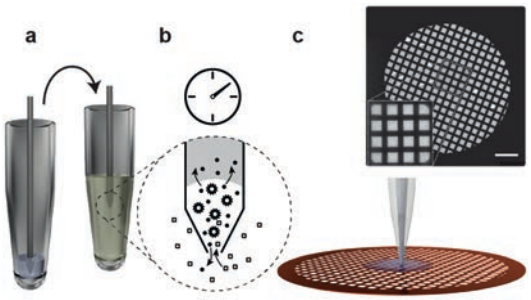

Fig. 1 Sample conditioning of nanoliter volumes for EM. (a) A few nanoliter of sample are loaded from a sample tube or crystallization screen into the tip of a microcapillary. (b) The microcapillary is now immersed in conditioning solution (e.g., negative stain, or trehalose). Within few minutes, the small sample plug is desalted and stain ions or trehalose molecules are introduced by diffusion. Note that the much larger proteins or nanocrystals exhibit significant lower diffusion constants and are retained in the capillary. (c) the conditioned sample plug is deposited on an EM grid and let to dry. Scale bar 500 µm.

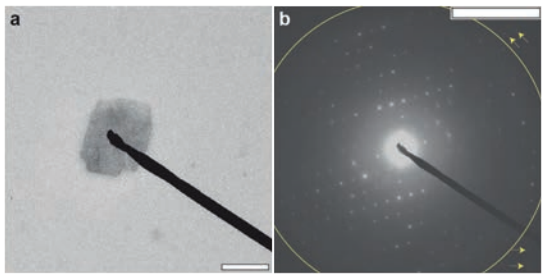

Fig. 2 (a) Nanocrystal conditioned in 2.5% (w/v) trehalose, scale bar 1 µm. (b) Electron diffraction of the nanocrystal depicted in (a). The yellow circle marks the resolution of 1/1 Å. Higher resolution diffraction spots are visible (yellow arrows). The scale bar represents 1/1.7 Å.

Figure 3a shows negatively stained 20S proteasome particles successfully prepared from 5 nL. In

combination with a previously developed single-cell lysis instrument [3], the new sample conditioning method further allowed the preparation of single-cell lysates for visual analysis by EM (Fig. 3b).

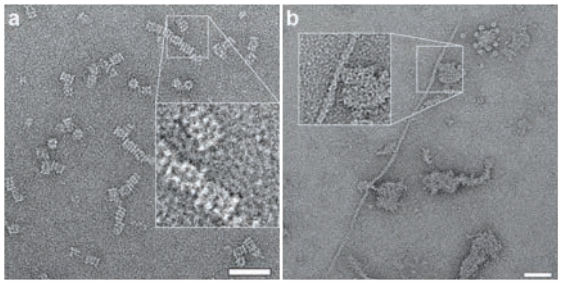

Fig. 3 (a) Negatively stained 20S proteasome particles. (b) Cell lysate collected from a single, adherently grown HEK 293 cell and prepared with the nanoliter sample conditioning method. Stain: 2% NanoW, pH 6.8. Scale bars represent 50 nm.

Nanoliter cryo-EM grid preparation

To benefit from high-resolution data acquisition using novel DED cameras and high-end cryo-EM, the instrument was further enhanced to perform cryo-preparation of nanoliter samples. The invented cryoWriter device is illustrated in figure 4, and proof-of-concept data in figure 5 and 6.

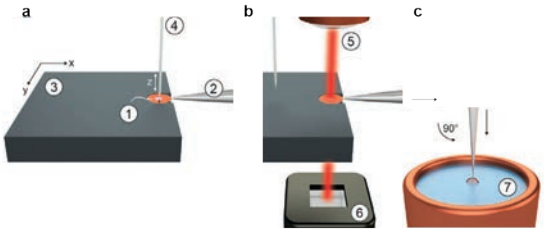

Fig. 4 Working principle of the cryoWriter device (adapted from [4]). (a) A standard holey carbon film EM grid (1) is mounted between the tips of tweezers (2) and positioned flat on a temperature-controlled stage (3). The stage temperature is set close to the dew point and can be regulated using a PID controller. The stage (3) is mounted on a motorized xy stage to move the grid relative to a microcapillary (4), which can be lowered to a few micrometers above the grid. This microcapillary deposits a few nanoliters of sample while the stage is moving in a sinuous pattern. (b) After sample deposition, the microcapillary is withdrawn and the stage (3) moves to position the grid (1) between an IR laser (λ=780 nm; 5) and a photodiode (6). Interference effects from the thin aqueous sample film on the grid cause a change in signal intensity as water evaporates. (c) A trigger automatically initiates plunge-freezing when the photodiode signal reaches a defined threshold level. The tweezers and grid are rapidly withdrawn from the stage, flipped by 90 degrees into the vertical position and plunged into a cryogen (7).

The cryoWriter's potential for high-resolution structural analysis was demonstrated with urease from *Yersinia enterocolitica* bacteria. Figure 6a documents the high quality of the sample grid imaged with a Titan Krios microscope equipped with a DED camera. Class averages selected from an initial 2D classification are shown in figure 6b. Particle refinement yielded a 3D reconstruction (Fig. 6c) of the tetrameric complex at a resolution of 5.03 Å.

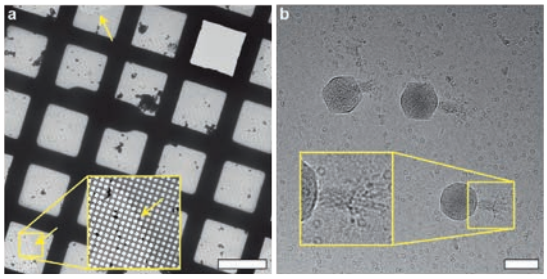

Fig. 5 Proof-of-concept data for cryo-grid preparation using the cryoWriter device (figure adapted from [4]). (a) Overview showing a thin film of vitreous ice. Yellow arrows indicate sample borders. Inset: four-fold enlargement of a border region after contrast adjustment to improve visibility. Note the homogenous layer of vitreous sample. Scale bar: 100 µm. (b) Apoferritin particles and bacteriophages in Tris-HCl buffer prepared by this method and imaged at high magnification and defocus to increase contrast. Inset: two-fold enlargement of the indicated region showing a bacteriophage tail and a few ring-shaped apoferritin complexes. Scale bar: 80 nm.

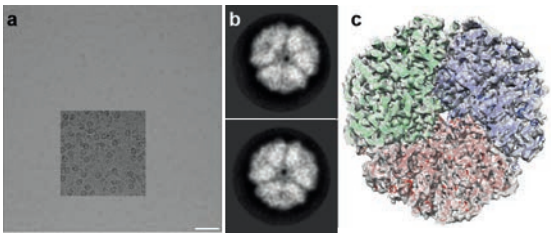

Fig. 6 Proof-of-concept use of the cryoWriter to prepare samples for high-resolution structural analysis; (figure adapted from [4]). (a) Drift-corrected cryo-EM image of urease particles embedded in vitreous ice. Inset: the particles with increased contrast. Scale bar, 50 nm. (b) 2D class averages including ~3'400 of the 10,000 particles initially selected. Scale bar, 5 nm. (c) A cross-section of the urease density map at 5.03 Å resolution with the fitted X-ray model (DOI: 10.2210/pdb4z42/pdb).

References

[1] N. Opara, I. Martiel, S.A. Arnold, T. Braun, H. Stahlberg, M. Makita, D. A. Christian, C. Padeste, *Direct protein crystallization on ultrathin membranes for diffraction measurements at X-ray free electron lasers*. J Appl Crystallography **50**, 909-18 (2017)

[2] S. A. Arnold, S. Albiez, N. Opara, M. Chami, C. Schmidli, A. Bieri, C. Paseste, H. Stahlberg, T. Braun. *Total Sample Conditioning and Preparation of Nanoliter Volumes for Electron Microscopy*. *ACS Nano* **10(5)**, 4981–4988 (2016).

[3] S. Kemmerlin, S.A. Arnold, B. A. Bircher, N. Sauter, C. Escobado, G. Dernick, A. Hierlemann, H. Stahlberg, T. Braun. *Single-cell lysis for visual analysis by electron microscopy*. J Struct Biol **183 (3)**, 467-73 (2013).

[4] S.A. Arnold, S. Albiez, A. Bieri, A. Syntychaki, R. Adaixo, R. A. McLeod, K. N. Goldie, H. Stahlberg, T. Braun. *Blotting-free and lossless cryo-electron microscopy grid preparation from nanoliter-sized protein samples and single-cell extracts*. J Struct Biol **197 (3)**, 220-226 (2017).

Active manipulation of individually trapped nanoparticles in nanofluidic devices

Project P1202 Electrostatic nanotrapping for single-macromolecule analysis
Project Leader: Y. Ekinci and T. Pfohl
Collaborators: M. Gerspach (SNI PhD Student) and N. Mojarad

Introduction

Monitoring the motion and interactions of single particles in solution is of great scientific and application interest since it provides information on local dynamics and reactions. Stable trapping of nano-objects smaller than 100 nm without changing their properties remains a major challenge. In the last years, especially one method has attracted the attention that enables contact-free and passively trapping and detection of nano-objects without the need of externally applied fields, the so-called geometry induced electrostatic (GIE) trapping [1,2]. In GIE trapping, single charged nano-objects are trapped by electrostatic repulsion from charged walls of fluidic channels with nanometer height (see 3D schematic in Fig. 1) [1-3].

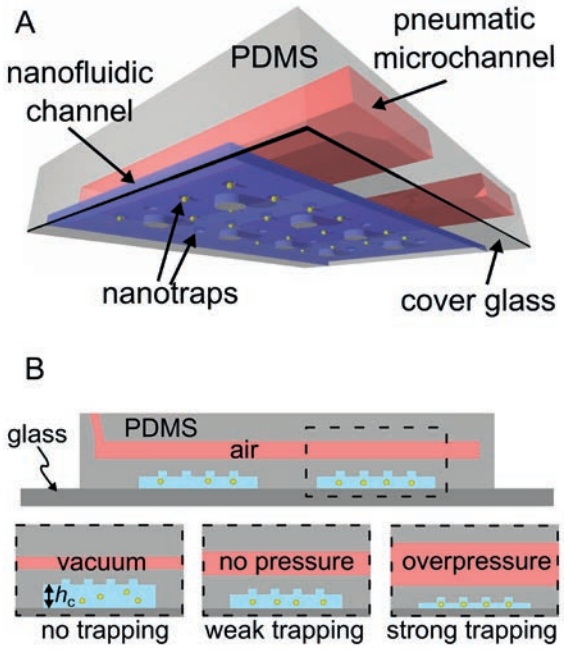

Fig. 1 3D schematic and principle of the pneumatic nanofluidic trapping device. A) Design of the multilayer PDMS device with an integrated pneumatic system for manipulating the trapping performance of the underlying nanofluidic trapping channel. B) Trapping and manipulation principle: If no pressure is applied in the pneumatic air channel, the particles are weakly confined in the pockets. If the gauge pressure p_g is increased, the nanofluidic channel height h_c is decreased, leading to a stronger trapping of the particles. If a vacuum is applied in the pneumatic channel, the particles are fully released.

However, the high-performance nanofabrication processes to produce the silicon and glass based GIE trapping devices makes the development and usage challenging, due to high costs and limited access to cleanroom facilities and nanofabrication tools. As reported in the SNI Annual Report 2016, GIE trapping devices made from replica molding of Polydimethylsiloxane (PDMS) simplifies fabrication and results in high-throughput and low-cost production [3]. Moreover, the ease of use and fast production makes them equally available for research and commercial applications.

However, due to the absence of an external applied control, there is a lack of active manipulation of the trapped objects during the experiment, even for the PDMS-based GIE trapping devices. The technique is limited by the initial geometrical design parameters, especially the nanofluidic channel height h_c. Here, we report on an integrated multilayer 3D pneumatic system that makes the PDMS-based GIE trapping devices capable of controlling the potential depth and trap stiffness by actively manipulating the nanofluidic channel height during the experiment.

Fabrication of the multilayer 3D PDMS-based GIE-trapping devices

The fabrication steps of the multilayer 3D PDMS-based GIE trapping devices are sketched in figure 2. The devices were fabricated by a multi-step soft lithography process. Two separate designs were needed for each multilayer, the nanofluidic trapping layer and the pneumatic microfluidic layer. The PDMS nanofluidic trapping layer was spin-coated on an OrmoStamp master to obtain a thin PDMS membrane of about 70 µm. The pneumatic microfluidic layer was PDMS molded, cured and subsequently plasma-bonded on top of the thin PDMS membrane. Finally, the devices were peeled off from the OrmoStamp master and plasma-bonded to a coverslip glass to seal the nanofluidic devices and provide optical access.

Influence of pneumatic gauge pressure p_g on the radial trapping stiffness k_r

The working principle of the device is sketched in figure 1B. If no pressure was applied in the upper pneumatic channel (p_g = 0 mbar), the particles were weakly trapped in the nanometer-sized pockets of the underlying nanofluidic trapping channel. The particles could enter and release the trap if they had enough kinetic energy to overcome the potential depth of the trap. Reducing the pressure and applying a vacuum in the pneumatic microchannel, increased the height h_c of the nanofluidic channel, which released all particles from the traps.

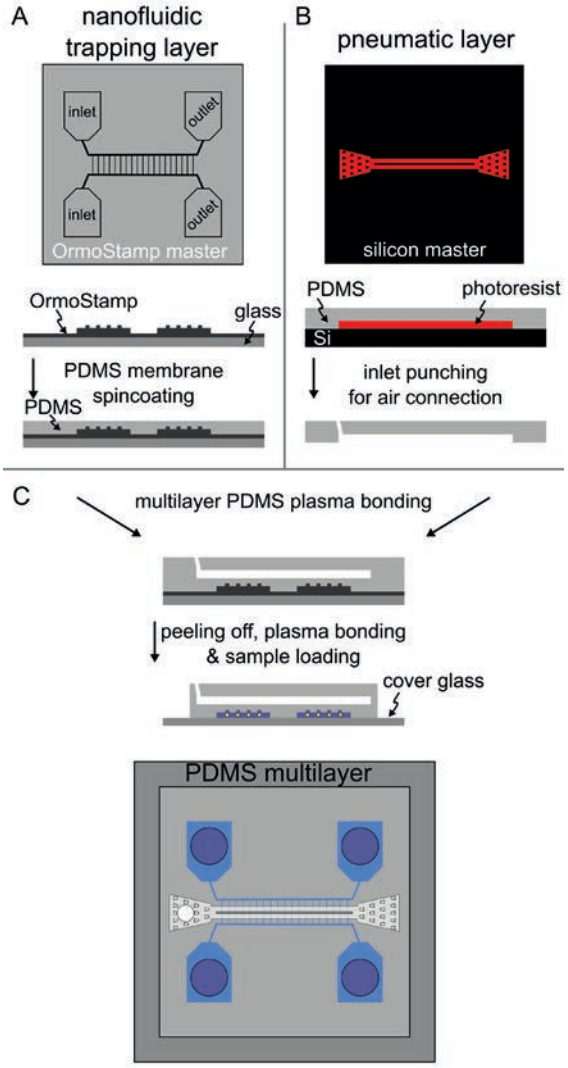

Fig. 2 Schematic of the fabrication steps of the PDMS multilayer GIE trapping device. First, two designs are fabricated individually: a nanofluidic trapping master and (A) and a pneumatic microfluidic master (B). The two separate PDMS layers are combined to a multilayer PDMS pneumatic GIE trapping device by covalently plasma binding (C).

If a controllable pressure p_g was applied in the pneumatic channel, the individual particles could be trapped strongly in the pockets. In figure 3, a stepwise increase of p_g up to 500 mbar is demonstrated. At a pressure p_g of 100 mBar, the particles are stably but loosely trapped with a trap stiffness of 0.9 fN/nm as seen in the broad radial displacement r of a 100 nm example particle. Increasing the p_g lowers the nanofluidic channel height h_c resulting in stronger confinement of the particle. At a pressure p_g of 500 mbar, the particle is strongly trapped with a more than two orders of magnitude higher trap stiffness of 0.11 pN/nm as seen in the confined radial displacement of the particle. At this stage, the particles could be individually trapped for several weeks and longer.

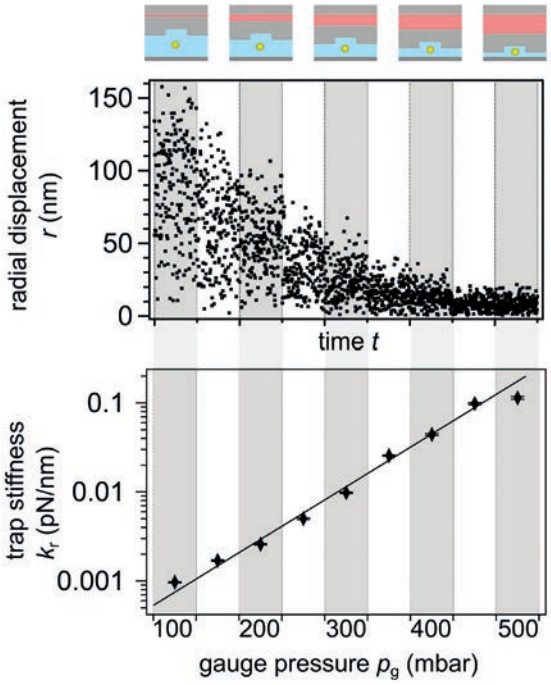

Fig. 3 Influence of the pressure change in the pneumatic microfluidic channel on the trapping strength of a 100 nm trapped AuNP in a w_p = 500 nm nanotrap. If the pressure in the air microchannel is increased, the particle is stronger confined (decrease of radial displacement r) resulting in a stronger trap stiffness k_r.

In summary, we introduced the fabrication of multilayer 3D PDMS pneumatic devices for contact-free electrostatic trapping and active manipulation of nano-objects in nanofluidic channels. The rapid and low-cost fabrication and simple usage of the devices open the door for individual nano-object analysis and experiments in aqueous environments for research and commercial applications equally. Furthermore, these features enable the possibility for fast analysis of multiple samples by releasing the trapped objects after measurements and flushing the nanofluidic channels with new sample solutions.

References

[1] M.A. Gerspach, N. Mojarad, T. Pfohl, Y. Ekinci, *Glass-based geometry-induced electro-static trapping devices for improved scattering contrast imaging of nano-objects*, Micro-electron Eng **145**, 43-48 (2015), 10.1016/j.mee.2015.02.035

[2] M.A. Gerspach, N. Mojarad, D. Sharma, T. Pfohl, Y. Ekinci, *Nanofluidic lab-on-a-chip trapping devices for screening electrostatics in concentration gradients*, Microelectron Eng **175**, 17-22 (2017), 10.1016/j.mee.2016.12.

[3] M.A. Gerspach, N. Mojarad, D. Sharma, T. Pfohl, Y. Ekinci, *Soft electrostatic trapping in nanofluidics*, Microsyst & Nanoeng, **3**, 1–10 (2017), 10.1038/micro-nano.2017.51

Functionalized 4,2':6',4"-terpyridine building blocks for programmed assembly into 2D-architectures on and off surface-platforms

Project P1203 On surface covalent assembly of coordination polymers with integrated read and write functions
Project Leader: C.E. Housecroft and E.C. Constable
Collaborators: T. Nijs (SNI PhD Student), T.A. Jung, S. Fatayer, A. Wäckerlin, S. Nowakowska, A. Ahsan, F.J. Malzner, Y.M. Klein, and S. Vujovic

Final Report

The 4-year project was designed to combine the synthetic design skills of our chemistry team with the expertise from the Nanolab group in a bottom-up approach to surface-assemblies. The project focused on the use of 4'-functionalized 4,2':6',4"-terpyridines **1**–**4** (Scheme 1) as V-shaped building blocks. In contrast to the chelating metal-binding mode of 2,2':6',2"- terpyridines, molecules **1**–**4** (and related compounds) bind metal ions/atoms only through the two outer N atoms shown in red in Scheme 1.

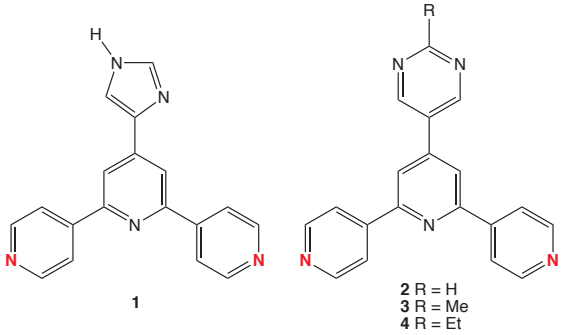

*Scheme 1 Imidazole **1** and pyrimidine-functionalized 4,2':6',4"-terpyridines **2**–**4**. Binding sites of the 4,2':6',4"-tpy domains are shown in red.*

Ligand 1 on Au(111) and Cu(111)

Initially, ligand 1 was deposited on Au(111) and high-resolution STM images (at 5 K) showed dimeric units as motifs within a hexagonal nanoporous hydrogen-bonded 2D-network (Fig. 1a). The addition of Cu-adatoms resulted in a transformation of the network into chains of linked metallomacrocycles, which generally follow the fcc domains of the Au(111)(22x√3) reconstruction. Both STM and X-ray photoelectron spectroscopy (XPS) data were used to visualize and understand these and later assemblies described in this report. The heterocyclic chains contain 4-, 5- and 6- membered rings (Fig. 1b) and proposed models of the metallomacrocycles are shown in figure 1c. Figure 1d shows the effects of changing the substrate from Au(111) to Cu(111). The dimeric units and hexagonal hydrogen-bonded 2D-network are still present, but the distance between the dimeric building blocks is larger on Cu(111) than on Au(111). Annealing of this network phase on Cu(111) produces Cu-adatoms by thermal release from kink and step-edge sites and a regular double row pattern with line defects is observed (Fig. 1e). The ladder-like arrays are modelled in figure 1f patterns formed by ligand 1 after annealing on Au(111).

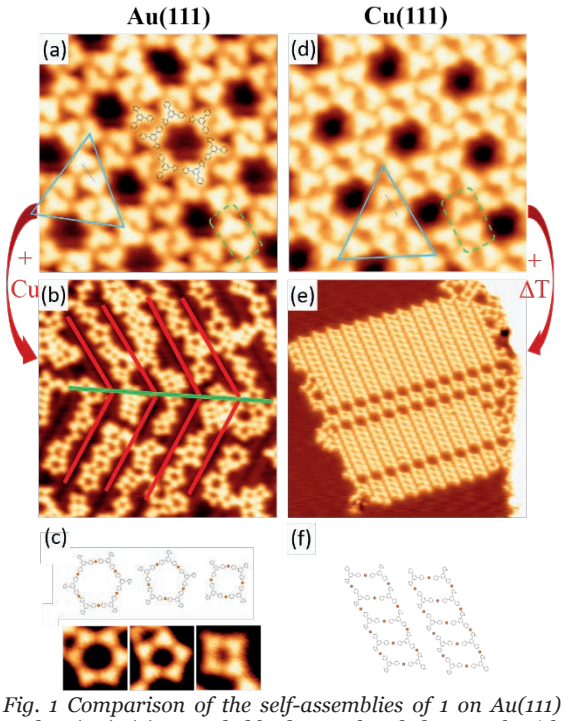

Fig. 1 Comparison of the self-assemblies of 1 on Au(111) and Cu(111). (a) Extended hydrogen-bonded network with superimposed molecular scheme (10nm x 10nm). (b) The Cu-coordinated assembly of 1 on Au(111) consists of chains of metallomacrocycles following the fcc domains of the herringbone reconstruction (red lines) (40nm x 40nm). (c) Models of metallomacrocycles and their corresponding STM images. (d) Extended network of 1 on Cu(111) (10nm x 10nm). (e) Copper-coordinated 2D-assembly after annealing of d (40nm x 40nm). (f) Proposed models of the ladders in image e.

Ligands 2–4 on Au(111) and Cu(111)

Compounds **2**, **3** and **4** contain the same 4,2':6',4"-terpyridine unit as **1**, but a pyrimidinyl-functionality rather than the imidazolyl featured in **1**. Moreover,

the R group (Scheme 1) acts as an 'imaging group' in STM images. This is clearly seen in figure 2 where the ethyl group in **4** unambiguously defines the orientation of the otherwise triangular molecule on the Au(111) surface. Deposition of **1** and **2** on Au(111) produces extended close-packed phases; for R = H or Me, a high packing density is possible. Differently oriented domains are separated by two types of boundaries (Fig. 3, molecules **2** and **3**). For **4** with R = Et (Fig. 2, right), a 2D-assembly with the omission of every second molecule is observed.

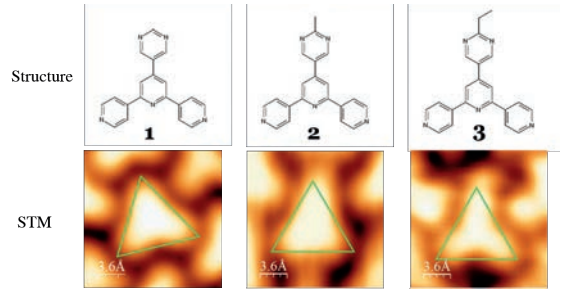

*Fig. 2 Structures and corresponding STM images (with overlaid equilateral triangle) of **2**, **3** and **4** on a Au(111) substrate (at 5 K).*

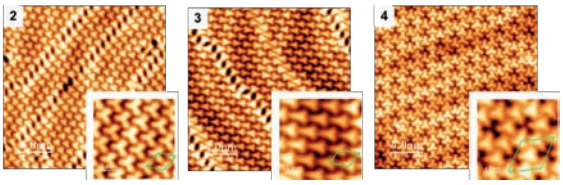

*Fig. 3 Molecules **2**, **3** and **4** on Au(111) at 5 K. **2** and **3** assemble into a close-packed layer, and **3** forms a regular porous vacancy pattern. Insets (5×5 nm) show the unit cell in green to emphasize the influence of the R group on the 2D-assembly.*

The addition of Cu adatoms (by thermal evaporation) leads to a striking change in the on-surface assembly. For each of **2**, **3** and **4**, "ladders" are formed (Fig. 4). These are remarkably similar both on an Au(111) or Cu(111) substrate. In figure 4, the ladders are defined by parallel blue lines (width = 2.3 nm in all images), and for both **3** and **4**, the R groups (imaged by STM, Fig. 4) lie on the outside of the ladders. The ladders are stable up to room temperature, but annealing on the Cu(111) substrate leads initially to the formation of [4+4] metallotetracycles and then to [6+6] metallo-hexacycles. For **3**, a quasi-hexagonal nanoporous network is observed.

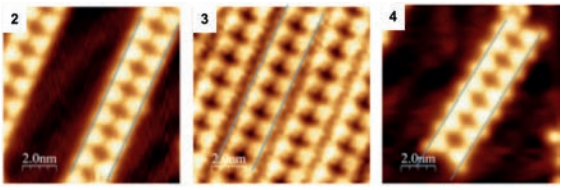

*Fig. 4 Ladder arrays formed by **2**, **3** and **4** on Au(111) after the addition of Cu adatoms (at 5 K). Analogous assemblies occur on a Cu(111) substrate.*

The final part of the project addresses a physical versus chemical conundrum. Because no formal oxidation states are assigned to Cu adatoms, and because the assemblies on Au(111) or Cu(111) with Cu adatoms are laid down in vacuo, the on-surface assemblies are devoid of the effects of counterions and solvents. This is not the case for metal-organic architectures assembled under conditions of single-crystal growth. Here, there are no "platforms" to direct or restrict the dimensionality of the assembly. Chemical input to the project came with an investigation of the architectures that self-assemble with ligand 4 reacts with copper(I) or copper(II) salts.

Combining 4 with copper(II) acetate or copper(I) triflate in MeOH solution resulted in single crystals, respectively, of [Cu2(OAc)4(4)]n or {[Cu(4)(OMe)(MeOH)][CF3SO3]MeOH}n. In the former, 'paddle-wheel' {Cu2(μ-OAc)4} nodes direct the formation of 1D-zigzag chains which pack into 2D sheets (Fig. 5a). In the triflate salt, the MeOH solvent acts as a ligand and generates {Cu2(μ-OMe)2} units which function as planar 4-connecting nodes to generate a 2D (4,4) net (Fig. 5b).

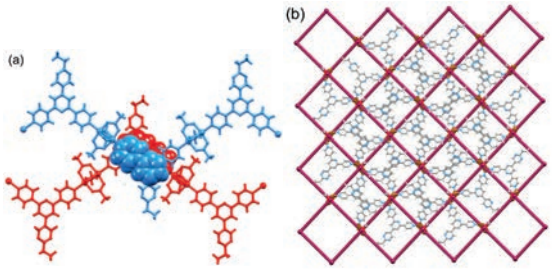

Fig. 5 (a) Parts of two 1D-chains in $[Cu_2(OAc)_4(\mathbf{4})]_n$; the chains are stacked through π-interactions. (b) Part of one 2D (4,4) net in $\{[Cu(\mathbf{4})(OMe)(MeOH)][CF_3SO_3]\cdot MeOH\}$. A grid-is overlaid on the structure to define the (4,4) connectivity of the network.

The metal-organic assembly in solution and the solvent-free coordination assembly in vacuum both feature 2D layers. On the one hand, the 'surface-supported' system is directed by the Au(111) or Cu(111) platform. On the other hand, the solution assembly follows the rules of coordination chemistry where the coordination requirements of the metal center and the donor properties or packaging effects of the solvent and anions are crucial. It is, therefore, remarkable that the general principles and algorithms determining the structures of solution grown crystalline material can be extended to surface assemblies.

References

[1] T. Nijs, F.J. Malzner, S. Fatayer, A. Wäckerlin, S. Nowakowska, E.C. Constable, C.E. Housecroft and T.A. Jung, *Programmed assembly of 4,2′:6′,4′′-terpyridine derivatives into porous, on-surface networks*, Chem Commun, **51**, 12297-12300 (2015)

[2] Y.M. Klein, E.C. Constable, C.E. Housecroft and J.A. Zampese, *4'-(Pyrimidin-5-yl)- and 4'-(2-methylpyrimidin-5-yl)-4,2':6',4"-terpyridines: Selective coordination to zinc(II) through the 4,2':6',4"-terpyridine domain*, Polyhedron, **81**, 98-104 (2014)

Diffusion and dynamics of nuclear pore complex proteins

Project P1205 Watching the nanomachinery of the nuclear pore complex at work by high speed-AFM
Project Leader: R.Y.H. Lim and C. Gerber
Collaborators: Y. Sakiyama (SNI PhD Student), S. Singh, F. Benning, and T. Maier

Introduction

Nuclear pore complexes (NPCs) are 50 nm-diameter channels that form the sole transport gateways between the nucleus and cytoplasm in eukaryotic cells. Despite being the largest pores in the cell, it remains challenging to resolve NPC structure and function because of its complicated molecular makeup. This consists of 30 types of proteins called nucleoporins (Nups) arranged in an octagonal geometry [1]. Previously, we used high-speed atomic force microscopy to resolve (i) highly dynamic intrinsically disordered proteins known as Phe-Gly nucleoporins (FG Nups) inside the NPC channel [2], and (ii) the overall structural dynamics of the NPC itself [3].

However, because it is not possible to discriminate between different proteins using HS-AFM, most recently we have started to analyze the biophysical behavior of FG Nup layers so as to understand how they facilitate the selective transport of soluble nuclear transport receptors such as importinβ (Impβ). Moreover, we have initiated collaborations with structural biologists (Prof. Ed Hurt, Uni. Heidelberg) to resolve the dynamics of Mlp1 (myosin-like protein) a key component of the nuclear basket.

Lipid-tethered FG Nups

To engineer surface tethered-FG Nups, we first prepared supported lipid bilayers with varying fractions of metal ion chelator (Ni-NTA) containing lipids (DGS) on mica formed via spontaneous liposome spreading. Histidine (His_6)-tagged FG Nups then bind the Ni-NTA forming either individual "mushrooms" or extended protein brushes at low and high surface densities, respectively (Fig. 1).

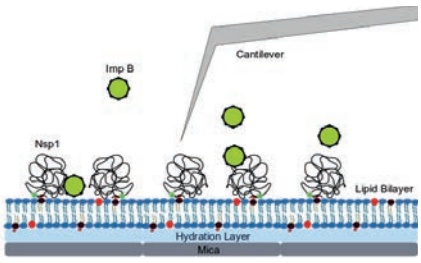

Fig. 1 His-tagged FG Nups are tethered onto a lipid bilayer exposing Ni-NTA binding sites. HS-AFM is able to capture the interactions between soluble Impβ and the FG Nups.

Using a syringe pump-injection system, we have the ability to exchange buffers during HS-AFM scanning. This provides the means to monitor molecular diffusion under exact concentrations of Impβ. Here, we find that Impβ mobility is slowest at low nanomolar concentrations (Fig. 2) being consistent with previous findings showing that Impβ-FG Nup binding avidity depends on Impβ concentration [4].

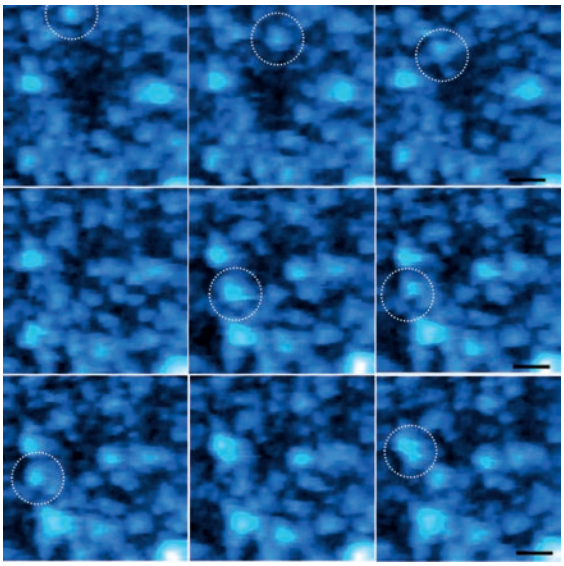

Fig. 2 HS-AFM reveals the movement of Impβ along a FG Nup surface layer. Obvious mobile features are encircled. The elapsed time between each frame is 150 ms. Scale bar = 30 nm.

Structural dynamics of Mlp1

Mlp1 is a structural component of the nuclear basket and plays a key role in mRNA export [5]. When investigating Mlp1 dynamics *in vitro*, Mlp1 exhibits a highly flexible domain whereas the remaining coiled coil structure is rigid.

To further analyse its length, we developed an automated protocol that analyses thousands of HS-AFM frames. Specifically, original HS-AFM data is converted to binary and skeletonized following noise reduction, tilt compensation, and thresholding. This is shown in figure 3.

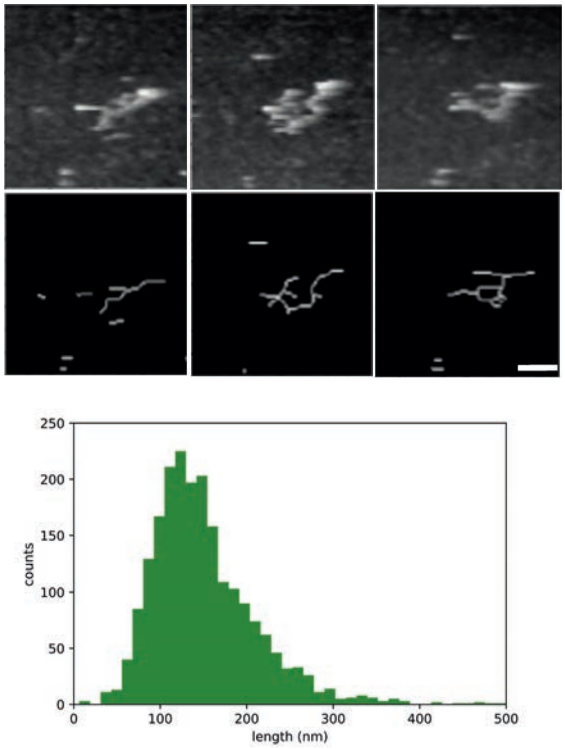

Fig. 3 Top: Sequential HS-AFM images of Mlp1 obtained at 150 ms/frame. The flexible domain is encircled. Scale: 50 nm. Middle: Corresponding images after skeletonization. Bottom: Mlp1 length measurements for 7 molecules collected over 2000 frames.

Large area imaging by HS-AFM

Our next goal is to capture NPCs at work in intact nuclei. This is challenging for two reasons. First, the HS-AFM scan area has to be placed precisely at a tangent over the top of the nucleus. Second, it is necessary to conduct large area scans (> 1 μm²) with minimal disturbance to the nuclear surface. For this, we are implementing two technical improvements for the HS-AFM system: (i) Fluorescence detection (Fig. 4), and (ii) an ultra-large area scanner [6].

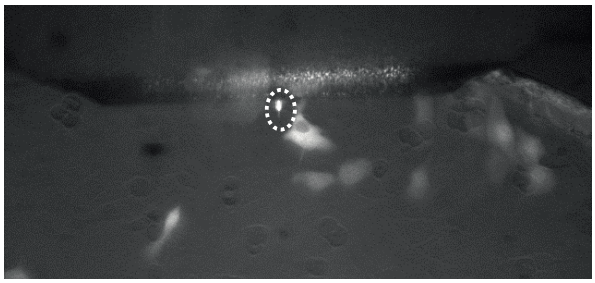

Fig. 4 A fluorescent protein-transfected MDCK cell is clearly visible next to a HS-AFM cantilever that is encircled.

Summary

Although we have resolved dynamic FG Nup behavior directly inside native NPCs at transport-relevant timescales, several questions remain as to how the FG Nups facilitate the speed and selectivity of transport receptors. Our current work captures FG Nup dynamics during the transport of individual transport receptors at ~100 ms time resolution substantiated with quantitative analysis. In the meantime, we have established successful collaborations to study other biological nanomachines by HS-AFM (e.g., fatty acid synthase with Prof. Timm Maier, Biozentrum, Uni. Basel) [7]. Needless to say, we recognize the importance of building a community of HS-AFM researchers in Basel, for which we are grateful to the SNI for its support.

References

[1] B. Fahrenkrog and U. Aebi, *The nuclear pore complex: nucleocytoplasmic transport and beyond*, Nat Rev Mol Cell Biol **4(10)**, 757–766 (2003)

[2] Y. Sakiyama, A. Mazur, L.E. Kapinos, R.Y.H. Lim, *Spatiotemporal dynamics of the nuclear pore complex transport barrier resolved by high-speed atomic force microscopy*, Nat. Nanotechnol. **11(8)**, 719-724 (2016)

[3] Y. Sakiyama, R. Panatala, R.Y.H. Lim, *Structural dynamics of the nuclear pore complex*. Sem. Cell Dev. Biol. **68**, 27-33 (2017)

[4] L.E. Kapinos, R.L. Schoch, R.S. Wagner, K.D. Schleicher, R.Y.H. Lim, *Karyopherin-centric control of nuclear pores based on molecular occupancy and kinetic analysis of multivalent binding with FG nucleoporins*, Biophys. J. **106(8)**, 1751–1762 (2014)

[5] A. Köhler and E. Hurt, *Exporting RNA from the nucleus to the cytoplasma*, Nat. Rev. Mol. Cell Biol. **8(10)**, 761-773 (2007)

[6] H. Watanabe, T. Uchihashi, T. Kobashi, M. Shibata, J. Nishiyama, R. Yasuda, T. Ando, *Wide-area scanner for high-speed atomic force microscopy*, Rev. Sci. Instr. **84(5)**, 053702 (2013).

[7] F.M.C. Benning, Y. Sakiyama, A. Mazur, H.S.T. Bukhari, R.Y.H. Lim, T. Maier, *High-speed atomic force microscopy visualization of the dynamics of the multienzyme fatty acid synthase*, ACS Nano **11(11)**, 10852-10859 (2017)

Hybrid spin-nanomechanics with diamond cantilevers

Project P1206 Nanomechanical oscillators for diamond spinoptomechanics
Project Leader: P. Maletinsky and R.J. Warburton
Collaborators: A. Barfuss (SNI PhD Student), J. Kölbl, L. Thiel, D. Jäger, and M. Kasperczyk

Introduction and motivation

An individual electronic spin coupled to a nanomechanical oscillator constitutes a prototypical 'hybrid quantum system'. Such systems form highly valuable quantum resources for fundamental investigations of quantum mechanics and for potential high-performance nanoscale sensors [1]. Specifically, these systems are highly attractive candidates for studying the crossover from quantum to classical physics and they have the potential to yield novel types of high-performance sensing devices for diverse quantities such as mass, acceleration or pressure. Furthermore, such hybrid systems can be exploited for efficient, coherent manipulation of a quantum system by purely mechanical means [2] – an approach which could be highly advantageous over established methods due to its compactness and efficiency.

In this project, we exploit a particular, novel hybrid spin-mechanical system consisting of a single, electronic 'Nitrogen-Vacancy' (NV) spin, embedded in a diamond mechanical oscillator. The individual sub-systems in our devices – the spin and the oscillator – are highly attractive for the experiments we envisage: Diamond nanomechanical resonators have been shown to exhibit very high quality-factors up to Q~10^6[3], and therefore form a well-isolated, high-quality nanomechanical system. NV center electronic spins are advantageous in this context for multiple reasons. They form a spin-1, three level system, which is highly quantum coherent, even at room temperature, with quantum coherence times approaching one second. The NV spin can be conveniently read out and initialized using optical means and coherently manipulated using microwave magnetic fields. Our NV-based hybrid spin-mechanical system is therefore ideally suited to study the subtle effects a single spin could have on the mechanical oscillator and vice versa.

Key experimental results

Our work in the past year focused on realizing a closed-contour interaction (CCI) scheme in the spin-1 ground state of the NV center and subsequently studying the occurring coherent spin dynamics. In the context of a three-level system, the term "closed contour interaction" refers to a scenario in which all three transitions are coherently driven by individual driving fields (see Fig. 1a). If these three fields fulfill the three-photon condition $\omega_1+\omega_3=\omega_2$, the system's coherent dynamics are expected to strongly depend on the global phase $\Phi = \phi_1+\phi_3-\phi_2$ [4]. Despite its attractive prospects, such as one-atom interferometry [4] or phase-dependent absorption [5], coherent CCI dynamics have not been observed yet due to fundamental limitations by selection rules of the involved transitions.

In our approach, we overcome these limitations by exploiting the unique properties of our hybrid-spin oscillator system. In particular, we combine spin manipulation through time-varying (AC) magnetic field (MW fields) to drive the $|0\rangle \leftrightarrow |\pm1\rangle$ transitions, with recently established AC strain manipulation of the magnetic-dipole forbidden spin transition $|-1\rangle \leftrightarrow |+1\rangle$ (see Fig. 1a) [2]. Phase-locking of the three driving fields then allows studying the phase-dependence of CCI dynamics in a single NV spin through optical readout of the spin population in $|0\rangle$ (Fig 1b).

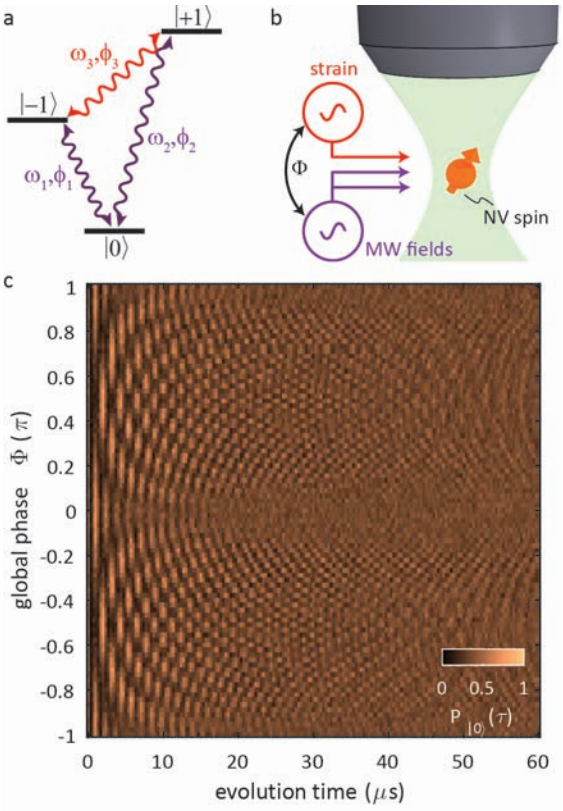

Fig. 1 CCI driving of the spin-1 NV ground state. a+b) Schematic representation and experimental setup of the three-level system, driven by two MW fields (purple arrows) and an AC strain field (red). c) Time evolution of $|0\rangle$ population, $P_{|0\rangle}(\tau)$, as a function of global phase Φ. $P_{|0\rangle}(\tau)$ oscillates at three frequencies $\Delta_{+1,-1}$, $\Delta_{+1,0}$ and $\Delta_{-1,0}$ and the overall interference pattern exhibits a strong dependence on the global phase.

To investigate occurring CCI spin dynamics, we performed Rabi oscillation measurements to

monitor the time evolution of $|0\rangle$ population vs. time, $P_{|0\rangle}(\tau)$. Varying the global phase yields the interference pattern shown in figure 1c, which exhibits strongly pronounced phase dependent spin-oscillations, indicating that the occurring spin dynamics are closely linked to the applied driving field phase.

Unexpectedly, our careful studies further revealed that the global phase Φ not only controls CCI spin dynamics. It also serves as a handle to effectively shield the NV spin from environmental noise, which results in long-living Rabi oscillation fringes (see Fig. 2). Notably, we were able to demonstrate a 62-fold enhancement of NV spin coherence compared to the un-driven NV center without applying complicated decoupling sequences. As we can tune the degree of protection of our system, our results promise to unveil a host of applications, from quantum state preparation and storage, to noise sensing and relaxometry using single spins on the nanoscale.

In addition to these room temperature studies of CCI spin dynamics, we continued investigating our hybrid spin-mechanical systems under cryogenic conditions. Based on theory, we there expected a five order of magnitude enhancement of strain coupling strengths compared to our current experiment. Indeed, first experiments which we conducted this year confirm this enhanced coupling and for example allowed us to observe strain-tuning of the NV zero-phonon emission line by tens of nanometers. This offers interesting perspectives for tuning NV emission in resonance with other quantum emitters or optical cavities.

Outlook

This report concludes the activities pursued within the SNI project "Hybrid spin-nanomechanics with diamond cantilevers", with which Arne Barfuss very successfully defended his PhD recently. Still, the project will be carried on, as several aspects of our hybrid spin-mechanical devices warrant further investigation. In the next year, we will further pursue the two lines of research highlighted in this report. We will on one hand continue investigations of room temperature coherent dynamics of the NV spin coupled to our nanomechanical oscillators, with a particular focus on adiabatic state preparation and detailed investigation of driven coherences. Furthermore, and supported by a new SNI project starting in 2018, we will explore novel aspects of coherent three-level dynamics, such as phase controlled Fano-resonances expected in the system. Additionally, we will further explore low-temperature dynamics of our system. The central goal there is to further increase the system's cooperativity; a key figure of merit in hybrid quantum system, which at sufficiently high values allows e.g. remote spin-spin entanglement to be mediated by the mechanical oscillator.

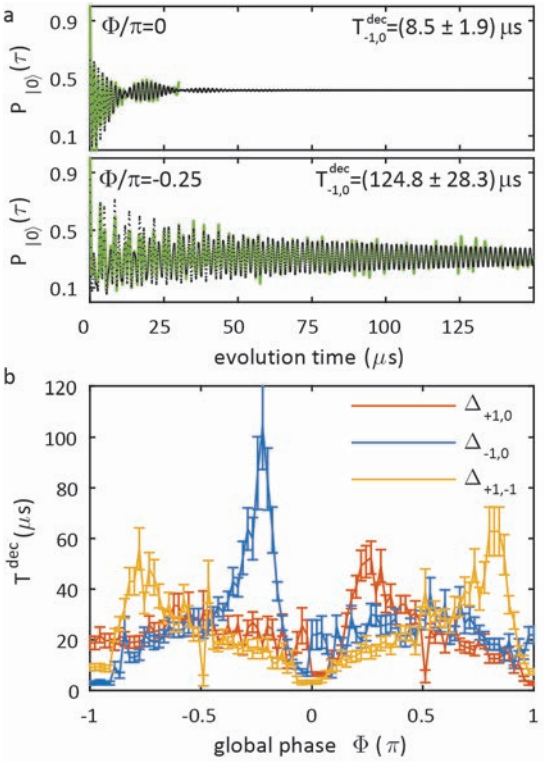

Fig. 2 Influence of Rabi decay time T^{dec} on global phase Φ. a) Changing the global phase allows tuning Rabi decay times between 8.5 μs (at Φ=0) and 124.8 μs (at Φ/π=1/4).b) The three frequency components exhibit maximized (minimized) decay times at Φ/π= ±1/4 and ±3/4(Φ/π= ±1,0).

References

[1] P. Treutlein, C. Genes, K. Hammerer, M. Poggio, P. Rabl, *"Hybrid Mechanical Systems"* (Springer, 2014)

[2] A. Barfuss, J. Teissier, E. Neu, A. Nunnenkamp, P. Maletinsky, *Strong mechanical driving of a singleelectron spin*, Nature Physics **11**, 820 (2015)

[3] P. Ovartchaiyapong, L.M.A. Pascal, B.A. Myers, P. Lauria, A.C. Bleszynski-Jayich, *High quality factor single-crystal diamond mechanical resonators*, Appl. Phys. Lett. **101**, 163505 (2012)

[4] S. Buckle, S. Barnett, P. Knight, M. Lauder, D. Pegg, *Atomic interferometers,* Optica Acta **33**, 1129 (1986)

[5] D.V. Kosachiov, B.G. Matisov, Y.V. Rozhdestvensky, *Coherent phenomena in multilevel systems with closed interaction contour,* Journal of Physics B: Atomic, Molecular and Optical Physics **25**, 3473 (1992)

Applied statistical modeling for membrane protein reconstitutions

Project P1207 Design of a polymer membrane-based molecular “hoover”
Project Leader: W. Meier and D.J. Müller
Collaborator: R. Goers (SNI PhD Student)

Introduction

The process of membrane protein reconstitutions is not only used in structural biology but also within the field of synthetic biology. The creation of nanocells that resemble a light-driven molecular hoover requires the functional assembly of synthetic membranes and certain membrane proteins, which provide the functionality. Commonly employed detergent-mediated processes depend on the starting conditions and the outcome of the self-assembly is hard to predict *a priori*. Methods from statistical modeling like design of experiments (DoE) allow researchers to analyze and optimize a given system in great detail (Fig. 1)[1].

Reconstitution of proteorhodopsin into lipid and polymer membranes

Proteorhodopsin (PR) was chosen as an energy generating module for the nanocell by generating a proton gradient upon illumination. In order to bypass the need for additional labeling and to influence the orientation after reconstitution, a fusion proteins (PR-GFP) of PR and the water soluble green fluorescent protein (GFP) was created [2]. The hydrophilic nature of GFP should influence the orientation of PR during reconstitution. The inner hydrophobic domain of the membrane should prevent GFP from passing through and thus, PR’s corresponding terminus should always be facing outwards of the vesicle. This should lead to proton transport into or out of the interior of the vesicle. Another challenge is that procedures used to reconstitute membrane proteins into lipid membranes are not easily applicable to polymer membranes. Comprehensive guidelines of necessary adaptions and key differences do not exist yet. Using DoE allowed us to study both membrane systems and identify their differences for membrane protein reconstitution. A definitive screening design was employed to analyze the influence of the detergent n-octyl-β-D-glucoside (OG), the pH value and to find proper ratios of PR to the lipid 1,2-Dioleoyl-sn-glycero-3-phosphocholine (DOPC) or to the PMOXA17-PDMS65-PMOXA17 (ABA) block copolymer, which were also used as parameters. The resulting structures were characterized via dynamic light scattering (DLS), transmission electron microscopy (TEM) and fluorescence correlation spectroscopy (FCS). In addition, we further characterized the proton pumping activity by encapsulating the pH sensitive fluorescent dye pyranine and recording its fluorescence intensity over time during illumination at 525 nm. The PdI, the size determined by FCS and DLS were defined as responses, as well as the relative change of pyranine’s fluorescence intensity. The results were used to construct a response surface (RS) which was then used to analyze the influence of these parameters and predict possible optimal conditions. The analysis of the experimental results was grouped in two steps: *i)* find conditions which yield proper vesicular structures (e.g. size >100 nm, PdI < 0.15) and *ii)* investigate the activity of these vesicles and maximize their proton pumping activity. Formation of proteoliposomes worked best within a broad range of detergent and high amounts of protein, whereas proteopolymersomes required low amounts of protein and detergent, as well as a slightly basic

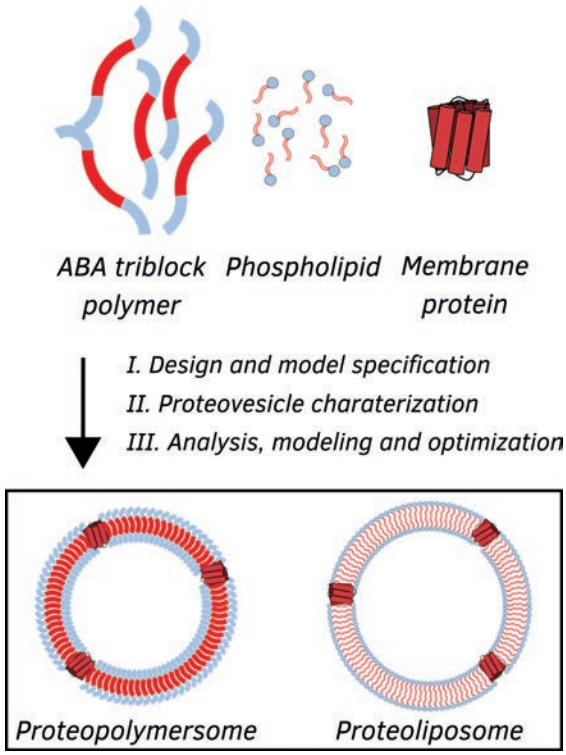

Fig. 1 Schematic visualization of the approach taken in this work. The assembly of either phospholipids or triblock copolymers together with membrane proteins is usually an induced self-assembly process whose resulting structure depends on the starting conditions. A priori knowledge about the factors’ (e.g. buffer conditions, protein concentration, membrane concentration) is usually lacking and optimal results not achievable. Having two different membrane building blocks further increases complexity. ***I.*** *By using DoE and defining influential factors along with characteristic responses one can devise an experimental plan to investigate the system’s behavior in resource-efficient way.* ***II.*** *Important characteristics can be the size, homogeneity and functionality.* ***III.*** *The results were used to fit a model for detailed analysis of the process and subsequent optimization which allowed to find optimal assembly conditions.*

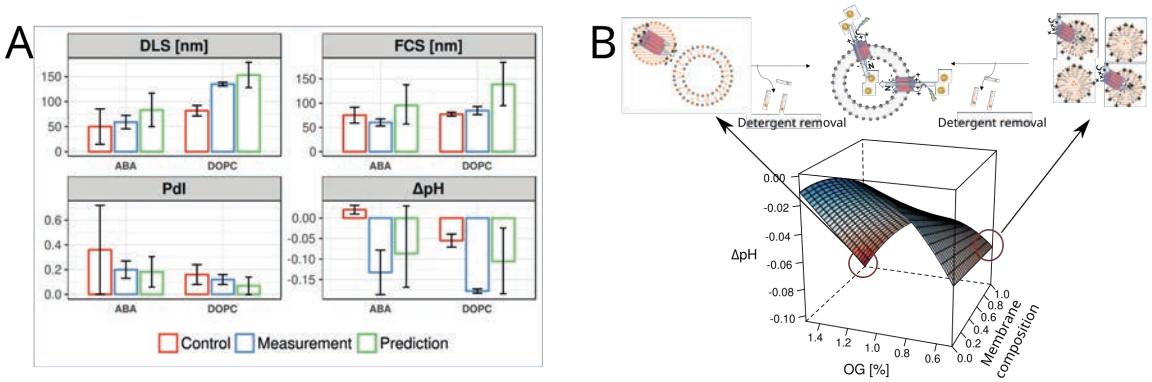

Fig. 2 ***A)*** *Comparison of the measurements, their controls and predictions for all four responses. The predictions and measurements are in good agreement.* ***B)*** *3D contour plot of the formed pH gradient depending on the OG concentration and the membrane composition. The membrane is composed of DOPC and DOTAP (+) and a value of 0 equals only DOPC and 1 only DOTAP. PR can take two different pathways during insertion into liposomes. One relies on the presence of low amounts of OG which is the main mediator here. The other requires the presence of charges on the membrane, which guide the protein during the insertion process.*

environment. In general, the formed polymer vesicles exhibited a smaller diameter (around 60 nm compared to 110 nm) and a higher PdI (around 0.2 compared to 0.1), which is in agreement to results from literature. Subsequent activity screening within this parameter space provided the necessary data to optimize the response surface. Highest activity for the proteoliposomes was found when the reconstitution was carried out. Measuring the proton pumping activity of vesicles formed with the optimal conditions showed that a gradient was formed in both cases and that the amplitude was in agreement with the predictions made by the derived model. We identified two separate factor combinations for both proteoliposomes (pH 6, 0.5 % OG and a LPR of 25) and proteopolymersomes (pH 7.8, 0.5 % OG and a PPR of 125) which yielded the desired functionality and structural characteristics (Fig. 2 A).

Two possible reconstitution pathways

In a second study, we analyzed the insertion of wild type PR into liposomes. At slightly acidic pH values (around 6.2), the extra-membrane domains of PR are oppositely charged. This can be exploited by using charged phospholipids in a mixture with neutral ones to polarize the liposome membrane. During the insertion, PR orients itself according to the applied charge. From earlier studies, it is known that the detergent OG has an influence on the final orientation of the membrane protein, even though it does not have any structural features (e.g. hydrophilic domain) which can serve as a guide [3]. We used DoE to investigate the effect of multiple factors (OG, KCl concentration, pH value, membrane composition) onto the insertion of PR. The vesicle membrane was composed of a mixture of DOPC and 1,2-dioleoyl-3-trimethylammonium-propane (DOTAP), which is positively charged. One crucial factor we identified was the concentration of KCl, which was tested in the range of 0 – 300 mM. Only the middle value of 150 mM resulted in successful insertions, values to close to 0 mM or 300 mM lead to rapid agglomeration of the protein. In terms of the reconstitution pathway we could determine that the charge mediated and detergent mediated one are not mutually exclusive but depend on the environmental conditions used during the reconstitution (Fig. 2 B). The detergent OG is the main mediator if used in lower amounts (0.5 – 0.8 %) and directs the protein in a preferential orientation. If charges are present on the membrane in higher abundance (>40 %), the protein's charged domains can interact with the vesicle surface and induce the preferred orientation.

Conclusion

In summary, the two projects demonstrate the usefulness of DoE in for membrane protein reconstitution. *i.* We derived a framework which allowed us to find optimal conditions for the reconstitution of PR-GFP into DOPC lipid and ABA triblock copolymer membranes. The model proved to be robust and reliable in its predictions. *ii.* A similar approach was used to study the insertion process itself under various conditions. We identified two possible reconstitution pathways and the conditions which direct the process towards one or the other.

References

[1] S.A. Weissman and N.G. Anderson, *Design of Experiments (DoE) and Process Optimization. A Review of Recent Publications*. Org. Process Res. Dev. **19**, 1605–1633 (2015)

[2] N. Ritzmann, J. Thoma, S. Hirschi, D. Kalbermatter, D. Fotiadis, D.J. Müller, *Fusion Domains Guide the Oriented Insertion of Light-Driven Proton Pumps into Liposomes,* Biophys. J. **113**, 1181–1186 (2017)

[3] R. Tunuguntla, M. Bangar, K. Kim, P. Stroeve, C.M. Ajo-Franklin, A Noy, *Lipid Bilayer Composition Can Influence the Orientation of Proteorhodopsin in Artificial Membranes*. Biophys. J. **105**, 1388–1396 (2013)

Altering the properties of graphene on Cu(111) by alkali halides

Project P1208 Ultra-sensitive force detection and molecular manipulation
Project Leader: E. Meyer and M. Poggio
Collaborators: M. Schulzendorf (SNI PhD Student), Th. Glatzel, A. Hinaut, P. Restuccia, and M. Clelia Righi

The project P1208 finished this summer and M. Schulzendorf defended his PhD thesis successfully. We continued working on the topic of intercalation of alkali halides between graphene and Cu(111) and started a collaboration with a theory group from the University of Modena in Italy (M. Clelia Righi) to support our experimental data. At this point we would like to review these results which are prepared for publication at the moment.

Results

Over the past few years, it has been discovered that a number of elements will "intercalate" between graphene and its substrate support, or between graphene layers. By intercalating different atoms or compounds between layers of graphite, it is possible to tune the physical properties of the graphene layer. For example, intercalating Na leads to an electron-doped graphene sheet [1] and intercalating Pb leads to the formation of a p-doped graphene layer [2]. We investigated the intercalation of graphene islands by KBr and NaCl thin-films on Cu(111) with a home-built AFM in ultra-high vacuum (UHV) at room temperature.

In our lab, we employed noncontact Atomic Force Microscopy (nc-AFM) and Kelvin Probe Force Microscopy (KPFM) [3] with a multimodal setup for our measurements, simultaneously actuating the cantilever mechanically and electronically at different eigenmodes. Our samples have been prepared in-situ. Graphene nano-flakes have been prepared according to Gao *et al.* [4]. Ethylene gas (CanGas) was directly dosed on a clean Cu(111) surface via a fine nozzle (outlet diameter 2 mm, distance 10 mm and 60 ° tilt in respect to surface) while flashing the sample to ~1000°C. The ionic crystals were evaporated thermally afterwards to the surface from a crucible containing small grains of the respective salts.

Figure 1 shows the topographies of three different samples. In a) only graphene islands have been prepared on the Cu(111) surfaces, appearing as hexagonal islands with a height of 337pm. The measurements have been performed by compensating the influences of the electrostatic force simultaneously to the topographic measurements by KPFM. Therefore, an absolute height measurement is possible. In b) and c) representative topographies after the deposition of NaCl or KBr on such a graphene/Cu(111) surface are presented, respectively. While NaCl forms islands or clusters around the graphene islands KBr stays nearly invisible on the surface. However, the island height of graphene is changing to 413pm while the one of the NaCl sample stays unchanged.

By means of KPFM, shown in figure 2, a clear shift of the local work function between the different areas was observed. While the work function difference between the graphene islands and the Cu(111) stays at 825mV for the graphene and the NaCl covered sample, it reduces to 580mV for the sample with KBr. Bare KBr or NaCl islands were observed on both samples show always lower work function values.

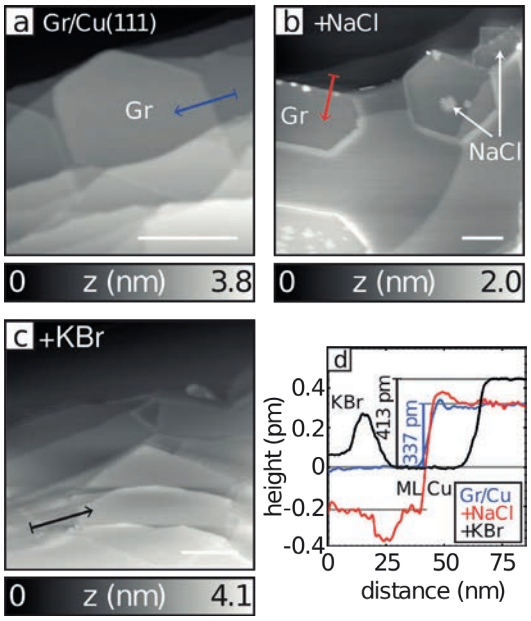

Fig. 1 Topographic images of graphene on Cu(111) a) with co-adsorbed NaCl found as islands on hexagons in b) and co-adsorbed KBr as carpets surrounding hexagonal flake in c). Cross sections along the direction of the arrows in d). All scale bars are 100 nm.

This strong change in the electronic properties was a first indication that graphene could have been intercalated. These experiments were complemented by X-Ray Photoelectron Spectroscopy at the Swiss Light Source (SLS) as presented in the last year's report.

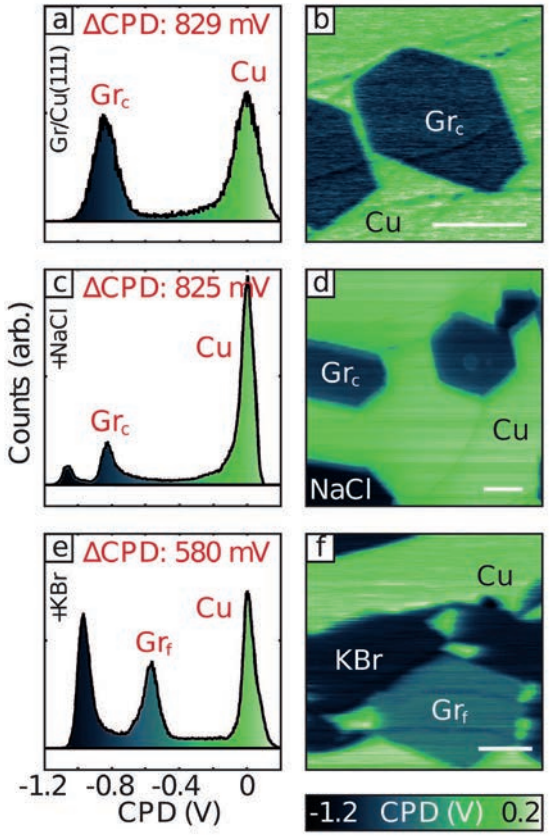

Fig. 2 Normalized histograms (left column) of KPFM images (right column). a,b) graphene reduces the work function of Cu(111). c,d) No change observed on co-adsorption of NaCl. e,f) On co-adsorption of KBr a shift was found for the ΔCPD. All scale bars are 100nm.

Modelling Absorption and intercalation

To model the observed effects, we performed density functional theory (DFT) calculations within the local Density Approximation (LDA) and optimized the structures of graphene and ML alkali halides adsorbed on Cu(111). The calculated equilibrium distances and binding energies obtained for graphene are in the typical range of physisorption (d=320pm, E_b=1.31eV/nm²). The adhesion of alkali halides on copper is stronger, almost twice that of graphene, and KBr and NaCl present very similar adsorption properties.

We investigated the possibility of intercalation by modelling bilayer adsorption. In particular, we compared the stability of the graphene/alkali-halides/Cu(111) and alkali-halides/graphen/Cu(111) systems. We found that the intercalation of alkali halides is more favourable than the intercalation of graphene, both in the case of KBr (by 1.81eV/nm²) and in the case of NaCl (by 1.75eV/nm²). The optimized structures of the most favourable intercalated systems are shown in figure 3. In the case of KBr intercalation, we notice an enhancement of the buckling within the KBr layer. This effect, most likely due to the K interaction with graphene, is absent in NaCl, whose adsorption geometry does not seem affected by the presence of graphene.

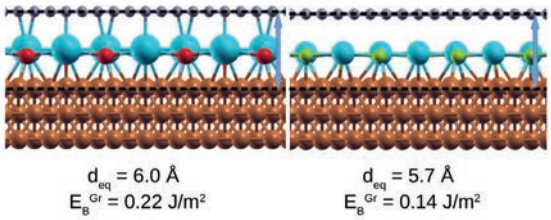

Fig. 3 Optimized configurations for alkali halides intercalation between graphene and Cu(111). The binding energy of graphene on the KBr/Cu (a) and NaCl/Cu (b) substrates is reported along with the graphene equilibrium distance relative to the Cu(111) surface.

Another important difference between the two intercalated structures of figure 3 is represented by the binding energy of graphene on the alkali-halide/Cu substrate, which is 1.37eV/nm² in the case of the KBr/Cu substrate and 0.87eV/nm² for the NaCl/Cu one. These results, along with the calculated binding energy for graphene on copper 1.31eV/nm², indicate that graphene adsorption is more favourable on the KBr/Cu substrate than on the bare metal.

Conclusion

Within this project we have shown experimentally and by DFT simulations that the intercalation of KBr between graphene and Cu(111) is more favourable than the intercalation of NaCl mainly due to the interaction of the alkali atoms.

References

[1] A. Sandin, T. Jayasekera, J.E. Rowe, K.W. Kim, M.B. Nardelli, D.B. Dougherty, *Multiple coexisting intercalation structures of sodium in epitaxial graphene-SiC interfaces*, Phys. Rev. B, **85**, 125410, (2012)

[2] A. Yurtsever et al., *Effects of Pb Intercalation on the Structural and Electronic Properties of Epitaxial Graphene on SiC*, Small, **12,** 3956, (2016)

[3] S. Sadewasser and Th. Glatzel (Eds.), *Kelvin Probe Force Microscopy Measuring and Compensating Electrostatic Forces,* Springer, (2011)

[4] L. Gao, J.R. Guest, N.P. Guisinger, *Epitaxial graphene on Cu(111)*, Nano Lett., **10**, 3512 (2010)

Design of polymer nanoreactors with triggered activity

Project P1209: Design of polymer nanoreactors with triggered activity
Project Leader: C.G. Palivan and J. Huwyler
Collaborator: T. Einfalt (SNI PhD Student)

Introduction

Mimicking biological processes, by engineering biomimetic nanostructures, is a fundamental concept relevant to various scientific fields such as materials science, chemistry, electronics and medicine. By using a bottom-up strategy of biomimicry it is possible to combine highly efficient and specific biological units (e.g. proteins, lipids, DNA) with robust synthetic materials (e.g. porous silica surfaces, block copolymers) [1]. In this way, compartmentalization found in cells can be imitated by biomimetic compartment platforms that contribute to progression from non-living materials to a living system.

Here, we introduce artificial organelles that are responsive to changes in intracellular redox potential (Fig. 1). These artificial organelles are obtained by encapsulation of enzymes inside nanocompartments named polymersomes and insertion of genetically modified membrane proteins in their membrane [2, 3]. Outer membrane protein F (OmpF) is chemically modified to attach a molecular cap, which serves to induce a stimuli-responsive behavior of the protein and transform it into a controlled "gate": in specific environmental conditions the pore of the modified OmpF (Ompf-M) is closed, and when they are changing, the cap is detached, restoring the molecular flow through OmpF pore [2]. Upon OmpF-M insertion in the membrane of polymersomes, and loading them with an enzyme, the resulting nanoreactor protects the enzyme and allows it to act *in situ*. This concept is suitable for intracellular functionality of such nanoreactors as artificial organelles.

Fig. 1 Concept of an artificial organelle based on a nanoreactor with triggered activity, which is produced by loading polymersomes with an enzyme and inserting a chemically engineered membrane protein to serve as "gate". Upon up-take, a change in the intracellular environment of the artificial organelles switches on the nanoreactor because it induces the release of the sensitive molecular cap (green dots) from the protein "gate" allowing the entrance of substrates (red dots), and the release of the products of the enzymatic reaction (yellow dots).

The proof of the concept has been successfully obtained by constructing nanoreactors with activity triggered by changes of pH in their environment [2]. A step further in enlarging this concept for other bio-relevant stimuli is based on attachment of molecular caps that can be detached by a change in the reductive conditions surrounding the nanoreactor. A triblock copolymer poly(2-methyl-oxazoline)-*block*-poly(dimethylsiloxane)-*block*-poly(2-methyloxazoline) served to produce polymersomes by self-assembly in dilute aqueous solution. Nanoreactors were prepared in the presence of horseradish peroxidase (HRP), and structurally modified OmpF-S-S-CF and were compared with polymersomes loaded with HRP without OmpF. HRP serves as catalyst to generate *in situ* a desired reduction sensitive reaction.

OmpF modification. First, two different molecular caps have been attached to thiol residues of the K89 R270 mutant of OmpF: i) SAMSA- carboxy-fluorescein (SAMSA-CF) (Scheme 1), and ii) bis-(2,2,5,5-tetramethyl- 3-imidazoline-1-oxyl-4-yl) di-sulfide. This step introduces the desired reduction responsive molecular cap, which is able of limiting the diffusion of molecules through the OmpF pore once attached to the cysteine residues.

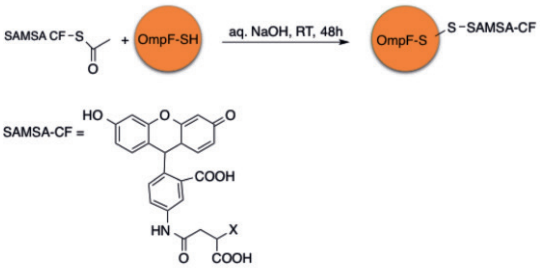

Scheme 1. Chemical modification of OmpF K89 R270 cysteine mutant with SAMSA-CF.

Design of the nanoreactors. Reductive-responsive nanoreactors were prepared from $PMOXA_6$-$PDMS_{44}$-$PMOXA_6$ copolymer, modified OmpF (OmpF-S-S-CF, OmpF-SH) and HRP in PBS buffer pH=7.4. They have been compared in terms of architecture and functionality with nanoreactors having OmpF-WT and polymersomes loaded with HRP but no OmpF. Non-encapsulated enzyme was removed from the nanoreactors by dialysis against PBS.

Characterization of the nanoreactors. A combination of transmission electron microscopy (TEM) and Static and Dynamic Light scattering (SLS, DLS) was applied to determine: (i) the architecture and size of the 3D assemblies, (ii) the influence of enzyme encapsulation and porin insertion of the self-

assembly process, and (iii) the stability of the poylmersomes/nanoreactors. The vesicular architecture of polymersomes and nanoreactors has been preserved even in the presence of milimolar amounts of reduction agents (glutathione) (Fig. 2). The average hydrodynamic radius of polymersomes and nanoreactors did not change upon addition of the reduction agent.

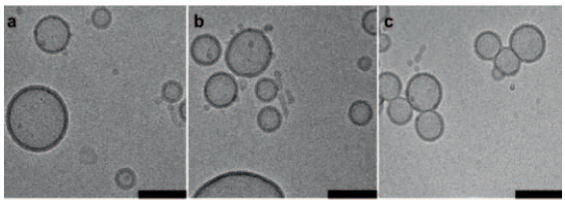

Fig. 2 Cryo-TEM micrographs of: a. nanoreactors without OmpF, B. nanoreactors with reconstituted OmpF-SH, and C. nanoreactors with reconstituted OmpF-S-S-CF. Scale bar = 100 nm.

Triggered activity of nanoreactors. We first investigated the specific binding of the SAMSA-CF fluorescent molecular cap to the thiol groups of OmpF-CA in order to determine whether the porin was appropriately modified with a reduction responsive cap and inserted into polymersomes (Fig. 3A).

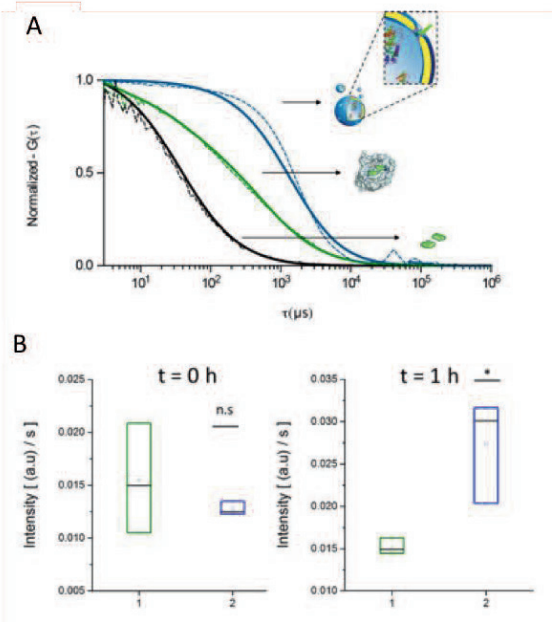

Fig. 3 A. FCS autocorrelation curves of SAMSA-CF: in PBS (Black), attached to OmpF-S-S and attached to OmpF-S-S- and inserted in the membrane of polymersomes (Blue). Dotted line – experimental auto correlation curves, Full line – fit. B. Substrate conversion kinetics of HRP loaded polymersomes equipped with different OmpFs: OmpF-S-S-CF (Green), OmpF-SH (Blue), Left: Directly after addition of 30mM glutathione, Right: 1 hour after addition of 30 mM glutathione.

Fluorescence correlation spectroscopy (FCS) indicates a significant difference in τ_d values between freely diffusing dye (SAMSA-CF) and polymersomes with reconstituted OmpF-S-S-CF, which showed that the molecular cap was successfully attached to the modified porin (Fig. 3A). The nanoreactors had a reduction triggered activity because the HRP product of the reaction has been released when the environment conditions of the nanoreactor changed and induced cleaving of the molecular cap (Fig. 3B).

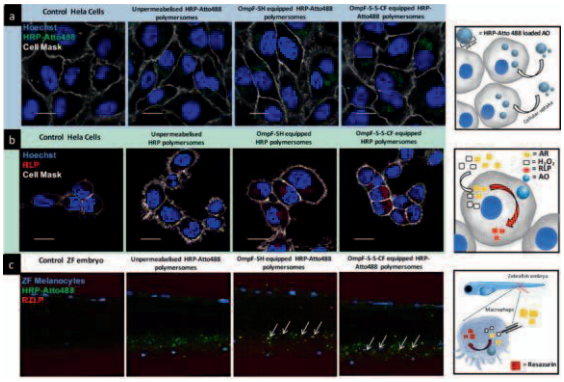

Fig. 4 Panel a: Cellular uptake of nanoreactors loaded with Atto-488 HRP (HeLa cells). Scale bar: 10μm. Panel b: Cellular uptake and intracellular activation of nanoreactors. Blue signal: Hoechst 33342 nucleus stain. Grey signal: CellMask Deep Red-Plasma membrane stain. Green signal: Atto-488 HRP. Red signal: resorufin-like product. Scale bar 20μm. Panel c: In vivo ZFE biodistribution and activity of nanoreactors – lateral view of the ZFE cross-section. Blue signal: ZFE melanocytes. Green signal: HRP-Atto488. Red signal: Resorufin-like product. Arrows show regions of enzymatic activity of AO.

Upon cellular integration, such nanoreactors with triggered functionality were capable of releasing the molecular cap blocking the OmpF porins and enabled the system to function as a stimuli responsive cell organelle. Zebra fish experiments (ZFE) indicate that the artificial organelles preserve their functionality *in vivo* (Fig. 4).

Conclusion. We designed nanoreactors with enzymatic activity triggered by a modified membrane protein serving as a stimuli-responsive gate. These nanoreactors have high potential for biosensing and therapeutic applications because they preserve functionality both *in vitro* and *in vivo*.

References

[1] M. Garni, T. Einfalt, M. Lomora, A. Car, C.G. Palivan, *Artificial Organelles: Reactions inside Protein–Polymer Supramolecular Assemblies, Chimia*, **70** (6), 424-427 (2016)

[2] T. Einfalt, R. Goers, A. Najer, I.A. Dinu, M. Spulber, O. Onaca-Fischer, C.G. Palivan, *Stimuli-Triggered Activity of Nanoreactors by Biomimetic Engineering Polymer Membranes,* Nano Letters, **15** (11), 7596-7603 (2015)

[3] C. Edlinger, T. Einfalt, M. Spulber, A. Car, W. Meier, C.G. Palivan, *Biomimetic Strategy to Reversibly Trigger Functionality of Catalytic Nanocompartments by the Insertion of pH-Responsive Biovalves*, Nano Letters, **9**, 5790-5798 (2017)

Nanowires as sensitive scanning sensors

Project P1210 Bottom-up nanowires as ultra-sensitive force transducers
Project Leader: M. Poggio and R.J. Warburton
Collaborator: D. Cadeddu (SNI PhD Student)

Introduction

In the final year of this project, we focused on a proof-of-principle demonstration, in which we use a quantum dot (QD) embedded in a nanowire (NW) tip a sensitive scanning sensor of electric field. Over the years, a number of nanoscale electric field sensors have been developed that can image single charges on surfaces. Due to intrinsic limitations of their electrical or mechanical detection schemes, however, most of these devices operate at frequencies below 1 kHz. Our experiments show a new type of scanning sensor based on an optically active semiconductor quantum dot, which promises to combine exquisite sensitivity and nanoscale resolution with record bandwidths. In addition to demonstrating the sensor's feasibility, we lay out the improvements required to take its performance to the physical limit. If further developed, this approach promises to enable measurements of charging dynamics and individual tunneling events in few electron and mesoscopic systems.

Quantum Fiber-pigtail

Semiconductor quantum-dots (QDs) are attractive single photon sources. They are robust, compact and provide on-demand single photons at rates in the GHz range. Their potential in the context of quantum optics however relies on the fulfillment of several demanding criteria: high efficiency, high photon purity, and simple operation. Recent progress has nevertheless brought QDs close to such applications. Single-photon operation has been obtained in a compact, table-top Stirling machine, offering a low-cost and user-friendly solution. Thanks to the increasing quality of the epitaxial material, spectrally pure emission has been demonstrated. The last challenge that needs to be addressed is to efficiently couple the emitted light into a single mode fiber. Great progress in this direction has been made with the integration of QDs into micro and nanoscale photonic structures, such as cavities and waveguides, which allow the control of spontaneous emission. In the last few years, important efforts to position the QD in an optimal way and to minimize the diffraction of light at the output of photonic NWs have pushed the collection efficiencies to values > 75% while maintaining a Gaussian spatial profile. These impressive results require, however, the use of objective lenses with large numerical apertures. In parallel, different strategies to couple the emitted light directly into a single mode fiber have emerged.

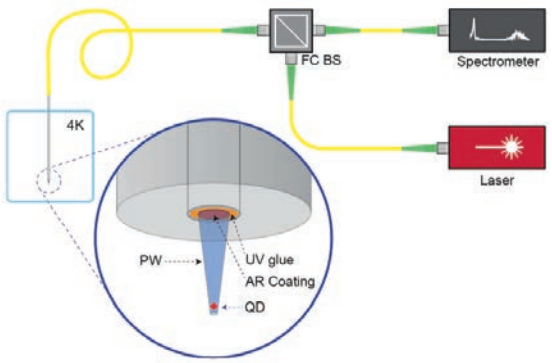

Fig. 1 The quantum fiber-pigtail is cooled down to 4K in liquid He. The QDs are excited with a CW laser diode (830 or 780 nm). The photoluminescence is analyzed with a spectrometer and a CCD camera (not shown) [1].

In the first part of this project, we realized the experimental realization of a quantum fiber-pigtail for convenient and efficient extraction of QD photons [1]. The device consists of a semiconductor quantum-dot embedded into a conical photonic wire that is directly connected to the core of a fiber-pigtail. We demonstrate a photon collection efficiency at the output of the fiber of 5.8% and suggest realistic improvements for the implementation of a useful device in the context of quantum information.

Scanning Electric-field Sensing

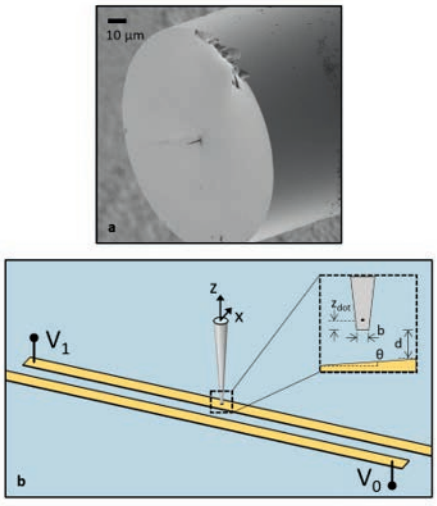

Fig. 2 (a) SEM of a quantum fiber-pigtail. (b) Schematic diagram of a quantum fiber-pigtail scanned above two patterned electrodes.

In the last year, we have focused on applying the quantum fiber-pigtail as a sensitive scanning sensor of electric field. Motivated by a desire to measure the electronic properties of surfaces and nano-objects, many nanoscale electric-field sensors have been developed over the years. Electrostatic force microscopy, scanning Kelvin probe force microscopy, sensing based on nitrogen-vacancy centers in diamond, and scanning single-electron transistors (SETs) have already established themselves as sensitive electric-field detectors reaching sub-elementary charge sensitivity and sub-nanometer spatial resolution. The most sensitive of these devices, the scanning SET, typically operates below 1 kHz due to the high intrinsic resistance of the SET and the capacitive load of the leads. This slow operation speed also exposes the sensor to $1/f$ charge noise, which limits its sensitivity to $10^{-4}\ e/\sqrt{\mathrm{Hz}}$ within 100 nm of the probe. Although radio frequency SETs achieve bandwidths in excess of 100 MHz and 100 times better sensitivity than conventional SETs, so far, they have been realized only as on-chip electrometers not amenable to spatial scanning.

In 2015, Wagner et al. used a noncontact atomic force and scanning tunneling microscope functionalized with a single molecule to image the dipole field of an adatom on a surface [3]. This first demonstration of scanning QD microscopy (SQDM) registered single-electron charging events of a molecular QD to produce three-dimensional images of the local electrostatic potential with sub-nanometer resolution. In transport experiments, gate-defined QDs are employed as single-charge detectors, and self-assembled QDs are employed as all-optical electrometers, demonstrating a sensitivity of 5 Hz. These kind of QDs are also used to determine the position of single-defect charges within 100 nm of a QD with a precision of 5 nm. Electric fields in QDs produce large Stark shifts, which, due to a built-in electric dipole, are nearly linear around zero field. Nevertheless, a scanning electric-field sensor based on an optically active semiconductor QD had not yet been realized. Such SQDM has the potential for a very large bandwidth, which, unlike electronic and mechanically addressable sensors, is limited only by the spontaneous emission rate of the QD and could therefore approach the gigahertz range.

In the last year, we showed the proof-of-principle application of an optical fiber-coupled semiconductor QD as a scanning electric-field sensor [2]. By tracking the induced energy shift on the peak of a single transition of a QD, we map the vertical component of an external applied field. Our device is composed of a self-assembled InAs QD located in the tip of a fiber-coupled GaAs photonic wire. The QD emits preferentially into the waveguide mode, which expands adiabatically through a tapering of the photonic wire and ensures good out-coupling. The design of the photonic wire ensures both efficient guiding of the QD fluorescence as well as proximity of the QD to the sample, which is a necessary condition for scanning probe microscopy. With the help of numerical simulations, we also investigate the unavoidable perturbation of the external field due to the dielectric nature of the probe, pointing toward geometric improvements to reduce this effect and increase sensitivity.

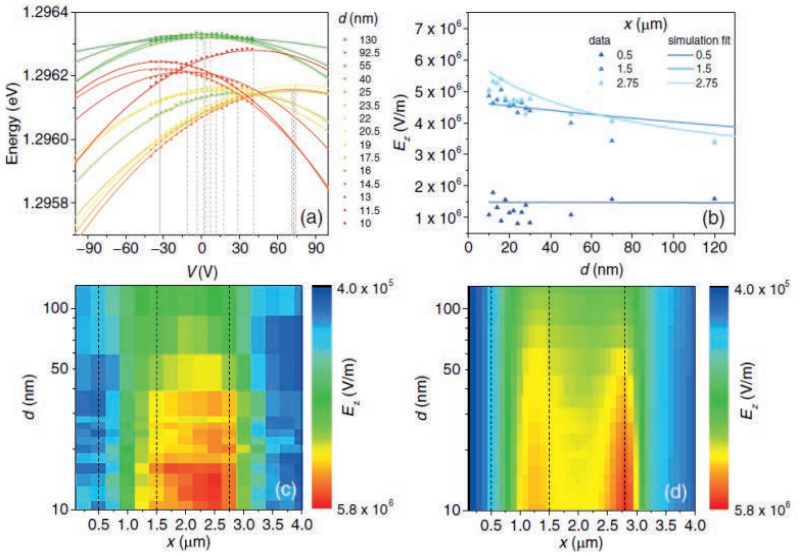

Fig. 3 Experimental results. (a) Energy of the QD emission peak vs the applied voltage V for different values of tip-electrode distance d. Solid lines are parabolic fits, and gray dashed lines indicate the vertices of each parabola. The tip is positioned at the center of the electrode (x = 2 μm). (b) Triangles represent E_z as a function of d at V = 40 V extracted from the curvature fits for different x positions; solid lines show corresponding simulated values of E_z. Full maps of E_z as a function of x and d at V = 40 V extracted from (c) measurements and (d) simulations. Simulations consider a z_{dot} = 110 nm with b ¼ 350 nm and a tilt angle of 5°. Black dashed lines correspond to the line cuts in (b). In both (b) and (c), each point requires 21 s of measurement time; the full map in (c) requires 68 min [2].

References

[1] Cadeddu et al. *A fiber-coupled quantum-dot on a photonic tip*. Appl. Phys. Lett. **108**, 011112 (2016)

[2] D. Cadeddu, M. Munsch, N. Rossi, J.M. Gerard, J. Claudon, R.J. Warburton, M. Poggio, *Electric field sensing with a scanning fiber-coupled quantum dot,* Phys. Rev. Appl. **8**, 031002 (2017)

[3] C. Wagner, M.F.B. Green, P. Leinen, T. Deilmann, P. Kruger, M. Rohlfing, R. Temirov, F.S. Tautz, *Scanning Quantum Dot Microscopy*. Phys. Rev. Lett. **115**, 026101 (2015)

Electron optics in encapsulated graphene

Project P1211 Electrical properties of ultraclean suspended graphene
Project Leader: C. Schönenberger and D. Zumbühl
Collaborators: C. Handschin (SNI PhD Student), P. Rickhaus, and P. Makk

Motivation

The excitement around graphene during the last decade can be attributed to several unique electronic properties. For example, the linear dispersion relation of the charge carriers, which makes electrons to behave as photons, the helical nature of charge carriers mimicking a Dirac system, the vanishing density of states at the Dirac point where conduction and valence bands touch, or the high mobility and ballistic electron motion with mean-free paths that can reach and exceed several micrometers, yielding highly conducting layers.

Research has shown, that in order to access the interesting physics of pristine graphene, the environmental influences (potential fluctuations from the substrate, unintentional chemical doping etc.) have to be reduced to a minimum. Currently the two most prominent techniques to obtain "clean" graphene are to either suspend the graphene freely or to encapsulate it between hexagonal boron-nitride (hBN), which like graphene is a layered material but a non-conducting one. Even though suspended graphene yields the highest graphene quality, the device geometries which can be realized are rather limited [1]. This can be circumvented by encapsulating graphene in hBN. Encapsulation of graphene in hBN holds several additional advantages, such as the possibility to create a superlattice in graphene with hBN [2], or to establish more complex device geometries. This can include multiple electrostatic gates and electrical contacts of different types, such as one-dimensional side-contacts [3], but as well inner point contacts [4]. Even though inner point contacts were realized in suspended devices via air-bridges, this is significantly simpler to achieve in encapsulated devices, as we have shown in [4].

Co-existence of classical snake states and Aharanov-Bohm oscillations along graphene *p-n* junctions

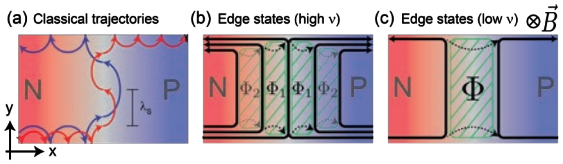

Fig. 1 ***Concept of snake states and Aharanov-Bohm interference along a graphene p-n junction. a,*** *Snake states seen in the framework of classical skipping orbits for two different magnetic field values (blue and red trajectories).* ***b,c,*** *Principle of Aharonov-Bohm interferences between edge-states propagating along a graphene p-n interface at high (b) and low (c) filling factors (ν).*

Snake states and Aharanov-Bohm (AB) interferences are examples of magnetoconductance oscillations, which can be observed along a graphene *p-n* junction as sketched in figure 1. They have been proposed as the cause of observed oscillations in both suspended and encapsulated devices. However, it is presently not clear whether the observed oscillations were properly assigned, since in previous works typically only *one* kind of oscillation was present with the difficulty that the signatures of snake state and AB oscillations are very similar. So far, snake state and AB oscillations were thought to be mutually excluding and therefore discussed independently, using either the picture of classical skipping trajectories or quantum Hall edge states – two models which seem to be based on different physical concepts.

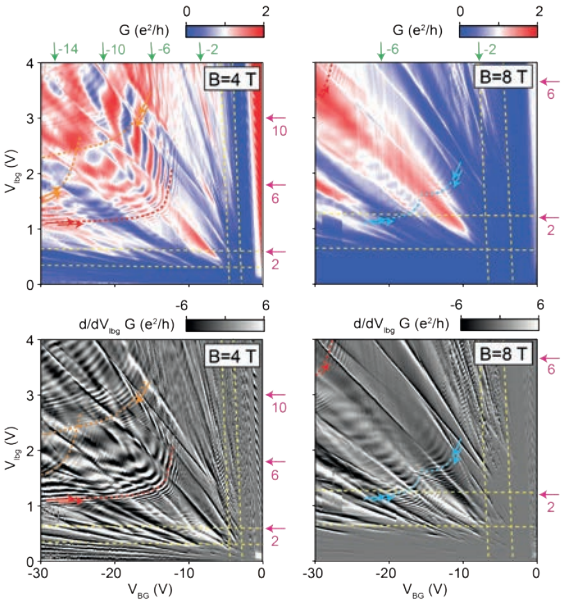

Fig. 2 ***Conductance and its numerical derivative of a p-n junction in the bipolar regime for two selected magnetic fields.*** *The filling factors are given in green for the cavity tuned by the global back-gate (horizontal axis) and in purple for the cavity tuned by the local bottom-gate (vertical axis). Note, that the two gates tune the carrier densities in the two regions of the pn junction. The yellow, dashed lines indicate filling factors 1 and 2. The different types of magnetoconductance oscillations are indicated with the red, orange and cyan arrows/dashed lines. It turns out the oscillation at intermediate filling factors (the red one) is due to snake state motion, while the other ones are AB oscillations. Red would correspond to Fig. 1(a), orange to (b) and blue to (c).*

We have recently observed simultaneously three partially overlapping oscillations in a single hBN encapsulated pn junction, (Fig. 2, indicated with the red, orange and cyan dashed lines), allowing a direct comparison of the latter. We analyzed them with respect to their charge carrier density (Fig. 2),

magnetic field, temperature and bias dependence in order to assign them to either snake state or AB oscillations. Surprisingly, we found that snake state and AB oscillations can co-exist within a limited parameter range.

Triggered by the co-existence of these effects within our measurements, we have put forward a physical picture based on the mixing of Landau levels at the edge of the sample and along the pn junction, in which both effects are compatible with each other. The mixing is thought to be due to edge disorder in the first case, while it is due to the electric field in the pn region in the latter. Such a mixing can yield both an AB oscillation and a periodic motion of the center of the wave package mimicking the classical snake motions. These results are currently written up.

Giant Valley-Isospin Conductance Oscillations in Ballistic Graphene

Besides the snake state and AB oscillations, we observed another type of magnetoconductance oscillation within the bipolar regime at high magnetic fields. In contrast to the snake state and the AB oscillations, the latter depend on the valley-degree of freedom (which is commonly denoted with K, K') of the charge carriers in graphene.

If a *p-n* junction is formed perpendicular to the graphene edges, similar to the situation required for the observation of snake state and AB oscillations, the quantum Hall channels co-propagate along the *p-n* junction (Fig. 3a). It has been predicted by Tworzidło and co-workers that if only the lowest Landau level is filled on both sides of the *p-n* junction, the conductance is determined by the valley (isospin) polarization at the edges and by the width of the flake [5]. This effect remained hidden so far due to scattering between the channels co-propagating along the *p-n* interface (equilibration).

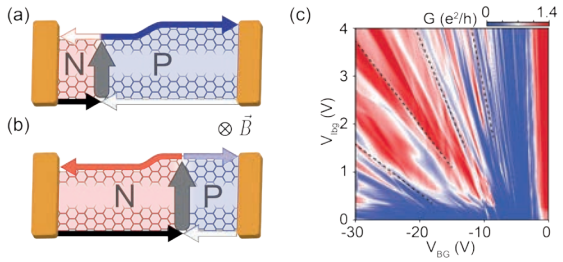

Fig. 3 ***Valley-isospin dependent conductance of a (simplified) two-terminal p–n junction at high magnetic fields. a,b,*** *Charge carriers are injected at the bottom-edge (black arrow) and guided along the p-n junction to the top-edge (grey arrow). Depending on the number of unit-cells between bottom and top edge, the charge carrier is either fully transmitted (a) or partially reflected (b).* ***c,*** *Conductance as a function of the two electrostatic gates at B = 8 T. The valley-isospin oscillations are visible in the form of radial fringes converging to the common CNP. The black, dashed lines are a guide to the eye showing the oscillation maximum for selected valley-isospin oscillations.*

In this study, we investigated *p-n* junctions with a movable *p-n* interface with which we were able to probe the local edge configuration of graphene flakes. We observed large quantum conductance oscillations on the order of e^2/h which solely depend on the *p-n* junction position (Fig. 3c), providing the first signature of isospin-defined conductance oscillations.

Our experiments were underlined by quantum transport calculations, which were performed by M.H. Liu from the University of Regensburg. Although we had no control on the exact edge character of the flake, the conductance was still defined by the local properties of the edges and the local width of the flake, in agreement with transport simulations. Furthermore, we could exclude that the equilibration between edge channels at the intersection between the *p-n* junction and the graphene edges (so-called hot-spots) were responsible for the conductance oscillations. We observed similar oscillation in more than 15 *p-n* and *p-n-p* junctions, some of them also having naturally cleaved graphene flakes (were there are presumably less edge defects compared to reactive ion etching), and also on suspended *p-n* junctions.

Finally, there are new techniques appearing, such as hydrogen-plasma etching or chemical synthesis of GNRs, allowing for a much better control over the edges. This could be used in further studies to draw a correlation between transport measurement and the edge of the measured samples (e.g., via atomic resolution imaging) underlining the isospin origin of these oscillations.

These results were published in Nano Letters [6].

We thank M. H. Liu and Klaus Richter from the University of Regensburg for the collaboration, supporting this work with tight-binding simulations. High-quality hBN was provided by K. Watanabe, T. Taniguchi from the National Institute for Material Science at Tsukuba, Japan.

References

[1] R. Maurand, P. Rickhaus, P. Makk, S. Hess, E. Tovari, C. Handschin, M. Weiss, C. Schönenberger, *Fabrication of ballistic suspended graphene with local-gating*, Carbon **79**, 486 (2014)

[2] C. Handschin, P. Makk, P. Rickhaus, M-H. Liu, K. Watanabe, T. Taniguchi, K. Richter, C. Schönenberger, *Fabry-Pérot Resonances in a Graphene/hBN Moiré Superlattice*, Nano Lett. **17**, 328 (2016)

[3] L. Wang et al. *One-Dimensional Electrical Contact to a Two-Dimensional Material,* Science **342**, 614-617 (2013)

[4] C. Handschin, B. Fülöp, P. Makk, S. Blanter, M. Weiss, K. Watanabe, T. Taniguchi, S. Csonka, C. Schönenberger, *Point contacts in encapsulated graphene*, APL **107**, 183105 (2015)

[5] J. Tworzidło, I. Snyman, A. Akhmerov, C. Beenakker, *Valley-isospin dependence of the quantum Hall effect in a graphene p-n junction*, PRB. **76**, 035411 (2007)

[6] C. Handschin, P. Makk, P. Rickhaus, R. Maurand, K. Watanabe, T. Taniguchi, K. Richter, M-H. Liu, C. Schönenberger, *Giant Valley-Isospin Conductance Oscillations in Ballistic Graphene*, Nano Lett. **17**, 5389 (2017)

Deterministic enhancement of coherent photon generation from a nitrogen-vacancy centre in ultrapure diamond

Project P1212 Nano-photonics with diamond (comb.12)
Project Leader: R.J. Warburton and P. Maletinsky
Collaborators: D. Riedel (SNI PhD Student), I. Söllner, B. J. Shields, P. Appel, and S. Flågan

The nitrogen-vacancy (NV) center in diamond has a coherent spin but emits incoherent photons. The main problem is that the probability of photon-free emission is small: in most cases, photon emission is accompanied by the creation of a phonon. The so-called zero-phonon-line (ZPL) accounts for just 3% of the emission. In the creation of spin-photon and spin-spin entanglements, only the ZPL process is useful.

A crucial insight is that the small ZPL fraction is not set in stone: it can be changed by engineering the photonic density of states. A peak in the density of states can be created with a cavity. Specifically, in a micro-cavity tuned to the ZPL frequency, emission into the ZPL is accelerated, thereby boosting the ZPL fraction. The physics is described with the Purcell effect, equivalently the weak coupling regime of cavity-QED. Theory suggests that even a micro-cavity with modest Q-factor is sufficient.

The potential enhancement of the ZPL fraction via a micro-cavity has been known for some time and there are several experiments along these lines. Serious problems related to the nano-fabrication arise. A photonic crystal cavity represents an extreme case. Creation of a diamond photonic crystal cavity (etched holes in a diamond membrane) requires aggressive etching – diamond is a very hard material – such that the optical properties of the NV centers degrade. Typically, large spectral wanderings are observed. Also, diamond photonic crystal cavities have small Q-factors. Under these circumstances, the micro-cavity can easily degrade rather than enhance the quality of the photons.

In this SNI project, we have opted for a new approach. Diamond fabrication is kept to the absolute minimum. We fabricate diamond membranes, a few hundred nanometers thick, from high-quality, single-crystal starting material. The optical properties of NV centers in the membrane are good, not yet perfect, but good enough. The micro-cavity consists of a highly miniaturized Fabry-Perot cavity. The diamond membrane is bonded (simply via a van der Waals force) to a planar dielectric mirror; the micro-cavity is completed with a curved dielectric mirror with radius of curvature 10-20 μm (Fig. 1). The curved mirror is positioned about a micron above the diamond membrane.

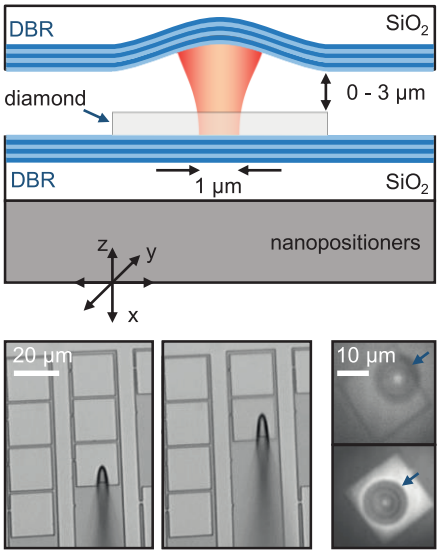

Fig. 1 Top: Schematic of the tunable micro-cavity containing a diamond membrane. Bottom left: detaching a 20 x 20 μm² membrane with a micro-manipulator. Bottom right: bird's-eye view of the curved mirror positioned above the diamond membrane.

Compared to a photonic crystal cavity, the Q-factor is much higher: we achieve values close to 10^5. The mode volume V with respect to a photonic crystal cavity is also much higher. Nevertheless, the Q:V ratio is favorable. A final point is that the micro-cavity can be widely tuned *in situ*, a feature not shared by a photonic crystal cavity or other form of monolithic device. This enables us to bring each NV center into resonance with the micro-cavity mode.

Implementing this idea required, first, the creation of diamond membranes. They were used initially to create an antenna structure. It was shown that the antenna directs most of the NV emission into a medium-angle cone in the forward direction [1]. Second, miniaturized Fabry-Perot cavities were designed, realized and tested [2]. The potential of the micro-cavities was explored initially with semiconductor quantum dots, emitters with large optical dipole moments [3]. Subsequently, curved mirrors with sub-10 μm radii were fabricated [4]. Finally, a cryogenic micro-cavity system was developed for the NV center wavelength, 637 nm.

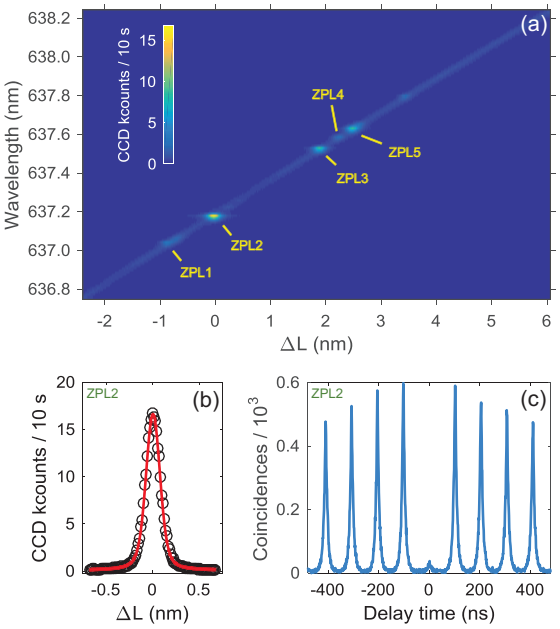

Fig. 2 (a) Photoluminescence (PL) spectra around the ZPL transition as the cavity length L is changed. Each resonance corresponds to the ZPL emission of a single NV center. (b) Integrated PL versus ΔL to determine the Q-factor of the cavity, 60,000. (c) Auto-correlation of the PL from ZPL2 (pulsed excitation) showing a clear anti-bunching at zero delay.

All these components were brought together into a common experiment [5]. Figure 2a shows the emission as a function of cavity length. There are clear resonances, each corresponding to a single NV center as demonstrated in the auto-correlation experiment (Fig. 2c). There is a clear Purcell effect, a dependence of the radiative lifetime on cavity detuning (Fig. 3a). Each ZPL exhibits a Purcell effect (Fig. 3b, c).

The overall Purcell factor is 2.0. This modest factor masks the profound changes at the emitter level. Emission into the plethora of lateral, "leaky" modes is not inhibited by this cavity design. Instead, the cavity relies entirely on boosting the emission into a single vertical mode. This boost must be very strong in order to have any effect on the overall emission rate. An analysis of the experimental data shows that the ZPL fraction increases from 3% to close to 50% in this experiment [5].

The main deficiency of this experiment was the loss in the dielectric mirrors which reduces the signal from the individual ZPLs. This will be rectified by using "super" mirrors for which the technology is already well developed. With resonant excitation, efficient photon generation is also hindered by the spectral wanderings of the ZPLs. It is hoped that membrane fabrication can be optimized with respect to this parameter. Once these issues have been addressed, the future goals are to generate coherent single photons from single NV centers and to demonstrate an efficient spin-photon interface.

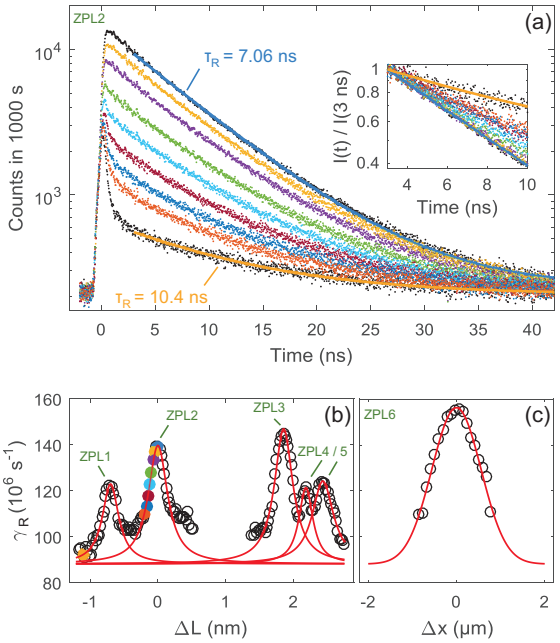

Fig. 3 (a) Decay curves following pulsed excitation of ZPL2 as a function of ΔL. The NV is located at the anti-node of the micro-cavity. (b) Recombination rate versus ΔL for a fixed lateral position. (c) Recombination rate versus lateral position for zero spectral detuning.

References

[1] D. Riedel, D. Rohner, M. Ganzhorn, T. Kaldewey, P. Appel, E. Neu, R.J. Warburton, P. Maletinsky, *Low-Loss Broadband Antenna for Efficient Photon Collection from a Coherent Spin in Diamond*, Phys. Rev. Appl. **2**, 064011 (2014)

[2] L. Greuter, S. Starosielec, D. Najer, A. Ludwig, L. Duempelmann, D. Rohner, R.J. Warburton, *A small mode volume tunable microcavity: Development and characterization*, Appl. Phys. Lett. **105**, 121105 (2014)

[3] L. Greuter, S. Starosielec, A.V. Kuhlmann, R.J. Warburton, *Towards high-cooperativity strong coupling of a quantum dot in a tunable microcavity*, Phys. Rev. B **92**, 045302 (2015)

[4] D. Najer, M. Renggli, D. Riedel, S. Starosielec, R.J. Warburton, *Fabrication of mirror templates in silica with micron-sized radii of curvature*, Appl. Phys. Lett. **110**, 011101 (2017)

[5] D. Riedel, I. Söllner, B.J Shields, S. Starosielec, P. Appel, E. Neu, P. Maletinsky, R.J. Warburton, *Deterministic Enhancement of Coherent Photon Generation from a Nitrogen-Vacancy Center in Ultrapure Diamond*, Phys. Rev. X **7**, 031040 (2017)

Photo-driven hydrogen production based on molecular nanofactories

Project P1213 Artificial metalloenzymes for molecular nanofactories
Project Leader: T.R. Ward and S. Panke
Collaborators: S. Keller (SNI PhD Student), T. Heinisch, B. Probst, and R. Alberto

Introduction

Splitting water into O_2 and H_2 using sunlight as an energy source offers an attractive means to address the World's growing need for energy. Renewable, clean energies including solar, wind- or hydroelectric-power plants are widely produced but generate electric energy, whose storage is challenging. A more economical way to store energy is within chemical bonds. It is desirable to produce an energy carrier that can be liquefied or transported as a gas. Hydrogen gas can be produced by a multitude of ways on an industrial scale, yet most of them rely on carbon sources, precious metal catalysts and are not energy efficient. Nature provides us with highly specialized enzymes known as hydrogenases [1]. These natural enzymes can be found in a variety of bacterial and archaeal organisms, where they discharge reducing equivalents in the form of H_2 or oxidize H_2 in reactions that require a reductant. These enzymes operate without the need of a high over-potential, at high reaction rates (1,500 – 20,000 turnovers per second) and under physiological conditions at pH 7 and 37°C in water. These hydrogenases are highly evolved, and contain specialized proton, dihydrogen and electron channels to deliver the substrates and extract the product. Most importantly these natural hydrogenases rely on earth-abundant metals (i.e. Ni and Fe), but require complex maturation machineries to assemble and display modest stabilities under non-physiological conditions. Furthermore, their oxygen sensitivity and production costs call for the development of artificial hydrogenases. There are many small molecule catalysts reported that mimic the catalytic center of hydrogenases, yet these catalysts hardly achieve the efficiency of hydrogenases. Thus, an incorporation into a protein scaffold could increase the efficiency of those small molecule catalysts. One possible way to incorporate a small molecule hydrogenase mimic into a protein is the biotin-streptavidin technology [2]. In the past decade, this technology has found widespread use for the assembly of artificial metalloenzymes (ArM) [3]. Streptavidin (Sav) is a remarkably stable and versatile homotetrameric protein (4 x 159 amino acids, ca. 65 kDa). Each of the four monomers can bind one equivalent of biotin with a supramolecular binding affinity of ca. 10^{13} M^{-1}, thus representing one of the strongest non-covalent bonds in nature. This feature offers the possibility to anchor an abiotic cofactor within a protein environment to create artificial metalloenzymes. We set out to incorporate a small molecule, Co-based hydrogen-evolution catalyst [CoBr(appy)-OH]Br that was biotinylated to [CoBr(appy)-Biot]Br into the protein (Fig. 1) [4].

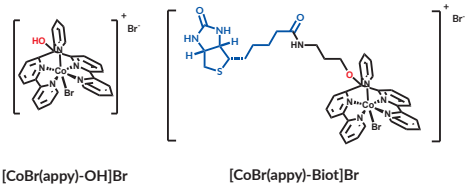

Fig. 1 Co-based hydrogen evolution catalyst [CoBr(appy)-OH]Br and its biotinylated congener [CoBr(appy)-Biot]Br with its biotin anchor (blue) for the localization within streptavidin.

We were able to obtain a crystal structure with the incorporated catalyst in a K121A mutation (Fig. 2). The residues S112 and K121 that lay in close proximity of the metal cofactor are known to show impact on catalysis.

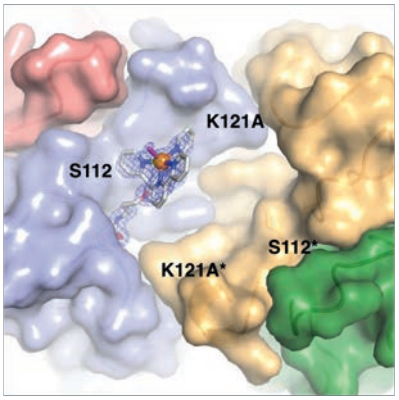

Fig. 2 Close-up view of the active site in the crystal structure of complex [CoH₂O(appy)-Biot] • Sav-K121A. The protein is displayed as surface and cartoon model and the cofactor as stick model. The orange sphere indicates a cobalt, the magenta stick a water molecule and the four monomers are displayed in different colours.

To compare the activity of the Co-precursor [CoBr(appy)-OH]Br and its biotinylated analogue [CoBr(appy)-Biot]Br, argon-flushed, buffered (pH = 5) aqueous solutions were charged with 5 µM catalyst, 1 M AscOH (sacrificial electron donor), 100 µM $[Ru(bpy)_3]Cl_2$ (photosensitizer) and were irradiated with a LED (453 nm). With no Sav present, both [CoBr(appy)-Biot]Br (black trace) and [CoBr(appy)-OH]Br (blue trace) display similar turnover numbers after 6.5 hours (Figure 3). Addition of SavWT (10 µM free biotin binding sites) did not impact the activity of [CoBr(appy)-OH]Br (grey trace). In contrast, the biotinylated HEC, bound to SavWT (green trace), displayed a significant decrease in activity highlighting the impact of second coordination sphere interactions on its hydrogenase activity.

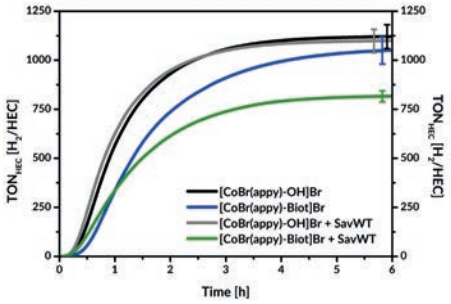

Fig. 3 Hydrogen evolution profile of the parent and the biotinylated complex with and without Sav: [CoBr(appy)-OH]Br (black trace), [CoBr(appy)-OH]Br with Sav WT (grey trace), [CoBr(appy)-Biot]Br (blue trace) and [CoBr(appy)-Biot]Br with Sav WT (green trace).

Then, we explored the impact of the second coordination sphere of Sav by screening a library of Sav single point mutants in positions S112 and K121. As displayed in figure 4, substitution of the serine residue S112 by either an Asp (Sav S112D, light green trace) or a Arg (Sav S112R, turquoise trace) lead to an increase in TON compared to SavWT (green trace).

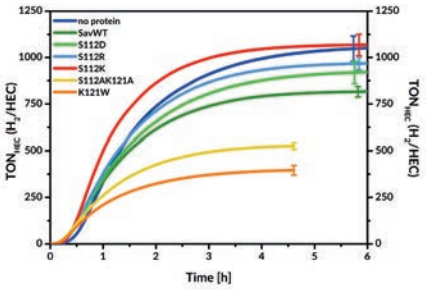

Fig. 4 Genetic optimization of the hydrogenase activity for [CoBr(appy)-Biot]Br in the presence of a variety of Sav mutants: no protein (blue trace), SavWT (green trace), Sav S112D (light green trace) Sav S112R (turquoise trace), Sav S112K (red trace), Sav S112AK121A (yellow trace) and Sav K121W (orange trace).

We speculate that this might be due to the presence of close lying aminoacids capable of acting as a proton relay, potentially facilitating outer-sphere protonation of the Co-H species, as suggested in related studies. This was confirmed by the improved activity of the S112K mutant (Ser → Lys) which displays the highest activity (red trace). To further investigate the critical role of residues capable of donating protons in the proximity of the Co–H moiety, the double mutant Sav S112AK121A, in which both the naturally occurring serine and lysine at position S112 and K121 were mutated to alanine, displays a marked decrease in activity (yellow trace). Replacement of the lysine by tryptophan (Sav K121W) shows an even higher erosion in activity (orange trace).

Not only the turnovers are higher when the lysines were present, but also the rates increased, upon screening at different pHs (Fig. 5).

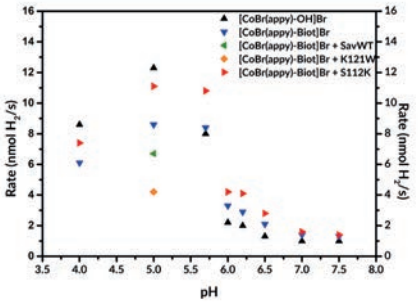

Fig. 5 Maximum dihydrogen production rates determined as a function of pH for [CoBr(appy)-OH]Br (black triangles) and [CoBr(appy)-Biot]Br • Sav S112K (red triangles), [CoBr(appy)-Biot]Br • Sav WT (green triangles), [CoBr(appy)-Biot]Br • Sav K121W (orange squares) and [CoBr(appy)-Biot]Br (blue triangles). The pH values were screened in buffered solutions.

At pH 4 and pH 5 [CoBr(appy)-OH]Br displays higher maximal rates than the biotinylated form [CoBr(appy)-Biot]Br either inside or outside the Sav S112K. Increasing the pH above 5.0, leads to an inversion in trend: at pH 5.7 the [CoBr(appy)-Biot]Br • Sav S112K displays the highest rates and turnover numbers. At pH values between 6 and 7.5 the dihydrogen production rates follow the following order: [CoBr(appy)-Biot]Br • Sav S112K > [CoBr(appy)-Biot]Br > [CoBr(appy)-OH]Br .

Conclusion and Outlook

We could demonstrate that incorporation of a biotinylated, molecular hydrogen evolution catalyst into the streptavidin mutant S112K as a protein scaffold effects its activity in a positive way. The nanocatalyst embedded within the protein not only showed higher turnovers at specific pH values but also higher maximum rates.
These findings suggest that such biohybrid nanofactories may readily be optimized by genetic means. Future studies will focus on applying directed evolution optimization schemes to improve the hydrogenase activity.

References

[1] W. Lubitz, H. Ogata, O. Rüdiger, E. Reijerse, O. Rüdiger, E. Reijerse, *Hydrogenases*, Chem. Rev. **114**, 4081 (2014)

[2] T. R. Ward, *Artificial Metalloenzymes based on the Biotin-Avidin Technology: Enantioselective Catalysis and beyond* Acc. Chem. Res. **44**, 47 (2011)

[3] F. Schwizer, Y. Okamoto, T. Heinisch, Y. Gu, M. M. Pellizzoni, V. Lebrun, R. Reuter, V. Köhler, J.C. Lewis, T.R. Ward, *Artificial Metalloenzymes: Reaction Scope and Optimization Strategies*, Chem. Rev. DOI:acs.chemrev.7b00014 (2017)

[4] C. Bachmann, M. Guttentag, B. Spingler and R. Alberto, *3d Element Complexes of Pentadentate Bipyridine-Pyridine-based Ligand Scaffolds: Structures and Photocatalytic Activities*, Inorg. Chem. **52**, 6055 (2013)

A miniaturised hybrid ion-atom chip trap

Project P1214 An ion-atom hybrid trap on a chip
Project Leader: S. Willitsch and P. Treutlein
Collaborators: I. Rouse (SNI PhD Student), A. Mokhberi, and R. Schmied

Introduction

Under typical laboratory conditions, studying the behaviour of a single atom would be next to impossible. At room temperature, particles move at hundreds of metres per second and constantly exchange energy with their surroundings, randomising their trajectory and making them difficult to locate amongst the vast number of other particles present. Under these circumstances, determining the precise mechanism of a chemical reaction or producing the desired quantum states required for applications in quantum computation is a big challenge.

The solution is to remove all the unwanted atoms and molecules, trap the particle of interest in a small region of space, and reduce their energy as far as possible. The first step is done by performing experiments in an ultra-high vacuum generated using a combination of mechanical and chemical pumps, while the motion of the particle can be slowed by exploiting laser- and advanced cooling techniques. Trapping particles requires different methods depending on the nature of the particle. Neutral atoms may be confined using magnetic fields, while for charged particles (ions) electric fields are used to control their motion.

A far greater range of experiments can be carried out when different types of particles are trapped together. “Hybrid” traps combining different trapping technologies have previously been demonstrated [1], allowing for ions and atoms to interact under controlled conditions. These macroscopic devices, however, are limited in terms of the degree of control over the particles that can be achieved. Miniaturisation of the hybrid trap would allow for more precise manipulation of the particles, and chip-based architectures for the separate trapping of ions or atoms have been shown to be highly effective at providing this control.

In this report, we present an overview of the development of a hybrid ion-atom chip trap designed to enable experiments to be performed on small ensembles of ultracold calcium ions and rubidium atoms, confined by precisely shaped electromagnetic fields and cooled to temperatures a fraction of a degree above absolute zero. This device offers a flexible platform for studying the fundamental interactions of charged and uncharged particles underpinning elementary chemical reactions [1] and a route to novel hybrid quantum systems. Furthermore, we also present recent developments in our analytical theory for describing the statistical mechanics of an ion interacting with a cloud of ultracold atoms, allowing for more precise control and interpretation of experiments carried out using the chip [2, 3].

Construction of the hybrid chip

Charged particles are confined through a combination of static and time-varying electric potentials, which in the case of the hybrid chip are generated by applying voltages to the gold-plated electrodes forming the upper layer. These electrodes are formed by the evaporation of gold onto a ceramic wafer and were produced in collaboration with CSEM and FHNW. Electrical connections to the electrodes are established by wirebonding these to a printed circuit board (PCB), which additionally contains a series of wires designed to produce the magnetic fields required to trap neutral atoms. By changing the current passing through each wire, the resulting magnetic fields can be precisely shaped in order to produce a variety of trapping potentials.

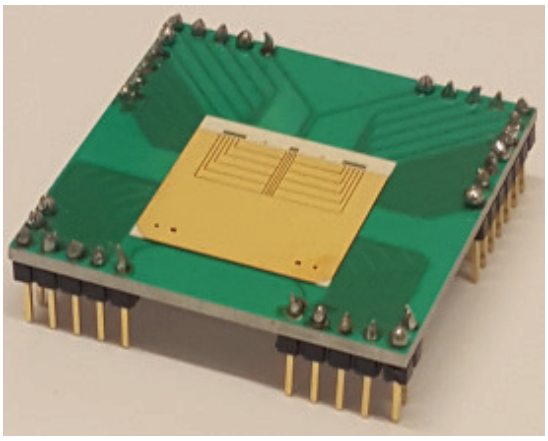

Fig. 1 A photograph of the completed hybrid chip. The gold electrodes produce electric fields for trapping charged particles, while the wires on the printed circuit board generate magnetic fields for the control of neutral atoms.

The neutral atoms must be initially cooled before they have a sufficiently low energy to be trapped by the magnetic fields generated by the chip. For this purpose, a copper U-bar is integrated into a heat sink below the PCB. By combining the magnetic field generated by current flowing through this U-bar with laser light reflected from the surface of the chip, a magneto-optical trap (MOT) is formed allowing for the capture of rubidium atoms from background vapour. Once these have been sufficiently cooled, they are transferred to a second MOT generated by the chip wires and are then compressed into a smaller trap to undergo evaporative cooling in order to reach even lower temperatures. The atoms are then transported to the location of the calcium ions via a moving magnetic “conveyer belt” potential so that the two species can interact.

An additional benefit of the miniaturised trap compared to previous macroscopic versions is that it is directly integrated into the vacuum chamber as one of the walls, greatly reducing the overall volume that needs to be pumped to produce the ultra-high vacuum conditions necessary for trapping particles. For this purpose, a fused silica cuvette was glued onto the hybrid chip using vacuum compatible epoxy. The result is a compact vapour cell which requires only a small, vibration-free ion pump to maintain vacuum during operation of the chip, eliminating the vibrations or chemical contamination associated with the pumps required to produce vacuum in larger systems. Furthermore, this setup provides a high degree of optical access for the lasers required to cool the atoms and also enables imaging of the trapped particles from a wide range of angles.

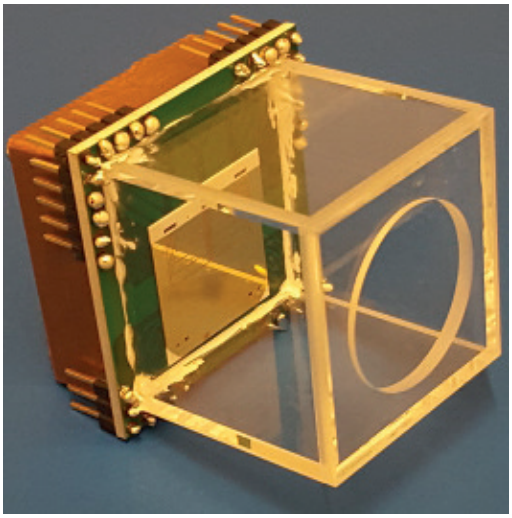

Fig. 2 The hybrid chip attached to a 3cm x 3cm fused silica cell forming a vacuum chamber for experiments. The copper block contains a water-cooling channel and a structure for generating the magnetic field for the initial magneto-optical trap.

Non-equilibrium thermodynamics

The laws of thermodynamics and everyday experiences tell us that bringing a hot object into contact with a cold one results in their temperatures equalising. It could therefore be expected that when ions and atoms are trapped together, they exchange energy and reach the same temperature. However, as a side effect of the time-varying electric fields used to confine ions in the trap, it becomes possible for the ion's energy to be significantly increased during a collision, preventing the establishment of thermal equilibrium. We have previously studied this effect and developed an analytical framework to predict the degree to which this will occur for a single ion interacting with cold atoms [2,3]. Recently, we have extended this treatment to take into account the influence of electric fields in addition to those used for trapping, which are present in the majority of experiments. Our results indicate that the presence of electric fields much weaker than those used to trap the ion may result in a substantial deviation from thermal statistics. Understanding these processes and their impact on the energy of the ion is vital for planning and correctly interpreting the experiments. Moreover, our formalism forms the basis of a deterministic control of the system to deliberately engineer states with non-thermal energy distributions.

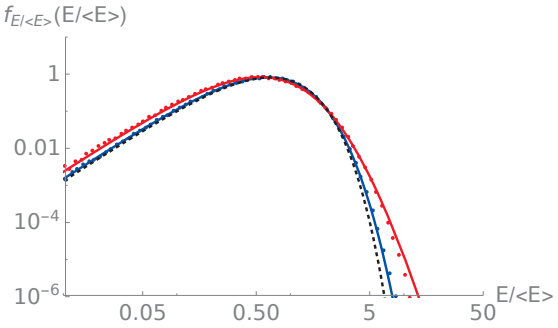

Fig. 3 Double-logarithmic plot of the energy distribution of an ion interacting with an ultracold buffer gas in the presence of a static uniform electric field (red) and in the absence of this field (blue). The solid lines indicate the predicted distributions, while the black dotted line gives the distribution at thermal equilibrium.

Outlook

Currently, the optical system required to laser cool the ions and atoms is being set up and optimised, and once this is complete experiments can begin. A first test of the system will be the generation of a magneto-optical trap using the atom chip to shape the resulting cloud and measure the influence this has on the energy of a simultaneously trapped ion. Subsequently, the atom chip will be used to produce a Bose-Einstein condensate to investigate ion-neutral reactions in the quantum regime inaccessible to standard experiments.

References

[1] S. Willitsch, *Coulomb-crystallised molecular ions in traps: methods, applications, prospects*, Int. Rev. Phys. Chem. **31**, 175 (2012)

[2] I. Rouse and S. Willitsch, *Superstatistical velocity distributions of cold trapped ions in molecular dynamics simulations*, Phys. Rev. A **92**, 053420 (2015)

[3] I. Rouse and S. Willitsch, *Superstatistical energy distributions of an ion in an ultracold buffer gas,* Phys. Rev. Lett. **118**, 143401 (2017)

On-and-off chip cooling of a Coulomb blockade thermometer down to 2.8 mK

Project P1215 Nanostructure quantum transport at micro Kelvin temperatures
Project Leader: D. Zumbühl and D. Loss
Collaborators: M. Palma (SNI PhD Student), C.P. Scheller, D. Maradan, B.K. Yemliha, A.V. Feschchenko, M. Meschke, and J. Pekola

Introduction

Ultralow temperatures can be key to novel quantum states of matter such as helical nuclear/electron spin phases [1], or fragile fractional quantum Hall states. In addition, the coherence of semiconductor and superconducting qubits as well as hybrid Majorana devices could benefit from lower temperatures. With this motivation in mind, we built a parallel network of 16 nuclear refrigerators (NR) to adapt the very well established cooling technique of adiabatic nuclear demagnetization (AND) for electronic transport experiments. We have tested the performance using metallic coulomb blockade thermometers (CBT). The device consists of an array of AlO_x tunnel junctions, separated by large metallic islands, consisting mainly of Copper and thus offering a large reservoir of nuclear spins available for demagnetization. The sample, mounted inside a Cu-box (Faraday cage) is placed onto a NR and demagnetized together with its leads (on-and-off chip cooling). The present approach is quite efficient and allows us to lower the device temperature by a factor of 8.6 from 24mK down to 2.8±0.1mK [2], thereby reducing the lowest reported electron temperature in a solid state device [3]. The CBT project is done in collaboration with the group of Jukka Pekola in Helsinki.

CBT thermometer

The CBT is fabricated by a two-angle shadow mask evaporation technique and consists of an array of tunnel junctions with large metallic islands in between (0.26mm*0.81mm). The first layer consists of (Al). After in-situ oxidation, a second Al layer is evaporated under different tilt angle, followed by a thick Cu layer (same geometry and tilt angle). At overlapping regions small, 1mm² sized tunnel junctions are formed.

The small size of the junctions gives raise to coulomb blockade effects, such that the device conductance is suppressed around zero bias (Fig.1a). Both, the width and the depth of the dip are temperature dependent. While using the depth of the dip as a thermometer requires pre-calibration, the width can in principle be used as a primary thermometer (in absence of joule heating). However, in particular at low temperatures overheating can no longer be neglected, as illustrated in figure 1a. Here the conductance measured while staying a zero bias (blue dot) is clearly lower than the minimum obtained from the bias sweep at the same temperature (dark blue trace). Therefore, the CBT is operated in secondary mode in the following.

The required for the secondary mode thermometer is shown in the inset of figure 1b, where the relative conductance dip size δg is recorded as a function of refrigerator temperature. A fit to Eq.1 [4] in the high temperature regime (T_{Cu}>30 mK) delivers the charging energy E_C=6.5 mK as the only free fitting parameter.

$$\delta g = u/6 - u^2/60 + u^3/630 \qquad (1)$$

Here, $u=E_C/k_BT_{CBT}$, where k_B is the Boltzmann constant and T_{CBT} the CBT electron temperature. Given the charging energy, the measured δg may be converted to electronic temperature for the whole temperature regime (Fig. 1b).

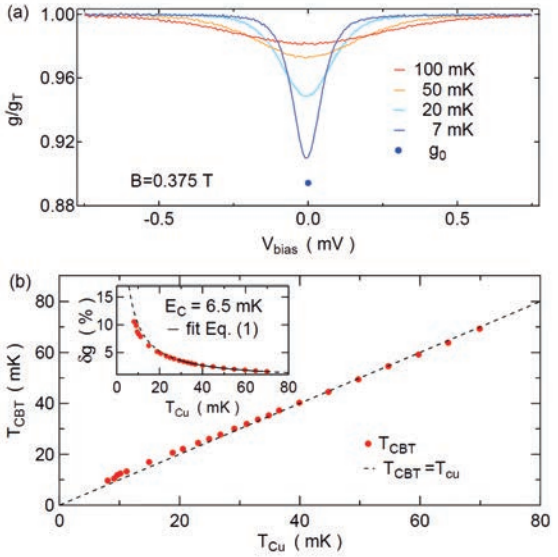

Fig. 1 Panel (a): Bias sweeps at various refrigerator temperatures as labeled. The conductance g_o is obtained while remaining at zero bias at 7 mK. Panel (b): The relative conductance dip size is shown in the inset as a function of the Cu plate temperature T_{Cu}. A fit, performed in the well thermalized high temperature regime (Cu plate temperature T_{Cu}>30 mK), delivers the charging energy as only free parameter. The corresponding CBT temperature T_{CBT} is shown in the main panel as a function of T_{Cu}.

Adiabatic Nuclear Demagnetization

The magnetic cooling comprises three steps, shown in figure 2. First, the external magnetic field is increased to its initial value B_i=9T (aligned in the plane of the sample), thereby producing a large amount of heat of magnetization that has to be drained by the mixing chamber. The evolution of various temperatures during the 3 days long precooling process is shown in figure 2a. The Cu plate temperature T_{Cu}≈10mK closely approaches the

mixing chamber temperature T_{MC}, giving a nuclear spin polarization of ≈40%. The CBT on the other hand saturates at much higher temperatures T_{CBT}≈24mK (17% polarization), indicating a significant heat leak onto the device and weak thermal coupling the Cu plate.

In the second step, shown in figure 2b, NRs and the CBT are thermally decoupled from the mixing chamber by means of superconducting Al heat switches (controlled with a small external magnet). Then magnetic field is slowly (adiabatically) reduced to a final value of B_f = 0.375, thereby reducing the nuclear spin temperature by the same fraction as the reduction in field for an ideal process. The efficiency ξ can then be expressed as the deviation from adiabaticity, $\xi=(T_i/T_f)/(B_i/B_f)$. The process runs almost ideal for the Cu plates ($\xi>0.9$) giving a final temperature of T_{Cu}=0.4 mK. Despite a reduced efficiency for the CBT ($\xi\approx0.35$), we obtain a significant reduction in T_{CBT} by a factor of 8.6, lowering the device temperature from 24mK to a record low temperature of 2.8±0.1mK.

In the last step, the warm up of the device is monitored. The CBT is observed to warm up immediately while the Cu plates are still cold, indicating good thermal decoupling and a limited spin reservoir within the CBT. Furthermore, the CBT does not recover its low temperature after performing a bias sweep after AND (not shown). These observations indicate that the CBT is demagnetized directly. The system remains below 3mK for roughly one hour, thus offering plenty of cold time for low temperature experiments.

Finally develop a simple thermal model, where the CBT carries the nuclear specific heat and the thermal subsystems (electrons, nuclei and phonons) are assumed to be in thermal equilibrium. The CBT is weakly coupled to the Cu plates and a parasitic heat to the CBT is introduced to subsume e.g. electronic noise or pulse tube heating (pulse tube seen in FFT of the current noise across the CBT). The model is able to qualitatively capture all three stages of the AND process.

In conclusion, we successfully implemented an AND system on a cryogen-free system with high efficiency and good performance. Metallic coulomb blockade thermometers were mounted onto a nuclear refrigerator and cooled directly by means of AND (on-and-off chip cooling). This allowed us to reduce their temperature by a factor of 8.6 from 24mK down to a record low electron temperature of 2.8±0.1mK. The system is limited by eddie current heating induced by the pulse tube vibrations of the cryo-free dilution refrigerator. First attempts to reduce the vibrations by rigidly fixing the NR to the mixing chamber and still shield already showed improvements, lowering T_{CBT} to 1.8mK. With improved decoupling, the micro Kelvin regime in nano electronics should be within reach.

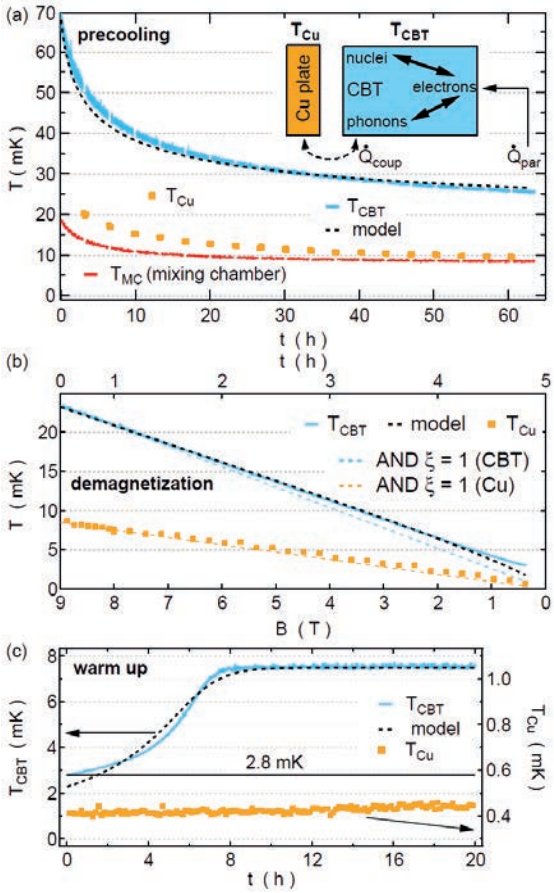

Fig. 2 Panel (a): Evolution of the CBT temperature T_{CBT} and the Cu plate temperature T_{Cu} during the precooling, the adiabatic nuclear demagnetization, and the subsequent warm up process are shown in panels (a), (b), and (c), respectively. Dashed black lines in all panels result from a thermal model that is schematically shown in the inset of panel (a). The Cu plate temperature is obtained from a magnetic field fluctuation thermometer that measures the thermal currents inside an annealed silver wire.

References

[1] P. Simon and D. Loss, *Nuclear Spin Ferromagnetic Phase Transition in an Interacting Two-Dimensional Electron Gas*, Phys. Rev. Lett. **98**, 156401 (2007)

[2] M. Palma, C.P. Scheller, D. Maradan, A.V. Feshchenko, M. Meschke, D.M. Zumbühl, *On-and-off chip cooling of a Coulomb blockade thermometer down to 2.8 mK,* Appl. Phys. Lett **111**, 253105 (2017)

[3] D.I. Bradley, R.E. George, D. Gunnarsson, R.P. Haley, H. Heikkinen, Yu. A. Pashkin, J. Penttila, J.R. Prance, M. Prunnila, L. Roschier and M. Sarsby *Nanoelectronic primary thermometry below 4 mK*, Nat. Comm. **7**, 10455 (2016)

[4] M. Meschke, J.P. Pekola, F. Gay, R.E. Rapp, H. Godfrin, *Electron Thermalization in Metallic Islands Probed by Coulomb Blockade Thermometry,* J. Low Temp. Phys. **134**, 1119 (2004)

Image states and electrostatic friction on Bi_2Te_3 surface

Project P1301 Energy dissipation over structural and electronic phase transitions
Project Leader: E. Meyer and M. Poggio
Collaborators: D. Yildiz (SNI PhD Student), M. Kisiel, U. Gysin, and Th. Glatzel

Current status of the research

Bodies in relative motion separated by few nanometers of vacuum experience a tiny friction force [1]. Such non-contact form of friction can be measured by highly sensitive cantilever oscillating like a pendulum over the surface. The established, "conventional" forms of energy dissipation are phononic friction where tip energy is lost to the creation of surface acoustic phonons and Joule dissipation where the oscillating tip provokes the local electric current [2]. Topological insulators (TI), offer a promising playground to observe exotic physical phenomena, such as Majorana fermion bounded states or magnetic monopoles [3]. Although electronic properties along with defect formation and TIs behavior of these systems have been studied [3], there is a poor understanding of these systems. Our aim is to understand the frictional response of Bi2Te3 in both the TI phase as well as when the TI phase is suppressed in an external magnetic field.

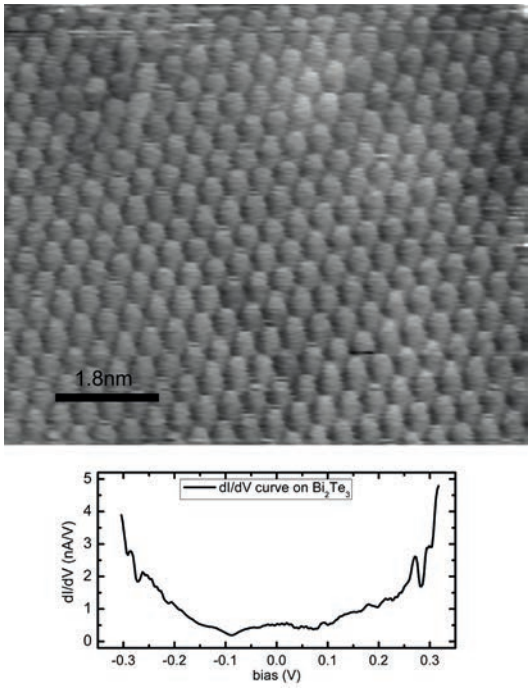

Fig. 1 STM image with atomic resolution (top) and dI/dV curve with a PtIr tip (bottom). The dI/dV curve was obtained by numerical derivation of the I/V curve measured in STS. The dI/dV spectroscopy shows the Dirac cone localized at V=-0.1V.

Here, we studied the surface of the most standard TI, namely Bi_2Te_3 – by means of the pendulum STM/AFM. The atomically flat surface of Bi2Te3 is shown in figure 1 together with STS spectrum showing a Dirac cone. Moreover, STM measurements demonstrate Rydberg series of image potential states extended few nanometers above the surface, and AFM data show dissipation peaks. The rise of energy dissipation is the subject of our work. We claim that the peaks are related to the enhancement of Joule dissipation due to the presence of quantum confined states. All the measurements were done at 5K and the same ATEC-NcAu cantilever (k=58 N/m) was used for STM spectroscopy and AFM dissipation measurements.

Image states/dissipation peaks on Bi_2Te_3 surface

Measurement of image states by means of Scanning tunneling spectroscopy (STS) were first reported in 1985 and helped to understand the chemical nature of the surface [4]. Here, STS data were acquired on Bi_2Te_3 surface. The STM tip is approached to the surface in constant current mode and gets retracted by STM feedback while sweeping the bias voltage of the sample. The presence of image charge states manifests itself as a Rydberg series in the STS spectra (Fig. 2a). At the same sample spot, AFM oscillating tip sensed a series of dissipation peaks, which are voltage controlled rather than force controlled and thus confirm the electronic character of energy dissipation. Moreover, at very close tip-sample distance dissipation maxima are positioned roughly at the same voltage as the image states (Fig 2c). Conventional pendulum AFM operates at larger tip sample distances as compared to STM. Therefore, to further establish the link between image states (STM) and energy dissipation peaks (AFM) we performed simultaneous AFM/STM measurements. STS spectra were acquired by oscillating the AFM tip. This was possible only for extremely small oscillation amplitudes (A=30pm). This way we can also monitor the dissipation channel. We noticed that image potential quantum states perfectly correlate with the AFM dissipation peak (Fig 2b). Therefore, we claim that the energy dissipation maxima are due to enhancement of capacitive coupling of the tip and sample caused by the presence of localized quantum states.

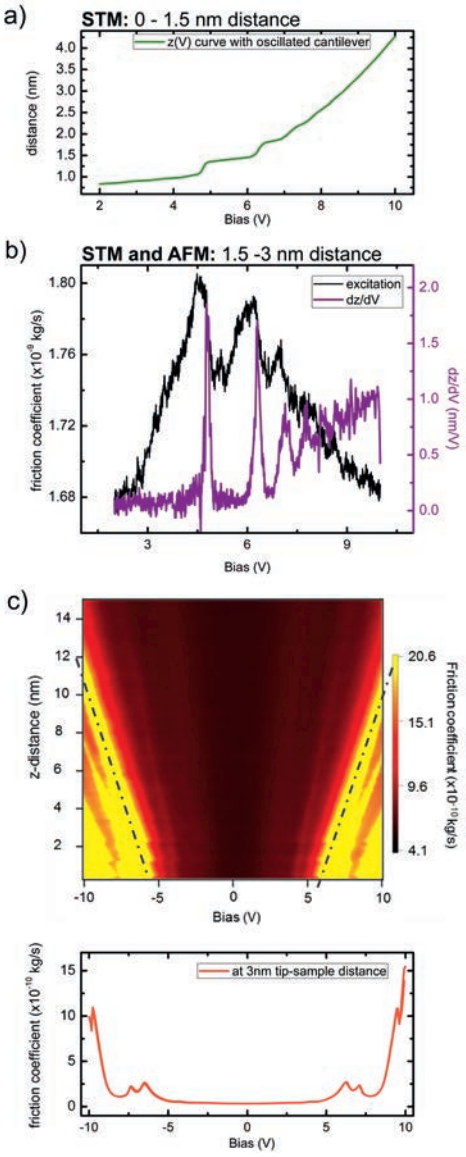

Fig. 2 (a) - z-V curve on Bi_2Te_3. Steps represent image potential states (>5V) of the crystal that are measured above the surface, (b) - image potential states (first derivative) measured together with AFM energy dissipation peaks at moderate tip – sample distance. The position of image states and dissipation peaks perfectly matches, (c) – AFM energy dissipation peaks observed at far tip sample distances as a function of tip – sample voltage and distance.

Dissipation on Bi_2Te_3 for varying B-Field

We performed energy dissipation measurements under external magnetic field from 0-0.8T and oriented perpendicularly to the sample surface. The cantilever tip was positioned 5nm above the surface and dissipation peaks were measured while sweeping the sample voltage. Dissipation maxima are shifted and suppressed as the magnetic field increases. Moreover, we observed the rise of overall dissipation plateaus even for tip-sample voltage equal to zero (Fig. 3a). The overall rise of dissipation vs. magnetic field follows a parabolic dependence as expected from Joule dissipation being proportional to the magnetoresistance of the sample, which under external magnetic field according to Kohler's rule is proportional to square of the magnetic field (Fig. 3b). The onset of dissipation above 200mT and deviation from parabolic behavior for small magnetic fields might suggests that eh AFM cantilever is sensitive to the effect of weak anti-localization – the unique property of the topological matter.

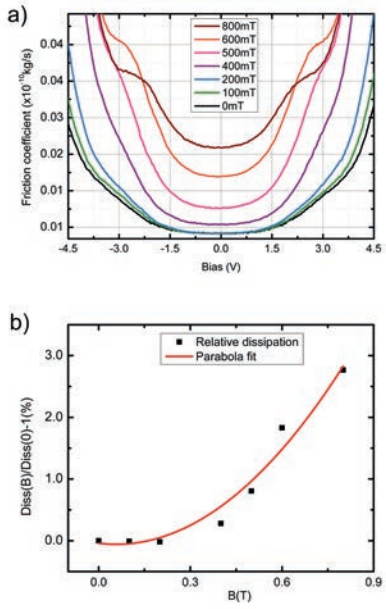

Fig. 3 (a) - Dissipation - bias curves for different external magnetic fields at a constant distance z=5nm from the surface. Overall dissipation rises versus magnetic field, (b) – the relative energy dissipation for U=0V bias voltage vs. magnetic field. The behavior of energy dissipation follows a parabolic dependence, suggesting strong relation to magnetoresistance of Bi_2Te_3, and therefore confirms the Joule loses as a main dissipation channel.

References

[1] M. Kisiel, E. Gnecco, U. Gysin, L. Marot, S. Rast, and E. Meyer, *Suppression of electronic friction on Nb films in the superconducting state,* Nat. Mat. **10**, 119-122 (2011)

[2] A. Volokitin, B.N.J. Persson, H. Ueba, *Giant enhancement of noncontact friction between closely spaced bodies by dielectric films and two-dimensional systems,* JETP **104**, 96-110 (2007)

[3] M.Z. Hasan and C.L. Kane, *Topological insulators,* Rev. Mod. Phys. **82**, 3045-3067 (2010)

[4] G. Binnig, K.H. Frank, H. Fuchs, N. Garcia, B. Reihl, H. Rohrer, F. Salvan, and A.R. Williams, *Tunneling Spectroscopy and Inverse Photo-emission: Image and Field States*, PRL **55**, 991-994 (1985)

Assessing flagellum and pili dynamics of predivisional bacterial cells

Project P1302 Dynamic and molecular principles of surface-based cell motility and mechanosensation
Project Leader: T. Pfohl and U. Jenal
Collaborators: N. Sauter (SNI PhD Student) and M. Sangermani

Introduction

One of the most predominant features of live is that it is dynamic on various time and length scales. To visualize and understand these dynamic processes, techniques that allow for real time imaging of these structures are necessary. Studies of living organisms in its environment are often challenging due to several reasons: The sample needs to be kept in a sample–friendly environment, i.e., mostly some form of liquid media. Usually the sample cannot be fixed, therefore it is susceptible to imaging-induced damaging, and ideally the method should be label free and easy to use. For nanoscale structures, such a method is X-ray ptychography, where the chromatin oscillation of living fission yeast was visualized [1]. Larger sample structures are less demanding concerning the magnification and spatial resolution of the imaging technique, however, the need for good time resolution, a sample-friendly environment, label free techniques and as little imaging-induced damaging remains unchanged.

Many bacteria undergo a transformation from swimmer cells to surface attached cells and finally forming biofilms. As biofilms are a source of bacterial infections and associated with bacterial resistance, methods to prevent biofilms are of great interest. In order to undergo the transition from a swimmer cell to an attached cell, the cell ultimately needs to be able to sense the surface and start a metabolic response to adhere and colonize the surface. Lately, it was shown that the flagellum, a propeller like organelle on the outside of the bacteria which is used for swimming, is also acting as a sense of touch, where the obstruction of the rotary motor leads to a metabolic response needed for surface attachment [2].

Most bacteria are also equipped with pili, which are dynamic hair like structures on the outside of the cell, involved in surface attachment and motility. Pili and flagellum are too small to be visualized in a light microscope without labeling.

Here, we present a method to study the activity of pili and flagellum without labeling. We take advantage of the asymmetric cell cycle of *C. crescentus* and the fact that during the transition from a swimmer cell to an attached cell, the cell irreversibly attaches to a surface. The attached cell produces a fresh daughter cell with a flagellum and pili (Fig. 1A). We get the cell attached to a solid surface or a polystyrene bead and get it grown to its predivisional state. If the cell is attached to a bead, we record the displacement of the bead over time, either in optical tweezers or in microfluidic chambers. This allows us to directly assess the activity of the flagellum and the pili.

Flagellum Activity of Predivisional Cells

We found that the flagellum of the predivisional daughter cell is active several minutes before cell division. Moreover, two different states of predivisional flagellum activity are observed. In the first state, which lasts several minutes, the connection between mother and daughter cell is still strong because the rigid cell wall is not yet divided and the activity of the flagellum results in movement of the whole predivisional cell (Fig. 1B). In the second part, which lasts some seconds, the cell wall is separated and the connection between mother and daughter is loosened. The beating of the flagellum forces the daughter cell to rotate, while the mother remains nearly stable (Fig. 1C). We let the cells attach to different surfaces (Fig. 1D) and found that the duration of the described states does most likely not depend on the kind of object the cell is attached to. In our experiments, we could also observe that the flagellum of the predivisional cell alters the direction of rotation, as described for free swarmer cells. Depending on the rotation direction of the flagellum, the cell is either pulled (CCW rotation of flagellum and CW rotation of cell body) or pushed (inverted flagellum and body rotation) by the flagellum [3]. The switching frequency of the direction change is similar to the one reported for free swimming cells and did not change during the cell division process.

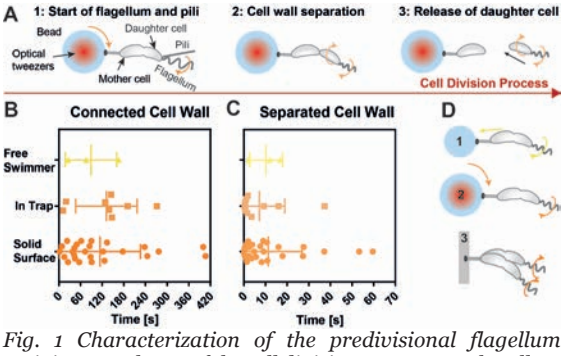

Fig. 1 Characterization of the predivisional flagellum activity. A: Scheme of the cell division process. 1: Flagellum and pili are active in the predivisional daughter cell, the cell wall is still connected. 2: The cell wall divides and the daughter cell rotates freely around the mother. 3: Release of daughter cell. B: Duration of the flagellum induced movement when the cell wall between mother cell and daughter cell is still connected. The beating of the flagellum results in a movement of the total system. C: Duration of the flagellum induced movement when the cell wall is separated. Now, the daughter cell rotates around the mother. D: Scheme of different experimental systems. 1: Cell is attached to a free bead; the rotating flagellum causes the cell-bead to swim. 2: Cell is attached to a bead and hold by optical tweezers; the bead rotates in the trap when the flagellum is beating. 3: Cell is attached to a solid surface, the active flagellum causes bending of the whole cell.

Pili Activity of Predivisional Cells

Cells without the ability to generate a flagellum got attached to 3 µm polystyrene beads and grown until they reached the predivisional state. The bead was then hold by optical tweezers and brought into close proximity to the surface of the device. We found that also the pili of the predivisional cell are highly dynamic. Whenever a pilus attaches to the surface and retracts, the bead shows a clear displacement from the center of the optical tweezers (Fig. 2A and 2B). Analyzing the displacement of the bead (Fig. 2B), we characterized the behavior of pili. A typical pilus attachment cycle consists of the following parts: 1. Attachment, 2. Retraction, 3. Hold and 4. Release. The average force generated by a single pilus is (2.9 ± 1.6) pN (Fig. 3C) and the average retraction speed is (144.3± 107.8) µm/s (Fig. 3D). Moreover, most pili attached for around 10 s and then got released. Because most cells are equipped with several pili, also several rounds of pili attachment and release events can be observed.

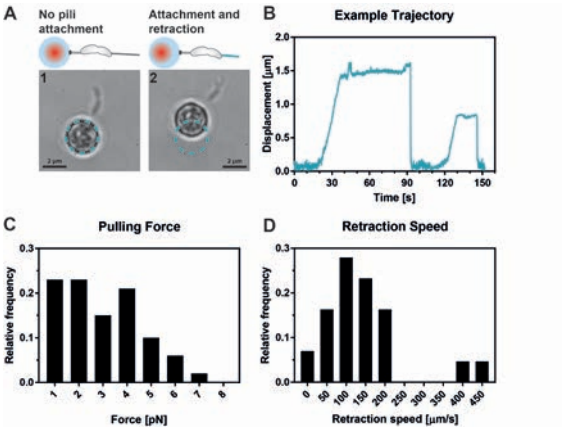

Fig. 2 Characterization of pili activity on predivisional daughter cells. A: Sketch and bright field image of predivisional cell and bead before (1) and after (2) attachment and retraction of a pilus. B: Exemplary trajectory of bead displacement, showing two consecutive pili attachment cycles. C: Histogram of the maximal force generated by a single pilus when dragging the bead out of the center of the optical tweezers. D: Histogram of the retraction speed when the pilus is retracting and dragging the bead out of the center of the optical tweezers.

Competition of Flagellum and Pili

In the wild type, flagellum and pili are present and active at the same time. The flagellum acts as a propeller for the cell to explore new spaces and the pili act as anchors to attach the cell to surfaces. Whoever wins this competition predominantly determines the fate of the cell. Either the cell swims away after being released from the mother, or it is already attached to the surface even before released from the mother. We investigated whether the presence of an active flagellum has an antagonistic effect on the attachment duration of pili. We used the same set-up as described before to study the interplay between flagellum and pili. Figure 3A shows an exemplary trajectory of the bead when the cell has an active flagellum and pili. In orange, the trajectory of the bead when the flagellum is beating is shown. The flagellar beating results in a repetitive circular displacement. When a pilus reaches the surface and can attach, the circular motion of the bead is immediately stopped and the bead is stabilized (green part in Fig. 3A). As soon as the pilus is released, the circular motion of the bead is resumed. We found that the presence of a beating flagellum did not have an effect on the length of an average pili attachment and release cycle (Fig. 3B). From this we conclude that the beating flagellum is not capable of shortening the attachment behavior of a pilus. This means that the attachment force generated by a single pilus must be larger than the force generated by the flagellum.

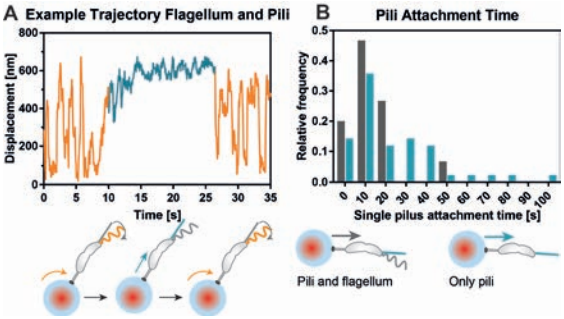

Fig. 3 Characterization of the competition between flagellum and pili. A: Exemplary trajectory of a cell that has an active flagellum and active pili. Orange: the flagellum is beating, causing a circular movement of the bead. In green: A pilus is attached to the surface, stopping the bead to further rotate and holding the bead in the same position for several seconds. When the pilus is released, the circular movement generated by the flagellum is reassumed. B: Duration of single pilus attachment cycle with (grey) and without beating flagellum (green) present.

Conclusion

In this work, we established an experimental approach for the characterization of pili and flagellum activity of *C. crescentus* in a high spatial and temporal resolution without labelling. We found that the flagellum of predivisional daughter cells starts beating several minutes before the cell is released and already shows the same switching frequency of the rotation direction as free-swimming swarmer cells. We can also observe the subsequent softening of the connection between the two cells and finally the division of the cells. In competition to the flagellum, pili are highly active in the predivisional daughter cell as well. The force generated by pili is in the lower pN range and higher than the force generated by the flagellum. We could not detect an impact of the active flagellum onto the attachment dynamics of pili.

References

[1] N. Strelnikova, N. Sauter, M. Guizar-Sicairos, M. Gollner, A. Diaz, P. Delivani, M. Chacon, I.M. Tolic, V. Zaburdaev, T. Pfohl, *Live cell X-ray imaging of autophagic vacuoles formation and chromatin dynamics in fission yeast*, Sci Rep **7**, 13775 (2017)

[2] I. Hug, S. Deshpande, K.S. Sprecher, T. Pfohl, U. Jenal, *Second messenger-mediated tactile response by a bacterial rotary motor*, Science **358**, 531-534 (2017)

[3] B. Liu, M. Gulino, M. Morse, J.X. Tang, T.R. Powers, K.S. Breuer, *Helical motion of the cell body enhances Caulobacter crescentus motility*, *PNAS* **111**, 11252-11256 (2014)

Recognition of OPE-chromophores in water

Project P1303 Assembly and investigation of electrochemically triggered molecular muscles
Project Leader: M. Mayor and M. Calame
Collaborators: Y. Aeschi (SNI PhD Student), S. Drayss-Orth, and M. Mayor

Introduction

For the design of sophisticated supramolecular machines it is most desirable to control thermodynamics and kinetics of complexation/decomplexation in host-guest chemistry [1]. The choice of a recognition motif relying on a hydrophobic effect gives rise to high association strength, which can be further adjusted by introduction of additional driving forces such as donor-acceptor- or electrostatic interactions. Fine-tuning of topological features in form of steric barriers offers opportunities to controlling kinetic factors. We synthesized host-guest systems based on water-soluble, cationic cyclophanes and anionic oligo-phenyleneethynylene (OPE) rods, which exhibit high complexation strength owing to a hydrophobic effect combined with complementary electrostatic features. The peripheral substitution pattern of these OPE rods with carboxylate groups has a strong influence on exchange kinetics. Furthermore, they are functionalized with azide substituents which can be readily used for integration into nano-architectures via Cu^{I}-catalyzed azide-alkyne cycloaddition *click*-chemistry [2,3]. These building blocks will ultimately be integrated into an optimized design for molecular daisy chains.

Design of water-soluble OPE rods

The aqueous click-assembly concept that was developed by our group [3] has been expanded to OPE-type chromophores from which Molecular daisy chains [4,5] have been synthesized. We found that Cyclophane **1** strongly complexes OPE rod **2** with an aggregation constant of $4*10^6$ $L^{-1}mol^{-1}$ as determined by isothermal titration calorimetry and fluorescence quenching titration.

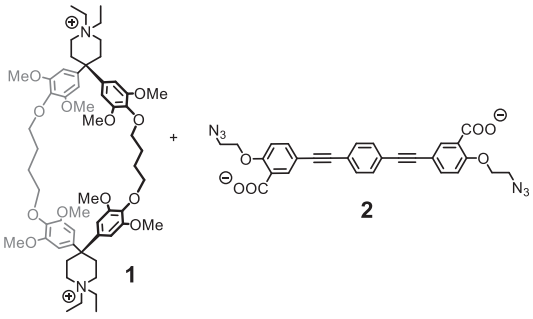

*Fig. 1 Molecular structures of cyclophane **1** and OPE **2***

OPE **2** is sparingly soluble in H_2O, as only 2 carboxylate groups provide solubilization in water. This is reflected in derivatives of **2**, which also tend to be sparingly soluble and usually require the addition of an organic co-solvent such as MeOH or DMSO, which tends to be disruptive towards association strength. We therefore envisaged the synthesis of multiply carboxylate-functionalized OPE rods to overcome this disadvantage. Appropriate functionalization of isophthalic- or terephthalic acid ester derivatives with azido- and iodo substituents resulted in compact and versatile precursors **3** and **5** for OPE rods with enhanced solubility. It is desirable to mask carboxylic acids or their anions as their corresponding methyl esters due to their inherent difficulty of purification. The iodo-subsituent serves as an excellent leaving group for Pd^0-based cross-couplings, giving the desired OPE rod, which can then be rendered water-soluble by hydrolysis of the carboxylic acid esters. Derivatization of the rod or a cyclophane/rod complex can then be conducted via facile click-chemistry owing to the azide groups.

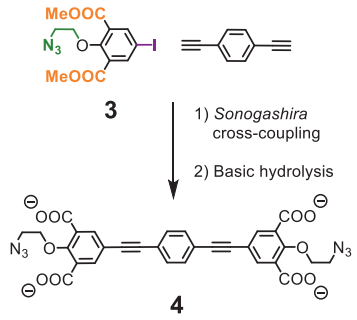

*Fig. 2 Synthesis of isophthalate-based OPE **4** via Sonogashira-cross-coupling followed by basic hydrolysis*

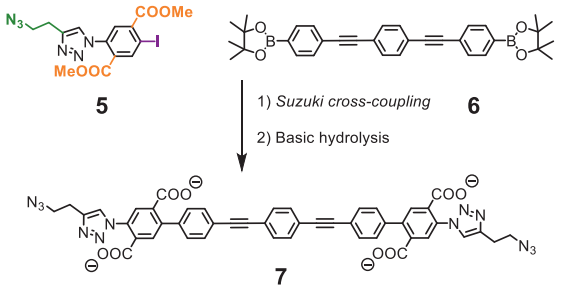

*Fig. 3 Synthesis of terephthalate-based OPE **7**, via Suzuki-cross-coupling followed by basic hydrolysis*

Synthesis & Characterization

3 was synthesized in 6 steps from 1,3-dimethyl-2-nitrobenzene and subsequently coupled to 1,4-diethynylbenzene. OPE **4** was obtained by final hydrolysis of the methyl esters and proved to be well soluble in water in the millimolar range. Exchange rates upon addition of cyclophane **1** proved to be very low, a 1:1 OPE : cyclophane mixture 0.5 mM in D_2O at 20 °C required 15 d to reach equilibrium as determined by ^{1}H-NMR. In contrast, mixtures of **1** and OPE **2** instantaneously equilibrate.

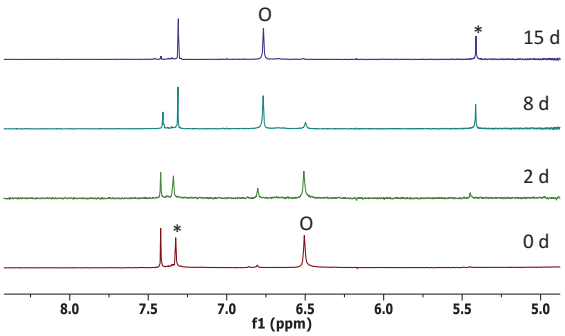

*Fig. 4 Time-dependent ¹H-NMR of a 0.5 mM solution of OPE **4** and cyclophane **1** in D_2O at 20 °C. The asterisk denotes the central phenylene protons, the circle denotes cyclophane aryl protons.*

5 was obtained in a 5-step procedure from dimethyl-2-aminoterephthalate. Coupling to 1,4-diethynyl-benzene was successful but following attempts of hydrolysis gave a complex mixture of products, which was attributed to instability of the acetylene ortho to a carboxylate group. Therefore, *Suzuki* cross-coupling to **6** was conducted and the final product could be hydrolyzed to obtain OPE **7**. Despite of its extended π-conjugated backbone, this compound was well soluble in water in the millimolar range. Time-dependent ¹H-NMR spectra revealed that complexation by **1** occurs at least by an order of magnitude faster compared to OPE **4**.

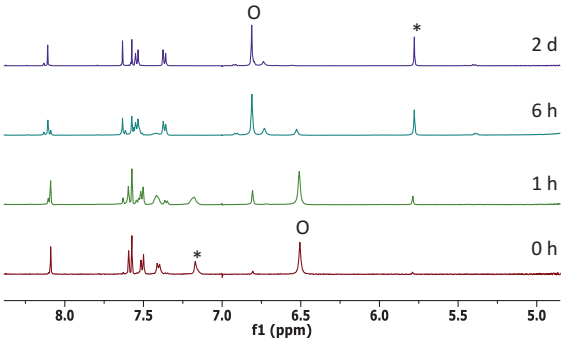

*Fig. 5 Time-dependent ¹H-NMR of a 0.5 mM solution of OPE **7** and cyclophane **1** in D_2O at 20 °C. The asterisk denotes the central phenylene protons, the circle denotes cyclophane aryl protons.*

Outlook

Quantitative characterization of thermodynamics and kinetics of pseudorotaxane formation is being conducted. In order to control aggregation thermodynamics and kinetics of molecular daisy chain formation, **9** is being synthesized from receptor **8** and an OPE rod incorporating a terephthalate solubilizing group.

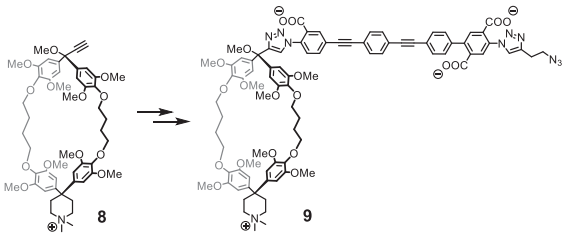

*Fig. 6 Conceptual synthesis of a daisy chain monomer based on acetylene-functionalized cyclophane **8** the terephthalate solubilizer.*

References

[1] C. Cheng, P.R. McGonigal, J.F. Stoddart, R. Dean, Astumian, *Design and Synthesis of Non-equilibrium Systems*, ACS Nano, **9**, 8672 (2015)

[2] M. Meldal, C.W. Tornøe, *Cu-Catalyzed Azide-Alkyne Cycloaddition*, Chem. Rev, **108**, 2952 (2008)

[3] Y. Aeschi, S. Drayss-Orth, M. Valášek, F. Raps, D. Häussin, M. Mayor, *Assembly of [2]-Rotaxanes in water*, Eur. J. Org. Chem, **28**, 4091 (2017)

[4] J. Rotzler, S. Drayss, D. Häussinger, O. Hampe, M. Mayor, *Molecular Daisy Chains: Syn-thesis and Aggregation Studies of an Amphi-philic Molecular rod,* Chem. Eur. J*,* **19,** 2089 (2013)

[5] J. Rotzler and M. Mayor, *Molecular daisy chains*, Chem. Soc. Rev, **42**, 44 (2013)

Monitoring β-barrel membrane protein folding

Project P1304 Folding mechanisms of β-barrel outer membrane proteins and their catalysis by natural holdases and foldases
Project Leader: S. Hiller and D.J. Müller
Collaborators: N. Ritzmann (SNI PhD Student), P. Rios Flores, T. Raschle, and J. Thoma

β-barrel membrane proteins are essential functional components of the outer membrane of Gram-negative bacteria, mitochondria and chloroplasts. Membrane proteins have highly interesting folding properties, since they fold in an external environment that comprises hydrophobic and hydrophilic phases. The biogenesis of these outer membrane proteins (Omps) poses a complex biophysical challenge to the pro- and eukaryotic cell, because the Omps are synthesized at locations distant from their target membrane. The overall essential biological function of Omp biogenesis is accomplished by molecular chaperones that pass the unfolded substrates from the ribosome to the destination membrane [1]. In the Gram-negative bacterium *E. coli*, the periplasmic chaperones SurA and Skp transport the substrate to the Bam complex, which folds and inserts them into the outer membrane [2]. The *in vitro* and the *in vivo* folding mechanisms of β-barrel Omps from mitochondria or Gram-negative bacteria are so far not understood at atomic resolution. The same polypeptide chains can refold *in vitro* in the absence of chaperones and other proteins, resulting in the same three-dimensional β-barrel structures. In this project, we employ structural biological and nanotechnological approaches to characterize the folding process of complex Omps at atomic resolution. In the following we report two papers, which we published since starting our project and thereafter provide an overview of the following challenges in this project.

Monitoring Backbone Hydrogen Bond Formation

The three-dimensional structure of a β-barrel membrane protein is defined by backbone hydrogen bonds between adjacent strands. The biogenesis pathways of β-barrel membrane proteins are essential, but the underlying mechanism is still unclear. To obtain insight into this process, we used the 8-stranded OmpX from *E. coli* as a model system. At the onset of the experiment, OmpX (148 aa) was solubilized in chaotropic denaturant solution, where the polypeptide was fully unfolded and adopted a random coil conformation without residual structure. Using a manually operated, custom-built setup, folding was triggered by rapid dilution with an aqueous folding buffer that contained the detergent micelles. This initial rapid dilution step was performed in deuterated solvent, leading to the incorporation of deuterons at all exchange-accessible backbone amide positions. The sample was then incubated for a variable folding time, after which a second rapid dilution step with hydrogen based folding buffer was performed, reducing the deuterium content in the solvent by about 80%. Finally, the sample was incubated until protein folding has progressed to completion.

With this experimental setup, we found that the residue-specific kinetics of interstrand hydrogen-bond formation are uniform in the entire β-barrel and synchronized to formation of the tertiary structure (Fig. 1). OmpX folding thus propagates *via* a long-lived conformational ensemble state in which all backbone amide protons engage in hydrogen bonds only transiently. Stable formation of the entire OmpX hydrogen bond network occurs downhill of the rate-limiting transition state and thus appears cooperative on the overall folding time scale.

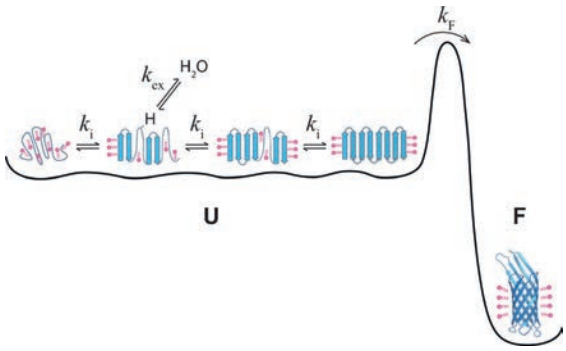

Fig. 1 Free energy diagram for OmpX folding into detergent micelles. Upon rapid dilution from a denatured state, OmpX associates with detergent micelles to a dynamic conformational ensemble state (U). Four arbitrary conformations are shown in cartoon representation, as representatives for the dynamic ensemble. In this state, multiple conformations rapidly interconvert with kinetic rate constants k_i. No long-lived hydrogen bonds are formed, so that all backbone amides are effectively accessible to chemical exchange (k_{ex}) with the solvent. The folded state of OmpX (F) is separated from the conformational ensemble by a rate-limiting folding step with a kinetic rate constant k_F on the minutes time scale. Image taken from ref [3].

Chaperone Assisted Insertion and Folding

The correct insertion and folding of membrane proteins is essential to function in living cells. Whereas in living cells molecular chaperones increase the folding yields of soluble proteins by suppressing misfolding and aggregation, it is not understood how they modulate the insertion and folding of integral membrane proteins into membranes. To study this process, we used single-molecule force spectroscopy (SMFS) and NMR spectroscopy to characterize how periplasmic holdase chaperones SurA and Skp shape the folding

trajectory of the large β-barrel Omp FhuA from *E. coli* [4]. After having unfolded and extracted a single FhuA from the lipid membrane by SMFS, we thus monitored how the unfolded polypeptide inserts and folds back into the membrane. The unfolded FhuA polypeptide is prone to misfolding and cannot insert back into the membrane to adopt its native, functional structure (Fig. 2). However, the presence of either of the two periplasmic chaperones SurA or Skp prevented misfolding by stabilizing a dynamic, unfolded state. Thereby SurA allowed the unfolded substrate to stepwise insert and fold the unfolded FhuA polypeptide towards its native structure.

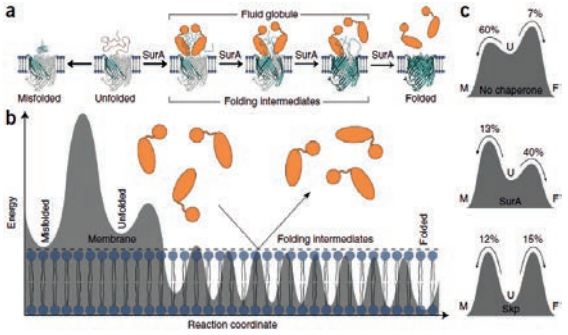

Fig. 2 Folding pathways and free-energy landscape of FhuA receptors. a) Insertion and folding pathways of FhuA in the absence of chaperones and in the presence of SurA (orange). Without chaperones, the majority of unfolded FhuA receptors misfold. SurA stabilizes the unfolded state of FhuA and promotes stepwise insertion and folding of β-hairpins in the lipid membrane. This stepwise insertion of secondary structures proceeds until the receptor completed folding. b) Hypothetical folding free-energy landscape of FhuA in the presence of SurA. SurA (orange) is spatially excluded from the lipid membrane (blue). Each β-hairpin inserted into the lipid membrane is stabilized by a free-energy well. c) Modulation of the folding free-energy landscape by chaperones. The free-energy barriers separating the unfolded (U) from the misfolded (M) and folded (F) states, are determined from the observed folding probabilities. Image taken from ref [4].

Maltoporin Unfolding Pathways

The next challenge in this project was to study whether Omps generally unfold and fold similarly to FhuA. We hence first unfolded maltoporin LamB from *E. coli* by SMFS [5]. It was observed that also maltoporin stepwise unfolds β-hairpins until the β-barrel has been completely unfolded and extracted from the membrane. Thereby the folding probability of a β-hairpin was found to be correlated to its mechanical stability. The study was fundamental to characterize at later stage the insertion and folding of other Omps by BAM.

Directed Insertion of Membrane Proteins

In an attempt to study how whether we could already apply the knowledge gained in this proposal and guide the insertion of membrane proteins, we engineered light-driven proton pumps having either a red (RFP) or green (GFP) fluorescent protein fused to its N- or C-terminus [6]. The hydrophilic fluorescent proteins allowed the directed insertion of proton pumps into liposomes and to select the liposomes depending on fluorescence. The thus manufactured nanoreactors were used to generate proton gradients by light, which is a prerequisite to power a broad variety biomolecular processes. In the future, this side project will enable to supply nanoscopic factories with energy and to translocate polypeptides or other molecules across membranes.

Latest progress and Challenges Ahead

Within the last year, we have made considerable progress in preparing outer membrane vesicles (OMVs) from *E. coli* and begun to characterize the Bam insertion machinery at close to native conditions. Currently we are in the process of gathering enough SMFS and NMR data to understand how the Bam complex facilitates the insertion and folding of complex Omps. However, given the complexity of the insertion and folding process and the multiple molecular machines involved in this process (BamA, -B, -C, -D and SurA, Skp, etc), the systematic study of this process requires much more efforts than anticipated. Encouraged by the preliminary results, we are confident that now after all these years of hard work we made a big step towards understanding how the periplasmic chaperones SurA and Skp transport the Omp substrate to the Bam complex, and how they together fold and insert the substrates into functional Omp structure. It may be only a matter of time until we can then use these insights to assemble nanomachines in membranes.

References

[1] T.J. Knowles, A. Scott-Tucker, M. Overduin, I.R. Henderson, *Membrane protein architects: the role of the BAM complex in outer membrane protein assembly*, Nat Rev Microbiol **7**, 206 (2009)

[2] J.G. Sklar, T. Wu, D. Kahne, T.J. Silhavy, *Defining the roles of the periplasmic chaperones SurA, Skp, and DegP in Escherichia coli*, Genes Dev **21**, 2473 (2007)

[3] T. Raschle, P. Rios Flores, C. Opitz, D.J. Müller, S. Hiller, *Monitoring backbone hydrogen bond formation in β-barrel membrane protein folding*, Angew Chem Int Ed **55**, 5952 (2016)

[4] J. Thoma, B.M. Burmann, S. Hiller, D.J. Müller, *Impact of holdase chaperones Skp and SurA on the folding of β-barrel outer membrane proteins*, Nat Struct Mol Biol **22**, 795 (2015)

[5] J. Thoma, N. Ritzmann, D. Wolf, E. Mulvihill, S. Hiller, D.J. Müller, *Maltoporin LamB unfolds beta-hairpins along mechanical stress-dependent unfolding pathways,* Structure **25**, 1139 (2017)

[6] N. Ritzmann, J. Thoma, S. Hirschi, D. Kalbermatter, D. Fotiadis, D.J. Müller, *Fusion domains guide the oriented insertion of light-driven proton pumps into liposomes*, Biophys J **113**, 1181 (2017)

Perforated for performance: solid supports for serial protein crystallography

Project P1305 X-FEL based dynamic studies on 2D and 3D nanocrystals of membrane proteins on solid supports
Project Leader: C. Padeste and H. Stahlberg
Collaborators: N. Opara (SNI PhD Student), T. Braun, X.-D. Li, I. Martiel, V. Guzenko, K. Vogelsang, and D. Marty

Ultrahigh brightness X-ray sources such as the X-ray Free Electron Laser SwissFEL open up the possibility to solve the atomic structure of protein nanocrystals, which is difficult to achieve with state-of-the-art synchrotrons. This has been demonstrated at XFELs by applying protein crystal handling methods such as liquid jet and lipidic cubic phase injection or fixed target technologies. The rapidly developing field of serial protein crystallography opens up cutting edge scientific opportunities as well as a new paradigm for macromolecular structural analysis for pharmaceutical industries.

In XFEL-based protein crystallography femtosecond X-ray pulses produce damage-free partial diffraction patterns, but due to their extreme intensity they immediately destroy the probed area of the crystals. Hence, data collection requires a large number of micro- or nanocrystals to be sequentially delivered to the beam in order to achieve complete data sets. The fixed target delivery methods, where the sample immobilized on a solid support is scanned through the beam, offer avenues for unmet efficacy and diffraction quality of X-ray data collection. Protecting the protein from dehydration is of utmost importance for high quality measurements and is achieved using humidity chambers, by enclosing or protective embedding of the sample for room temperature measurements, or by plunge-freezing in liquid nitrogen for measurements under cryo-conditions.

In this project, we are focusing on novel concepts and optimization of fixed targets for serial protein crystallography. In particular, we developed a silicon/silicon nitride-based system for in-situ crystallization and hermetic sealing of large protein crystals for x-ray pump/x-ray probe measurements [1].

Here, we report on two novel types of supports, aiming at minimized background which is originating either from the liquor surrounding the crystals, or from the support material. The “cryo-mesh” supports consist of less than 2 µm thick perforated polymer films glued to polymer frames. They are designed for blotting of the mother liquor of deposited crystal suspensions through the pores, immediately before freezing the sample in liquid nitrogen. The nanoimprint-based fabrication method (Fig. 1) was adapted from Gel *et al.* [2]: A silicon stamp with arrays of 2 µm wide and 2 µm high pillars is hot embossed into a polymer double layer consisting of polyvinyl alcohol (PVA, red) and cycloolefin copolymer (COC, blue), which are sequentially spin-coated onto a silicon wafer (1). After release of the stamp (2) the residual COC layer is etched in oxygen plasma (3). Polymer frames (yellow) are glued onto the layer (4) and the structure is released by immersion in water to dissolve the water-soluble PVA underlayer (5). Alternative to nanoimprint lithography we also used e-beam lithography for structure definition in poly-methyl methacrylate (PMMA) instead of COC, which gives a higher design freedom, however, on the expense of lower throughput.

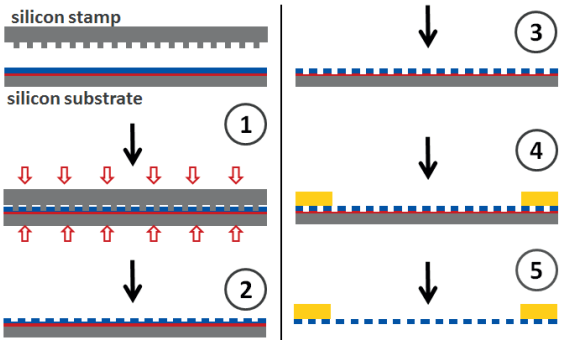

Fig. 1 Fabrication of cryo-mesh supports: (1) hot embossing of a stamp with pillar arrays into a spin-coated polymer double layer; (2) release and (3) etching in oxygen plasma; (4) gluing of polymer frames and (5) dissolution of the water-soluble polymer underlayer.

Membranes with perforations of 2-4 µm in diameter and 4-20 µm in distance have been produced and successfully used for crystal deposition and blotting (Fig. 2). While the size and density of the perforations had minimal influence on the efficiency of the blotting, control of hydrophilicity of the material by additional plasma treatments proved to be essential for the blotting process. Preliminary experiments at the Swiss Light Source and at LCLS (the XFEL in Stanford) showed that crystal densities suitable for efficient measurements could be achieved. In particular the perforated membranes provided enough mechanical stability for probing the sample in 100 µm distances with non-attenuated XFEL pulses.

The second type of supports under development addresses measurements of 2D crystals. These are periodic and ordered arrangements of molecules in single layers representing an important crystalline form for, *e.g.*, membrane proteins. Resolution in the range of 4 Å for measurements using an XFEL beam focused to sub-micrometer dimensions (“nanofocus beam”) at room temperature has been demonstrated [3], making the method attractive for the investigation of molecular motion using pump-probe techniques. For such measurements, high sample throughput and minimizing of the background are

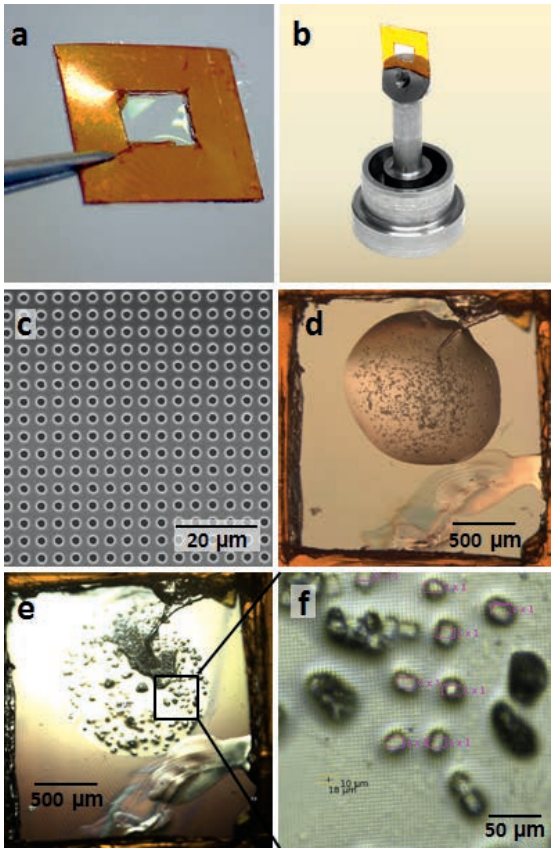

Fig. 2 Prototypes of cryo-mesh supports produced at LMN, loaded with lysozyme crystals. The sequence shows (a) the polyimide frame with the 2 µm thick polymer film comprising dense arrays of 2 µm diameter holes over an area of 2 x 2 mm², (b) the support mounted on a holder, (c) an SEM image of the suspended film, in this case structured with e-beam lithography, (d) the crystal suspension deposited on the surface before and (e) after blotting of the liquid and flash-cooling, and (f) a zoomed-in view of cryo-cooled lysozyme crystals (PX beamline at SLS).

of pivotal importance. Low background can in principle be reached using less than 100 nm thick films of silicon nitride or polymers as the supports. However, high probing density is limited due to the limited stability of the silicon nitride (membranes typically break on the first non-attenuated laser pulse) and geometrical constraints of silicon microfabrication. To overcome this limitation and to optimize sample consumption and measuring time we propose a membrane-in-the-membrane concept of a relatively thin perforated Si3N4 membrane covered with an ultrathin polymer film (Fig. 3). The polymer spanning over the holes should break locally upon exposure with an XFEL pulse without affecting the rest of the membrane. Perforated membranes have been produced using silicon microfabrication technology: Openings for the membranes and perforations were first defined on two sides of silicon nitride-coated silicon wafers using photolithography and reactive ion etching. The silicon was then selectively etched in KOH. Arrays of 12 x 12 membranes were realized in 2.5 x 2.5 cm² area of a wafer. Each membrane hosts 12 x 12 holes of 10 x 10 µm² in size. This results in a total of 12^4 = 20736 probing sites per chip. Next steps will include transfer of ultrathin polymer films onto the perforated membranes and testing of the stability and of the deposition of 2D crystals.

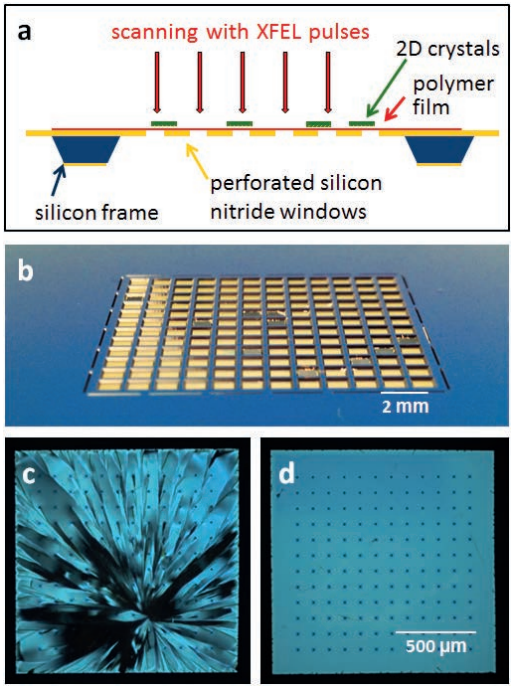

Fig. 3 a) Membrane-in-the-membrane concept for supports for 2D protein crystals (cross-sectional view). b) Micro-fabricated perforated membranes. The yield of intact membranes was up to 95 %. c) and d) Details of broken and intact membranes.

References

[1] N. Opara, I. Martiel, S.A. Arnold, T. Braun, H. Stahlberg, M. Makita, D.A. Christian, C. Padeste, *Direct protein crystallization on ultrathin membranes for diffraction measurements at X-ray free electron lasers*, J. Appl. Cryst. **50**, 909-918 (2017)

[2] M. Gel, S. Kandasamy, K. Cartledge, D. Haylock, *Fabrication of free standing microporous COC membranes optimized for in vitro barrier tissue models*, Sensors Actuators A **215**, 51-55 (2014)

[3] C. Casadei et al., *Resolution extension by image summing in serial femtosecond crystallography of two-dimensional crystals*, IUCrJ. **5**, 103–117 (2018)

Nano-pills for mosquitoes to interrupt malaria transmission

Project P1306 Slow-release nano-pills for mosquitoes for interrupting malaria transmission
Project Leader: P. Hunziker and R. Brun/E.C. Constable
Collaborators: D. Gonçalves (SNI PhD Student), K. Liu, P. Müller, and M. Rottmann

Introduction

Malaria remains one of the top tropical and infectious diseases in the world both, in terms of morbidity and mortality, with an estimated of 200 million clinical cases every year. In recent years an official research and development agenda for malaria eradication (malERA) was established. The goal is to completely eliminate and, if possible, eradicate the disease from as many areas as possible and control the others. To achieve this, and to complement the human stages tools in malaria portfolio, Transmission Blocking strategies (TBs) focusing on the mosquito stages of the parasite life cycle have been developed and some already implemented in the field [1].

In this project a new radical approach is being studied to use self-assembly polymers to form drug-carrier nanoparticles (NPs) [2], to design a setup to lure mosquitoes into ingestion [3], that would clear, or at least reduce, the parasite density to levels that would render it non-infective and interrupt the disease transmission and propagation. Aiming for a mosquito survival strategy, it is expected to avoid selective pressure towards drug-free mosquitoes and reduce likeness of resistance to appear as opposed to the insecticide strategy. To achieve this, whole cycle models were established and different systems tested to optimize the design in terms of assembly, stability, targeting and release of the nano-pills.

Here we report the last stages of the project and work in progress that will validate not only the concept but also study the best way to implement it in the field in an impactful way.

Results and Discussion

Rodent model infection

With the optimized design of the nano-pill and delivery system, the mosquito/mice model was scaled up for statistically meaningful results and full cycle impact assessment of parasites intensity and transmission, at different stages and using two different orthogonal methods for quantification: fluorescence and microscope counting. To assess the pharmacodynamics of the nano-pill with the carrier drug (mainly pentamidine) two different regimes were tested in parallel: pre and post-infection feeding; and only post-infection feeding. Both where designed with multiple controls (drug only, infected and non-infected mosquitoes) and different concentrations and critical time-points to determine dose response curves. All the data was then statistically validated and few key indicators were determined such as oocysts and sporozoites intensity and prevalence (and mosquito toxicity) to be further used in simulation models to predict the optimal setup conditions and impact of transmission in the field (R_0 and EIR). Depending on the regime and concentration of the nano-pill we were able to achieve 40 to 80% reduction of parasites in the oocyst stage and 80-100% of reduction in the sporozoite stage. One generation mice-mosquito-mice complete transmission cycle is now being assessed with the optimal concentration to achieve 100% transmission-blocking effect in laboratory conditions.

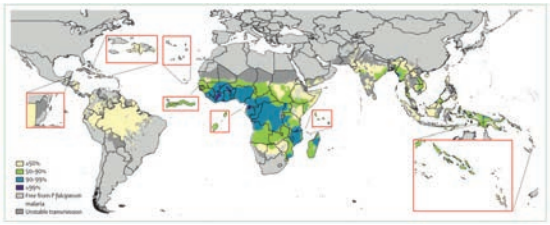

Fig 1. Map of P. falciparum incidence, indicating the extent to which transmission needs to be reduced to achieve elimination.

Single mosquito experiments

New method to assess pharmacokinetics of nano-pills in single mosquito using fluorescence and mass spectrometry and a unique 96 well plate setup with parafilm. By feeding different nano-pill doses and fluorescent loadings; bite frequency, Cmax, and excretion can be determined for every mosquito and different time points. This data will then lead to a better understanding of the ADMET profile of the nano-pills and extrapolate the best conditions for different antimalarial drugs in the transmission-blocking portfolio.

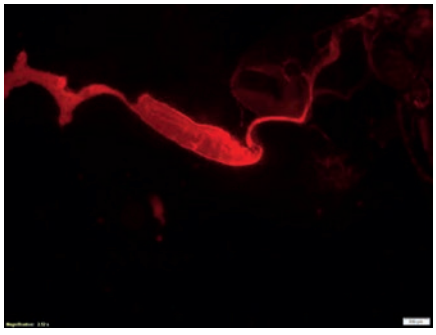

Fig. 2 Single Anopheles midgut with fluorescent nano-pills

Testing trap setups and layout in the field

Field work was made with commercial traps and the optimized setup for nano-pills delivery. Attraction, feeding behavior and flight distance was tested with common blood sucking mosquitoes found in Switzerland, in different locations and habitats. Variations in feeding medium (liquid or solid) and using different food dies as markers enabled to optimize the setup and estimate important parameters to use in future simulations.

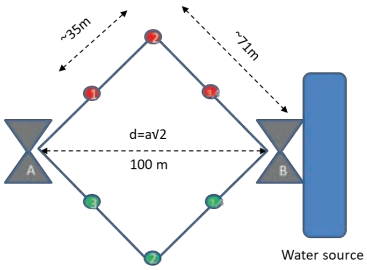

Fig. 3 Scheme of traps (A, B) and feeding sources, red or green (1-4), used in the field, to simulate the exophilic behaviour of mosquitoes.

Models and Simulation

The ultimate goal of the project is to develop a tool that can be used in combination of many others already in used or being studied. The best way for a successful strategy implementation is to have a model prediction and quantification of its impact in local and global settings [5]. To do this there are two important clinical and epidemiological metrics that allows us to track the disease endemicity and progress, are the reproductive number (R0) and the entomological inoculation rate (EIR).

By using our results in the mice model transmission and the field trap simulations, we are trying now to construct models to be able to estimate the impact in malaria transmission at different local settings and in combination with other strategies.

Summary and outlook

The project is now in its final stages. Translation of the data collected, and field simulations of the results will then allow to estimate the impact and best way(s) to an eventual implementation in the field.

The final outcome will then be a cross analysis and combination of the different knowledge gathered in the fields of polymer and medicinal gathered in the fields of polymer and medicinal chemistry, infection biology and mathematical modeling with the common thread of nanomedicine.

References

[1] D. Gonçalves, P. Hunziker, *Transmission-blocking strategies: the roadmap from laboratory bench to the community*, Malaria Journal, **15**:95 (2016)

[2] P. Broz, P. Hunziker, *Nanotechnologies for targeted delivery of drugs*, Wiley-VCH, 3731-3732 (2007)

[3] B.G.J. Knols, *Odour-mediated host-seeking behaviour of the Afro-tropical malaria vector Anopheles gambiae Giles,* Parasitology Today, 159–161 (1996)

[4] K.G. Liu, Z. Zhu, X.Y. Wang, D. Goncalves, B. Zhang, A. Hierlemann, P. Hunziker, *Microfluidics-based single-step preparation of injection-ready polymeric nanosystems for medical imaging and drug delivery,* Nanoscale, **7(40)**, 16983-16993 (2015)

[5] The malERA Refresh Consultative Panel on Combination Interventions and Modelling, *malERA: An updated research agenda for combination interventions and modelling in malaria elimination and eradication,* PLoS Med **14(11)**: e1002453 (2017).

Optoelectronic characterization of graphene-based nanojunctions

Project P1307 Optoelectronic nanojunctions
Project Leader: M. Calame and M. Mayor
Collaborators: J. Overbeck (SNI PhD Student), L. Wang, O. Braun, G. Borin Barin, R. Fasel, P. Makk, A. Baumgartner, and C. Schönenberger

Introduction

In this project, we are using optoelectronic techniques to investigate the interplay between nanometer sized junctions of different materials. Building on the expertise in our group in the field of molecular junctions with metal electrodes formed by the mechanically controlled break junction (MCBJ) technique [1] and graphene nanogaps created via an electrical breakdown process [2] we are working towards combining the benefits of both approaches. We are in particular interested in an in-depth understanding of optoelectronic processes at the interfaces of different nanoscale objects which provide an additional source of information compared to purely electrical characterization of these systems.

Vacuum & Raman Setups

Building on the development of an MCBJ setup with optical access (see the report of 2016) we built a vacuum break junction setup with optical access (Fig. 1a) to allow the characterization of samples without the influence of atmospheric contaminants. Because of its compact and lightweight design, it can be installed in a variety of optics setups such as the WITec Raman systems available at *University of Basel* and the *Laboratory of Transport at Nanoscale Interfaces* at *Empa* as well as in most open optics setups. The Raman system at *Empa* has the added capability to control the polarization of both incident and detected light. Having automatized a significant part of this setup allows us to perform full polarization dependent overnight mappings of samples without manual interaction.

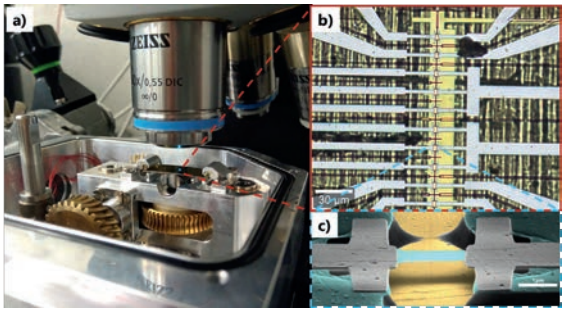

Fig. 1 ***a****) New vacuum break junction setup (lid removed) installed in a WITec system with a long working distance objective.* ***b****) Sample layout comprised of ten individually contacted nanojunctions with a common gate.* ***c****) Colorized SEM image of a suspended graphene junction for strain measurements.*

Strain in Suspended Graphene Nanojunctions & Determining the Crystallographic Orientation

In order to use suspended graphene as an electrode material in a break junction type experiment its mechanical behaviour needs to be assessed. Raman measurements preformed on suspended graphene samples (Fig. 1 b/c, cf. the report 2016 for details on fabrication) show a reproducible redshift of the 2D and G peaks upon bending of the sample.

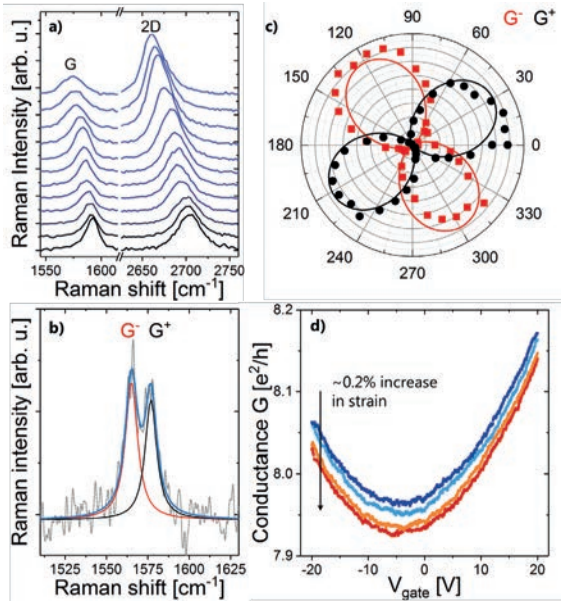

Fig. 2 ***a****) Redshift of the 2D and G peaks with increasing strain from bottom to top.* ***b)*** *At higher strain levels, a splitting of the G-peak can be observed and fitted by two Lorentzians.* ***c)*** *Polarization dependent measurements show a clear intensity variation for the two vibrational modes comprising the G-peak under strain.* ***d)*** *Gate-dependent conductance measurement of a suspended graphene device for increasing strain levels.*

At higher strain levels a splitting of the otherwise degenerate vibrational modes along and perpendicular to the strain direction can be observed (Fig. 2b). These modes, indicated $G^{+/-}$, exhibit a strongly polarization dependent Raman intensity. From the polar plot in Fig. 2c) we can extract the orientation of the graphene lattice [3] directly on the sample, which otherwise is difficult. This knowledge is relevant to understanding the interaction of graphene with molecules at a later stage e.g. via covalent bonds at graphene edges or with anchoring groups based on π-π stacking.

Transport in Suspended Graphene

Being able to optically characterize suspended graphene samples we have started to perform electrical measurements. Strain dependent effects on transport are being investigated in collaboration with Lujun Wang & colleagues (SNI Project 1504). By measuring under vacuum conditions, we could achieve graphene devices with a charge neutrality point at low gate voltages. This allows us to observe the effects of strain for both hole and electron transport regimes (Fig. 2d). The data acquired so far show a small change in conductivity, however higher mobility graphene samples are needed to properly distinguish effects of contact resistance from changes in charge carrier mobility. Two approaches, current annealing [4] and encapsulation with boron nitride are currently being investigated (see report of project 1504). The fabrication & measurement techniques established here can in principle be applied to studying strain effects in other 2D materials as well.

Investigation of Bottom up Synthesized Graphene Nanoribbons

Having established the characterization of suspended graphene we started to investigate functional units that can be contacted in this geometry. Atomically precise graphene nanoribbons (GNRs) can be synthesized from specifically designed molecular precursors [5]. The lateral confinement of charge carriers in GNRs leads to a width-dependent gap in the electronic density of states which can be chemically tuned through the design of precursor molecules. With lengths of several tens of nanometers we expect that GNRs will be easier to contact via π- π-stacking than most molecules, possibly also exhibiting smaller junction resistances. GNRs have interesting optical properties as confirmed by the recent observations of photo- and electroluminescence [6, 7].

As a starting point, we investigated the transfer process from the growth substrate to a sample. Figure 3 shows a cascade of Raman spectra acquired on aligned GNRs transferred to a metal substrate. The polarization dependent intensity shows that the alignment of GNRs is preserved during transfer and the visibility of the width-dependent breathing-like mode confirms overall structural integrity.

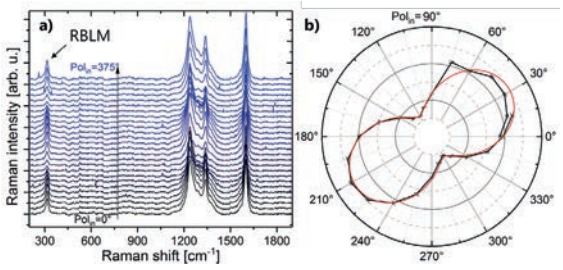

Fig. 3 ***a)*** *Cascade of Raman spectra on aligned GNRs for different polarizations.* ***b)*** *Polarization dependent intensity of the G-mode at ~1600 rel. cm⁻¹.*

Summary and Outlook

We have successfully established the optoelectronic characterization of suspended graphene devices and continue optimizing the mobility to investigate strain related effects in collaboration with SNI Project 1504. Moreover, we have an ongoing collaboration with Svenja Neumann in the group of O. Wenger for MCBJ measurements of molecules. Having demonstrated the successful transfer of GNRs onto substrates we are now moving towards contacting and suspending GNRs and other (macro) molecules on devices with graphene electrodes.

Acknowledgements

We thank Kishan Thodkar for help in growing graphene, Sascha Martin & Heinz Breitenstein for support with the new setup and Maria El Abbassi, Mickael Perrin, Marta de Luca and Ilaria Zardo for fruitful discussions.

References

[1] S. Wu, M.T. González, R. Huber, S. Grunder, et al. *Molecular junctions based on aromatic coupling*. Nature Nanotech **3,** 569 (2008)

[2] M. El Abbassi, L. Pósa, P. Makk, C. Nef, et al. *From electroburning to sublimation. Substrate and environmental effects in the electrical breakdown process of monolayer graphene.* Nanoscale **9,** 17312 (2017)

[3] T.M.G. Mohiuddin, A. Lombardo, R.R. Nair, A. Bonetti, et al. *Uniaxial strain in graphene by Raman spectroscopy. G peak splitting, Grüneisen parameters, and sample orientation*. Phys. Rev. B **79** (2009)

[4] R. Maurand, P. Rickhaus, P. Makk, S. Hess et al. *Fabrication of ballistic suspended graphene with local gating*, Carbon. **79**, 486 (2014)

[5] J. Cai, P. Ruffieux, R. Jaafar, M. Bieri, *et al. Atomically precise bottom-up fabrication of graphene nanoribbons.* Nature **466,** 470 (2010)

[6] B.V. Senkovskiy, M. Pfeiffer, S.K. Alavi, A. Bliesener et al. *Making Graphene Nanoribbons Photoluminescent*. Nano letters **17,** 4029 (2017)

Crystalline and free-standing two-dimensional supramolecular organic networks based on calixarene

Project P1308 Supramolecular charge and spin architectures produced by chemical clipping
Project Leader: P. Shahgaldian and T.A. Jung
Collaborator: M. Moradi (SNI PhD Student)

Introduction

There is a resurgence of interest in 2-dimensional (2D) materials ignited by the discovery of graphene and fueled by the importance of this type of materials for a range of applications. This has prompted scientists to develop a variety of bottom-up design strategies for the production of monomolecular layers with precise control of the organization of the constitutive building blocks at the molecular level.

This PhD project aims to develop a novel approach for the design of supramolecular layers with an atomically precise architecture and thickness on solid surfaces. It stems from findings achieved by the project partners on the stabilization of Langmuir-Blodgett (LB) films through a self-assembly process using supramolecular clips [1]. We have recently demonstrated that carefully designed calixarene synthons can be used to produce crystalline two-dimensional networks through coordination, of Cu(II) ions at the air water interface. The so-produced layers can be transferred on hydrophobic solid surfaces using the Langmuir-Schaeffer method without losing the crystallinity [2].

These encouraging results prompted us to further explore the possibility to produce crystalline 2D networks exploiting non-covalent dipole-dipole interactions instead of a metal coordination node. To that end, we designed a novel calixarene building block. Calixarenes are a class of macrocyclic molecules widely studied in Supramolecular Chemistry. Produced by the base-catalyzed reaction of *p-tert*-Bu-phenol and formaldehyde, they represent a class of macrocyclic skeletons that can be modified *à façon* to synthesize designer amphiphiles [3]. In the present project, a calix[4]arene derivative possessing short *n*-propyl chains at the lower rim and methyl-cyano functions at the upper rim has been synthesized. The short alkyl chains are expected to lock the flexibility of the calixarene macrocycle in the cone conformation. The cyano function has been widely studied for its ability to form surface supported -CN···NC- (dipole-dipole) interactions and metal coordination networks e.g. via Cu, with moderate geometric constraints. Here, at the air-water interface, CN functions were expected to form CN···NC bonds among neighboring calixarene molecules resulting in the formation of large and crystalline monolayers. To the best of our knowledge this new calixarene building block allowed to produce the first crystalline and self-standing supramolecular organic network (SON) stabilized through dipole-dipole interactions.

Results

The title compound, **1**, was produced through the lower rim Williamson alkylation of the parent calix[4]arene. This derivative was then modified at the upper rim to introduce chloro-methyl functions that were further modified to produce **1** in a quantitative yield. The surface pressure-area compression isotherm of **1** has been measured by means of the Langmuir balance technique on pure water (Fig. 1).

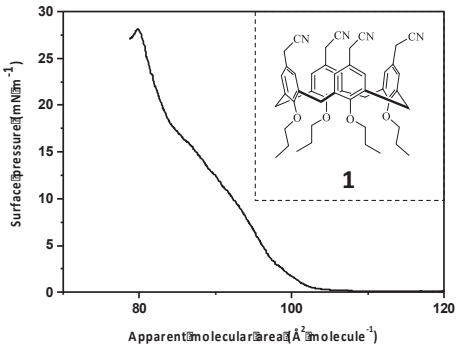

*Fig. 1 Surface pressure-area compression isotherm of **1** on pure water and chemical structure of **1**.*

The Langmuir balance study showed that **1** forms a stable monolayer on pure water, with a collapse pressure value of 28 mNm^{-1}. The compression isotherm reveals a fairly complex interfacial behavior, with two distinct phase transitions at 3.5 and 18 $mN\ m^{-1}$. The area values are consistent with the orientation of **1** with the central pseudo-symmetry axis orthogonal to the interface. The interfacial behavior of **1** has been further investigated using Brewster angle microscopy (BAM); representative micrographs are given in figure 2.

From the BAM micrographs, it can be recognized that on pure water, the monolayer of **1** exhibits a gas phase prior to compression. After the first phase transition, distinct 2-dimensional crystalline domains appear. Upon further compression, the monolayer covers the whole available surface while maintaining crystallinity. The influence of different divalent cations on the interfacial behavior of **1** was tested; in no case any relevant change on the

compression isotherm or on the BAM images have been measured.

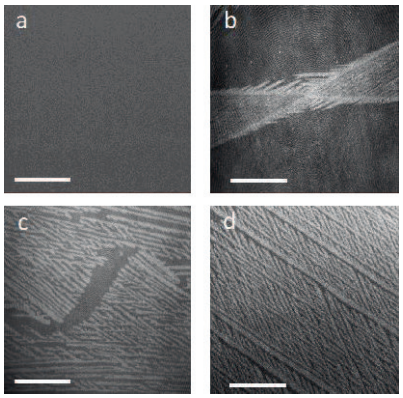

Fig. 2 BAM micrographs of the monolayer of ***1*** *on pure water acquired at the isotherm takeoff (a), at surface tensions of π=10 (b), π=15 (c) and π=20 mNm⁻¹ (d). Scale bars represent 100 μm.*

The monolayer of **1** was successfully transferred onto highly oriented pyrolytic graphite (HOPG) by the Langmuir Schaefer (LS) method and at a transfer ratio close to unity. *X*-ray photoelectron spectroscopy (XPS) chemical analysis of **1** on HOPG showed only one N1s peak at 399.7 eV, a characteristic value of N in the CN groups. The ratio between of O:N is ~1, as expected from the chemical structure of **1**, with a negligible amount of water.

In order to further study the LS films and to establish a molecular model of the monolayer on solid surface, near-edge *X*-ray absorption fine structure (NEXAFS) measurements at the N K edge were carried out (Fig. 3). The spectra exhibit a very simple line shape consisting only of the signals of transitions into the π* (400.6 eV) and σ* (~425 eV) molecular orbitals (MOs) of the CN groups. The angle dependence of the π* LD is modeled as a plane type orbital. We find an average angle of the CN groups with respect to the surface normal <γ>=57 ± 1°.

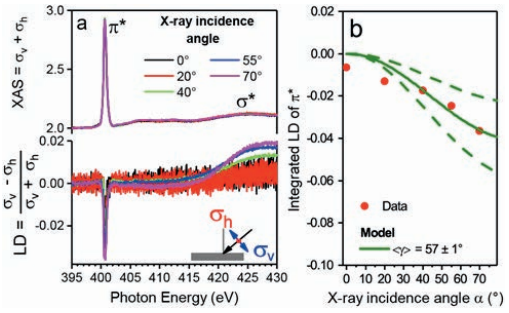

Fig. 3 N K edge X-ray absorption spectra ($\sigma_v + \sigma_h$) and linear dichroism LD of the SON of ***1*** *on HOPG. The transition into the unoccupied π* MOs of the CN groups is visible as a distinct peak at 400.6 eV (a). The integrated intensity of the linear dichroism of the π* signal as a function of the X-ray incidence angle with respect to the surface normal (b).*

Atomic force microscopy (AFM) investigations, performed on the transferred monolayer allowed acquiring molecular resolution images of the layer. The images revealed a closely packed and highly-crystalline monolayer (Fig. 4). The layer thickness was measured to be 1 ± 0.4 nm in agreement with the dimension of one monomolecular layer of **1**. Combining the NEXAFS, AFM and *X*-ray structure data of **1**, a molecular model of the SON of **1** could be obtained. In this model, **1** self-assembles via dipole-dipole interactions and forms a crystalline supramolecular organic network.

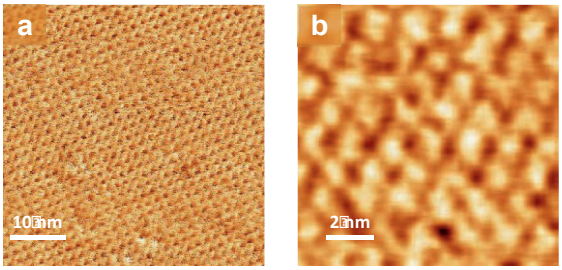

Fig. 4 Molecular resolution AFM images of the SON of ***1*** *transferred by the LS method (a). Zoom section showing single molecules of* ***1*** *in the network assembly*

Transmission electron microscopy (TEM) analysis has been conducted on the SON of **1** transferred on a TEM grid coated with a layer of Lacey carbon. The results showed that the SON of **1** is free-standing over an area as large as 3×3 μm. The free-standing layer does not show crystallinity. We attribute this to the absence of a substrate underneath the layer. Research is underway to improve our understanding of the structure of the monolayer of **1** and to investigate different molecular building blocks.

Conclusion

We show the first crystalline and free-standing supramolecular organic network layer stabilized mainly via dipole-dipole interactions. The molecules of **1** form a monocrystalline layer at the air-water interface that can be transferred successfully onto a solid substrate, without losing crystallinity. Combining NEXAFS, AFM and *X*-ray single crystal diffraction analyses, we have established a model explaining the packing of **1** at the air-water interface and on solid substrates. More work is underway to study the formation of calix[4]arene layers at the air-water interface and on solid substrates.

References

[1] N. Moridi, C. Wäckerlin, V. Rullaud, R. Schelldorfer, T.A. Jung, P. Shahgaldian, *Langmuir–Blodgett monolayer stabilization using supramolecular clips,* Chem. Commun. **49**, 367 (2013)

[2] M. Moradi, L.G. Tulli, J. Nowakowski, M. Baljozovic, T.A. Jung, P. Shahgaldian, *Two-dimensional Calix[4]arene-based metal-organic coordination networks of tunable crystallinity*, Angew. Chem., Int. Ed. **56**, 14395 (2017)

[3] L.G. Tulli and P. Shahgaldian, *Calixarenes and resorcinarenes at interfaces* in *calixarenes: functionalization and applications*, P. Neri, J. L. Sessler and M.-X. Wang, Springer, (2016)

Interfacing nanomechanical oscillators and ultracold atoms with laser light

Project P1309 Cooling and control of a nanomechanical membrane with cold atoms
Project Leader: P. Treutlein and P. Maletinsky
Collaborators: T. Karg (SNI PhD Student) and B. Gouraud

Interfaces of light and matter play an important role in quantum science and technology. In our project, we explore the use of laser light to interface ultracold atoms and a nanomechanical membrane oscillator [1]. The resulting hybrid atom-opto-mechanical system offers new possibilities for quantum control of mechanical vibrations, precision sensing, and quantum-level signal transduction [2]. Our group reported the first experiments along these lines, demonstrating sympathetic cooling of a nanomechanical membrane by coupling to ultracold atoms [3]. Although impressive cooling factors of about 1000 were reached, the mechanical oscillator was still operating in the classical regime in these experiments, mainly because it was placed in a room-temperature environment. To reach the quantum regime of mechanical motion, we have developed a new membrane optomechanical system with improved parameters that is placed in a cryostat. In addition, we have developed an interface between laser light and the spin state of an atomic ensemble. To couple atoms and membrane on the quantum level, we have developed a novel scheme and analyzed it in a fully quantum mechanical framework, including optical losses between the two systems.

Cryogenic Optomechanical Cavity

Cryogenic operation is required to suppress the rate of thermal decoherence of the mechanical oscillator below the rate at which information about its quantum state can be read out. This is equivalent to reaching the regime of large quantum cooperativity. To benefit from the reduced thermal noise inside a cryostat a number of technical problems need to be solved. To avoid detrimental technical vibrations a quiet liquid helium flow cryostat with a base temperature of 4.3 K was chosen (see Fig. 1a). Moreover, the optomechanical cavity needs to be robust and stable enough to withstand thermal cycling and maintain alignment between the optical and the mechanical mode during cool-down. At the same time the cavity must be tuned into resonance with a laser whose frequency is fixed with respect to the atomic transition, ruling out a fully monolithic design. To solve this problem, we built compact and rigid cavities whose mirrors can be moved along the optical axis using piezoelectric actuators (see Fig. 1 b). Thereby we manage to both lock the cavity at cryogenic temperatures and position the membrane at the slope of the intra-cavity intensity standing wave where the radiation pressure coupling is maximal. We will soon test the system's performance via optomechanical cooling and optomechanical correlation measurements at low temperature.

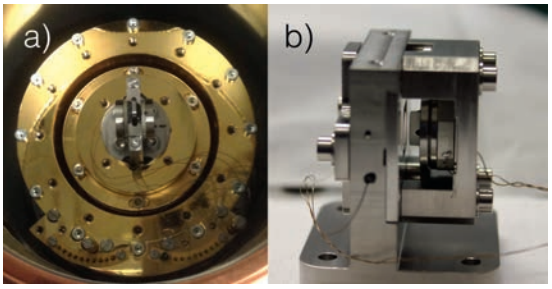

Fig. 1 a) Cavity on gold plated cold plate of flow cryostat seen from top. b) New cavity prototype for improved stability. The membrane chip is later placed in the gap between the two mirrors and aligned in situ.

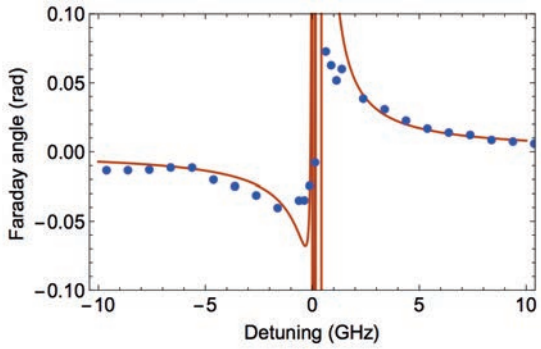

Fig. 2 Preliminary measurement of the Faraday rotation angle as a function of laser detuning from the atomic transition. The red line is a theoretical curve corresponding to an optical depth of 50.

Atom-Light Interface

In parallel to developing a cryogenic optomechanics platform another major achievement has been the setup of an atom-light interface based on the Faraday effect [4]. By sending a detuned laser beam through the atomic cloud this interaction allows to map a collective atomic spin observable onto the polarization of the laser. A first step was the measurement of the polarization rotation of the laser beam due to an ensemble of atomic spins all oriented parallel to the laser propagation axis (see Fig. 2). From such a measurement, one can infer the strength of the atom-light coupling. The figure of merit in this case is the optical depth, which amounts to a large value of 50 in our measurements, implying that strong coupling is achieved. We explored this system further by driving Rabi oscillations of the atomic spin and optically reading out its precession around a magnetic field orthogonal to the laser axis. In these measurements, we observed that spin coherence in our system is limited by residual gradients of the magnetic stray

field. This problem will be solved by magnetic shielding and a magnetic field compensation system.

General Theory of Light-Mediated Interactions

Working towards interfacing the atomic and the optomechanical system we devised a new coupling scheme that improved on a previous theoretical proposal [5] in various aspects. Not only did we manage to find an experimentally feasible coupling scheme, we also generalized the theoretical framework to describe systems whose interactions are mediated by light.

The coupling scheme (see Fig. 3) is based on the cascaded interaction of the atoms and the membrane with a common optical mode. The atoms are simultaneously placed at the input and the output of a Mach-Zehnder interferometer with the optomechanical cavity in one arm. This configuration implements unitary transformations of the light field quadratures required to transmit information from one system to the other. Another simplification arises from the fact that the atoms now couple to a traveling optical wave instead of a standing wave, thereby enabling a homogeneous atom-light coupling and relaxing the requirements on the atomic trap.

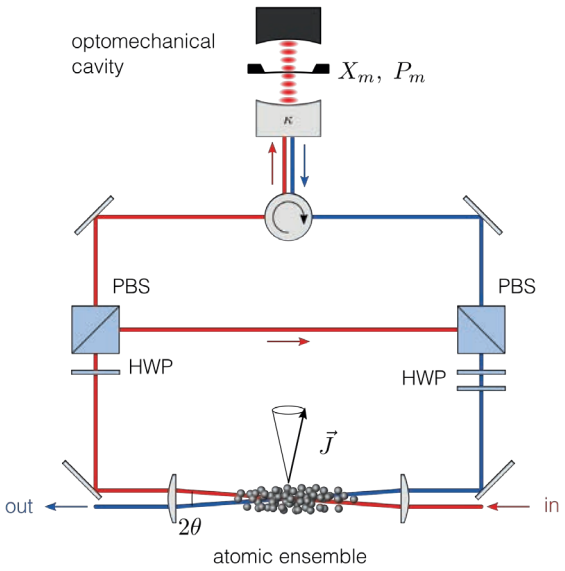

Fig. 3 Sketch of the new experimental scheme to couple a membrane oscillator in a cavity to an atomic spin. PBS: polarizing beam splitter, HWP: half-wave-plate.

To describe the dynamics of this system we derive a quantum optical master equation by adiabatically eliminating the optical field. In doing so we can identify different Hamiltonian and dissipative terms. Apart from the known terms for coherent atom-membrane coupling and decoherence on the individual systems, we find another previously neglected dissipative process that we can attribute to information loss between the systems. Any loss can be interpreted as a projective measurement with discarded results and will therefore destroy coherence. This poses a severe constraint on the cooperativity of the hybrid system, which is inversely proportional to the optical loss probability per path from atoms to membrane or membrane to atoms. The cooperativity of the ideal loss-free system can only be approached if the losses remain smaller than the inverse of the atomic optical depth. Thanks to the design of our membrane cavity system, which allows for very good mode matching between the laser and the cavity mode and low losses on the optical path, we can expect overall losses of about 10%, resulting in a total cooperativity of about 4 at the experimental optical atomic depth. This indicates that the requirement on the cooperativity to exceed unity can be met, making our atom-membrane interface suitable for the implementation of quantum protocols.

References

[1] M. Aspelmeyer, P. Meystre, and K. Schwab, *Quantum optomechanics*, Phys. Today **65**, 29 (July, 2012)

[2] P. Treutlein, C. Genes, K. Hammerer, M. Poggio, and P. Rabl, *Hybrid Mechanical Systems*, in "Cavity Optomechanics" (eds M. Aspelmeyer, T. Kippenberg, and F. Marquardt) 327–351 (Springer, 2014)

[3] A. Jöckel, A. Faber, T. Kampschulte, M. Korppi, M. T. Rakher, and P. Treutlein, *Sympathetic cooling of a membrane oscillator in a hybrid mechanical–atomic system*, Nat. Nanotechnol., **10**, 55–59 (2015)

[4] M. Kubasik, M. Koschorreck, M. Napolitano, S. R. de Echaniz, H. Crepaz, J. Eschner, E.S. Polzik, and M.W. Mitchell, *Polarization-based light-atom quantum interface with an all-optical trap*, Phys. Rev. A **79**, 043815 (2009)

[5] B. Vogell, T. Kampschulte, M.T. Rakher, A. Faber, P. Treutlein, K. Hammerer, and P. Zoller, *Long distance coupling of a quantum mechanical oscillator to the internal states of an atomic ensemble*, New J of Phys **17,** 034044 (2015)

Functionalized elastomeric nanofluidic systems

Project P1310 Plasmonic sensing in biomimetic nanopores
Project Leader: Y. Ekinci and R.Y.H. Lim
Collaborator: D. Sharma (SNI PhD Student)

Introduction

Geometry-induced electrostatic (GIE) trapping has emerged as a robust method for the passive trapping and manipulation of charged nanoparticles. It provides a controlled fluidic environment for high throughput contact-free confinement of nanoparticles in the range of 150 nm to 10 nm [1-5]. GIE-trapping relies on the geometry of the fluidic device and on the electrostatic repulsion between charged surface of the fluidic device and the charged nanoparticles [3]. To acquire charged surface GIE-trapping devices are mainly fabricated using SiO_2-based substrates such as glass [2, 3], silicon [1, 4], and PDMS [6]. These substrates have silanol groups on the surface, which go through self-deprotonation in presence of aqueous solution (pH > 2) [7] and result in a negatively charged surface. Thus, SiO_2 substrate-based fluidic devices can be used for negatively charged nanoparticles. However, for use in positively charged particle trapping, the device surface requires modification to a positively charged surface through surface functionalization.

In our previous work, we have demonstrated the functionalization of glass-based nanofluidic devices using polyelectrolytes i.e. poly(ethylene imine) (PEI) and its application for trapping of positively charged nanoparticles [3]. The fabricated GIE-trapping fluidic device comprises of two buffers supplying microchannels, which are connected via nanochannels that are embedded with nanopockets. Surface functionalization of a glass-based nanofluidic device can only be performed after developing final device (Fig. 1). This process is time consuming and takes ~ 5 days to prepare a single device for experiment due to diffusion based buffer exchange and slow drying process (Fig. 2). Thus, to reduce fabrication and functionalization time of GIE-trapping nanofluidic devices, we present here functionalization of polydimethylsiloxane (PDMS) based fluidic devices, which substantially increase the throughput of the fabrication in comparison to that for the glass or silicon-based devices. As shown in figure 3, surface modification of PDMS-based devices can be performed before the assembly of final GIE-trapping device. For the functionalization process, cationic (PEI) and anionic polyelectrolyte i.e. poly(styrenesulfonate) were used to achieve final negatively charged surface.

As published in our recent work, for PDMS-based nanofluidic device a PDMS mold is fabricated using soft lithography and bound to a cover glass after air plasma activation of both glass and PDMS mold surface. In PDMS-based devices, the nanoparticle solution is loaded to nanochannels in PDMS mold

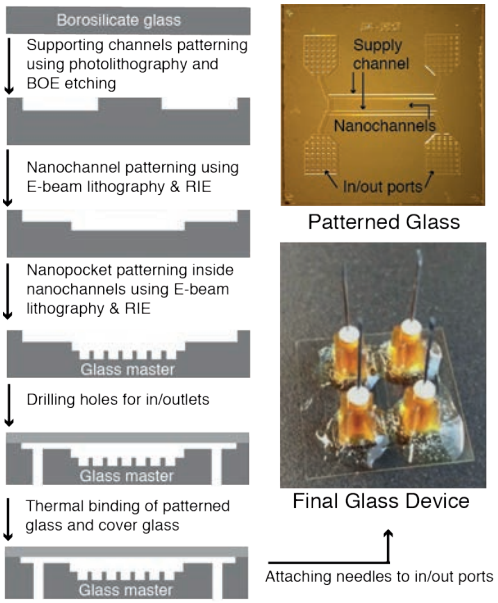

Fig. 1 Fabrication and development of glass-based GIE-trapping nanofluidic device using state of art lithography processes. The final GIE-trapping nanofluidic device is developed using thermal binding of patterned glass and a cover glass. For buffer exchange in/out ports of the fluidic device are attached to needles using glue.

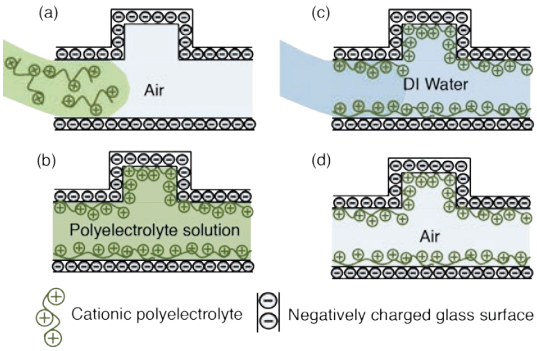

Fig. 2 Schematics of surface functionalization of nanochannels and nanopockets inside a nanofluidic device: (a) Injection of cationic polyelectrolyte solution in nanochannels via capillary force. (b) Adsorption of cationic polymers on a glass surface. (c) Washing away non-adsorbed polyelectrolyte by flushing de-ionized water through nanochannels via diffusion process. (d) Drying of nanochannels and nanopockets by flushing N_2 gas from one side and sucking out water and air from the other side of nanochannel.

prior to PDMS mold and glass binding [6]. For surface functionalization both PDMS mold and cover glass is functionalized with cationic and anionic polyelectrolytes, as shown in figure 3, to achieve first a positive surface and then a negative

surface. Both functionalized PDMS mold and cover glass were bound together after nanoparticle solution loading to the PDMS mold. The flexibility of functionalizing both PDMS and glass part of the PDMS-based nanofluidic device makes the surface modification step much faster and allows for multi-layer functionalization to attain homogeneous surface charge density.

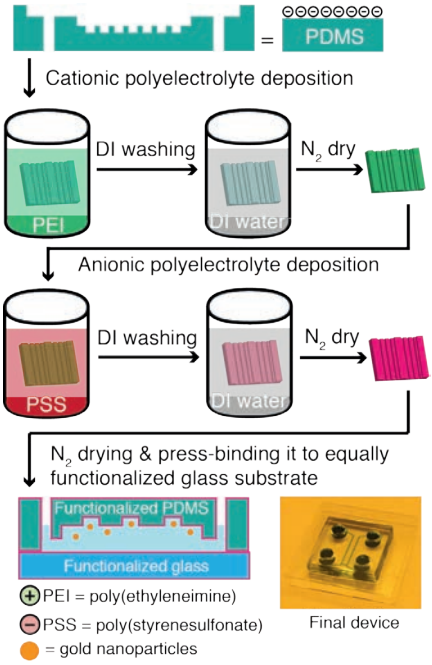

Fig. 3 Schematics of surface functionalization of PDMS based nanofluidic device using polyelectrolytes: PDMS mold and two cover glasses were functionalized using cationic and anionic polyelectrolyte as sequentially. After functionalization nanoparticle solution was injected into nanochannels and both PDMS mold and cover glass were pressed together to achieve final device.

We performed experiments with two-layer (PEI & PSS) functionalized PDMS nanofluidic device for single negatively charged 80 nm diameter gold nanoparticle (Au NPs) trapping. To compare experimental results and homogeneity of the obtained functionalized surface, similar experiments were performed using non-functionalized PDMS devices. In both experiments trapped particles were imaged using interferometric scattering detection (iSCAT) method and collected images were fitted with the Gaussian profile to obtain particle-center and its frame-by-frame displacement. Using the trajectory of the trapped particle mean square displacement (MSD) value (Fig. 4) and stiffness constant for the nano-trap was calculated. $MSD_{(xy)}$ values at plateau is related to stiffness constant of nano trap by $MSD_{(xy)} = 4k_BT/k_{(xy)}$.

Stiffness values were calculated for both layers functionalized and non-functionalized PDMS devices. Results show comparable stiffness values for trapped single nanoparticle before and after device functionalization (Fig. 5). This denotes successful functionalization of nano-structures as well as opens up a new direction of device application where a controlled and selective functionalization can bring possibility to trap both positive and negative single nanoparticles in the same device.

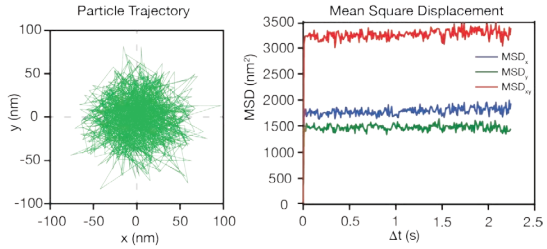

Fig. 4 The trajectory of a trapped particle inside a 500 nm nanopocket. The displacement of the particle inside the nanopocket from frame to frame is used to calculate mean square displacement plot.

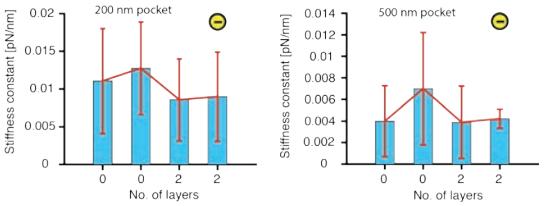

Fig. 5 Stiffness constant value range of trapped single 80 nm gold nanoparticles for 200 nm and 500 nm pockets. Experimental values were obtained for two-layers functionalized and non-functionalized PDMS nanofluidic device. Obtained stiffness values for functionalized device is comparable to native PDMS device demonstrating homogeneous and successful functionalization.

References

[1] M. Krishnan, N. Mojarad, P. Kukura, V. Sandoghdar, *Geometry-induced electrostatic trapping of nanometric objects in a fluid*, Nature **467**, 692 (2010)

[2] M.A. Gerspach, N. Mojarad, D. Sharma, T. Pfohl, Y. Ekinci, *Nanofluidic lab-on-a-chip trapping devices for screening electrostatics in concentration gradients*, Microelectron Eng **175**, 17 (2017)

[3] D. Sharma, M.A. Gerspach, T. Pfohl, R.Y.H. Lim, Y. Ekinci, *Single positively charged particle trapping in nanofluidic systems*, Microelectron Eng **175**, 43 (2017)

[4] M.A. Gerspach, N. Mojarad, T. Pfohl, and Y. Ekinci, *Glass-based geometry-induced electrostatic trapping devices for improved scattering contrast imaging of nano-objects*, Microelectron Eng **145**, 43 (2015)

[5] J. Tae Kim, S. Spindler, V. Sandoghdar, *Scanning-aperture trapping and manipulation of single charged nanoparticles*, Nat Commun **5**, 3380 (2014)

[6] M.A. Gerspach, N. Mojarad, D. Sharma, T. Pfohl, Y. Ekinci, *Soft electrostatic trapping in nano-fluidics*, Microsyst Nanoeng **3**, 17051 (2017)

[7] B.M. Lowe, C.K. Skylaris, N.G. Green, *Acid-base dissociation mechanisms and energetics at the silica-water interface: An activationless process*, J Colloid Interface Sci **451**, 231 (2015)

Targeted proteomics to study spreading of protein aggregation

Project P1401 Targeted single cell proteomics using magnetic nanoparticles to study prion-like spreading of amyloid nanoparticles
Project Leader: T. Braun and H. Stahlberg
Collaborators: C. Schmidli (SNI PhD Student), A. Bieri, R. Sütterlin, A. Hierlemann, M. Leist, and S. Gutbier

Introduction

Stereotypic spreading of protein aggregation through the nervous system is a hallmark of many neurodegenerative diseases. For the Parkinson's disease (PD) evidence accumulates that '*structural information*' for α-synuclein (α-syn) is transmitted between cells, leading to the typical protein aggregation in the target cell. A prion-like proliferation of 'structural strains' is a potential mechanism for the disease progression. However, the mechanism how such 'infectious' nanoparticles are transmitted from one cell to the next is unknown.

This project aims to study this proliferation of protein aggregates by combining two technologies: (i) *Microfluidic cell cultures*: Here neuron-like cells are cultivated in microfluidic chips, enforcing a defined geometrical arrangement of differentiated cells. Two chambers hosting the cell bodies are connected via narrow channels only allowing the growth of neurites between the chambers (Fig. 1). (ii) *Microfluidic protein fishing, labeling and sample preparation for electron microscopy (EM):* This new technology allows the specific isolation of untagged target proteins directly combined with EM grid preparation (Fig. 2 & 3). Importantly, this method does not only allow the detection of target proteins, but also provides structural information, therefore allowing detecting different 'structural strains'.

(i) Microfluidic cell cultures

To study the prion like cell-intrusion and spreading of protein aggregation of α-syn, we use the Lund human mesencephalic (LUHMES) cell line, which can be differentiated to dopaminergic-like neurons [1]. To enforce two spatially separated cell populations, such as diseased and healthy cells, we use microfluidic chips as shown in figure 1. These chips now allow to 'infect' cells in one compartment and with α-syn filament fragments and to observe the spreading of the α-syn aggregation via the neuritis to calls at the other side of the chip by 'seeding and transmission' experiments.

These experiments are now analyzed by classical methods, e.g., fluorescence light microscopy. However, today's biophysical and biochemical methods can trace the presence of proteins, but do not allow detecting *and* monitoring the structural arrangement of the involved proteins or structural strains. Visual proteomics [2, 3] promises to overcome these limitations and complements classical analysis methods.

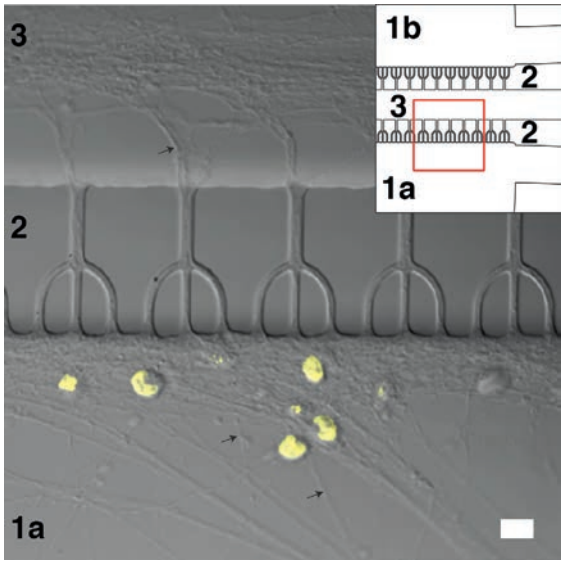

Fig. 1 LUHMES cells differentiated for 12 days in a 2nd generation microfluidic chip. The inset shows the arrangement of the different compartments of the chip; the red rectangle indicates the region of the light microscopy (LM) image. Cell somas are grown in two separated compartments (1a&b). The LM image is shown with the DAPI fluorescence label (yellow) of the nuclei. Narrow channels (2) with a width and height of approx. 3 µm allow the outgrowth of neuritis only, visible as shaded lines in the DIC image (few are labeled by arrows). The central channel (3) in the middle allows dendrite growth and serves as meeting area between cells from the upper (1b) and lower cell deposition regions (1a). Scale bar reads 10 µm.

(ii) Targeted visual proteomics

Only tiny amounts of cells can be harvested by 'seeding and transmission experiments'. Therefore, cell harvesting, protein isolation and sample preparation for EM must be miniaturized, automated and able to handle nanolitersized volumes. We developed a simple but versatile toolset for EM grid preparation for negative stain [2] and cryo-EM [3]. We also developed a microfluidic protein fishing method [4], which is now directly integrated into the set-up for EM grid preparation called cryoWriter.

This method is using antibody for target protein recognition and binding. These antibodies are coupled to superparamagnetic particles. We are using two forms of this composite material,

depending of the experiment and purpose: First, larger magnetic particles (Fig. 2a). These particles are too large for electron microscopy. Here, the antibody is coupled via a photo-cleavable cross-linker. Second, superparamagnetic nanoparticles (12 to 30 nm in diameter) are employed (Fig. 2b). Often, the antibody is directly linked to the particle and serves as electron-dense label in the EM for diagnostic purposes. A magnetic trap can immobilize both particle types in our microfluidic systems. Figure 3 explains to individual steps for microfluidic protein isolation, and figure 4 shows the integration of the magnetic trap in the cryoWriter set-up.

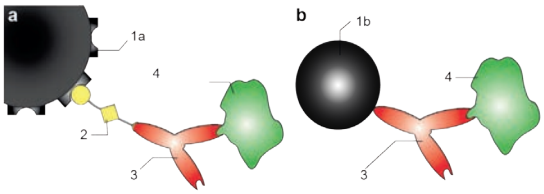

Fig. 2 Capturing antibodies linked to super-paramagnetic particles. (a) Antibody bound to super-paramagnetic particles via a photo-cleavable crosslinker. (b) The antibody is linked to the nanoparticles (diameter 12 to 30 nm), which serve as electro-dense label in the EM. (1a) Large latex bead spiked with super paramagnetic particles. (1b) Superparamagnetic nanoparticle. (2) Photo-cleavable crosslinker. (3) Capturing antibody. (4) Target protein.

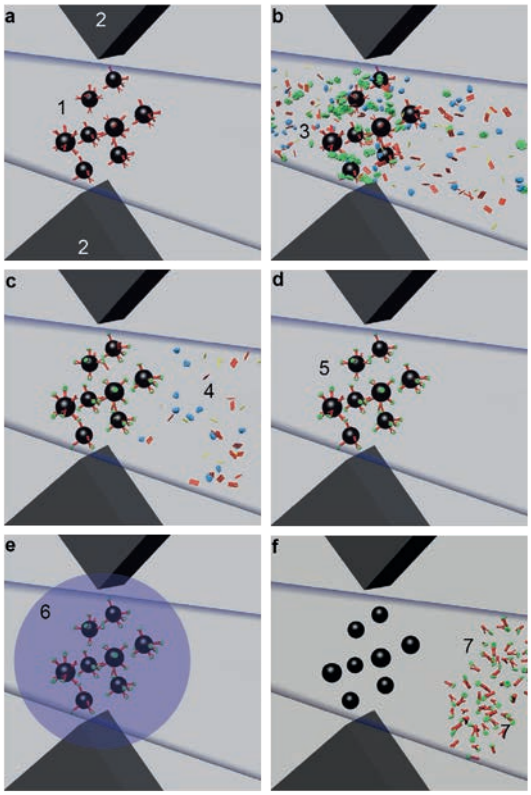

Fig. 3 Isolation of protein complexes using a magnetic trap and super-paramagnetic nanoparticles: (a) Magnetic beads or nanoparticles are trapped in a microcapillary by a magnetic field gradient, created by external magnets. (b) Cell lysate is flushed across the trapped particles, and the target protein binds to the capturing antibodies. (c) Non-bound lysate components are flushed away. (d) Only the captured target protein bound to magnetic beads or nanoparticles remains inside the magnetic trap. (e) Illumination with UV light breaks the photo-cleavable crosslinker, the isolated and purified target protein can be removed from the microcapillary and deposited on an EM grid (f). Alternatively, the target protein coupled to magnetic nanoparticles can be applied on an EM grid together. The magnetic nanoparticles thus serve as electron dense labels for diagnostic purposes.

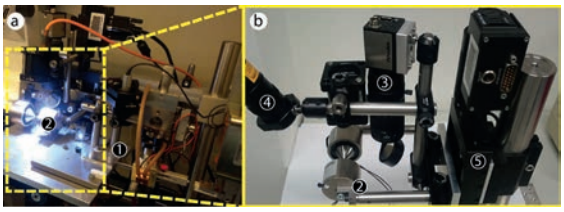

Fig. 4 Integration of the miniaturized magnetic trap in the cryoWriter set-up for EM grid preparation. a) Overview. (1) Dew point station and EM-grid for EM-grid preparation. b) Detailed view of the magnetic trap (un-mounted from the set-up). (2) Electromagnet. (3) Observation camera and optics to observe the trapping of super-paramagnetic particles via a mirror. (4) Illumination system to photo-cleave linkers. (5) Motor to co-move the trap with the nozzle. This allows to exchange buffers without releasing or moving the particle-plug.

References

[1] D. Scholz, D. Poeltl, A. Genewsky, M. Weng, T. Waldmann, S. Schildknecht, M. Leist, *Rapid, complete and large-scale generation of post-mitotic neurons from the human LUHMES cell line,* J. Neurochem.; **119(5)**, 957–971 (2011)

[2] S.A. Arnold, S. Albiez, N. Opara, M. Chami, C. Schmidli, A. Bieri, H. Stahlberg, C. Padeste, T. Braun, *Total sample conditioning and preparation of nanoliter volumes for electron microscopy*, ACS Nano; **10(5)**: 4981-4988 (2016)

[3] S.A. Arnold, S. Albiez, A. Bieri, A. Syntychaki, R. Adaixo, R.A. McLeod, K.N. Goldie, H. Stahlberg, T. Braun, *Blotting-free and lossless cryo-electron microscopy grid preparation from nanoliter-sized protein samples and single-cell extracts*, JSB **197**, 3(2017)

[4] D. Giss, S. Kemmerling, V. Dandey, S. Stahlberg, T. Braun, *Exploring the interactome: microfluidic isolation of proteins and interacting partners for quantitative analysis by electron microscopy*, Anal. Chem. **86**, 4680–4687 (2014)

Pushing the limits of lightweight materials

Project P1402 Lightweight structures based on hierarchical composites
Project Leader: C. Dransfeld and C. Schönenberger
Collaborators: W. Szmyt (SNI PhD Student), J. Gobrecht, M. Calame, K. Kröning, and B. Fiedler

Context

Multifunctional materials are constantly generating significant interest, while they can significantly reduce the device design complexity, decrease the ultimate mass of the product, improve the energy efficiency, etc. A promising candidate for such a material is a polymer reinforced with microscale carbon fibre (CF) grafted with nanoscale carbon nanotubes (CNTs), referred to as hierarchical composite. CNTs exhibit outstanding mechanical properties as well as heat and electrical conductivity, opening a range of possible functional extensions. Analogous materials are currently investigated by numerous research groups for damage sensing [1], enhanced electromagnetic shielding [2], energy storage [3] and more. Our work is focused on a novel approach to grow dense and high quality CNTs directly on the CF surface employing chemical vapour deposition technique. The previously conducted mechanical tests have revealed that the strength of CF decreases significantly in the process [4]. We are currently focused on overcoming this detrimental effect by exploration of alternative growth catalyst configurations using iron and nickel nanoparticles pre-delivered on the CF surface as well as the delivery of iron catalyst from the gas phase during the synthesis. We aim to obtain the material of enhanced mechanical properties as compared to the classical CF-based composite, opening the path to the emergence its extra functionalities.

Experimental and results

There have been hypotheses that during the direct growth of carbon nanotubes on carbon fibre, the diffusion of iron nanoparticles into the fibre is a phenomenon significant to the creation of defects in the fibre [5,6]. Our previous study verified the hypotheses by means of ptychographic X-ray computed tomography (PXCT) [7]. In our latest study, we examined the influence of the catalyst system choice on the magnitude of the destructive diffusion effect. We employed a CVD process of CNT synthesis with a vaporized mixture of toluene and ferrocene as a carbon source and a catalyst delivered in the gas phase referred to as floating catalyst CVD (see Fig. 1).

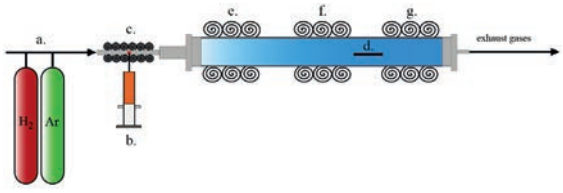

Fig. 1 CVD experimental setup. a) bottles with hydrogen and argon, b) carbon source and iron catalyst injection unit, c) vaporization section with heating, d) sample placed inside the quartz tube, e, f, g) the heating zones 1, 2, 3, respectively.

This process has been proven to yield well-aligned and dense vertical arrays of CNTs for electrically conductive and mechanically robust nanocomposites [8]. We have obtained a large yield of the grown CNTs with this method (see Fig. 2).

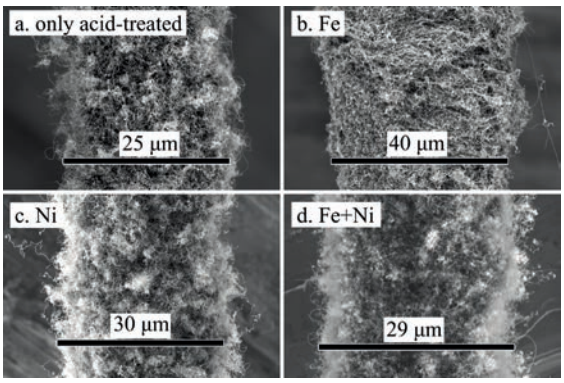

Fig. 2 The SEM images of the CNT-grafted CFs. a) fiber only after the acid treatment, b) fiber coated with iron NPs, c) fiber coated with nickel NPs, d) fiber coated with NPs composed of iron and nickel.

As modifications of the catalyst systems we have carried out an additional dip-coating synthesis of metallic NPs on the surface of the CF prior to the CVD process. Three cases of NP composition were considered: NPs composed of iron, nickel and of a mixture of iron and nickel. It can be hypothesized that such a pretreatment of the fibre may allow for a shortening the time of the CNT synthesis, which is critical to the preservation of the CF mechanical properties in the harsh CVD conditions. It is so, while the CNT growth in a floating catalyst CVD has an initiation period attributed to NP formation [9], which can be effectively omitted.

The expected detrimental NP diffusion effect has been examined by means of focused ion beam (FIB) cross-sectioning of the CNT-grafted-CFs followed by SEM examination and energy-dispersive X-ray spectroscopy (EDX) elemental analysis of the interesting regions of the cross sections (see Fig. 3).

The entire procedure has been carried out in the Helios NanoLab™ 650 DualBeam™ microscope produced by FEI Company, which is equipped with a gallium focused ion gun for FIB, electron gun for SEM and an EDX detector for fluorescent elemental analysis at nanoscale (Fig. 4).

The smallest NP diffusion was observed in the case of CF coated with iron NPs prior to the CVD process. For this sample, we have also observed the densest NP coating and the greatest yield of the grown CNTs. On the other hand, nickel has not been identified as a diffusing species (EDX results, Fig. 5), therefore

it could be less harmful to the CFs as compared to iron.

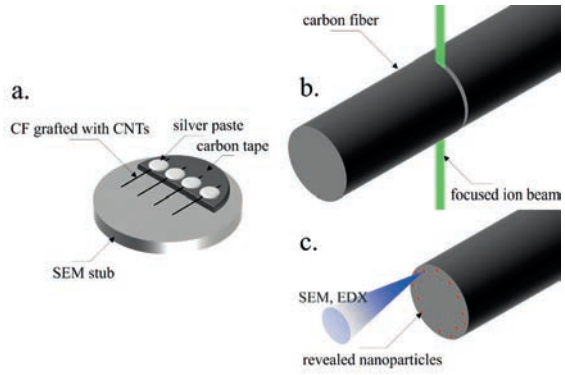

Fig. 3 CFs grafted with CNTs placed on an SEM stub a) overview schematic, b) FIB cut, c) CF cross section revealing the NPs for further examination. CNTs are not shown.

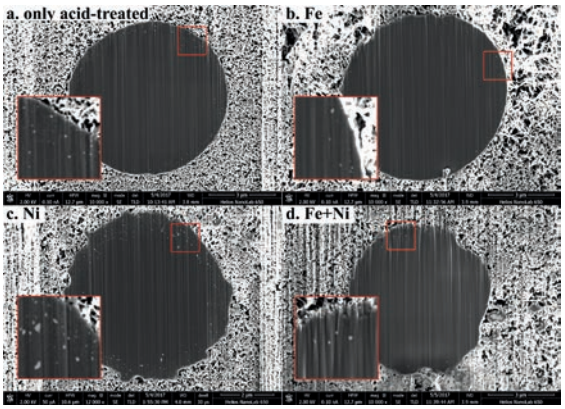

Fig. 4 The SEM images of the CNT-grafted CFs. a) fibre only after the acid treatment, b) fibre coated with iron NPs, c) fiber coated with nickel NPs, d) fiber coated with NPs composed of iron and nickel.

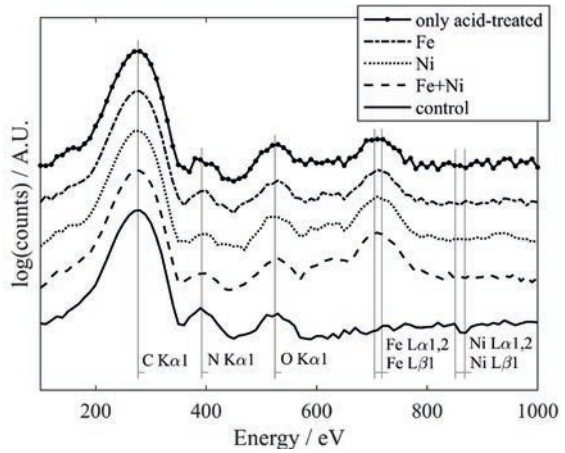

Fig. 5 The EDX spectra of the examined diffused NPs Solid black line – control spectrum collected at the middle of the fiber cross section, dot-dashed line – CF coated with iron NPs, dotted line – CF coated with nickel NPs, dashed line – CF coated with NPs composed of nickel and iron, solid line with full circles – CF only acid treated. We cee that only iron is identified as a constituent element.

Although, its potential as a sole CNT growth catalyst in our system remains yet to be verified.

The current results show a new perspective on the effects of the CNT synthesis on the CF. Understanding of this process is critical to the establishment of effective manufacturing methods of hierarchical composites. Therefore, this study constitutes a promising step towards the development of the hierarchical composites and multifunctional materials.

References

[1] G.J. Gallo and E.T. Thostenson, *Spatial damage detection in electrically anisotropic fiber-reinforced composites using carbon nanotube networks,* Compos. Struct. **141,** 14–23 (2016)

[2] D. Micheli, A. Vricella, R. Pastore, A. Delfini, A. Giusti, M. Albano, M. Marchetti, F. Moglie, V.M. Primiani, *Ballistic and electromagnetic shielding behaviour of multifunctional Kevlar fiber reinforced epoxy composites modified by carbon nanotubes,* Carbon **104,** 141–156 (2016)

[3] M.S. Islam, Y. Deng, L.Y. Tong, S.N. Faisal, A.K. Roy, A.I. Minett, V.G. Gomes, *Grafting carbon nanotubes directly onto carbon fibers for superior mechanical stability: Towards next generation aerospace composites and energy storage applications*, Carbon **96,** 701–710 (2016)

[4] S. Vogel, C. Dransfeld, B. Fiedler, J. Gobrecht, *Protective effect of thin alumina layer on carbon fibre to preserve tensile strength during CNT growth by CVD*, Proceedings of ECCM16, Seville, Spain, June 22nd-26th (2014)

[5] H. Qian, E.S. Greenhalgh, M.S.P. Shaffer, A. Bismarck, *Carbon nanotube-based hierarchical composites: a review*, J. Mater. Chem. **20,** 4751 (2010)

[6] H. Qian, A. Bismarck, E.S. Greenhalgh, M.S.P. Shaffer, *Carbon nanotube grafted carbon fibres: A study of wetting and fibre fragmentation*, Compos. Part Appl. Sci. Manuf. **41,** 1107–1114 (2010)

[7] W. Szmyt, S. Vogel, A. Diaz, M. Holler, J. Gobrecht, M. Calame, C. Dransfeld, *Protective effect of ultrathin alumina film against diffusion of iron into carbon fiber during growth of carbon nanotubes for hierarchical composites investigated by ptychographic X-ray computed tomography*, Carbon **115,** 347–362 (2017)

[8] M. Mecklenburg, D. Mizushima, N. Ohtake, W. Bauhofer, B. Fiedler, K. Schulte, *On the manufacturing and electrical and mechanical properties of ultra-high wt.% fraction aligned MWCNT and randomly oriented CNT epoxy composites*, Carbon **91,** 275–290 (2015)

[9] C. Singh, M.S. Schaffer, A.H. Windle, *Production of controlled architectures of aligned carbon nanotubes by an injection chemical vapour deposition method*, Carbon **41,** 359–368 (2003)

Charge-neutral biomolecules in the gas phase

Project P1403 Tailor-made proteins and peptides for quantum interference experiments
Project Leader: V. Köhler and M. Mayor
Collaborators: J. Schätti (SNI PhD Student), U. Sezer, S. Pedalino, J.P. Cotter, M. Debossiac, M. Kriegleder, P. Geyer, A. Shayegi, and M. Arndt

Molecular beams for interferometry

Molecular interferometry has significant potential for the determination of molecular properties in the absence of intermolecular interactions. It could for example enable the determination of inherent folding preferences of biomolecules by studying their conformation in the gas phase. Slow and charge-neutral molecular beams are however required for interferometry. To form such beams from biomolecules, which display typically strong intermolecular interactions and are rather fragile, constitutes a considerable challenge [1].

Tailoring the volatility and stability of oligopeptides

The stability and volatility of a range of peptide constructs was studied under thermal evaporation and subsequent VUV-ionization (Fig. 1, see also annual report 2015 and 2016) [1].

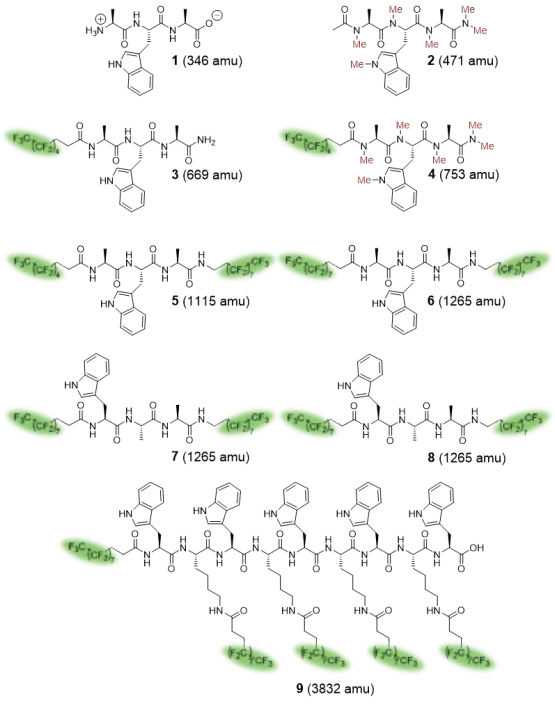

Fig. 1 Peptides investigated for molecular beams by thermal evaporation. Methylgroups are highlighted in red, perfluoro alkyl chains in green.

In order to reduce intermolecular interactions in oligopeptides we investigated i) the removal of internal charges, i.e. acylation and amidation of N- and C-terminus, respectively, ii) removal of hydrogen bond donors by methylation [2], iii) the decoration with perfluoroalkyl-tags.

The peptide constructs were heated in an oven and the vaporized molecules VUV-ionized at 157 nm for mass detection. The following observations were made: i) no parent peak (M^+) was observed for non-derivatized tripeptide **1**, ii) methylated peptide **2** without internal charges allowed observation of the parent signal next to a high proportion of fragments, iii) a single terminal perfluoroalkyl chain as in **3** was sufficient to render M^+ the dominant signal when excluding the commonly observed indole and skatole cations (Fig. 2), iv) while methylation of the construct (**4**) increased fragmentation strongly. Introducing a second perfluoroalkyl chain and increasing the number of difluoromethylene units (**5** - **8**) led for two constructs (**7**, **8**) even to a stronger signal of the parent ion than the indole and skatole cations while little other fragments were observed. Although preliminary studies in a set-up with a short path length and collection of seemingly condensed material were encouraging (annual report 2016), the extension of the concept to heavily perfluoro-alkylated nonapeptide **9** was unsuccessful and only fragments were observed in the VUV-ionization coupled experiment, thereby revealing the limits of the thermal launch approach.

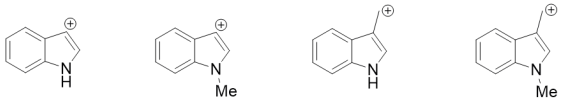

Fig. 2 Indole and skatole cations.

We are currently working to conclude a study on the gas phase transition of peptide constructs by laser desorption methods in combination with VUV-ionization. Results obtained so far are promising in respect to higher mass regimes.

Controlling molecules by photocleavage in high vacuum

The photocleavage [3] of designed tags allows the manipulation of molecules in the gas phase as has been recently shown in a proof of concept study [4]. A molecular beam of an *ortho*-nitrobenzyl ether formed by laser desorption into an adiabatically expanding neon gas jet was successfully depleted upon irradiation at 266 nm.

Inspired by this study we synthesized a set of functionalized peptides with photocleavable tags and investigated their behaviour upon laser irradiation in high vacuum.

References

[1] J. Schätti, U. Sezer, S. Pedalino, J. P. Cotter, M. Arndt, M. Mayor, V. Köhler, *Tailoring the volatility and stability of oligopeptides,* J. Mass. Spectrom. **52**, *550* (2017)

[2] B. C. Das, S. D. Gero, E. Lederer, *N-methylation of N-acyl oligopeptides,* Biochem. Biophys. Res. Commun. **29**, *211* (1967)

[3] P. Klán, T. Šolomek, C. G. Bochet, A. Blanc, R. Givens, M. Rubina, V. Popik, A. Kostikov, J. Wirz, *Photoremovable Protecting Groups in Chemistry and Biology: Reaction Mechanisms and Efficacy,* Chem. Rev. **113**, 119, (2013)

[4] U. Sezer, P. Geyer, M. Kriegleder, M. Debossiac, A. Shayeghi, M. Arndt, L. Felix, M. Mayor, *Selective photodissociation of tailored molecular tags as a tool for quantum optics,* Beilstein J. Nanotechnol. **8**, 325 (2017).

Polymeric vesicles that deliver cargoes into the cell nucleus

Project P1404 Selective transport of functionalized nanocarriers into biomimetic and natural nuclear pore complexes
Project Leader: R.Y.H. Lim and C.G. Palivan
Collaborator: C. Zelmer (SNI PhD Student)

Introduction

The cell nucleus is the ultimate target for the therapeutic treatment of diseases such as cancer, brain disorders and heart dysfunctions. Here, nanocarriers may be advantageous for delivering sufficient concentrations of the active therapeutic substance *in situ*. However, little is known about how large, foreign objects traverse through nuclear pore complexes (NPC) that guard the entry into the nucleus.

In this work, we have developed nanocarriers (NC) that are selectively uptaken into the cell nucleus. This is achieved by covalently functionalizing the NC surface with multiple copies of nuclear localization sequences (NLSs). Each NLS-NC is thereby recognized by soluble nuclear transport receptors (NTRs also known as karyopherins or Kaps) [1, 2] to form stable transport-competent complexes. In this manner, the NLS-NCs are recognized as authentic cargoes that are trafficked by the nuclear transport machinery (Fig. 1). Subsequent binding of the NTRs to NPCs [3, 4] facilitates the entry of NLS-NC into the nucleus. Following which, the import factor RanGTP binds to the NTRs and concomitantly releases the NLS-NCs from the NPCs into the nucleus [4].

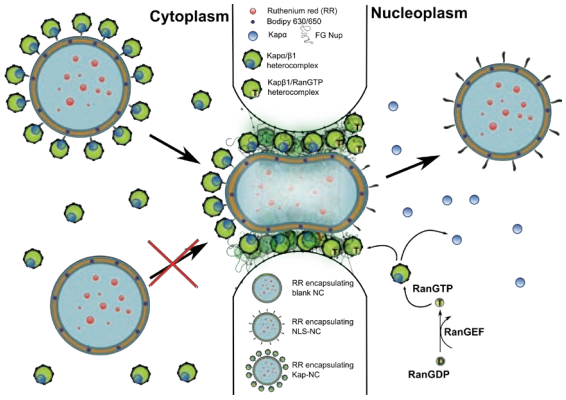

Fig. 1 Functional NLS-nanocarrier charged with hydrophilic ruthenium red and lipophilic Bodipy is transported into the cell nucleus via active transport mechanism. Blank nanocarrier is rejected by the NPC.

Further, we have labelled the polymeric membrane with Bodipy 630/650 and encapsulated ruthenium red (RR) inside the NCs to act as a model "theranostic" agent. Protected against premature cell secretion, RR together with Bodipy are translocated and accumulate in the cell nucleus. In the same manner, drugs, genes or other bioactive substances may be incorporated into the NC structure, making them versatile vehicles for delivering specific nuclear cargoes.

Engineering nuclear targeting nanocarriers

NCs have been synthesized using the amphiphilic triblock copolymer $PMOXA_4$-*block*-$PDMS_{44}$-*block*-$PMOXA_4$ as a scaffold material. By a spontaneous self-assembly process, it forms soft polymeric vesicles (or polymersomes) with excellent biocompatibility, as well as superior membrane stability and strength over liposomes [5-7]. Applying the so-called film rehydration method for vesicle formation allows us to simultaneously co-encapsulate Ruthenium Red and Bodipy into the assembled structure (Fig. 2).

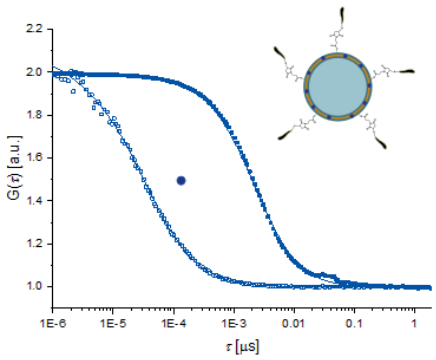

Fig. 2 Autocorrelation curves extracted from dual color fluorescence lifetime correlation spectroscopy (dcFLCS) of Ruthenium Red (red curve) and Bodipy (magenta curve). The cross-correlation of both (black curve) confirms co-encapsulation in NLS-polymersome structure.

Subsequently, NC functionalization with NLS tags is achieved by polymersome co-assembly with partially maleimide end-group functionalized $PMOXA_4$-*block*-$PDMS_{44}$-*block*-$PMOXA_4$. Extrusion through 50 nm filters further yields NLS-nanocarriers that are 53 ± 25 nm large as determined by fluorescence lifetime correlation spectroscopy (FLSC) and 44 ± 27 nm as confirmed by transmission electron microscopy (TEM).

Cellular internalization and nuclear uptake of polymer vesicles *in vitro* vs. *in vivo*

First, we tested the *in vitro* nuclear update of NLS-NCs using digitonin-permeabilized HeLa cells. In this case, the cells are no longer functional but the undamaged nucleus takes up NLS-NCs in the presence of recombinant nuclear transport factors and an energy supply (Fig. 3).

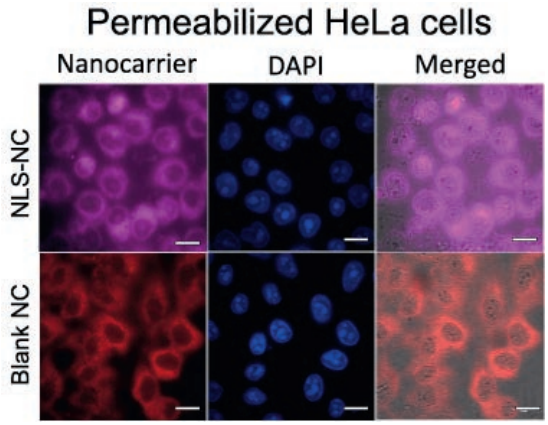

Fig. 3 Nuclear import of functional NLS-nanocarriers compared to blank nanocarriers in vitro. Scale bar = 10 μm.

Upon exposure, live HeLa cells naturally engulf the NLS-NCs and take them up into the nucleus *in vivo* (Fig. 4). This clearly shows that the endogenous nuclear trafficking machinery recognizes the NLS-NCs as authentic cargoes. As a key control, the nuclear uptake of blank NCs labelled with Nile Red 552/636 was largely inhibited. Further experiments are ongoing to characterise their cellular uptake, distribution and nuclear import efficiency.

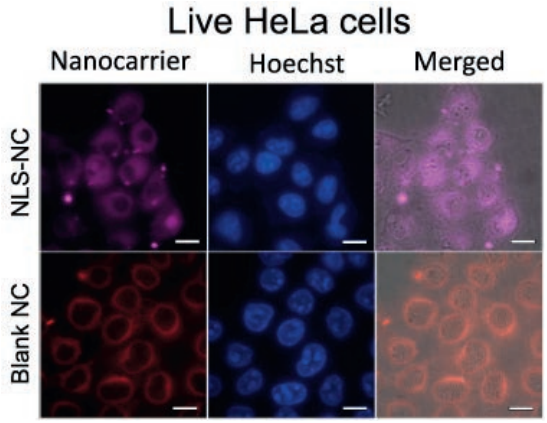

Fig. 4 Nuclear import of functional NLS-nanocarriers compared to blank nanocarriers in vivo. Scale bar = 10 μm.

Transmission electron microscopy

Moreover, we have employed transmission electron microscopy (TEM) to visualize the NLS-NLCs within permeabilized HeLa cells. Here, several NLS-NCs are seen at the cytoplasmic periphery of NPCs, presumably being associated with the FG-repeat nucleoporins that gate the pore (Fig. 5). Indeed, this might represent the first mechanistic step of entry into NPCs.

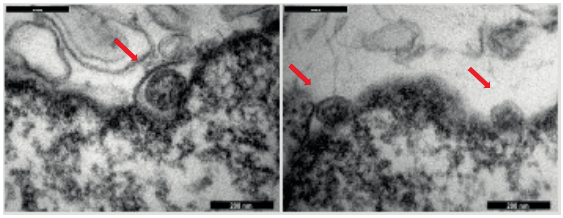

Fig. 5 Ruthenium Red encapsulated NLS-NCs are located at cytoplasmic NPC entry sites. Scale bar = 200 nm.

Summary

In a collaborative effort of the Lim and the Palivan labs, we have developed a novel polymer based nanocarrier system for selective nuclear cargo delivery. Next, we will study the nanocarrier stability in the cellular context and with that the potential release of cargoes into cell nuclei.

References

[1] M. Stewart, *Molecular mechanism of the nuclear protein import cycle,* Nat. Rev. Mol. Cell Biol. **8(3)**, 195-208 (2007)

[2] A. Hoelz, E.W. Debler, G. Blobel, *The structure of the nuclear pore complex*, Ann. Rev. Biochem. **80**, 613-643 (2011)

[3] S. Vujica, C. Zelmer, R. Panatala, R.Y.H. Lim, *Nucleocytoplasmic transport: a paradigm for molecular logistic in artificial systems*, CHIMIA **70(6)**, 413-417, (2016)

[4] L.E. Kapinos, B. Huang, R.Y.H. Lim, *Karyopherins regulate nuclear pore complex barrier and transport function,* J. Cell Biol. **216(11)**, 3609-3624 (2017)

[5] D. Wu, M. Spulber, F. Itel, M. Chami, C.G. Palivan, W. Meier, *Effect of molecular parameters on the architecture and membrane properties of 3D assemblies of amphiphilic copolymers,* Macromolecules **47(15)**, 5060-5069 (2014)

[6] C.G. Palivan, R. Goers, A. Najer, X. Zhang, W. Meier, *Bioinspired polymer vesicles and membranes for biological and medical applications,* Chem. Soc. Rev, **45(2)**, 377-411 (2016)

[7] V. Mikhalevich, C. Zelmer, A. Car, C.G. Palivan, W. Meier, *Bioinspired membranes*, RSC Polymer Chemistry Series, **22**, 221-258 (2017)

Diamond surface functionalization for nanoscale quantum sensing

Project P1405 Surface-functionalization of diamond nano-magnetometers for applications in nano- and life sciences
Project Leader: U. Pieles and P. Maletinsky
Collaborators: M. Batzer (SNI PhD Student), P. Appel, A. Barfuss, L Thiel, and S. Saxer

Introduction

This project aims at taming diamonds notoriously "noisy" surface through targeted, chemical surface functionalization of diamond for its use in quantum sensing applications with single spins. Over the last years, such spins in diamond have been established as highly attractive platforms to perform nanoscale quantum sensing with highest spatial resolution and sensitivity [1]. Various architectures are being pursued [2], from scanning probe tips [3], over diamond mechanical oscillators to "wide-field imaging" geometries containing large ensembles of spins for magnetometry. Common to all these approaches is the fact that the spins in question (spins contained in negatively charged "Nitrogen-Vacancy", NV^-, color centers in diamond) need to be placed to within few nanometers of the diamond surface to maximize sensing performance. However, this proximity is also known to negatively affect the spins quantum coherence properties through ubiquitous, but poorly understood noise sources (such as fluctuating electric-, magnetic- or strain-fields). The goal of this project is to overcome this key limitation to diamond-based sensing technologies by devising and implementing suitable strategies to passivate diamonds noisy surface.

Key experimental results

Our focus in the last year was on exploring and exploiting diamond hydrogen termination of for the purpose of coherence protection of shallow NV^- centers. Hydrogen termination in this context appears appealing, as it offers a simple chemical termination that would easily saturate possible dangling bonds on the diamond surface and thereby reduce magnetic (spin) and electric (charge) fluctuations. Our first result was the successful establishment of a reversible method for hydrogen termination of diamond by annealing in a hydrogen atmosphere (conducted in furnace of the group of Prof. C. Schönenberger and with valuable input from the group of Prof. B. Abel, Leipzig). We confirmed hydrogen termination indirectly through X-ray photoemission spectroscopy (see last year's report) and more directly through fluorescence measurements of near-surface NVs (Fig. 1). Such NVs are known to undergo a charge-state change from NV^- to NV^0, when close to a hydrogen terminated diamond surface under ambient conditions [4]. This de-charging is a result of band-bending induced by water desorbed on the hydrogen terminated surface (Fig. 2). We confirmed the reversibility of the hydrogen termination process by oxygen termination in acids, which fully restored NV^- fluorescence.

To benefit from the potentially calm, H-terminated diamond surface, but overcome limitations due to water-induced band bending, we followed steps to create a passivated, hydrogen terminated diamond sample, free of surface water layers. One approach, sketched in figure 1, consists in protecting a dry, H-terminate diamond surface with a passivation agent, such as hBN or a thin oxide layer, which prevents the formation of a water layer directly in contact with the H-terminated diamond surface. We successfully performed transfer of such hBN flakes (in collaboration with C. Handschin; Ph.D. student in the Schönenberger group) onto a diamond test sample. However, first attempts in observing NV^- in these samples were unsuccessful, in all likelihood due to residual water being trapped between diamond and hBN.

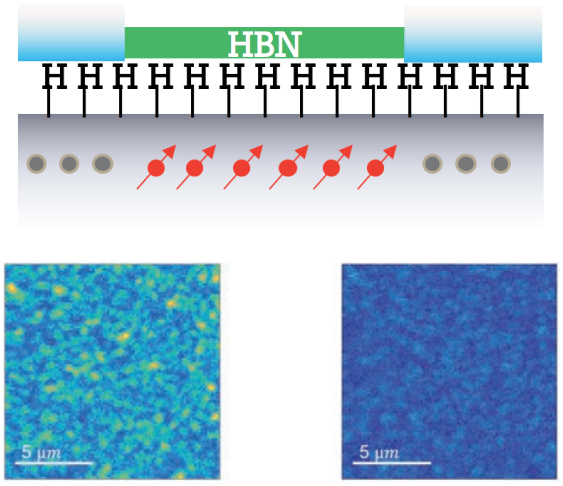

Fig. 1 (top) Schematic of the diamond surface protection for shallow NV spins (red arrows) targeted here. Our strategy is based on hydrogen surface termination and subsequent capping of the diamond to prevent the detrimental effect of water-layers on the underlying NV centers. (bottom) representative confocal optical images of shallow NV centers in oxygen (left) and hydrogen (right) terminated diamond. The color-scales are linear and identical in the two images and correspond to ~50kcps maximum. The two images show the reduced fluorescence rates in hydrogen terminated diamond, which result from band-bending induced de-charging of NV^- to NV^0.

We subsequently conducted systematic studies of diamond surface chemistry and wetting of the diamond surface using Kelvin-Probe-Microscopy (KPM) in collaboration with the group of Prof. E. Meyer. In short, KPM exploits electrostatic, capacitive interactions between samples and

scanning probe tips to determine changes in a sample's contact potential (i.e. the work function) on the nanoscale. KPM was performed in a dry glove-boy with in-situ bake-out capabilities to remove water from the surface. To our surprise, annealing to >350° C was required to get rid of surface water layers, in which case we saw a clear signature in the KMP signal (Fig. 2, bottom). Convincingly, we observed reversible and deterministic changes of the contact potential when comparing "wet" and "dry" diamond surfaces, in a fully reproducible way.

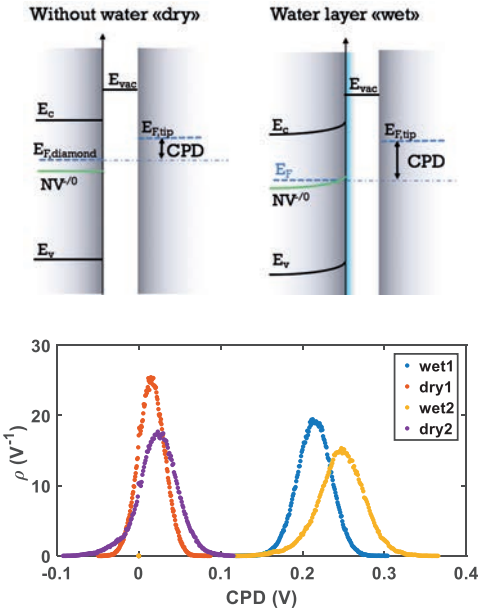

Fig. 2 (top) Mechanism of band-bending near the surface of hydrogen-terminated diamond. E_c, E_v, E_F, and E_{vac}, are conduction-band, valence-band, Fermi- and vacuum-energies of the respective constituents. The drawing also illustrates the marked difference in contact potential difference (CPD) expected in Kelvin Force microscopy (KFM) in the two cases. (bottom) Histogram of CPD values measured in KPM for diamond with and without surface water layer. The results show a clear and deterministic signal indicating if a surface is "dry" or "wet". The result here were obtained on O-terminated diamond and similar data has recently been taken by us on diamond with H-termination as well.

Outlook

Our plan for the next year is to consolidate our achievements thus far and study the coherence and charge properties of NV centre spins close to hydrogen-terminated dry diamond surfaces. For this, we will pursue our now established approach for hydrogen termination and subsequent water removal from the diamond. To maintain a "dry" H-termination, we will cap the diamond either using hBN flakes (an approach we already demonstrated), through ALD-based oxide deposition, where preliminary results look promising, or through a protective sample chamber offering a dry atmosphere under which our samples can be studied using confocal microscopy.

These results of next year will be decisive for future steps. In case of a successful recipe for diamond surface passivation as outlined above, we will include the process developed here into our established diamond tip fabrication process, with the goal of achieving highly coherent NV centre spins for nanoscale magnetometry, just few nanometres below a diamond surface.

Ultimately, the H-termination we here demonstrated will also form an ideal basis for further diamond surface functionalisation. These may include methods to adhere interesting bio-materials for sensing onto the diamond surface, or the realisation of more complex diamond surface chemistries [5], which may prove even more ideal to preserve the NVs fragile spin states next to the surface.

References

[1] J. Taylor J.M. Taylor, P. Cappellaro, L. Childress, L. Jiang, D. Budker, P.R. Hemmer, A. Yacoby, R. Walsworth, M.D. Lukin, *High-sensitivity diamond magnetometer with nanoscale resolution*, Nature Physics **4**, 482 (2008)

[2] L. Rondin, J.-P. Tetienne, T. Hingant, J.-F. Roch, P. Maletinsky, V. Jacques, *Magnetometry with nitrogen-vacancy defects in diamond*, Rep. Prog. Phys. **77**, 056503 (2014)

[3] P. Appel, E. Neu, M. Ganzhorn, A. Barfuss, M. Batzer, M. Gratz, A. Tschoepe, P. Maletinsky, *Fabrication of all diamond scanning probes for nanoscale magnetometry*, Rev. Sci. Instrum. **87**, 063703 (2016)

[4] M.V. Hauf, B. Grotz, B. Naydenov, M. Dankerl, S. Pezzagna, J. Meijer, F. Jelezko, J. Wrachtrup, M. Stutzmann, F. Reinhard, J.A. Garrido, *Chemical control of the charge state of nitrogen-vacancy centers in diamond*, PRB **83**, 081304 (2011)

[5] M. Kaviani, P. Deák, B. Aradi, T. Frauenheim, J. Chou, A. Gali, *Proper Surface Termination for Luminescent Near-Surface NV Centers in Diamond,* Nano Letters **14**, 4772 (2014)

Unusual distance dependences of electron transfer rates in molecular systems

Project P1406 Charge transfer versus charge transport in molecular systems
Project Leader: O.S. Wenger and M. Calame
Collaborators: S. Neumann (SNI PhD Student) and J. Overbeck

Introduction

Electron transfer rates (k_{ET}) commonly decrease with increasing distance (r_{DA}) between a donor and an acceptor [1, 2]. Recently our group discovered that under some conditions, k_{ET} increases over a certain distance range before the usually observed trend of decreasing k_{ET} with increasing r_{DA} is detected [3, 4]. In the course of this SNI-funded project, we aimed to shed more light on this potentially important and counter-intuitive phenomenon by synthesizing a series of new donor-bridge-acceptor compounds, and by exploring them with electrochemical methods as well as time-resolved laser spectroscopy. Over the past year of the funding period, we have made significant progress along this line of research and consequently there is less focus here on the charge transport studies emphasized in prior annual reports.

New donor-sensitizer-acceptor compounds

Our current studies concentrate on photoinduced electron transfer in donor-sensitizer-acceptor (D-S-A) compounds in fluid solution and on studying the rates for subsequent thermal electron-hole pair recombination (k_{ET}). We previously reported on a series of D-S-A systems comprised of a triarylamine (TAA) donor, a $Ru(bpy)_3^{2+}$ (Ru) sensitizer, and an anthraquinone (AQ) acceptor (Fig. 1a) [3, 4]. Thermal charge recombination as a function of r_{DA} (modulated by adjusting the number (n) of bridging *p*-xylene units) was investigated by pump-probe UV-Vis spectroscopy. The driving-force for charge recombination in these systems is approximately 1.6 eV according to cyclic voltammetry. We found that the shortest member (n=1) of this D-S-A triad series exhibits k_{ET} of ca. 10^5 s^{-1} at r_{DA} of 22.0 Å. Elongating r_{DA} to 30.6 Å accelerated charge recombination and led to k_{ET} of ca. 10^6 s^{-1}[3, 4].

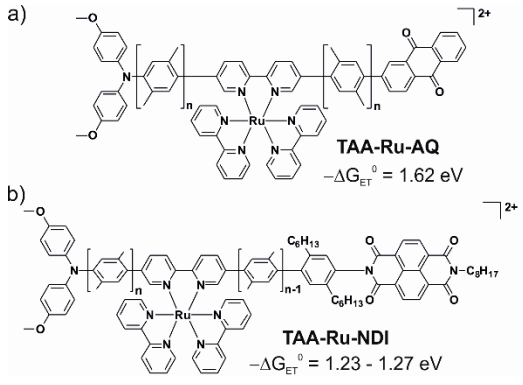

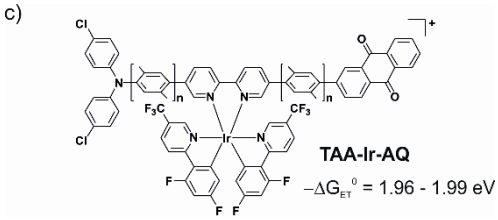

Fig. 1 Donor-sensitizer-acceptor (D-S-A) triads. Reaction free energies (ΔG_{ET}^o) for thermal charge recombination of D^+ / A^- pairs are as indicated.

This unusual distance dependence was interpreted in the framework of Marcus theory. With a reaction free energy (ΔG_{ET}^o) of ca. -1.6 eV, charge recombination likely occurs in the so-called inverted zone for the shortest member of this D-S-A series (Fig. 2, purple square). Upon increasing r_{DA}, the reorganization energy (λ) associated with charge recombination increases, shifting the Marcus parabola to the right in figure 2 [3, 4]. In the inverted zone, this can then lead to an increase of k_{ET} upon increasing r_{DA} (right vertical dotted line in figure 2), and consequently charge recombination is faster for the compound with n=2 (green square) than for n=1 (purple square). If this interpretation is correct, then one would expect this effect to disappear when going to lower driving forces (left vertical dotted line in figure 2). Conversely, the effect could become even more pronounced when the driving force is increased. In order to test these two hypotheses, we synthesized and explored two new series of D-S-A triads.

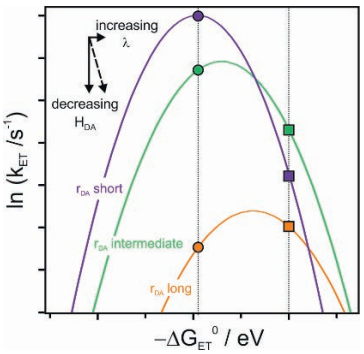

Fig. 2 Schematic driving-force dependence of the electron transfer rate for different donor-acceptor distances. Squares: Representative for a reaction with a large driving-force; circles: Representative for the expected behavior for a reaction with a small driving-force.

The D-S-A triad series in figure 1b combines a TAA donor and a Ru sensitizer with a naphthalene diimide (NDI) acceptor. This new combination leads

to a driving-force for thermal charge recombination between D^+ and A^- of only ca. 1.2 eV. Conversely, in the D-S-A in Figure 1c, an electron-deficient TAA donor is combined with an iridium photosensitizer and an anthraquinone acceptor, leading to a driving-force of ca. 2.0 eV. Thus, we are now in a position to explore the distance dependence of k_{ET} as a function of driving-force. ΔG_{ET}^0 is varied from -1.2 to -1.6 and -2.0 eV, while the distance is increased from 22.0 to 30.6 to 39.2 Å.

New distance dependence studies of charge recombination rates

The new D-S-A triad compounds were studied by time-resolved UV-Vis spectroscopy, using laser pulses of ca. 10 ns duration to excite the photosensitizers selectively. Transient absorption spectroscopy in combination with spectro-electrochemistry provides unambiguous evidence for the rapid formation of electron-hole pairs (D^+ / A^-) in all cases. By monitoring the decay of the transient absorption signals at different wavelengths, we obtain direct information about the rates for intramolecular charge recombination (k_{ET}).

We found that in the D-S-A system with a comparatively low driving-force of 1.2 eV, k_{ET} decreases with increasing r_{DA}, i. e., the distance dependence is as intuitively expected. This confirms our hypothesis that at lower driving-force the distance dependence of k_{ET} is normal (left dotted vertical line in figure 2). In the D-S-A system with maximized driving-force (2.0 eV), the distance dependence is similar to what we initially observed for the previously investigated system with ΔG_{ET}^0 = -1.6 eV.

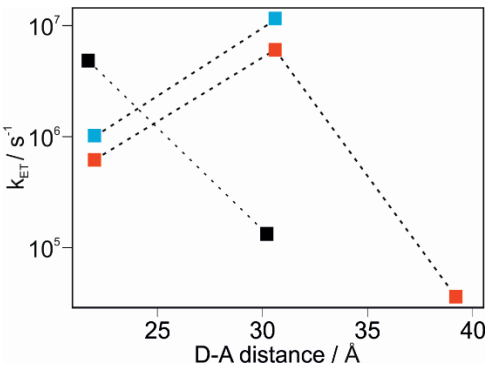

*Fig. 3 Distance-dependence of the electron transfer rate for thermal charge recombination for **TAA-Ru-NDI** (black), **TAA-Ir-AQ** (blue) and **TAA-Ru-AQ** (red)*[3].

Conclusion

Our new work demonstrates that the distance dependence of electron transfer rates can be controlled by variation of the reaction free energy. Very high driving forces (1.6 or 2.0 eV) lead to qualitatively different distance dependences than lower driving forces (1.2 eV). The unusual distance dependence with electron transfer rate maxima at large donor-acceptor distances is evidently a phenomenon that is encountered only at large driving forces.

Future studies in this context may be geared at investigating different types of molecular bridges, for example by replacing the *p*-xylene units by other rigid rod-like spacers.

This work is relevant in the context of a possible future molecular electronics technology, for which the precise control of charge transfer and charge transport rates is highly desirable.

References

[1] P.P. Edwards, H.B. Gray, M.T.J. Lodge, R.J.P. Williams, *Electron transfer and electronic conduction through an intervening medium*, Angew. Chem. Int. Ed. **47**, 6758 (2008)
[2] M. Cordes, B. Giese, *Electron transfer in peptides and proteins*, Chem. Soc. Rev. **38**, 892 (2009)
[3] M. Kuss-Petermann, O.S. Wenger, *Increasing Electron-Transfer Rates with Increasing Donor-Acceptor Distance*, Angew. Chem. Int. Ed. **55**, 815 (2016)
[4] M. Kuss-Petermann, O.S. Wenger, *Electron Transfer Rate Maxima at Large Donor-Acceptor Distances*, J. Am. Chem. Soc. **138**, 1349 (2016)

Coupling an ultracold ion to a metallic nanowire

Project P1407 Coupling a single ion to a nanomechanical oscillator
Project Leader: S. Willitsch and M. Poggio
Collaborator: P. Fountas (SNI PhD Student)

Introduction

At present, considerable efforts are undertaken towards creating hybrid quantum systems for the development of quantum technologies. The motivation for a solid state-atomic interface emerges from the possibility to combine the advantages of both platforms. Trapped ultracold atoms offer very good coherence properties. One of the most promising candidates for an atomic system is an ultracold ion which can be isolated from the environment by being trapped with radiofrequency electric fields in ultra-high vacuum [1]. By laser cooling the ion to its motional ground state, one can manipulate its motional and spin degrees of freedom with high accuracy. Conversely, metallic nanowires are nanomechanical systems that are highly scalable and integrable and can be interfaced with diverse quantum devices. A great challenge is the coupling of the two systems while maintaining good coherence properties. In order to combine the aforementioned advantages, one has to be able to transfer quantum states between them.

Here, we report progress towards the implementation of an interface between an ultracold ion and a metallic nanowire in a miniaturized segmented-layer ion trap (Fig. 1) in order to study the coupling between these two systems mediated by electric fields. We also propose a scheme for engineering the ion's motional quantum states using the mechanical drive of the charged nanowire. Our immediate aim is to study experimentally the coupling mechanisms underlying this new interface. At a later stage of the project, we envisage the realization of the aforementioned state engineering schemes.

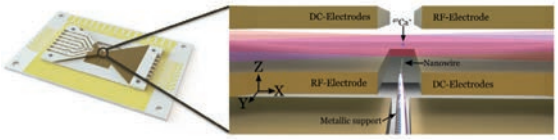

Fig. 1 Left figure: Miniaturized segmented-layer ion trap consisting of a stack of gold-coated alumina wafers clamped together on a printed circuit board. Right figure: Schematic representation of the experiment in the trapping region.

Classical simulations of the ion in the trap under the action of the nanowire

A combination of finite elements calculations (FEM) for solving Laplace's equation and molecular dynamics (MD) simulations for solving Newton's equations of motion for this system have been performed in order to aid in the design of the ion trap. In the MD simulations, we implemented the nanowire's effect as a force acting on the motion of a $^{40}Ca^{+}$ ion along with all the other forces that the ion is experiencing in a radiofrequency (RF) trap. We defined the parameters needed to realize the resonant excitation of the ion by the nanowire, e.g. the relative distance between these two systems, the nanowire's amplitude of oscillation and the DC voltage applied to the nanowire. With this classical treatment, we were able to study the ion's motion under the action of the vibrating nanowire for resonant and non-resonant coupling. Figure 2 presents the trajectory of the ion as a function of time when the ion motion is unperturbed, near resonance and off-resonance from the nanowire. One can clearly see the effect of the nanowire on the ion motion for each case.

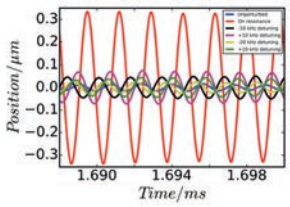

Fig. 2 Trajectory of a trapped $^{40}Ca^{+}$ ion unperturbed (blue solid line) and resonantly excited (red solid line) by driven nanowire. The magenta (green) and black (yellow) solid lines represent the ion trajectories with the cantilever frequency detuned by 10 kHz (20 kHz) above and below the resonance frequency, respectively.

Quantum dynamics calculations

To study the evolution of the ion motion in the quantum regime, we solved numerically the Lindblad master equation,

$$\frac{d\hat{\rho}}{dt} = -\frac{i}{\hbar}[\hat{\mathcal{H}}_{tot}, \hat{\rho}] + \hat{\mathcal{L}}\hat{\rho}$$

where we implemented motional decoherence based on realistic experimental parameters. We treated the nanowire as an oscillating electric field generated by a spherically charged particle located on its tip. We initialized the ion in its ground vibrational state which can be achieved experimentally by resolved-sideband cooling. The total Hamiltonian in frequency units reads

$$\hat{\mathcal{H}}_{tot} = \omega(\hat{a}^{\dagger}\hat{a} + \frac{1}{2}) - s(\hat{a}^{\dagger} + \hat{a})^2 + g(\hat{a}^{\dagger} + \hat{a})cos(\Omega t)$$

The second term which is quadratic in the sum of the ladder operators gives a shift in the vibrational levels of the ion and introduces squeezing. The last

term incorporates the coupling to the driving field and introduces a displacement of the ion. With this treatment, we were able to study the possibility of creating Gaussian and non-Gaussian quantum states of the ion by the driving field of the nanowire held at room temperature. In the simulations, we varied the factors that have different effects on the dynamics for the creation of different quantum states. These include the harmonic and anharmonic contributions of the ion-trap potential and the frequency mismatch of the motion of the ion with respect to the nanowire. Selected results are presented in figure 3.

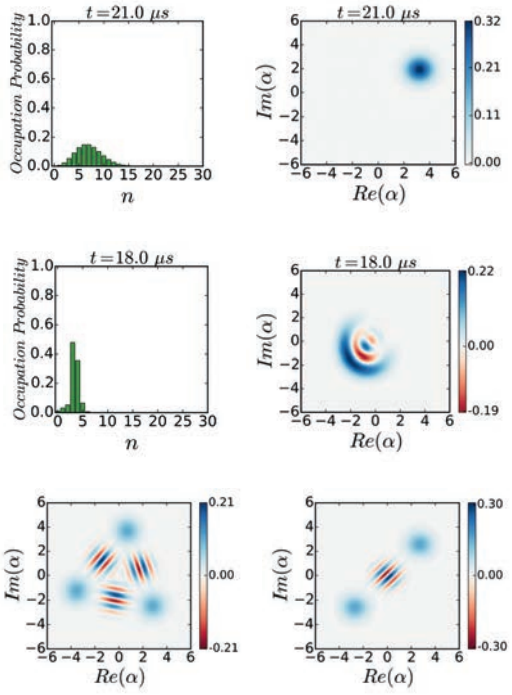

Fig. 3 First row: Fock distribution and Wigner function of a coherent state of the ion created by the oscillating nanowire. Second row: Fock distribution and Wigner function of an arbitrary non-Gaussian state of the ion generated during the time evolution by the drive of the nanooscillator. Third row: Snapshots of the evolution of a coherent state under the anharmonicities of the trap potential. At different points in the time evolution, the Wigner function of the ion wavepacket splits into three and two parts. The latter situation corresponds to a Schrödinger cat state.

We recently also initiated calculations describing the interactions in this system under cryogenic conditions when the motion of the nanowire is also quantized. The coupling Hamiltonian between the ion and the nanowire then reads

$$\hat{\mathcal{H}}_{coupling} = g(\hat{a}^\dagger + \hat{a})(\hat{b}^\dagger + \hat{b})$$

where $\hat{a}^\dagger$, $\hat{a}$, and $\hat{b}^\dagger$, $\hat{b}$ are the ladder operators of the ion and the nanowire, respectively, and g is the coupling strength. In a set of preliminary simualtions, we considered as initial condition the ion to be in its ground vibrational state and the nanowire cooled to a thermal state with an average phonon number of 3. To describe the dissipation in the system, we formulated Lindblad superoperators assuming that both systems are oscillators with Q-factors of 30000 and that the nanowire's effective mass is at most six orders of magnitude higher than the mass of the calcium ion (which is the case for, e.g., a carbon nanofiber). Figure 4 presents the phonon dynamics of the ion and the nanowire. One can see that every 40 ms, a complete energy transfer from one system to the other occurs. Thus, it appears feasible to cool the nanowire down to its ground vibrational state with the ultracold ion. We have also confirmed that this energy transfer also corresponds to a state transfer (not shown here).

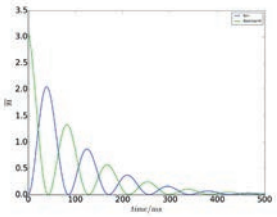

Fig. 4 Phonon dynamics of an ultracold ion (blue solid line) coupled to a charged nanowire (green solid line).

From both the semi-classical and full quantum descriptions, we conclude that the quantum motion of one system is mapped accurately onto the other, which may open up new possibilities for quantum sensing and quantum entanglement. Furthermore, the nanowire is coupled directly to the electric monopole of the ion. In this way, one can create coherent states with very large amplitudes without the need of, e.g., ultrafast potential switching with laser fields which cannot excite more than 20 phonons due to the weaker coupling with the electric dipole and quadrupole of the ion [2].

Outlook

The fabrication of the trap has finished and the experimental setup is currently under construction. Based on our theoretical results, we believe that this system will prove promising for fundamental studies on the borders of classical and quantum mechanics, and also as a probe of decoherence processes of quantum and macroscopic bodies. Finally, our setup might prove fruitful for various applications in spectroscopy, quantum sensing and quantum technologies.

References

[1] S. Willitsch, *Coulomb-crystallised molecular ions in traps: methods, applications, prospects*, International Reviews in Physical Chemistry **31(2)**, 175 (2012)

[2] J. Alonso, F.M. Leupold, Z.U. Soler, M. Fadel, M. Marinelli, B.C. Keitch, V. Negnevitsky, J.P. Home, *Generation of large coherent states by bang-bang control of a trapped-ion oscillator*, Nature Communications **7(11243)**, 11243 (2016)

Clean zigzag and armchair graphene nanoribbons

Project P1408 Clean zigzag and armchair graphene nanoribbons
Project Leader: D. Zumbühl and D. Loss
Collaborators: M. Rehmann (SNI PhD Student), Y. B. Kalyoncu, F. Froning, and F. Braakman

Edge Quality of Hydrogen Plasma Defined Graphene Edges

Graphene has emerged as a material very rich in interesting physical phenomena and holds great promise for the discovery of new effects, which are potentially valuable for both fundamental research and applications. Graphene nanoribbons (GNRs) are of particular interest as a playground for novel quantum states: in ribbons with crystallographic zigzag (zz) edge termination, ferromagnetic order of electron spins localized on the edge has been predicted [1], with spins at opposite ribbon edges pointing potentially in opposite directions due to inter-edge exchange. High quality zz edges are required to observe the predicted physical effects. However, fabricating clean GNRs with high quality crystallographic edges is very challenging. We developed a technique employing a cold remote hydrogen (H) plasma [2] which exhibits highly anisotropic etching yielding hexagonal shaped etch pits with edges pointing along the zz direction. We have shown [2], that anisotropic etching is not only possible for graphite surfaces, but is also present for single layer (SL) graphene if supported by a hexagonal Boron Nitride (hBN) substrate rather than SiO_2. Although the AFM images look very promising for the edges to be of high quality, it remains unclear how large the edge disorder really is. To investigate the edge quality of H plasma defined graphene edges, we use Raman spectroscopy. It is known, that a pure zz edge does not show any D peak in the Raman spectrum [3, 4], thus the D peak presence can be used as the litmus test. Furthermore, we investigate the edge quality of H plasma defined edges by means of electronic transport measurements at low temperatures. We plan to condense our findings into a follow-up publication to our first paper on the characterization of the H plasma etching technique [2].

Figure 1 shows AFM images of an artificial defect created in SL graphene on a hBN substrate before (a) and after (b) exposure to the remote H plasma. It is clearly visible that the round shaped hole evolves into a hexagonal etch pit, reflecting the anisotropy of the etch. In figure 1c Raman spectra are shown which were acquired at the edge regions indicated by black dashed circles in a) and b). Apparently, the D peak intensity increases upon H plasma exposure pointing towards an increased amount of armchair (ac) segments for the H plasma defined edge compared to the reactive ion etched (RIE) defined graphene edge. Further investigations are necessary to identify the origin of the relatively large D peak intensity and to find out how the etching process can possibly be optimized in order to create purer zz edges.

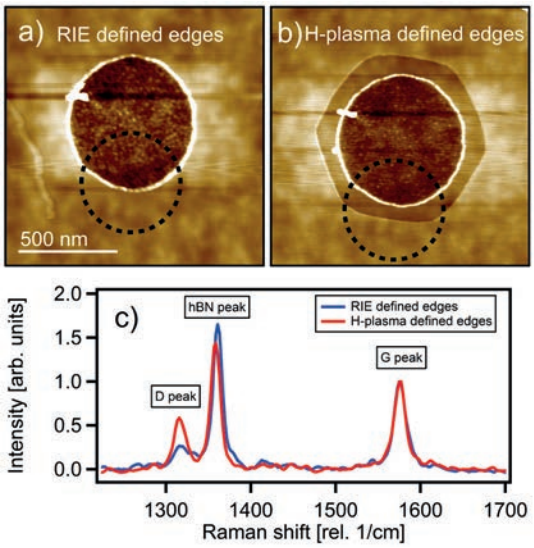

Fig. 1 a) AFM topography image of a RIE defined round shaped hole in a SL graphene flake. b) hexagonal etch pit after 2h of H plasma exposure. Scale bar valid for both AFM images. c) Raman spectra recorded at the regions indicated by the black dashed circles in a) and b). The single spectra are normalized to the graphene G peak and were recorded with a red laser (λ = 633 nm), circularly polarized light, an intensity of 1.5 mW and an integration time of 60 s with one accumulation.

Hole Spins in Germanium-Silicon (GeSi) Core-shell Nanowires (NWs)

Hole spins in GeSi core-shell NWs are excellent candidates for the implementation of spin qubits. Due to the possibility of isotopical purification of the host materials and no contact hyperfine interaction, such hole spins are expected to exhibit high coherence times. Moreover, theoretical proposals [5] predict a strong and tunable spin orbit interaction (SOI) of Rashba type. Indeed, the special dipole coupled SOI, also called “direct Rashba SOI”, is expected to be one order of magnitude larger compared to the conventional Rashba SOI [5]. The strength and tunability of the SOI leads to important and desirable consequences. In particular such systems could provide fast spin manipulation, low spin decoherence and individually addressable spins. However, so far a thorough characterization of this SOI has not been made. We electrostatically tune hole quantum dots of variable length to very low hole occupation numbers and study their excited state spectrum, allowing us to make comparisons to theoretical predictions on the nature and strength of the SOI.

Figure 2a shows a scanning electron microscope (SEM) image of a GeSi NW device and b) depicts a schematic representation of a similar device. Five bottom gates (g_1 to g_5) consisting of Titanium (Ti) and Paladium (Pd) with a height of approx. 15 nm are fabricated on top of a p^{++} doped Si substrate with 300 nm thermal oxide. The relatively small gate pitch of 50 nm enables the possibility to tune the quantum dots to very low occupation numbers. The NW is placed on a 20 nm thick Al_2O_3 dielectric grown over the bottom gate structure by atomic layer deposition (ALD). The electrical contacts (Ti/Pd) are evaporated after an HF etch to remove the Si shell and enable electrical contact. In figure 2c, we show the differential conductance dI/dV as a function of applied source drain voltage (V_{SD}) and gate voltage on gate g_2 (V_{g2}). Regular and well defined Coulomb diamonds are visible and illustrate the high electronic quality and tunability of the device.

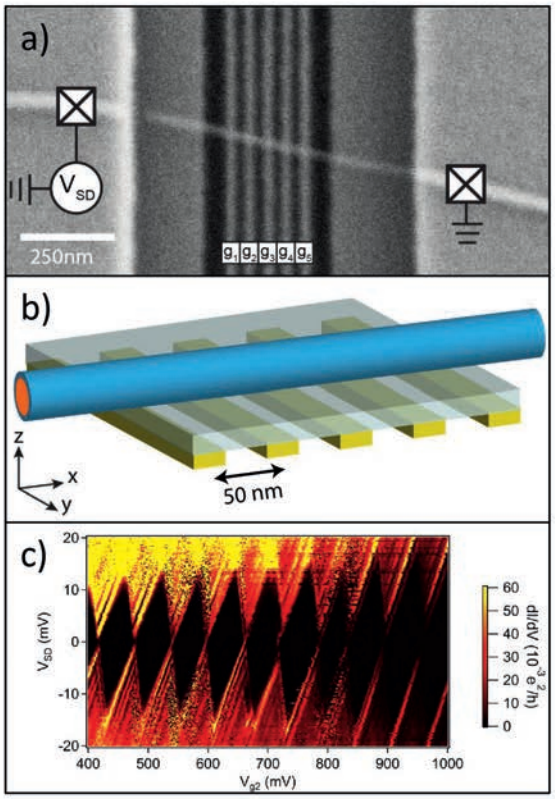

Fig. 2 a) SEM image showing an electrically contacted GeSi core-shell NW placed on top of five bottom gates (labeled g_1 to g_5). b) Schematic representation of the device shown in a). The Germanium- (red) Silicon (blue) core-shell NW lays on a 20 nm thick Al_2O_3 dielectric which electrically isolates it from the five bottom gates (yellow) The gate pitch is 50 nm. c) Differential conductance dI/dV as a function of V_{SD} and V_{g2} at barrier voltages g_1 = 2000 mV and g_3 = 4000 mV. Regular and well defined coulomb diamonds are visible. Standard lock-in techniques were used with a AC-bias of 100 uV at a frequency of 177.73 Hz at a temperature of T = 1.6 K.

Further measurements have shown, that we are able to vary the dot size from about 50 nm (dot in between two adjacent gates) to about 200 nm (dot between g_1 and g_5). First magnetic field measurements allowed us to get an estimate of the g-factor in our device. Moreover, we can tune the system into a double quantum dot regime by using g_1, g_3 and g_5 as barrier gates while g_2 and g_4 can be used as plunger gates. In this double dot configuration, we observe Pauli spin blockade physics and are currently investigating the leakage current as a function of the inter dot coupling to get insight into the nature and strength of the SOI in these systems.

Future experiments will focus on the investigation and establishment of the tunability of the SOI by electric fields. For this purpose, we intend to fabricate local side gates giving us the possibility to tune the electric field strength across the NW. In a next step we intend to implement spin manipulation via the spin-orbit interaction. After realizing a single qubit, long-distance qubit-qubit interaction needs to be established in order to create two-qubit entangling gates. There are two ideas how this long-distance qubit-qubit interaction can be achieved. First, metallic floating gates could capacitively connect qubit pairs [6]. Such a capacitive spin-spin connection is expected to be on the same order as the exchange energy of spins in neighbouring quantum dots. A second idea is based on the coupling of hole spins to a superconducting microwave cavity [7]. Thereby the interaction of the spins with the cavity field is mediated via the dipole moment of their charge degree of freedom and the SOI.

The extension of the P1408 project to experiments with GeSi NWs was approved by Prof. Dominik M. Zumbühl and Prof. Daniel Loss.

References

[1] Y. Son, M.L. Cohen, S.G. Louie, *Half-metallic graphene nanoribbons*, Nature **444**, 347 (2006)

[2] D. Hug, S. Zihlmann, M.K. Rehmann, Y.B. Kalyoncu, T.N. Camenzind, L. Marot, K. Watanabe, T. Taiguchi, D.M. Zumbuhl, *Anisotropic etching of graphite and graphene in a remote hydrogen plasma*, Npj 2D Mater Appl. **1**, 21 (2017)

[3] B. Krauss, P. Nemes-Incze, V. Skakalova, L.P. Biro, K. von Klitzing, J.H. Smet, *Raman Scattering at Pure Graphene Zigzag Edges*, Nano Lett. **10**, 4544 (2010)

[4] C. Casiraghi, A. Hartschuh, H. Qian, S. Piscanec, C. Georgi, A. Fasoli, K.S. Novoselov, D.M. Basko, A.C. Ferrari, *Raman Spectroscopy of Graphene Edges*, Nano Lett. **9**, 1433 (2009)

[5] C. Kloeffel, M. Trif, D. Loss, *Strong spin-orbit interaction and helical hole states in Ge/Si nanowires,* Phys. Rev. B **84**, 195314 (2011)

[6] L. Trifunovic, O. Dial, M. Trif, J.R. Wootton, R. Abebe, A. Yacoby, D. Loss, *Long-Distance Spin-Spin Coupling via Floating Gates*, Phys. Rev. X **2**, 011006 (2012)

[7] C. Kloeffel, M. Trif, P. Stano, D. Loss, *Circuit QED with hole-spin qubits in Ge/Si nanowire quantum dots*, Phys. Rev. B **88**, 241405 (2013)

Nanomechanical membranes for fast viscosity and liquid density measurements

Project P1501 Nanomechanical mass and viscosity measurement-platform for cell imaging
Project Leader: T. Braun and E. Meyer
Collaborators: P. Oliva (SNI PhD Student), B. Bircher, C. Padeste, N. Opara, C.-A. Schönenberger, F. Huber, and H.P. Lang

Introduction

To date, most methods used to determine the viscosity and mass density of liquids have two drawbacks: Long measurement time (in the range of minutes) and high sample consumption (in the range of milliliters). Nanomechanical transducers promise to overcome these limitations.

We previously developed a high-throughput micro-viscometer allowing liquid characterization using nano-mechanical cantilevers. The instrument is geared to measure viscosity and liquid density values of small aqueous droplets in a two-phase microfluidic system with a time resolution in the millisecond range [1] (Fig. 1).

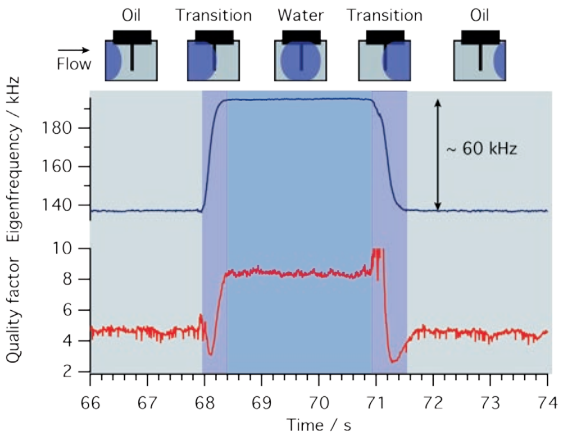

Fig. 1 Screening of aqueous droplets in a two-phase microfluidics using a nanomechanical cantilever transducer. The passage of an individual droplet is shown. Sideband tracking with a dual phase lock loop (PLL) was used to measure eigenfrequency and quality factor. These two values allow the calculation of liquid density and viscosity. When the oil–water interface passes the microcantilever, the laser beams are scattered and the PLL controllers adjust to the new values, resulting in a transition region of several 100 ms. Immersed in sample, a new stable value is achieved, until the droplet is replaced by oil again. Figure adjusted from [1].

Micro-viscometer using nano-mechanical membranes

We now developed a new set-up employing fully clamped membranes as resonators (Fig. 2). These Si_3N_4 membranes on a silica wafer form a well for sample deposition. The membrane side towards the optics is gold coated for optimal actuation of the membrane by the photothermal excitation system. This conception has several potential advantages: (i) The small cavity allows further reduction of the sample volume; (ii) the sample can be loaded from the top using a microcapillary coupled to a high-precision pump. This also allows triggering of reactions by adding effector molecules as shown in Fig. 3; (iii) arrays of Si3N4 membranes allow the multiplexed characterization of samples; (iv), the quality factor of these resonators is significantly higher than of fully immersed cantilevers; and (iv), the optical excitation and detection system does not need to pass through the liquid. Therefore, also non-transparent samples can be characterized.

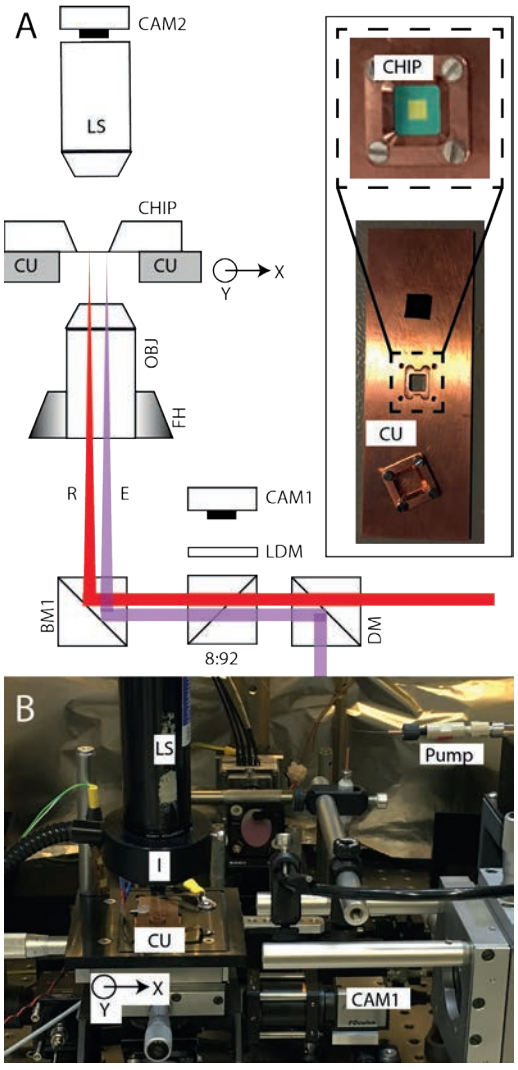

Fig. 2. Measurement set-up. A) Schematic of the photothermal excitation system. The chip with the Si_3N_4 membrane is placed on a copper plate (CU), which is temperature controlled via two small peltier elements. The copper plate is mounted on a x,y-stage, which allows

the chip to be moved relative to the excitation (E, λ = 406 nm) and read-out laser (R, λ = 780 nm). The two lasers are focused by an achromatic objective (OBJ), which is mounted on a focussing mechanic (FH). Focussing and alignment on the membrane can be observed via a camera (CAM1), a broadband (BM1) and an 8:92 mirror. The excitation and read out laser are combined using a dichroic mirror (DM). The measurement can also be observed via a lens system (LS) and an observation camera (CAM2). Inset: Photographs of chip holder from copper (CU) and mounted chip (CHIP). B) Photograph of set-up. Visible are the x,y-stage, chip holder (CU), alignment camera (CAM1) and observation lens (LS) with illumination system (I). Note, that the high precision pump allows sample loading from the top via a microcapillary.

The set-up is now ready to be used for measurements. The experiments confirmed that the quality factors of the membrane vibration are indeed significantly higher than employing fully immersed nano-mechanical cantilevers. The implemented pump system allows easy and precise priming of the chip-well above the membrane. A humidity chamber avoids evaporation of liquid from the sample well. Upon calibration [2], the new viscometer provides reliable liquid density and viscosity measurements (data not shown).

Biological experiments

As preliminary biological experiments, we investigated the assembly of filamentous proteins (Fig. 3). After loading of the protein in the monomeric form into the measurement well, the eigenfrequency shifts to lower values. This is due to unspecific adsorption of the monomer onto the membrane interface, increasing the mass of the resonator. After 10 min, the eigenfrequency stabilizes and the membrane is saturated. Subsequently, adding effector molecules triggers the aggregation of the monomeric protein to filaments. Growing fibrils are expected to shift the viscosity to higher values. Indeed, the Q-factor decrease, due to higher damping, which is related to an increase of the viscosity (Fig. 3).

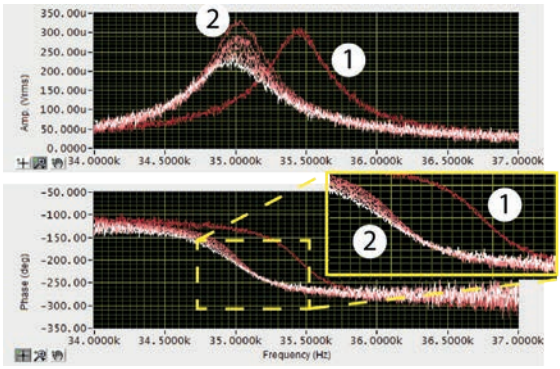

Fig. 3. Preliminary characterization of the protein aggregation of a filamentous protein. The protein is first loaded as monomer in the chip well (1). The reaction is triggered by adding effector molecules (2). The upper panel shows the amplitude spectrum, the lower the phase response. Start of the experiment is shown in red getting white towards the end of the experiment. The amplitude peak gets lower and broader (decreasing of the Q-factor) but only marginally shifts to lower frequencies (no mass adsorption, no significant change of liquid density).

Summary and outlook

The instrument and the corresponding control software are now completed and biological experiments are ongoing.

References

[1] B.A. Bircher, R. Krenger T. Braun. *Automated high-throughput viscosity and density sensor using nanomechanical resonators*, Sens. Actuators, B, **223(C),** 784–90 (2016)

[2] M. Heinisch, T. Voglhuber-Brunnmaier, E.K. Reichel, I. Dufour, B. Jakoby, *Reduced order models for resonant viscosity and mass density sensors,* Sens. Actuators, B, **220(C)**, 76–84 (2014)

Antiferromagnetic order probed in individual 3D-transition metal oxide nanoparticles

Project P1502 Investigating individual multiferroic and oxidic nanoparticles
Project Leader: A. Kleibert and M. Poggio
Collaborators: D.M. Bracher (SNI PhD Student), M. Testa Anta, T.M. Savchenko, M. Wyss, G. Olivieri, M.A. Brown, F. Nolting, and V. Salgueiriño

Introduction

Antiferromagnetic materials become increasingly important for modern spintronics devices such as spin valves and magnetic random access memories and for the development of novel ultra-hard magnetic materials [1,2]. Some antiferromagnetic materials are further multiferroic, i.e. exhibit additional ferro-electric order, and may therefore allow the manipulation of the magnetic order by electric fields [3,4]. While the properties of such materials are intensively investigated in their respective bulk and thin film forms the nanoscale properties still are poorly understood. However, the absence of net magnetic moments in antiferromagnetic systems makes studying nanostructures with antiferro-magnetic order very challenging. In this project, we aim to correlate magnetic, electronic and chemical properties with their morphology combining scanning electron microscopy (SEM) and X-ray photoemission electron microscopy (X-PEEM) by means of X-ray absorption (XA) and X-ray linear dichroism (XLD) spectromicroscopy.

In our previous report, we presented evidence for room temperature (RT) magnetic order in individual goethite nanoparticles (α-FeOOH). Temperature-dependent X-ray linear dichroism (XLD) spectra of individual goethite nanoparticles suggested antiferromagnetic order at room RT. However, we found no direct correlation between morphology and the linear dichroism, which we attribute to the typical polycrystalline morphology of our goethite nano-particles, which can lead to non-trivial magnetic properties. Here, we apply our experimental approach to single crystalline Cobalt oxide CoO/Co_3O_4 nanooctahedra. Previous experiments revealed ferromagnetic moments at the strained CoO/Co_3O_4 interface [2]. However, the relation between the strain-induced moments and the antiferromagnetic spin axis of the core as well as the actual orientation of the latter with respect to the crystal lattice of CoO remained unclear so far.

Experimental

The CoO/Co_3O_4 nanooctahedra are dispersed on silicon substrates with gold marker structures by drop casting. The gold marker structures are used to identify the very same nanoparticles in X-PEEM and SEM measurements. X-PEEM experiments are performed at the Surface/Interface Microscopy (SIM) beamline of the Swiss Light Source. Synchrotron radiation provides highly brilliant, very intense and polarized X-rays required for these investigations (Fig. 1a). Spatially resolved XA spectra recorded with linearly horizontally and vertically polarized X-rays are used to probe X-ray linear dichroism (XLD) at the Cobalt L_3 edge.

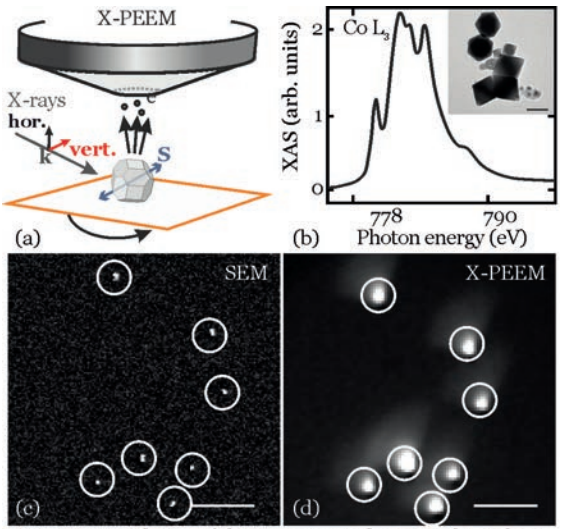

Fig. 1 a) Scheme of the experimental setup, where the X-ray propagation direction (k) and the particles spin axis (S) are indicated, b) Co L_3 reference spectrum recorded on a CoO single crystal [7]. In the inset, a TEM image of the CoO nanooctahedra (scale bar: 100 nm). In c) and d) the same spots imaged by SEM and X-PEEM at the Co L_3 edge, respectively. The white circles indicate the same CoO nanooctahedra. Scale bar: 1 µm.

Results

Figure 1b shows a XA spectrum of a single crystal CoO reference [5]. The inset shows a TEM image of the CoO nanooctahedra with different orientations [2]. Figure 1c and 1d display an SEM and an X-PEEM at the Co L_3 edge of the same spot on the sample, which show the very same nanooctahedra.

Figures 2a and 2e display high resolution SEM images of two individual CoO nanooctehedra with the top facets top {111} facet indicated by the black dashed lines, cf. Ref. [2]. Figures 2b and 2f show the respective XA spectra recorded with linear horizontally (solid black line) and vertically (dashed red line) polarized radiation at room temperature (RT). The respective XLD spectra are presented in figures 2c and 2g reveal almost no linear dichroism.

However, when cooling the sample down to 120 K, we observe in both particles a significant XLD signal as shown in figures 2d and h.

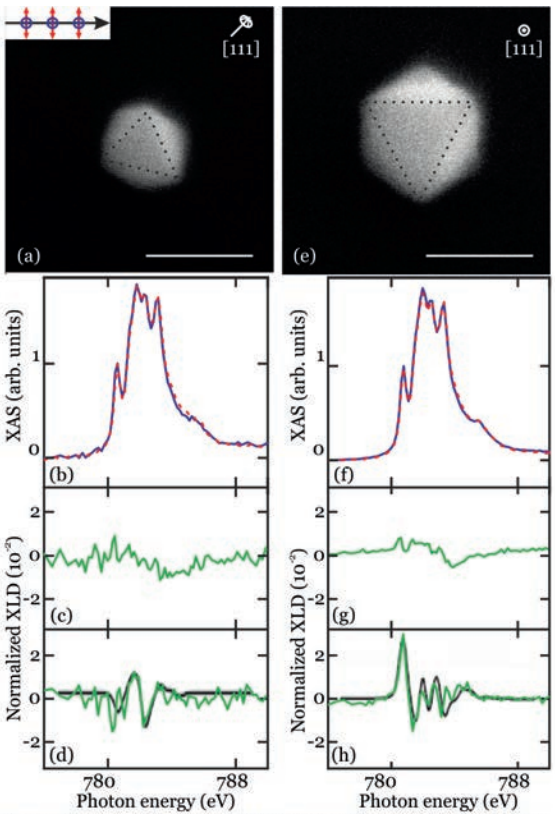

Fig. 2 a) and e) are SEM images of two individual CoO nanoparticles. The inset shows the X-ray propagation direction (black), and the linear horizontal (blue) and vertical polarization (red) in the experiment. The white arrows indicate the respective [111] directions of the top with respect to the top facets [111]. b)-d) and f)-h) show the XA spectra in linear polarization, the XLD spectra at RT and 120 K (green) and the reference spectra [8] (black lines), respectively.

These data reveal two remarkable findings. On the one hand the change in the XLD spectra from RT to 120 K indicates a magnetic phase transition from an unordered towards a magnetically ordered state. On the other hand, distinctly different XLD spectra for the two individual nanoparticles were found (Fig. 2d and h). For bulk CoO it is known that the magnetic order is driven by lattice distortion from a cubic to a tetragonal lattice [6]. Further it is known, that both, magnetic and structural phase transitions contribute to XLD spectra [6]. The magnetic ordering temperature of similar CoO nanoparticles has been found to be around 285 K which corresponds to the bulks Néel temperature [2]. Further, it is known that the XLD effect depends on the relative orientation of X-ray polarization vector, crystal axes, and antiferromagnetic spin axis. Thus, the individual character of the XLD spectra in figure 2d and h might be due to the distinct orientation of the particles with respect to the X-ray propagation vector (Fig. 2a and e). The spectral shape we find is supported by literature reference spectra [8] but the correlation has to be analyzed further to get more quantitative insights.

Summary and Outlook

We measured XA and XLD spectra of individual CoO/Co_3O_4 core–shell nanooctahedra at different temperatures by means of X-PEEM. SEM images of the very same nanoparticles reveal information on the morphology of the nanoparticles, e.g. surface facets, which allow us to correlate the XLD spectra with the structure of the particles. Our temperature-dependent XLD data indicate a magneto-structural phase transition in the nanoparticles in a temperature window between 120 K and RT. Further, we plan to measure XLD as a function of azimuthal sample orientation (in-plane rotation indicated by the black arrow in Fig. 1a). This will allow us to exploit the known relation between X-ray polarization vector, crystal axes and magnetization axes in order to determine the spontaneous orientation of the antiferromagnetic spin axis with respect to the crystal lattice of the nanooctahedra. Influences of micro-structural defects will be studied further by means of TEM.

References

[1] S. Morup, D.E. Madsen, C. Frandsen, C.R.H. Bahl, M.F. Hansen, *Experimental and theoretical studies of antiferromagnetic materials*, J. Phys.: Condens. Matter **19**, 213202 (2007)

[2] N. Fontaíña-Troitiño, S. Liebana-Vinas, B. Rodriguez-Gonzalez, Z.A. Li, M. Spasova, M. Farle, V. Salgueirino, *Room-temperature ferromagne-tism in antiferromagnetic cobalt oxide nanoocta-hedra*, Nano Lett. **14**, 640 (2014)

[3] T.-J. Park, G.C. Papaefthymiou, A.J. Viescas, A.R. Moodenbaugh, S.S. Wong, *Size-dependent mag-netic properties of single-crystalline multiferroic $BiFeO_3$ nanoparticles*, Nano Lett. **7**, 766 (2007)

[4] Q. He, Y.H. Chu, J.T. Heron, S.Y. Yang, W.I. Liang *et al.*, *Electrically controllable spontaneous magnetism in nanoscale mixed phase multi-ferroics*, Nat. Commun. **2**, 225 (2011)

[5] S.Y. Istomin, O.A. Tyablikov, S.M. Kazakov, E.V. Antipov, A.I. Kurbakov *et al.*, *An unusual high-spin ground state of Co^{3+} in octahedral coordination in brownmillerite cobalt oxide*, Dalton Trans. **44**, 10708 (2015)

[6] G. van der Laan, E. Arenholz, R.V. Chopdekar, Y. Suzuki, *Influence of crystal field on anisotropic x-ray magnetic linear dichroism at the Co^{2+} $L_{2,3}$ edges*, Phys. *Rev. B* **77**, 064407 (2008)

Filming biological factories

Project P1503 Watching giant multienzymes at work using high-speed AFM
Project Leader: T. Maier and R.Y.H. Lim
Collaborators: S. Singh (SNI PhD Student), Y. Sakiyama, and F. Benning

Multienzymes are biological assembly lines

Metabolism is an essential characteristic of life. It involves all processes for the biosynthesis and degradation of chemical compounds required to replicate cells and to form tissues, organs and entire organisms. Proteins are required to catalyze many metabolic reactions for efficient turnover under biological conditions. Most common enzymes catalyze only a single reaction step before releasing the products into the cellular environment. However, several classes of important and complex biomolecules require more elaborate biosynthetic systems, because their biosynthesis involves reactive or poorly soluble intermediates or requires a strict order of multiple reaction steps. Multienzymes integrate multiple catalytic activities at different sites into giant polypeptides and employ specific shuttling mechanisms to transfer intermediates between the different active sites. Most multienzymes are highly dynamic, however, the contribution of dynamics to the overall emergent properties of these giant protein factories remains poorly understood.

In this project, we aim to (i) develop methods for the visualization and analysis of multienzyme dynamics at the single molecule level and (ii) to apply these methods to studies of key enzymes in human metabolism or in microbial secondary metabolite production.

To study the dynamic behavior of multienzymes, we are developing two complimentary methods towards the application to complex protein systems. First, High Speed Atomic Force Microscopy (HS-AFM) provides direct visualization of single multienzyme dynamics, however, with severely limited time- and spatial resolution and the limitation to convoluted surface representations. Second, single molecule (sm) fluorescence methods, in particular those based on Förster resonance energy transfer (FRET) permit highest temporal and spatial resolution, but require difficult labeling and provide only indirect information based on attached fluorescent labels.

We are studying the mammalian fatty acid synthase (FAS) (Fig. 1). FAS is arguably the most complex multienzyme present in humans and comprises six different catalytic sites, which catalyze more than 40 individual reaction steps in the biosynthesis of palmitoyl-coenzyme A from carbohydrate derived precursors [1]. FAS also integrates a flexibly linked carrier protein unit (ACP) that covalently tethers acyl intermediates and shuttles them to the individual catalytic sites. The active form of FAS is a 540kDA dimer of two identical 2500 amino acid polypeptides. Functional studies and in particular crystallographic and electron microscopy analysis have revealed asymmetric states and large-scale dynamics of FAS, with initial hints towards a correlation between structural and functional states [1].

FAS shares many, although not all, principles of its structural organization with related polyketide synthases (PKS) [2]. Microbial PKS utilize the same chemical logic as FAS for stepwise precursor elongation. However, by controlling the extent of precursor modification they can produce more complex products than just saturated fatty acids. FAS always acts in iterative cycles. While some PKS also act iteratively, others catalyze only a single round of precursor extension as part of a large chain of covalently or non-covalently tethered PKSs. Substrates are vectorially shuttled through these chains of PKS, which truly act as modular assembly lines. The polyketide products of PKS include many clinically relevant drugs, including antibiotics and immunosuppressants. Systematic re-engineering of PKS would open a path to unlock the full potential of polyketides in drug discovery. However, due to a lack of understanding of structural constraints, many attempts for PKS engineering have been inefficient.

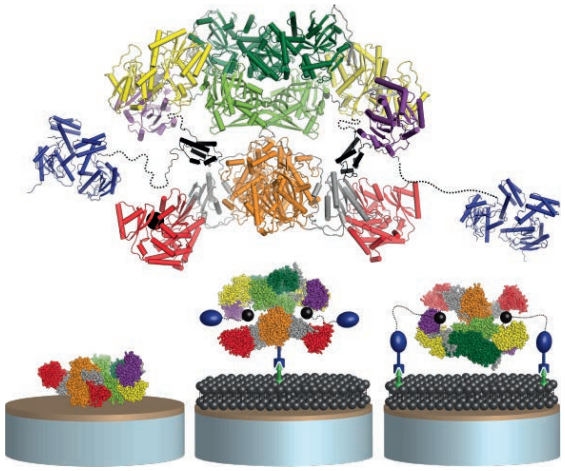

Fig. 1 FAS structure and setup for multi-view HS-AFM filming of FAS. Upper panel: Structural model of FAS. Lower panel: FAS was non-specifically immobilized on mica (left), or selectively immobilized bilayers with N-(center) or C-terminal (right) tags on functionalized lipid bilayers.

High-speed AFM analysis of multienzymes

Atomic Force Microscopy (AFM) is a high resolution (sub-nanometer) surface topography imaging technique, which uses a microscopic cantilever tip to probe the surface of the sample. Since AFM can be performed on samples in aqueous environment under biological conditions, it is uniquely suited to study biomolecules under native conditions. HS-AFM is uniquely suited to studies of the dynamic behavior of macromolecules, because it uses low imaging forces and high scanning rates [3]. Here, we

apply HS-AFM to FAS in an attempt to visualize large-scale conformational changes [4], which were expected to occur on a 10-500ms timescale and involve structural changes in the 1-10nm domain.

Compared to samples comprising higher oligomers or filaments, the dimeric FAS is a highly challenging sample. To overcome problems of preferential orientation and surface effects on protein dynamics, we have combined unspecific immobilization on mica with different modes of selective tethering to functionalized lipid bilayers (Fig. 1). HS-AFM scanning was performed with up to 10 frames per second and achieved approx. 2-5nm lateral and 1.5nm vertical resolution. The obtained data are consistent with synthetic AFM data simulated using in-house developed software based on X-ray crystal structures. Based on auto-correlation analysis, the imaging process reaches a time-resolution that is suited for analysis of large-scale domain motions.

For the analysis of HS-AFM movie frame series, we have applied a similar strategy as used in the analysis of single particles in electron microscopy. An algorithm for reference-free classification of 2D projection TEM images was used to classify individual movie frames of FAS recordings, which had been extracted from the original movie context. Classification was sufficiently effective to preferentially re-group frames according to their original movie context and to identify common views of FAS states across and within different FAS movies (Fig. 2). As a result, we have established an approach for analyzing distinct states of multienzymes as well as their transition kinetics between states in aqueous solution. Next steps are to apply this approach to study other multienzymes and to probe dynamics in different states of catalysis.

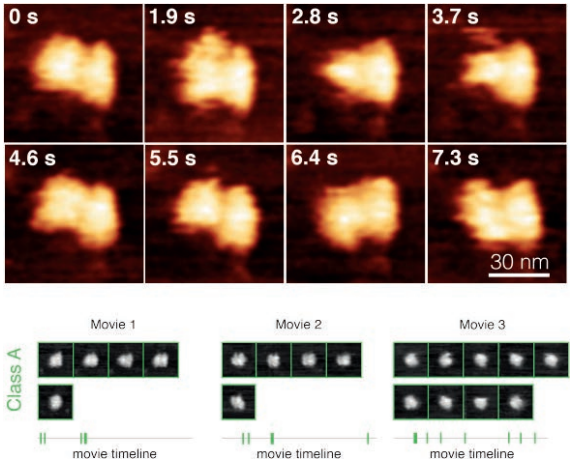

Fig. 2 HS-AFM characterization of FAS. Upper panel: Time-series of HS-AFM images from a single movie of FAS. Lower panel: Example of reference-free classification of individual movie frames of FAS across and within movies.

Towards single-molecule fluorescence studies

smFRET is very well suited for studies of protein dynamics because of its high temporal (ns time scale) and spatial resolution in resolving distances between fluorophores in a limited distance range (1-10 nm). smFRET uses diluted fluorescently labeled protein samples in a small confocal excitation volume to measure signals from single molecules. A prerequisite for smFRET studies is labeling of proteins with donor and acceptor fluorophores. For proteins, this is generally done by genetically introducing fluorescent proteins or via selective chemical labeling e.g. of cysteine or lysine amino acids. However, fluorescent protein tags may impair multienzymes dynamics and provide limited resolution. Chemical labelling targets reactive groups, which are essential for function in FAS (and most other multienzymes) and thus conflicts with protein function. A promising alternative is the incorporation of bio-orthogonal handles into proteins for selective chemical labelling via introduction of unnatural amino acids by genetic code expansion (GCE). GCE is well established in bacterial systems for single-site labelling. However, dual or multi-site labelling and GCE in eukaryotic expression systems still present substantial challenges.

Due to their large size and essential post-translational modifications, FAS and other multienzymes are most effectively produced in eukaryotic systems, e.g. in insect and mammalian cells. Currently, we are introducing GCE systems into mammalian and insect cell expression systems for incorporating two or more unnatural amino acids into multienzymes. After labelling the different domains of multienzymes, we aim to use smFRET and FCS (Fluorescence Correlation Spectro-scopy) measurements to study the short-range and long-range motions in FAS and other multienzymes. The genetic incorporation of fluorescent unnatural amino acids may also enable performing *in-vivo* studies.

Overall, we have demonstrated the feasibility of filming multienzymes by HS-AFM to analyze large-scale conformational dynamics. We now expand this approach and develop complementary fluorescence-based analysis. Our work shall reveal the structural basis of the emergent properties multienzymes and ultimately provide blueprints for the engineering of novel, efficient bio-inspired molecular factories.

References

[1] T. Maier, M. Leibundgut, D. Boehringer, N. Ban, *Structure and function of eukaryotic fatty acid synthases*, Q Rev Biophys **43**, 373 (2010)

[2] D.A. Herbst, R. P. Jakob, F. Zähringer, T. Maier, *Mycocerosic acid synthase exemplifies the architecture of reducing polyketide synthases*, Nature, **531** 533 (2016)

[3] T. Ando, *High-speed atomic force microscopy and its future prospects,* Biophys Rev, doi: 10.1007/s12551-017-0356-5 (2017)

[4] F.M.C. Benning, Y. Sakiyama, A. Mazur, H.S.T. Bukhari, R.Y.H. Lim, T. Maier, *High-Speed Atomic Force Microscopy Visualization of the Dynamics of the Multienzyme Fatty Acid Synthase, ACS Nano* **11** 10852 (2017)

Valleytronics in strain-engineered graphene

Project P1504 Valleytronics in strain-engineered graphene
Project Leader: C. Schönenberger and M. Calame
Collaborators: L. Wang (SNI PhD Student), A. Baumgartner, P. Makk, J. Overbeck, and O. Braun

Introduction

The valley degree of freedom (VDoF) in graphene stems from energetically degenerate, but nonequivalent local minima (maxima) of the conduction (valence) band at the corners of the Brillouin zone. Since the two valleys are far away from each other in momentum space, intervalley scattering is strongly suppressed, suggesting a potential use of the VDoF for electronic applications, referred to as valleytronics.

Short-range disorder potentials, such as local defects, may cause intervalley scattering in graphene. To avoid valley mixing, ultraclean graphene is a prerequisite. This can be achieved by current annealing suspended graphene [1] or encapsulating graphene with hBN [2]. Secondly, one needs a handle to control the VDoF for generating and detecting a "valley current". It has been predicted that non-uniform strain can generate a pseudo-magnetic field in graphene which acts on the two different valleys with opposite signs [3]. So, strain is a possible way to address the VdoF. The main challenge is then to generate strain in graphene in a controllable way. In collaboration with the group of M. Calame, we have successfully been able to apply strain in graphene in a controllable manner using the break-junction (BJ) technique, confirmed by Raman spectroscopy. Recently, a low temperature BJ setup has been constructed in our group and first transport measurements of strained graphene are under investigation at low temperature.

Strain characterization by Raman spectroscopy

The mechanism of BJ is shown schematically in figure 1a. The device is fabricated in the center of a bendable substrate which is mounted between the counter-supports and the pushing-wedge. Controllable strain can then be generated in graphene by bending the substrate, which is described by the distance Δz the wedge is pushed up. Raman spectroscopy is a powerful tool to characterize strain in graphene. Here we focus on the 2D peak of the spectrum, which red-shifts with increasing strain [4].

We first studied a suspended graphene sample, where Raman spectra were measured at different bending levels of the substrate. The position of the 2D peak and the corresponding strain are plotted in Fig.1b. The substrate was first bent stepwise to a certain extent, then gradually relaxed and bent up again. The position of the Raman 2D peak responded accordingly, indicating a good controllability of the strain in graphene by BJ technique.

Since encapsulating by hBN can give clean graphene without current annealing and make the device more robust, we then tried to strain encapsulated graphene by the same technique. A typical suspended encapsulated device is shown in the inset of figure 1a. Although the stack is much thicker than a monolayer graphene, approximately 0.3% strain was achieved in one of the devices before it broke (Fig. 1c).

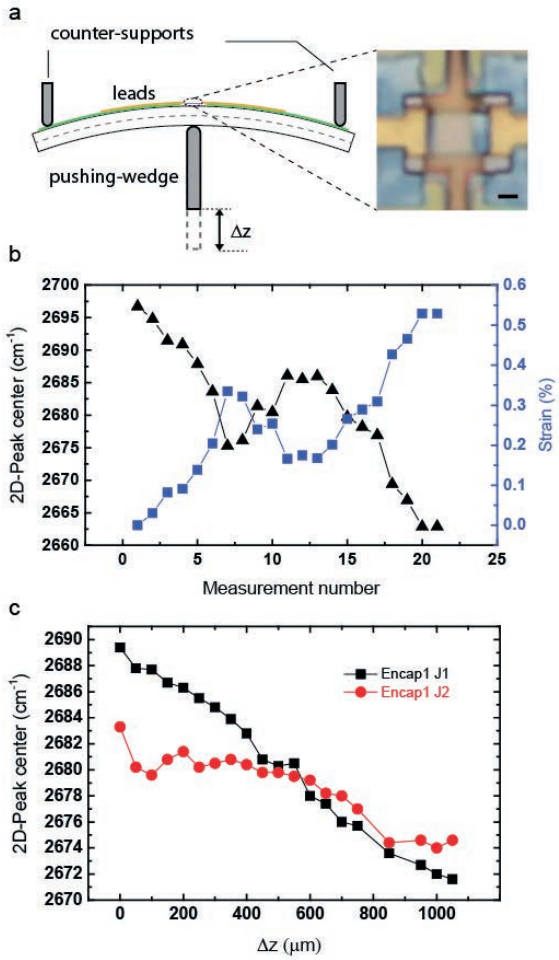

Fig. 1 (a) Schematics of the BJ setup. The inset is the optical image of a typical suspended and in hBN encapsulated graphene device. Source and drain contacts are seen on the left and right. The other vertically running electrical line is a gate structure located below the suspended graphene flake. The scale bar corresponds to 1 μm. (b) Raman 2D peak position and corresponding strain of a suspended graphene device plotted as a function of measurement number. During the measurements, the bending of the substrate was first increased, then decreased and increased again. (c) Raman 2D peak position of two different samples of the suspended encapsulated device Encap1 plotted as the bending of the substrate.

First low-temperature transport measurements

Recently a BJ dipstick has been fabricated for transport measurements a low-temperature (Fig. 2). The whole stick is enclosed in a vacuum tube, which can be inserted into a dewar containing liquid helium. The bending of the substrate is controlled mechanically by the knob on the top.

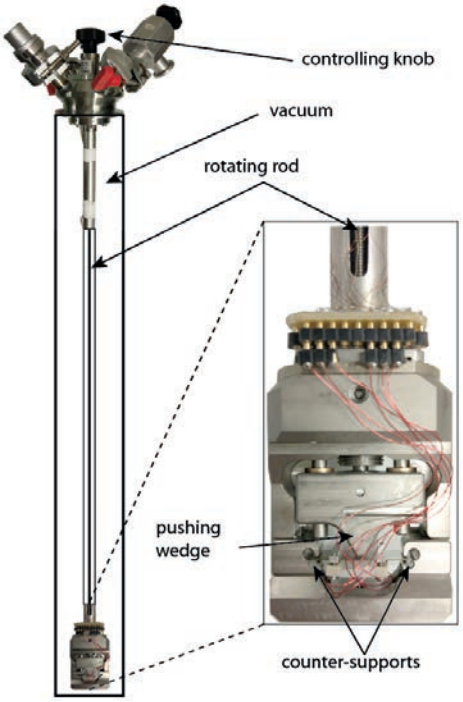

Fig. 2 Image of the low-temperature BJ dipstick. The vacuum has been removed to take the picture and is indicated here as black border.

First, low-temperature measurements have been done on an encapsulated device. We have measured two-terminal resistance as a function of gate voltage at different bending level of the substrate (Fig. 3). The resistance in each measurement saturates to the same value at high doping (high gate voltage V_g), indicating that the contact resistance does not change while bending the substrate. The asymmetry in gate voltage is due to the p-n junction formed close to the contact. The main effect observed here is that the curves shift towards zero gate voltage when increasing the bending (Fig. 3a) and it is reversible when the bending is relaxed (not shown here). This effect can be explained by the bending-induced gate capacitance change. In a plate capacitor model, the induced charge Q and the gate voltage V are related by Q = CV, where C is the gate capacitance. The gate capacitance change leads to a change in the gating efficiency, which can then be corrected by scaling the curves in gate voltage. In Fig.3b, the curves are scaled with respect to zero gate voltage by matching the CNP point of each curve to that of the curve measured without substrate bending. All the curves collapse to one curve after scaling, which confirms that the origin of the effect is the bending induced change of gate capacitance.

Summary and outlook

We have developed a method to generate and control strain in graphene. First low temperature transport measurements have been carried out. For further experiments, the encapsulated graphene devices will not be suspended so that the bending induced gate capacitance change can be avoided. This will the also allow to study multi-terminal devices, e.g. Hall-bars.

We are grateful to Jan Overbeck, Oliver Braun, Ilaria Zardo and Michel Calame for intense and fruitful collaboration. High-quality hBN was provided by K. Watanabe, T. Taniguchi from the National Institute for Material Science at Tsukuba, Japan.

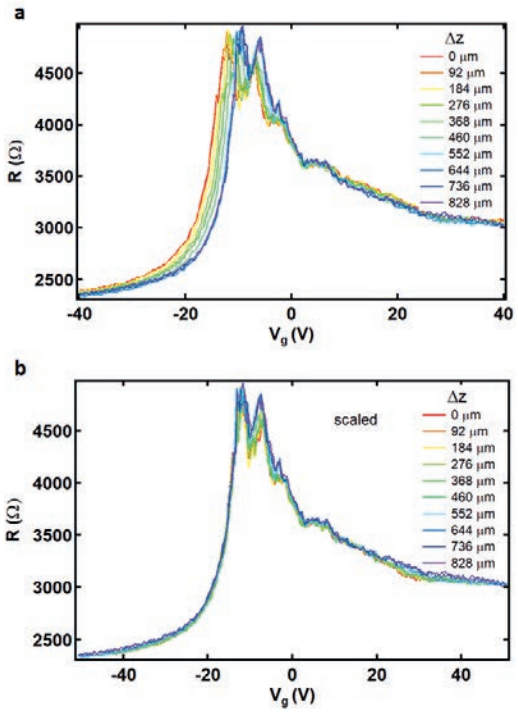

Fig. 3 (a) Resistance of device J1 on sample Encap2 measured as a function of gate voltage at 4.2K. Different color stands for different bending. (b) Curves at different bending are scaled with respect to zero gate voltage by matching the CNP point of each curve to that of the curve without bending.

References

[1] R. Maurand, P. Rickhaus, P. Makk, S. Hess, E. Tovari, C. Handschin, M. Weiss, C. Schoenenberger, *Fabrication of ballistic suspended graphene with local gating*, Carbon. **79**, 486(2014)

[2] L. Wang, I. Meric, P.Y. Huang, Q. Gao, H. Tran et al, *One-dimensional electrical contact to a two-dimensional material*, Science. **342**, 614 (2013)

[3] F. Guinea, A.K. Geim, M.I. Katsnelson, K.S. Novoselov, *Generating quantizing pseudo-magnetic fields by bending graphene ribbons*, Phys. Rev. B **81**, 035408 (2010)

[4] T.M.G. Mohiuddin, A. Lombardo, R.R. Nair, A. Bonetti, G. Savini et al, *Uniaxial strain in graphene by Raman spectroscopy: G peak splitting, Grüneisen parameters, and sample orientation*, Phys. Rev. B **79**, 205433 (2009)

Fabrication of nano-apertures for spatial modulation of electron wave

Project P1505 A programmable e-beam shaper for diffractive imaging of biological structures at Å resolution
Project Leader: S. Tsujino and J.P. Abrahams
Collaborator: P. Thakkar (SNI PhD Student)

Introduction

Since the invention of first electromagnetic lens in 1926 by Hans Busch, the concept of electron microscope became realistic. Compared to optical microscope, electron microscope (EM) has the advantage of imaging at higher resolution; however, there are certain limitations to imaging biological samples with EM. High energy electrons cause a significant damage to biological specimens, generally composed of carbon, nitrogen and oxygen which are neighbors in periodic table and hence do not provide good amplitude contrast. Which means it does not considerably change the amplitude of the incident electron wave but they change the phase of the wave and hence can be considered as weak phase objects [1]. There is no direct way to detect the phase modulations. To deal with the problem of poor contrast, scientists have developed methods to convert the phase modulations of the exit wave into amplitude/intensity modulations. Defocusing in bright-field imaging mode has been widely used until the realization of thin film phase plates by Nagayama and Danev [2], but defocusing an image reduces the resolution.

Diffractive imaging would be a sophisticated approach to retrieve the phase information without compromising resolution. It is a lensless technique to reconstruct aberration-free images from diffraction pattern. It also offers an added advantage of being insensitive to translational movement of the specimen.

Phase modulation of electron wave

Electron wave undergoes a phase shift when travelling through an electric field. There has been a substantial amount of research going on which exploits this simple fact. Electrostatic phase plates, beam shaping, and aberration correction are to name a few. Introducing a phase shifting device between unscattered wave and scattered wave is expected to increase the phase contrast in a controllable way without introducing the defocusing imaging conditions. We aim to design a tunable device which will manipulate the phase of the incident electron wave and retrieve the phase information of the diffracted wave. This will ameliorate structural analysis of molecules at angstrom resolution. As the first step, we fabricated a closely spaced nano-aperture pair as a static modulator of the electron wave via diffraction and interference.

Fabrication of nano-apertures

To manipulate the electron beam in transverse direction, nano-apertures were fabricated in Si_3N_4 membranes supported on silicon (Si) substrates by electron-beam lithography method using Vistec EBPG 5000PLusES. The fabrication process started with the evaporation of metal mask, electron lithography step, and the etching of the nano-apertures by the reactive ion etching. The process parameters are optimized iteratively to achieve optimum results. PMMA is used as e-beam resist (positive tone) as the mask to pattern the etching mask Chromium (Cr) [3] for etching through the 200 nm-thick Si_3N_4 membrane. For these samples, we choose thin Cr layer (~30 nm) on top of 200 nm-thick Si_3N_4 membranes that allows finite background transmission for experiments with TEM at 200 keV beam energy as shown by the Monte Carlo simulation (Fig. 2). However, this does not affect the purpose of the experiment as discussed later. Cr also acts as a conducting medium and reduces charging effects [4].

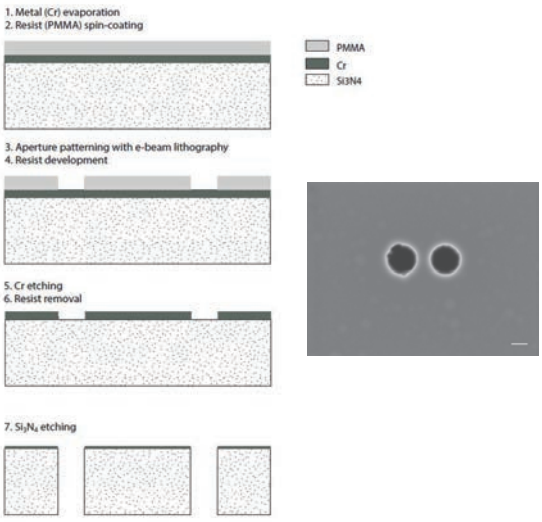

Fig. 1 Left: Schematic fabrication process of nano-apertures. The cross-sections of the membrane during different process steps are shown. Scale bar of the Scanning electron microscope (SEM) image (right) of fabricated aperture pairs: 200nm.

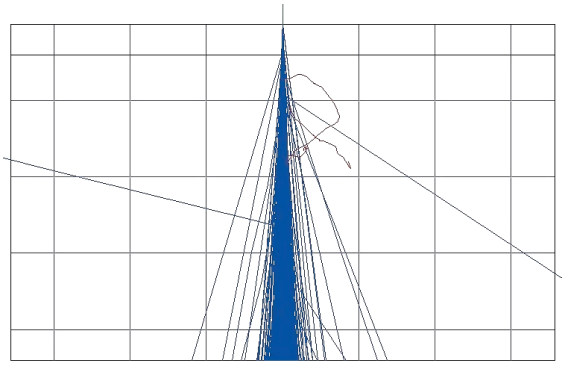

Fig. 2 Monte Carlo Simulation of 20nm Cr (top) and 200nm Si_3N_4 (bottom) for 200keV electron beam.

Experiment

We loaded the fabricated nano-aperture sample into the sample compartment of a field-emission-gun transmission electron microscope (TEM, JEOL JEM 2200FS) and performed the electron beam transmission experiment at the beam energy of 200 keV.

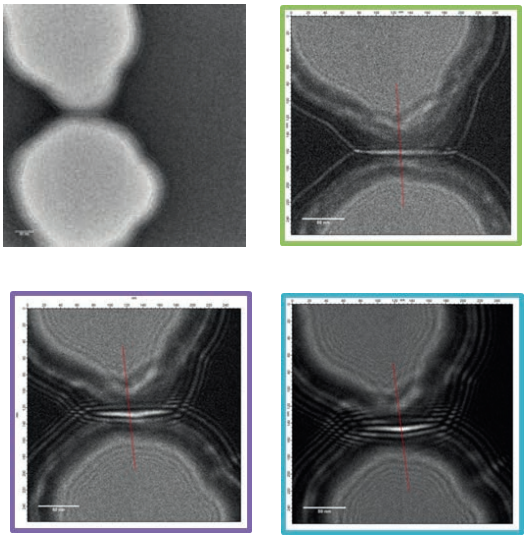

Fig. 3 (top left), shows the transmission of the electron beam through the nano-apertures when the objective lens was roughly focused on one side of the sample. The sloped side-wall of the apertures that were not apparent in the SEM image at low beam energy (~3 keV, Fig. 1 right panel) is imaged as a graded aperture edges; scale bar: 40nm, (top right), overfocus 39.9 µm overfocus, (bottom left) 70.5 µm and (bottom right) 94.3 µm. Scale bar is 50nm for rest three images. The modulation in the transmitted electron wave is clearly visible here. Also, it can be observed that the interference is stronger for the highest overfocus at 94.3µm.

Next, to observe the influence of the nano-apertures on the electron beam propagation, we introduced defocusing to the objective lens. This way, we were able to observe the Fresnel diffraction of the incident coherent beam that produces Fresnel fringes inside and outside of the apertures (Fig. 3, top right, and bottom panel). As the defocusing is increased, relatively small Fresnel diffraction fringes are observed outside of the apertures. Most importantly, a strong interference of the Fresnel fringes at the middle of the two apertures was observed as a consequence of the coherent transmission of the electron beam from the two apertures: The respective line scans of the images are shown in figure 4.

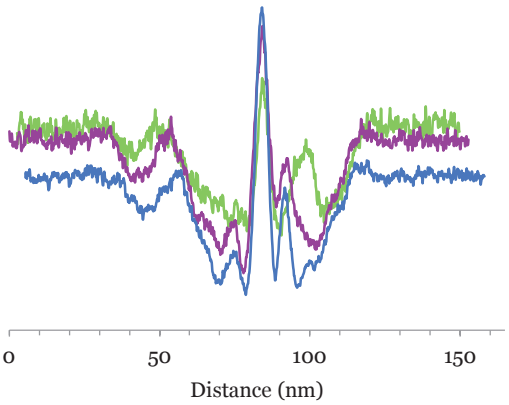

Fig. 4 Line scans near the central peak of overfocused images shown in figure 3. The color of the graphs corresponds to the color of the outline of images in figure 3 and hence the respective overfocus.

Summary and Outlook

In conclusion, we demonstrate that it is possible to modulate the incident electron wave with nano-apertures. We further aim to upgrade our device with electrostatic potential around the apertures which makes it possible to tune the electron beam to introduce desired localized phase shift in the electron beam.

References

[1] R.M. Glaeser, *Invited Review Article: Methods for imaging weak-phase objects in electron microscopy*, Rev. Sci. Instrum. **84,** 111101 (2013)

[2] K. Nagayama, and R. Danev, *Phase-plate electron microscopy: a novel imaging tool to reveal close-to-life nano-structures*. Biophys. Rev. **1,** 37–42 (2009)

[3] N. Khamnualthong, K. Siangchaew, P. Limsuwan, *Study of Chromium Hard Mask Formation and Wall Angle Control for Deep Etching Application*, Procedia Eng. **32,** 922–928 (2012)

[4] J. Brink, H. Gross, P. Tittmann, M.B. Sherman, W. Chiu. *Reduction of charging in protein electron cryomicroscopy*, J. Microsc.Oxford **191,** 67–73 (2002)

Theoretical study of enhanced water splitting with plasmonic nanostructures

Project P1601 Optical plasmonic nanostructures for enhanced photochemistry
Project Leader: E.C. Constable and S. Fricke
Collaborators: L. Driencourt (SNI PhD Student), B. Gallinet, and C.E. Housecroft

Introduction

Hydrogen is expected to be one of the main fuels in the near future. Given the progressive depletion of fossil fuels and the climate change that becomes more and more apparent, it is necessary to use fuels that are environmentally friendly and that can be produced using renewable energies. Production of dihydrogen is currently mainly achieved with steam reforming of methane, a method that uses natural gas to react with water vapor at high temperature and that releases CO_2.

Water splitting using sunlight is a promising technique for clean dihydrogen production. It also enables storage of large amount of solar energy into chemical bonds for later release. The water splitting reaction is decomposed in water oxidation and protons reduction. It requires that an overall energy of 1.23V is brought to the system. Several approaches have been investigated to perform solar water splitting. An extensively studied one uses the energy of a photovoltaic (PV) cell as a power source for water electrolysis. Photoelectrochemical (PEC) water splitting uses a semiconductor electrode immersed in the electrolyte both for light harvesting and as a catalyst of the reaction. So far, PEC water splitting has not demonstrated the same efficiencies of water electrolysis using a PV cell. On the other hand, it has the potential to be less expensive [1].

PEC water-splitting

Figure 1a shows the working principle of a PEC cell. Exposition to solar light generates electron/hole pairs in the semiconductor electrode. The photogenerated holes catalyse the water oxidation reaction:

$$2H_2O \rightarrow O_2 + 4H^+ + 4e^-,$$

whereas the electrons are transferred to the metallic counter electrode and catalyse the reduction reaction:

$$2H^+ + 2e^- \rightarrow H_2.$$

Figure 1 shows the principle of PEC water splitting using an n-type semiconductor electrode. In this case the electrons are the majority charge carriers and the semiconductor electrode acts as a photoanode. In building an efficient device, the design of the electrode is a critical step. Materials with high yields such as crystalline silicon cannot be used because they are subject to corrosion in aqueous solution. Using metal oxides such as titanium dioxide (TiO_2), hematite (α-Fe_2O_3) or tungsten trioxide (WO_3) is very promising due to their high stability and their very low cost.

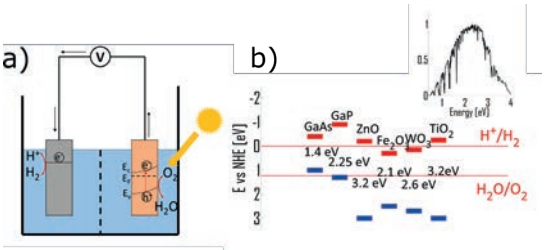

Fig. 1 Principle of photoelectrochemical water splitting. a) Scheme of a two electrode PEC cell. b) Band positions (versus normal hydrogen electrode) and bandgap of several semiconductors in contact with an aqueous electrolyte at pH=1. AM1.5 spectrum is also represented.

Figure 1b shows the band positions of some semiconductors in an aqueous solution. TiO_2 has a large bandgap that allows only absorption in the UV. This material has been widely studied and several attempts have been made for increasing its absorption in the visible. GaP is a high cost p-type semiconductor that is poorly stable in aqueous conditions. Hematite has an appealing bandgap allowing a theoretical solar to hydrogen conversion efficiency of 17%. However, it has poor charge transport properties. Its minority carrier's diffusion length is only 2-4 nm without an external bias [2]. Therefore, holes that are generated further from the semiconductor-liquid junction recombines before reaching it. Moreover, its band edges do not perfectly overlap with the half reactions energy and an additional reduction potential has to be provided to the photocathode.

Plasmonic nanoparticles for enhanced efficiency

Adding metallic nanoparticles can increase the efficiency of PEC water splitting by two effects: generation of hot electrons and confinement of the electromagnetic field. When resonant plasmonic nanostructures are placed in contact with the semiconductor electrode, "hot" electrons having an energy above the Fermi level can be generated from the decay of the plasmon and transferred to the conduction band of the neighboring semiconductor. In this case, a "hot" hole is left in the metal. This effect enables potentially electron/hole pairs generation at an energy below the bandgap of the semiconductor. Generation and injection of hot electrons are widely studied topics but utilization of this effect for enhanced water splitting has only shown low efficiency so far [3]. Plasmonic nanoparticles can also be used to reduce the size of the region where incident light is absorbed (Fig. 2a). The light that is scattered by a resonating plasmonic nanoparticle can

be strongly confined in its close surrounding. This effect can be potentially used to generate more electron/hole pairs close to the interface.

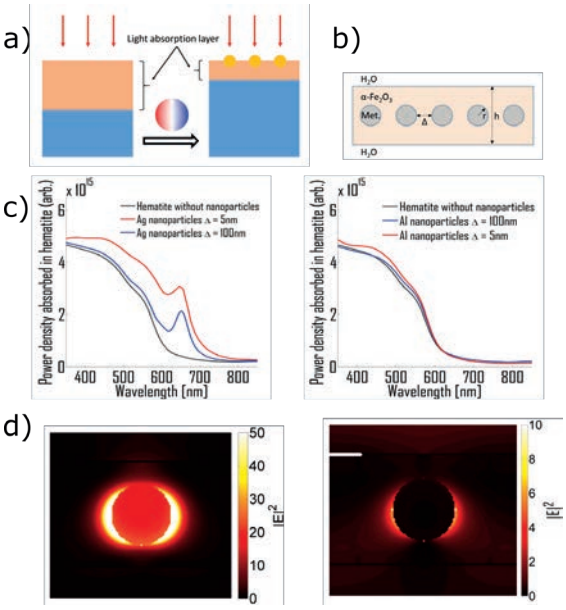

Fig. 2 SIE simulations of a hematite film that contains metallic nanospheres. a) Adding resonant plasmonic nanoparticles to a semiconductor electrode can decrease the thickness of the light absorption layer. b) Cross section of the simulated geometry. c) Spectrum of the effective power density absorbed in hematite when the metallic nanoparticles are in silver (left) and aluminum (right) and for two different separations between the nanospheres. The other parameters are h=70 nm and r=20 nm. d) Corresponding map of the light intensity for the case $\Delta =$ *100 nm at the resonant wavelength:* $\lambda =$ *658 nm (left) and* $\lambda =$ *587 nm (right).*

This phenomenon is studied in the following, utilizing electromagnetic simulations based on the surface integral equation (SIE) method in order to estimate the efficiency of light confinement by plasmonic particles embedded in a thin of hematite [4]. This technique enables very precise computation of the near field for a system made with isolated or periodically distributed scatterers. The simulated geometry is represented in figure 2b. A film of hematite of thickness *h* is placed in water. It contains metallic nanoparticles that are periodically distributed in 2D and that are centered at the middle of the film in the longitudinal direction. The influence of various geometrical parameters can be investigated with such a geometry and different metals can be compared. For each design, the effective power density absorbed in hematite is computed:

$$p(\lambda) = \frac{1}{V_0} \int_{V_H} |\boldsymbol{E}(\boldsymbol{r}, \lambda)|^2 Re[\sigma(\lambda)] dV,$$

where V_0 is the total volume of the unit cell, V_H is the volume of hematite in one unit cell, $\sigma = -i\omega(\varepsilon - 1)$ is the complex conductivity of hematite and **E** is the electric field. Candidate plasmonic materials are silver and aluminum. The plasmonic resonance wavelength of these materials spectrally overlap with the bandgap of hematite, which is not the case of other standard plasmonic materials such as gold. Results for two different geometries having different separation between the nanospheres (Fig. 2c).

In the case of silver, addition of nanoparticles strongly enhances the light absorption in hematite. This enhancement is stronger if the separation between the nanospheres is small, even if the quantity of hematite within one unit cell is decreased. Moreover, the resonance broadens when the nanoparticles are getting closer, which produces an enhanced absorption over a larger wavelength range. The results are different in the case of aluminum nanospheres. It can be observed that very few enhancement is obtained for both geometries compared to silver. The maps of the light intensity at resonant wavelength (Fig. 2d) show that the near field intensity is much higher for silver nanoparticles. When the nanospheres are closer, the field confinement gets stronger and this does more than compensate for the reduction in hematite quantity. The scattering effect from aluminium is too weak to provide a sufficient enhancement of the hematite absorption.

Conclusion & Outlook

A study of light absorption in a hematite film containing plasmonic nanoparticles has been performed with numerical simulations. The simple geometry chosen has several degrees of freedom that can be separately investigated in order to make design rules for increasing the water splitting efficiency of a semiconductor electrode by adding plasmonic nanoparticles. Silver has been found to be an interesting material, but suffers from a much lower chemical stability compared to gold. A stabilization process for silver nanoparticles has been reported by Wang *et al.* [5].

References

[1] J. Nowotny, T. Bak, D.W. Chu, S. Fiechter, G.E. Murch, T.N. Veziroglu, *Sustainable practices: Solar hydrogen fuel and education program on sustainable energy systems*, Int. J. Hydrogen Energy **39**, 4151 (2014)

[2] A.G. Tamirat, J. Rick, A.A. Dubale, W.N. Su, B.J. Hwang, *Using hematite for photoelectro-chemical water splitting: a review of current progress and challenges*, Nanoscale Horiz. **1,** 243 (2016)

[3] S. Mubeen, J. Lee, N. Singh, S. Kramer, G.D. Stucky, M. Moskovits, *An autonomous photosynthetic device in which all charge carriers derive from surface plasmons*, Nat. Nanotechnol. **8**, 247(2013)

[4] B. Gallinet, A.M. Kern, O.J.F. Martin, *Accurate and versatile modeling of electromagnetic scattering on periodic nanostructures with a surface integral approach,* J. Opt. Soc. Am. A, **27,** 2261 (2010)

[5] X. Wang, C. Santschi, O.J.F. Martin, *Strong Improvement of Long-Term Chemical and Thermal Stability of Plasmonic Silver Nanoantennas and Films*, Adv. Sc. News **13,** 1700044 (2017)

Characterization of hybrid polymer-lipid membranes

Project P1604 Selective reconstitution of biomolecules in polymer-lipid membranes
Project Leader: W. Meier and U. Pieles
Collaborator: S. Di Leone (SNI PhD Student)

Introduction

Understanding of the structural organization of cell membranes is highly relevant for the development of pharmaceutical drugs and functional combination with biomolecules (e.g. proteins, enzymes, etc.). Amphiphilic block copolymers are interesting as model systems that can self-assemble in aqueous media into membranes with high stability, and properties that can be optimized by varying their molar mass, and hydrophilic-to-hydrophobic block length ratio. In previous studies, we have shown that mixtures of amphiphilic block copolymers and lipids form membranes of distinct domains: lipid (3-5 nm thickness) and copolymer (5-20 nm thickness) phases with enhanced stability of the polymer domains and enhanced mobility in the lipid domains.[1,2] The phase of the polymer and lipid domains significantly influences the insertion of membrane proteins. In this project, we plan to use functionalized amphiphilic block copolymers to further modulate the polymer-lipid hybrid membrane for selective combination with more than one type of biomolecule. We selected poly(dimethylsiloxane)-block-poly(2-methyl-2-oxazoline) (PDMS-b-PMOXA) block copolymers and saturated (DPPC, DPPE or similar) or unsaturated (e.g. POPE) lipids to form membranes that could be used as models for selective insertion/attachment of biomolecules. A selective (partial) crosslinking of functional lipid- or polymer- domains will locally fix the biomolecules so that in a second step another type of biomolecule will decorate the second type of membrane domain. As model membrane protein, we will use a mutant of OmpF,[3] which allows diffusion of molecules through the membrane triggered by specific pH values. As a second biomolecule we plan to insert arginylglycylaspartic acid (RGD peptides) for adhesion of cells into the second domain (Fig. 1). The desired selective distribution and function of the two types of biomolecules in the polymer-lipid membranes will be evaluated.

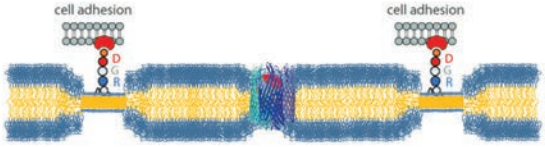

Fig. 1 Scheme for selective and spontaneous reconstitution of pH triggered OmpF in the block copolymer domains and RGD peptide attached to lipid domains for cell adhesion.

Material and Methods

In the first part of the project we focus on flexibility and mobility of hybrid membranes. These parameters play a fundamental role for protein insertion. End group functionalized, amphiphilic diblock copolymers were synthesized with different functional groups, e.g. –NH2, -COOH, -biotin. The modified polymers have been characterized by ^{1}H NMR and GPC (Fig. 2).

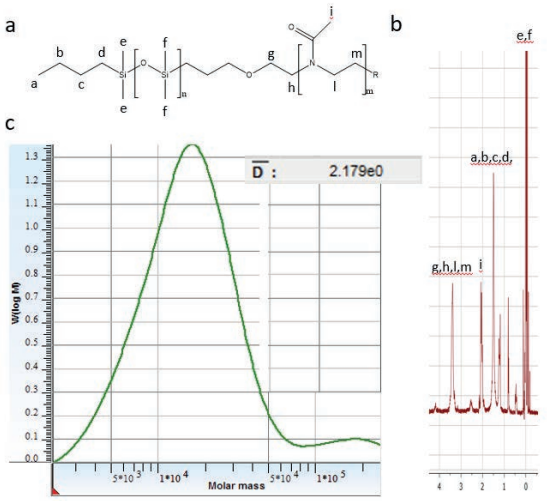

Fig. 2 (a) Chemical structure of the PDMS-b-PMOXA polymer. The R group in this case is carboxylic acid; (b) ^{1}H NMR spectrum and (c) GPC trace this polymer. This data allow calculation of the ratios between the blocks and the dispersity: The polymer has 92 PDMS and 11 PMOXA units.

To improve the features of these polymer-lipid membranes, different parameters can be tuned: content of cholesterol, temperature, deposition of bi- and multi- layers. Cholesterol is a molecule with interesting properties: it is a building block of cell membranes and stabilizes them by insertion between lipids. We tested the miscibility of cholesterol in lipid or polymer domains and investigated how it improves the mobility at different temperatures. It is known that beyond the transition temperature of the lipids, cholesterol inserts and thereby alters their packing and reduces their stiffness. Hybrid membranes with different polymer-lipid rations (lipid excess) have been characterized by Brewster angle microscopy (BAM) (Fig. 3) to understand how domains change their shape and size. These insights would be interesting for insertion of biomolecules of different dimensions. Langmuir isotherms and BAM were tested using a polymer (PDMS-b-PMOXA-COOH)

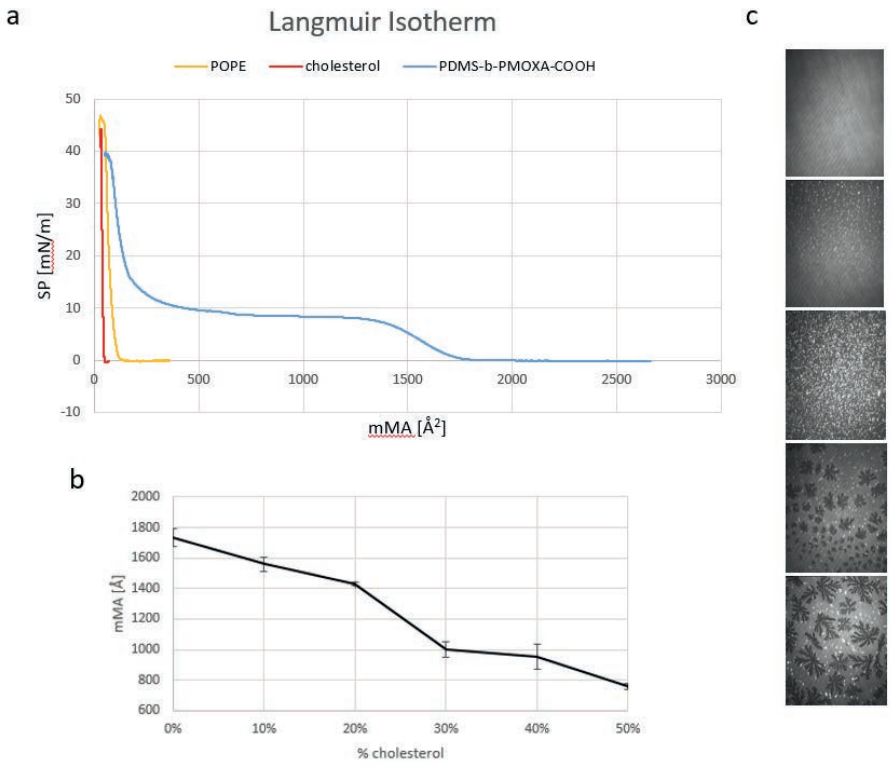

Fig. 3 (a) Comparison of Langmuir isotherms of PDMS-b-PMOXA-COOH, cholesterol and POPE; (b) Miscibility test between cholesterol and the polymer. The graph shows how the mean molecular area changes with increasing molar ratio of cholesterol up to 50%; (c) BAM images of polymer-lipid monolayer domain formation during the time.

and a lipid (POPE) and the miscibility of them with cholesterol at different ratios.

Results and discussion

NMR and GPC show that these polymers are composed of a longer hydrophobic part and they are polydisperse (Đ = 2.2) (Fig. 2c). It has been observed in previous work that high polydispersivity could help protein insertion. The analysis of BAM and Langmuir isotherms shows that this polymer forms homogeneous domains at low cholesterol molar ratio. As seen from the lower slopes of the monolayer formation in the graph, our polymer shows better compressibility compared to the lipid. This result reflects the flexibility of our membrane, which is important for biomolecule insertion. Next, the behavior of the lipid and of lipids in presence of cholesterol was analyzed. Further characterization will consist of techniques like Langmuir-Blodgett deposition, atomic force microscopy, ellipsometry and contact angle. Mobility of solid supported membranes will be tested with EPR on spin-labelled lipids and polymers.

Conclusions

These solid-supported membranes will be prepared for the second step: insertion/attachment of biomolecules like OmpF. The different properties of the lipid and polymer domains of the hybrid membrane in different conditions will be exploited to induce a selective interaction with the biomolecules. Systematic investigation of the effect of different domains on biomolecule functionality will allow optimization of the hybrid membranes.

The final aim of this project is building a complex, stable and flexible system, in which the biomolecules inserted/attached at different domains cooperate together. This approach will serve as a model for further insertion of different types of membrane proteins with high industrial and medical interest.

References

[1] J. Kowal, D. Wu, V. Mikhalevich, C.G. Palivan, W. Meier, *Hybrid Polymer–Lipid Films as Platforms for Directed Membrane Protein Insertion* Langmuir **31**, 4868–4877, (2015)

[2] F. Itel, M. Chami, A. Najer, S. Lörcher, D. Wu, I. A. Dinu and W. Meier, *Molecular Organization and Dynamics in Polymersome Membranes: A Lateral Diffusion Study,* Macromolecules **47**, 7588–7596 (2014)

[3] X. Zhang, W. Fu, C.G. Palivan, W. Meier, *Natural channel protein inserts and functions in a completely artificial, solid-supported bilayer membrane,* Sci Rep, **3**, 2196 (2013)

Electron spectroscopy of a DCA-Cu metal-organic network

Project P1605 Topological electronic states in metal-coordinated organic networks
Project Leader: M. Muntwiler and T.A. Jung
Collaborators: D. Sostina (SNI PhD Student) and J. Zhang

Introduction

Organic topological insulators (OTI) are organic materials that, in analogy to their well-investigated inorganic counterparts, exhibit topologically protected gapless electronic states at their low-dimensional boundary while the valence and conduction bands are separated by a finite band gap within their volume due to the spin-orbit interaction [1]. Within this paradigm, two-dimensional supramolecular networks are expected to provide a route to the bottom-up synthesis of molecular electronic devices and circuits on the nano-scale that take advantage of topology [2].

Goals

In this project, we investigate a two-dimensional metal-organic network based on 9,10-dicyano-anthracene ($C_{16}H_2N_2$, DCA) [3; 4] with respect to its topological properties. Theoretical calculations predict that a free-standing layer of metal-coordinated DCA exhibits topological edge states at the domain boundary [5] The states are expected in a small energy region in the unoccupied band structure, which render their experimental observation difficult. Furthermore, the influence of the (experimentally indispensable) substrate on the topological states is unknown and needs to be carefully addressed in the experiments.

Our goals are to look for dispersive electronic states derived from the frontier orbitals of DCA using scanning tunneling spectroscopy (STS) and angle-resolved photoelectron spectroscopy (ARPES). STS provides a local probe of edge states at domain boundaries of the DCA network and is also capable of probing unoccupied states. ARPES, on the other hand, easily distinguishes localized and dispersive bands formation in reciprocal space. For the verification of theoretical models, we further investigate the detailed atomic structure of the molecular network. In this respect, photoelectron diffraction (XPD) is the tool of choice to measure bonding angles and distances in the crucial metal-organic coordination bond [6].

Results

The project started in August 2017. So far, we have studied the preparation and atomic structure of monolayers of DCA on Cu(111). On this substrate, a metal-organic network is readily formed through the coordination of the cyano groups of DCA with Cu ad-atoms [4]. Figure 1 shows two topographic images from STM. The DCA molecules appear as bright, elongated shapes that are assembled in hexagonal lattice with a lattice constant of 2.08 nm and three molecules per unit mesh. Due to nucleation on different sites, defect lines such as in panel (a) appear where two laterally shifted domains meet. In the close-up in panel (b), it is evident how the DCA molecules arrange in a star pattern around a central pore. The CN side groups and Cu adatoms appear as dim features in the interior of the triangles.

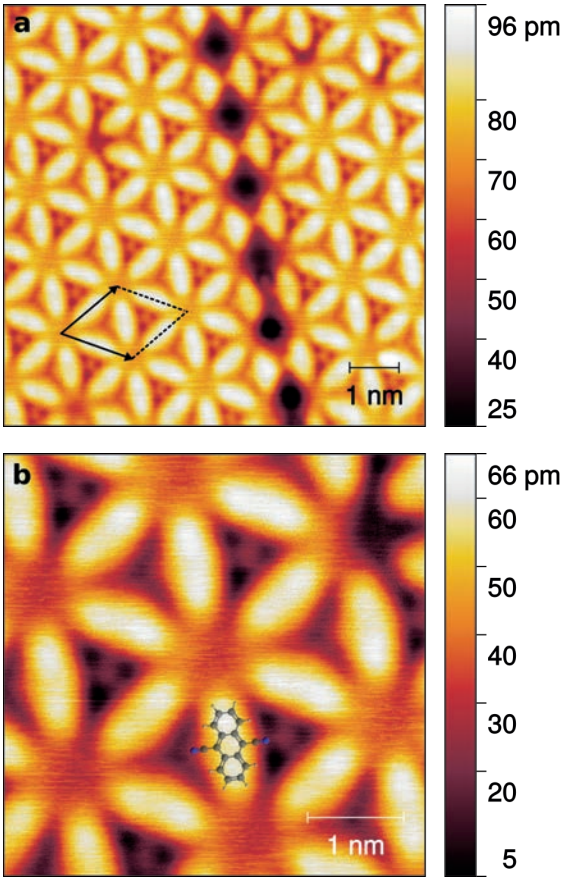

Fig. 1 STM topography scans of DCA network on Cu(111) substrate. (+0.8 V, 150 pA, 4.6 K, metallic tip). (a) Overview of the periodic network structure with a domain boundary line running across the image. (b) Detail image of a pore. The model of a DCA molecule is overlaid.

Looking for the valence states we measure the photoelectron spectra in figure 2. As can be seen in the top spectrum, DCA contributes a weak peak at 0.65 eV binding energy. To distinguish it clearly from Cu-related states, we have dosed oxygen on the system which suppresses the surface state feature just below the Fermi level. The middle curve shows that the density of states of the pure O/Cu(111) surface is featureless up to 1.7 eV in binding energy. Combining the binding energy of the HOMO with the previously measured position of the LUMO 0.75 eV

above the Fermi level [4], the HOMO-LUMO gap on the Cu surface amounts to 1.4 eV.

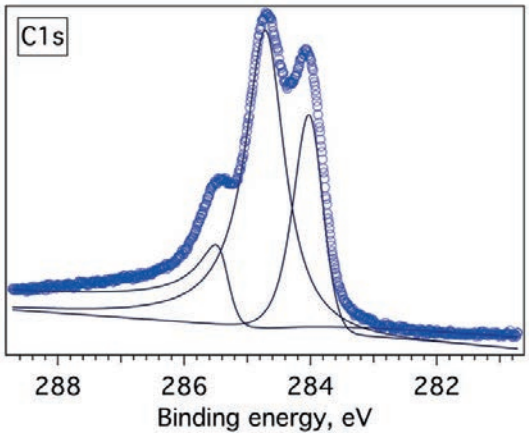

Fig. 2 High-resolution XPS spectrum of the C 1s core level peak of DCA on Cu(111) (hν = 400 eV).

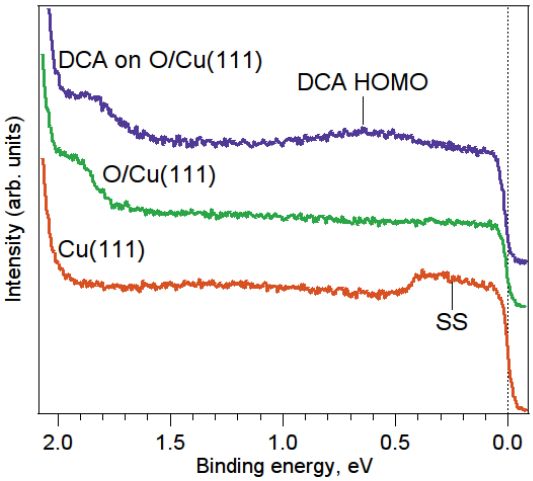

Fig. 3 Valence band photoelectron spectra of Cu(111), O/Cu(111) and DCA on O/Cu(111) measured with 21.2 eV photons. The peak at 0.65 eV binding energy is attributed to the HOMO of DCA. The broad feature SS originates from the Shockley surface state of Cu(111).

Outlook

At the time of writing, the search for edge states in STS measurements of DCA/Cu(111) is in progress. This task involves tuning the growth parameters of the molecular network in order to produce the various kinds of domain boundaries possible and optimizing the measurement parameters of the STM.

XPD measurements have been taken on the C 1s core levels to elucidate the bonding geometry of the molecules. As can be seen in figure 3, the C 1s core level peak consists of three distinct components for the inequivalent carbon atoms of the molecule. Based on the spectral weight we attribute the peak at 285.5 eV to the carbon atom in the cyano group. The modulation of its intensity as a function of emission angle should give information on the bonding geometry within the CN group. The analysis of the data is in progress.

References

[1] M.Z. Hasan and C.L. Kane, *Colloquium: Topological insulators*, Rev. Mod. Phys. **82**, 3045 (2010)

[2] Z. Wang, Z. Liu, F. Liu, *Organic topological insulators in organometallic lattices*, Nat. Commun. **4**, 1471 (2013)

[3] G. Pawin, K.L. Wong, D. Kim, D. Sun, L. Bartels, S. Hong, T.S. Rahman, R. Carp, M. Marsella, *A Surface Coordination Network Based on Substrate-Derived Metal Adatoms with Local Charge Excess*, Angew. Chem. Int. Ed. **47**, 8442 (2008)

[4] J. Zhang, A. Shchyrba, S. Nowakowska, E. Meyer, T.A. Jung, M. Muntwiler, *Probing the spatial and momentum distribution of confined surface states in a metal coordination network*, Chem. Commun. **50**, 12289 (2014)

[5] Z.F. Wang, N. Su, F. Liu, *Prediction of a Two-Dimensional Organic Topological Insulator*, Nano Lett. **13**, 2842 (2013)

[6] M. Muntwiler, J. Zhang, R. Stania, F. Matsui, P. Oberta et al., *Surface science at the PEARL beamline of the Swiss Light Source*, J Synchrotron Radiat. **24**, 354 (2017)

Smart peptide nanoparticles for efficient and safe gene therapy

Project P1606 Smart peptide nanoparticles for efficient and safe gene therapy
Project Leader: C.G. Palivan and Y. Benenson
Collaborator: S. Tarvirdipour (SNI PhD Student)

Introduction

Gene-based therapy, as an influential part of biotherapies, represents a novel strategy based on viral and non-viral delivery systems, which act by insertion of therapeutic DNA into nuclei of target cells followed by either genome editing, gene expression or gene silencing [1]. Whilst three marketed gene therapy products have been approved, there are considerable disadvantages, such as high immunogenicity, limitation in size of transgenic DNA, low availability and high development cost. Therefore non-viral strategies based on encapsulation/entrapment of DNA inside nanometer size systems (micelles, nanoparticles, vesicles) are on focus today due to several advantages over viral delivery systems, such as safety profile, localized gene expression and cost-effectiveness. In this respect, there is a considerable increase in the number of non-viral systems proposed for DNA delivery (at least 40 nanoparticle-based gene therapy-oriented systems) entering in various stages of clinical trials since 2010 [2]. However, to the best our knowledge none is based on stimuli-responsive peptide assemblies.

In this project, we are interested to introduce amphiphilic peptide-based nanoparticles with responsive properties as a new class of non-viral delivery systems able to release the payload "on demand", when a specific stimulus is present in their environment. Such peptide-based nanoparticles have the advantages of a high flexibility in the peptide design, no cytotoxicity to normal tissues and biodegradability [3]. We already designed peptide nanoparticles with stimuli-responsive properties for co-delivery of drugs and oligonucleotides and for producing highly efficient contrast agents for MRI [3, 4]. The first step of this project aims to synthesize such stimuli-responsive peptides and self-assemble them in the presence various DNA (single strands, double strands) (Fig. 1).

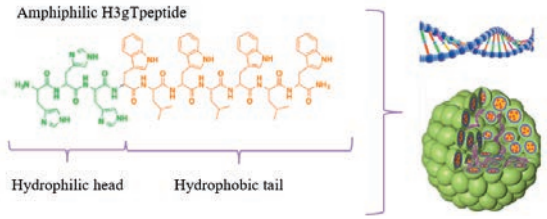

Fig. 1 Schematic representation of amphiphilic peptides, which self-assemble into nanoparticles with a multicompartment micelle morphology and are able to entrap DNA through electrostatic interaction with the histidine domain.

Based on the optimization of the peptide sequence and self-assembles nanoparticles in terms of DNA entrapment efficiency and up-take inside cells, the second step will be to modify the peptide-carriers (peptide sequence, size and charge of nanoparticles, entrapment process, release process) to cope with high molar mass DNAs, which are normally used in gene-based therapy.

Peptide synthesis and nanoparticle formation

First, an amphiphilic peptide, H3gT, which consists of an amino acid sequence, with a hydrophobic L-tryptophan-D-leucine repeating unit and a hydrophilic histidine domain has been synthesised. The hydrophobic domain supports the self-assembly of such amphiphilic peptides into supramolecular assemblies, whilst the hydrophilic histidine domain facilitates DNA binding (Fig. 1). The peptide was synthesized on a rink amide resin using standard fluorenylmethoxycarbonyl (Fmoc) solid phase peptide synthesizer chemistry and DIC/OXYMA coupling methods. The resulting peptidyl resin was isolated and washed alternating DMF and dichloromethane. The peptide cleavage from the resin and removal of the protective groups were performed using a mixture of trifluoroacetic acid (TFA), triisopropylsilane and H2O. The filtrate was precipitated in cold diethylether, centrifuged and placed in the freezer for 1 h before repeating the centrifugation. The crude peptide was filtered, solubilized with ACN and aqueous TFA (0.05%, v/v) and lyophilized. In order to characterise the peptide, we used high performance liquid chromatography (HPLC) and liquid chromatography mass spectrometry (LC-MS). The peptides were measured both before and after the purification procedure. The synthesized peptide after purification by preparative HPLC, represented a $[M+2H]^{2+}$ at 757.01 m/z and $[M+H]^{+}$ at 1514.17 m/z (Fig.2).

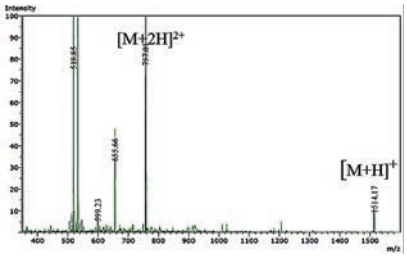

Fig. 2 LC-MS data of the purified H3gT peptide.

Then, H3gT peptides were self-assembled in a mixture of ethanol and water both without and in the presence of a short 22-mer single strand DNA (ssDNA). 22-mer ssDNA-loaded peptide supra-molecular assemblies were prepared by addition of 4

µL of 100 µM AON solution to 100 µL peptide solutions (1 mg/mL) and dilution to 500 µL with 35% ethanol.

Characterization of the self-assembled DNA loaded peptide assemblies

In order to characterize the supramolecular assemblies resulting from the self-assembly of the peptides in the presence of DNA we used dynamic light scattering (DLS) and zeta potential measurements. Together, these methods serve to obtain information regarding the size distribution and charge of the DNA-loaded H3gT peptide nanoparticles (Fig. 3A). DNA-loaded peptide assemblies have a size below 200 nm for concentrations of ssDNA smaller than 3.2 µg/ml (Table 1) with a neutral surface charge, which indicates that DNA is entrapped inside the assembly[2]. We used fluorescence correlation spectroscopy, FCS to analyse in more details the efficiency of the DNA entrapment (Fig. 3C). A 67% entrapment efficiency has been obtained for an initial concentration of ssDNA of 0.8 µg/ml. Transmission electron microscope (TEM) shows spherical nanoparticles (Fig. 3 A), which do not aggregate both before and after entrapment of ssDNA (initial concentration of ssDNA of 0.8µg/ml).

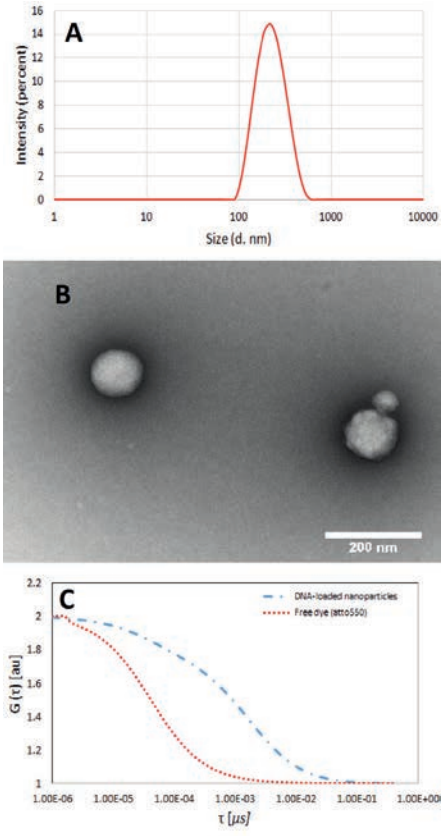

Fig. 3 Dynamic light scattering (A), TEM micrograph (B) of DNA-loaded H3gT peptide nanoparticles, and FCS autocorrelation curves for ATTO550 (red), and ATTO550--DNA-loaded peptide assemblies (blue).

Effect of the DNA concentration on self-assembly of peptides

In order to evaluate whether DNA concentration affect the self-assembly process of H3gT peptides, three different ssDNA initial concentrations have been used (0.8; 1.6; 3.2 µg/ml). By increasing the DNA concentration higher than 1.6 µg/ml, the self-assembly process has been disturbed due to a high charged ssDNA population, which could not be compensated by the peptides. Therefore, at high initial concentration of ssDNA an aggregation process took place. (Fig. 4C compared to Fig. 4A).

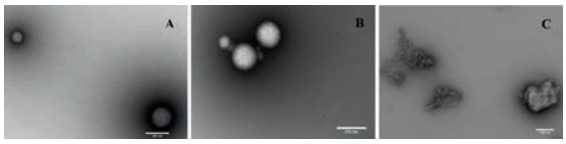

Fig. 4 TEM micrographs of H3gT peptides after self-assembly in the presence of ssDNA: 0.8 µg/ml ssDNA *(A) 1.6* µg/ml ssDNA *(B) and 3.2* µg/ml ssDNA *(C). Scale bar = 200nm.*

Table 1 Peptide nanoparticles size without and in the presence of different initial concentrations of ssDNA.

DNA Conc. (µg/ml)	0.8	1.6	3.2
Hydrodynamic diameter (nm)	120±40	200±11	420±30
Aggregation	-	-	✓

Conclusion and outlook

The first six month of the project have been devoted to the synthesis, characterisation and entrapment of ssDNA in peptide nanoparticles already reported, to co-load DNA and doxorubicin in order optimize the entrapment conditions of small DNA strands. We successfully entrapped 22-mer DNA strands inside the H3gT peptide nanoparticles via electrostatic interaction with the histidine domain. These results serve as input data to prepare the next steps of entrapment of high molecular mass DNA strands, which represent a real challenge in terms of self-assembly process and preservation of the nanoparticles morphology. The next steps of the project aim to produce high molecular mass DNA strands and study their interaction with the peptides in order to improve the physical and chemical properties of these peptide such to obtain efficient nonviral delivery systems.

References

[1] L.W. Seymour, A.J. Thrasher, *Gene therapy matures in the clinic*, Nat. Biotechnol. ***30*(7)**, 588-593 (2012)

[2] M. Foldvari, D.W. Chen, N. Nafissi, D. Calderon, L. Narsineni, A. Rafiee, *Non-viral gene therapy: gains and challenges of non-invasive administration methods*, J. Control. Release, **240**, 165-190 (2016)

[3] S.J. Sigg, V. Postupalenko, J.T. Duskey, C.G. Palivan, W. Meier, *Stimuli-Responsive Codelivery of Oligonucleotides and Drugs by Self-Assembled Peptide Nanoparticles*, Biomacromolecules, **17(3)**, 935-945 (2016)

[4] S.J. Sigg, F. Santini, A. Najer, P.U. Richard, W.P. Meier, C.G. Palivan, *Nanoparticle-based highly sensitive MRI contrast agents with enhanced sensitivity to reductive milieu*, Chem. Comm. **52(64)**, 9937-9940 (2016)

Understanding phonon propagation in nanodevices

Project P1607 Understanding and engineering of phonon propagation in nanodevices by employing energy resolved phonon emission and adsorption spectroscopy
Project Leader: I. Zardo and C. Schönenberger
Collaborator: L. Gubser (SNI PhD Student)

Introduction

During the last few decades, research has improved our knowledge and control over electrons and photons, enabling impressing advances for electronic and optoelectronic applications. The same degree of control is still lacking for phonons. The ability to manipulate phonons and phonon transport on a quantum level would lead to full control over heat flow in nanodevices. This could be used in the form of phonon transistors [1] or is also proposed as a building block for logic gates [2].

The main issue so far is that no phonon detectors exist that are comparably efficient to those for electrons. This is mostly due to the discrepancy between thermal and electrical insulators. The effectiveness of charge detection is based on low loss capacitors, where current can be accumulated to a measurable amount. The availability of very good electrical conductors as well as insulators makes this possible. For heat transport (i.e. phonons) this is very different. The range of thermal conductivity is much narrower, providing no good thermal insulators.

The goal of the project is twofold. First, efficient phonon emitters and detectors have to be developed. Those can then be used to investigate and engineer phonon band structure. To realise this, the tunnelling through a double quantum dot will be modulated using bottom gates or inbuilt barriers.

DQD phonon emitter/detector

The group of Jason Petta has demonstrated a maser driven by single-electron tunnelling through a double quantum dot (DQD) in a semiconducting nanowire (NW)[3, 4, 5]. This happens by inelastic tunnelling through the energy states of the two quantum dots, when the system is driven by an applied finite bias voltage.

To understand the principle of this DQD system, a schematic is shown in figure 1. Due to the applied bias an electron is injected in the eigenstate E_1 of QD_1, tunnels to the state E_2 in QD_2, where it is free to be absorbed by the drain contact.

If E1 is equal to E2 the tunnelling is elastic. Inelastic tunnelling takes place if the energy levels are detuned. The electron will then tunnel through the DQD emitting a photon/phonon (or a combination). A particle is emitted when $E_1 > E_2$. By detuning the levels so that $E_2 > E_1$ a detector can be fabricated. Namely, the electron can only tunnel through the dot under absorption of a particle.

For the research of Petta et al., the DQD system was coupled to a microwave cavity. This was used to collect and measure monochromatic photons. By tuning the energy levels of the DQD maser activity could be shown. When no maser activity is observed, the phonon emission surpasses the photon emission. This makes the DQD system an excellent design to emit and detect phonons of a well-defined spectral distribution.

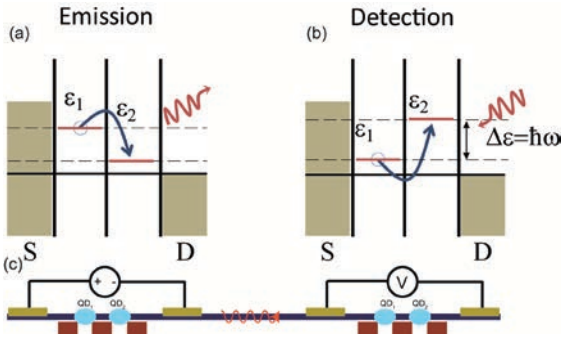

Fig. 1 (a) Schematic illustration of a phonon emitter and detector (b) using a double quantum dot system. Driven by a finite applied bias inelastic tunnelling between the dots is used to either generate or detect phonons. (c) Schematic of the aimed at final device. Inside the semiconducting nanowire (blue) two double quantum dots (light blue) are defined by local bottom gates (red). Phonons are then generated by an applied bias through source drain contacts (brown) in one DQD system, and detected by measuring the voltage in the second DQD system.

To move as close as possible to an ideal 1D system the diameter of the NWs should be as small as possible, as long as they can still be used for low temperature measurements. For this reason, the group of Lucia Sorba (NCR Nano, Pisa) provided InAs NWs with a diameter of 40 nm.

Results

During these first few months the focus was set on developing robust fabrication recipes for both the bottom gates, as well as the nanowire contacting. The bottom gates are fabricated from Ti/Au and a SiN layer is used as a gate dielectric (Fig. 2). To form good ohmic contacts the NWs are treated with a $(NH_4)_2S_x$ etch step to remove the native oxide, before the contacts are evaporated.

Low temperature (4.2K) four terminal conductance measurements in a dipstick setup were used to test both, the quality of the contacts, as well as the characteristics of the NW. These measurements, which were only recently concluded show the

reliability of the fabrication process. Furthermore, the wires exhibit good electrical conductance with an expected behavior to gating using a global backgate.

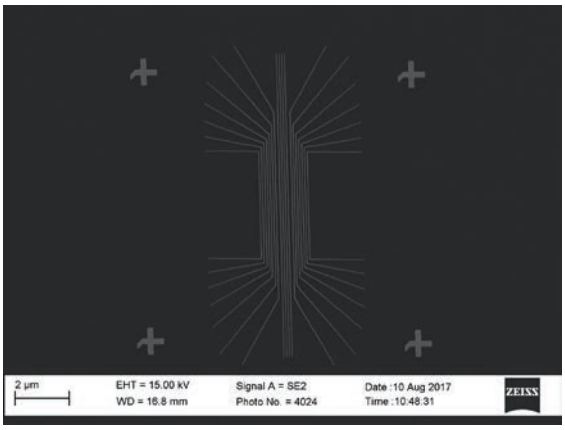

Fig. 2 Scanning electron microscope image of the first bottom gate design. The gates are designed with a pitch of 100 nm and a width of 45 nm.

Outlook

With the initial wire characterisation all but completed the next step is the deposition of the wires on the local gates using a micromanipulator, to probe the DQD behaviour. These experiments will also determine the need for optimization of the bottom gate design.

Once the electrical properties of the DQD are known first experiments probing phonon interaction will be performed. There one DQD will be used as a phonon detector, while the phonon emission will still be provided by laser excitation.

Although the electrostatically defined confinement can be tuned in-situ, the self-screening of the NW imposes limitations. The effects of local gates on the potential landscape of the NW depend for example on the width of the gates, their spacing and the gate-NW distance. To be able to circumvent those possible restrictions and achieve a stronger confinement of electrons in the NW, inbuilt barriers are desirable [6]. These will be grown using two materials with a different bandgap but similar crystal structure, like InAs/InP (Fig. 3).

To help our growers to achieve this structure we will provide them with well-designed (lithographically written) gold particles arrays as catalysts on the growth substrate. The so achieved uniformity circumvents the random nature of the usual colloids deposition and should allow for perfect growth conditions.

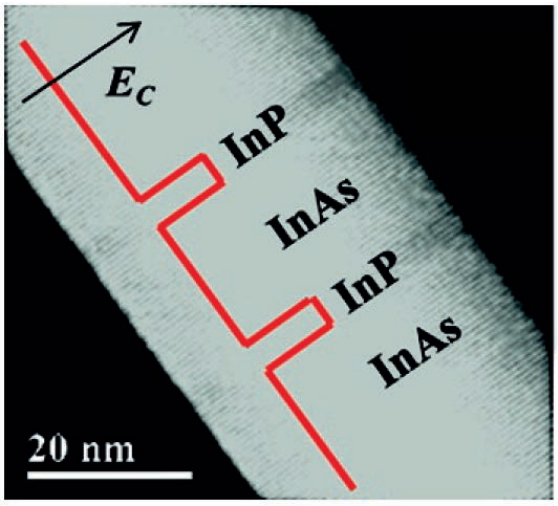

Fig. 3 Transmission electron microscope image of a InAs nanowire grown with periodic InP barriers. Due to the difference in bandgap of the materials (InAs: 0.354 eV; InP: 1.344 eV) tunnel barriers are formed. These inbuilt barriers should provide a better confinement than local gates, although at the cost of less flexibility.

References

[1] B. Li, L. Wang, G. Casati, *Negative differential thermal resistance and thermal transistor*, Appl. Phys. Lett. **88**, 143501 (2006)

[2] L. Wang and B. Li, *Thermal Logic Gates: Computation with Phonons*, Phys. Rev. Lett. **99**, 177208 (2007)

[3] Y.-Y. Liu, J. Stehlik, C. Eichler, M.J. Gullans, J. M. Taylor, J.R. Petta, *Semiconductor double quantum dot micromaser,* Science **347**(6219), 285-287 (2015)

[4] Y.-Y. Liu, K.D. Petersson, J. Stehlik, J.M. Taylor and J. R. Petta, *Photon Emission from a Cavity-Coupled Double Quantum Dot*, Phys. Rev. Lett. **113**, 036801 (2014)

[5] M.J. Gullans, Y.-Y. Liu, J. Stehlik, J.R. Petta, J.M. Taylor, *Phonon-Assisted Gain in a Semiconductor Double Quantum Dot Maser,* Phys. Rev. Lett. **114**, 196802 (2015)

[6] S. Roddaro, A. Pescaglini, D. Ercolani, L. Sorba, F. Beltram, *Manipulation of Electron Orbitals in Hard-Wall InAs/InP Nanowire Quantum Dots,* Nano Lett. **11(4)**, pp 1695-1699 (2011)

Atomic-Scale Analysis of the SiC/Oxide Interface to Improve High-Power MOSFET Devices

Project A10.08 Atolys (University of Basel, PSI, ABB Switzerland Ltd, Corporate Research, Baden-Dättwil)
Project Leader: S. Goedecker
Collaborators: D. Dutta, D. De, B. Schaefer, M. Camarda, S. Gerstl, E. Mueller, H. Bartolf, T. Jung, J. Lehmann, and G. Alfieri

Introduction

An obstacle towards the wide distribution of silicon carbide (SiC) wide-bandgap semiconductor devices for advanced high power and high temperature electronic applications is the limited Metal Insulator Semiconductor (MIS)-channel mobility after thermal growth of the insulator. In contrast to the commercially available SiC Schottky rectifier technology, SiC power MIS-Field Eeffect Transistor (FET) technology is still compromised by low channel mobilities and by threshold voltage instabilities due to the poor quality of the SiC and the insulator which in this case is native silicon oxide (SiO_2) [1]. In order to obtain higher carrier-mobilities in the inversion channel below the SiC/SiO_2 interface, the density of these defects has been plausibly related to the complicated oxidation process that necessitates the removal of carbon in the form of CO and CO_2 from the SiC crystal [2]. This carbon removal which goes on at all stages of oxidation introduces different defects at and near the interface (dangling bonds, carbon clusters, near-interface traps, etc.). These have to be minimized, at least in their impact on the channel mobility. The introduction of post-oxidation annealing in nitric oxide ambient comprised a breakthrough for improving the MOS interface [3], but nevertheless the microscopic origin of the passivation mechanism is not yet fully understood [4]. In this abstract we report about the outcome of a combined theoretical and experimental approach to analyze the interface between SiC/SiO_2 towards a deeper understanding of impurities, crystal-defects and carbon clusters as they affect the electronic performance of the MOS-channel.

Interface Defect – Simulations Theoretical studies of the $SiC-SiO_2$ interface have been performed using the minima hopping method (MHM). Defects have been observed in our numerical simulations to emulate the structural evolution of the interface near SiC and within the amorphous SiO_2 during the oxidation process. This MHM framework involves (i) a fast method for calculating the energy, force, stress etc. (the Density Functional Tight Binding scheme (DFTB)), (ii) full density functional schemes and (iii) conformational and transition path sampling methods. Also in our "in silico" study, we have explored different configurations of 4H–SiC reacting in different environments such as oxygen, nitric oxide (NO) and nitrous oxide (N_2O). During oxidation, we have observed that carbon silicon chains, which consist of carbon silicon rings, appear at the interface of SiO_2/4H-SiC (see Fig. 1). It is also observed that these chains are stable only near the interface. By simulating the N_2O and NO passivation, we have observed that N_2, CO, C-N, SiO_2 and carbon clusters form at the interface. These findings provide novel insight into the structural and electronic properties of the SiO2/SiC interface for fabricated MOSFETs.

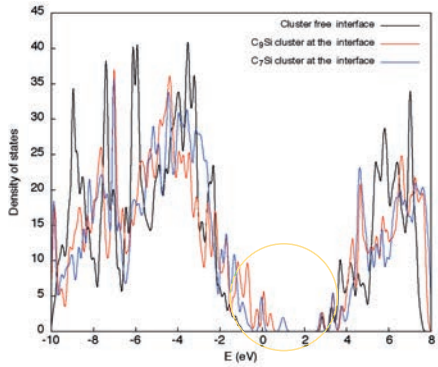

Fig. 1 The calculated DOS of SiC/SiO2 interface structures without any Carbon cluster and with 6-atom carbon clusters and 5-atom carbon cluster. In absence of carbon clusters the energy gap is around 3.1 eV. In presence of a C9 (red line) and C7 (blue line) cluster new states arise near the valance band edge.

To correlate our theoretical work with experimental results we have analyzed the interface of two different thermally grown oxides, one grown in the presence of passivating N_2O and the other grown in pure oxygen atmosphere. These oxides have been already electronically characterized in our previous

work [4]. Atomic Force Microscopy (AFM) analysis of the interface after removal of the oxide showed that the interface grown under a passivating atmosphere exhibits a reduced roughness with respect to the one grown in pure oxygen. This reduced interface-roughness might contribute to the improved MOS performance / channel mobility of the devices comprising gate oxide layers grown in passivating atmosphere [4]. The AFM analysis of interfaces grown in pure oxide, after removal of the oxide, in contrast showed localized regions of composition or phase change near the SiC/SiO_2 interface as identified by their lower etch rate. These observations motivated further investigations of the chemical composition and the predominant bonding in these regions. Raman spectroscopy has been employed to characterize the carbon defects at the different interfaces. Due to the wavelength of the light used (532 nm) and the optical properties of the SiC, the information depth is in the order of 5 micrometers. Thus, the spectra contain information about the inclusion of C, at the SiC/SiO_2 interface itself (see Fig. 2). The secondary peaks of SiC tend to mask the peaks for carbon defects: The D (defect peak) at around 1470 and the G (graphitic peak) between 1600 to 1800 region is shown in Figure 2. The carbon peaks have been identified based on literature values (Fig. 2b). Remarkable and characteristic differences are recognized by comparing Raman spectra for SiC wafers with oxide stripped interfaces. From this analysis, there is consistent evidence of near oxide carbon. These observations are in good agreement with theory.

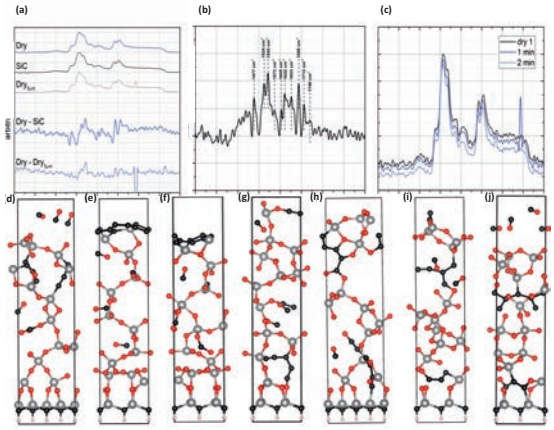

Fig. 2 (a) Raman spectra obtained with the focus set at the specimen surface i.e. at the interface position after careful oxide removal. A spectrum taken with a beam focus 5 µm below the interface i.e. corresponding to pure SiC is used as a reference. The secondary peaks of SiC tend to mask the unwanted carbon peaks: D (defect peak) and G (graphitic peak); For visibility and quantification, difference spectra after subtracting the SiC reference have been calculated and analyzed in the lower panel; (b) G peaks associated with different C bonds along with D peak have been identified and marked based on literature values. The Raman spectrum of interface specimens grown in pure oxygen has been subtracted from a reference spectrum of a clean SiC wafer to discriminate the carbon which is modified by the oxidation from the sp_3 carbon in SiC. (c) The effect of an initial oxide etch (1 min HF) and of further (2 min HF) etching of a defect-rich interface grown in pure oxygen. Model simulations of the SiC surface oxidized with large amounts of oxygen. Different kind of carbon clusters evolved: d) carbon cluster in SiO_2, e) and f) carbon cluster formed on the surface of SiO_2. g)-j) carbon cluster in SiO_2 as well as at the interface of SiO_2 and SiC and also at the surface of SiO_2.

Further, Scanning Transmission Electron Microscopy (STEM) has been used to generate a detailed image of an intact, thin sliced 4H-SiC/SiO_2-interface to prove the presence of the undesired five-carbon clusters as they have been evidenced in our DFTB study.

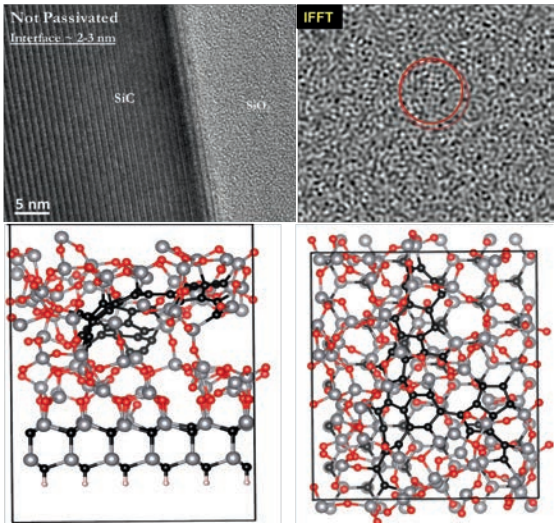

Fig. 3 The interface as seen in HRTEM is not sharp. After thorough investigation of the oxide-near interface using Inverse Fast Fourier transform (IFFT) we found a sheet of C-defects formed by interconnected rings. This observation was confirmed by DFTB modelling. In the simulation, the C-defects from the interface break and join as they move into the SiO_2 and form sheet-like structures.

References

[1] G. Liu, B.R. Tuttle, S. Dhar, *Silicon carbide: A unique platform for metal-oxide-semi-conductor physics*, Appl. Phys. Rev., 2(2), 021307, (2015)

[2] T. Christen, A. Ioannidis, C. Winkelmann, *A model for thermal oxidation of Si and SiC including material expansion*, J. Appl. Phys., 117, 084501 (2015)

[3] A. Gavrikov, A. Knizhnik, A. Safonov, A. Scherbinin, A. Bagaturyants, B. Potapkin1, A. Chatterjee, K. Matocha, *First-principles-based investigation of kinetic mechanism of SiC(0001) dry oxidation including defect generation and passivation*, J. Appl. Phys., 104, 9, (2008)

[4] A.I. Mikhaylov, A.V. Afanasyev, V.V. Luchinin, S.A. Reshanov, A. Schöner, L. Knoll, R. Amaral Minamisawa, G. Alfieri, H. Bartolf, *Passivation of 4H-SiC/SiO2 Interface Traps by Oxidation of a Thin Silicon Nitride Layer*, Materials Science Forum 821-823, 508-511, (2015)

Antibacterial nanostructures mimicking cicada wings for consumer products (Nano-Cicada-Wing)

Project A10.10 Nano-Cicada-Wing (Universität Basel, FHNW, DMS Nutritional Products Kaiseraugst)
Project Leader: E. Meyer
Collaborators: M. Kisiel, Th. Glatzel, M. Wasser, J. Köser, L. Marot, Y. Grether, F. Abazaj, and H. Hug

Project overview

Recently the antimicrobial activity of biological and biomimetic nanostructured surfaces has gained large interest [1]. Such surfaces are of great interest since due to the absence of chemical biocides their application currently does not require special regulatory steps. While structured surfaces of certain insect wings and structured nanomaterials like graphene or black silicone exhibit bactericidal activity other mimicking surfaces lack this effect but show reduced adhesion of different bacterial strains [2, 3]. Within the Nano Cicada Wing project, we try to mimic antibacterial insect wing surfaces by means of nanostructured and chemically modified polymer surfaces. We combine plasma exposure polymer surface structuration of different polymers (polyether ether ketone (PEEK), polypropylene (PP), polycarbonate (PC), polyethylene terephthalate (PET)), chemical functionalization and antimicrobial activity assays with Fluorescence Microscopy, Scanning Electron Microscopy (SEM) and Atomic Force Microscopy (AFM). Similarly, we modify titanium surfaces.

Generation of nanostructured polymer surfaces and visualization of bacterial integrity

Nanostructured polymer surfaces were generated by low energy plasma etching. Typical structures obtained by this procedure are shown in figure 1. The height of the produced pillars and distance between them strongly depend on plasma power, exposure time and plasma composition [4].

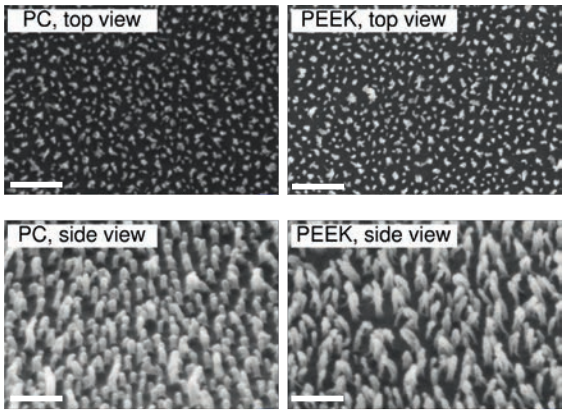

Fig. 1 Comparison of nanostructured PC and PEEK. Please note the different magnifications of top view images and side view images. Scalebars are 300 nm.

When *E.coli* in liquid came in contact with nanostructured PC surfaces they survived to a similar extend like on unstructured reference polymer surfaces. Unlike reported on cicada wing structures they also appeared seemingly intact besides being in contact with numerous nanopillars (Fig. 2a).

To investigate the influence of the surface chemistry on a bactericidal effect of the nanostructured polymer surfaces they were modified by several different means: a) silanization with hydrophobic octadeclytriethoxysilane (OTS), b) silanization with cell wall interacting 3-(trimethoxysilyl)propyl dimethyl octadecyl ammonium chloride, c) coating with a cationic polyelectrolyte (PEI). None of these modified surfaces exhibited a strong bactericidal efficacy although on silanized surfaces occasionally ruptured bacteria were observed (Fig. 2b).

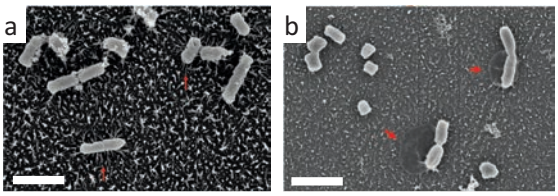

Fig. 2 SEM images of E. coli following ON incubation on nanostructured PEEK (a) versus quaternary amine silane modified nanostructured PEEK (b). The arrows in a) mark positions were interactions between nanopillars and bacteria are most obvious, in b) bacteria with leaked content are marked. Scalebars are 2 µm.

Reduced adhesion of *E.coli* on certain nanostructured polymers

While microscopy reveals details on the structural integrity of bacteria on nanostructured surfaces the analysis of larger number of samples and the exact quantification of living bacteria as compared to reference surfaces is facilitated by the use of biochemical assays which quantify the cell metabolism.

We used alamar blue assays to quantify the extend of adhesion of living bacteria on various polymer surfaces upon overnight incubation in PBS followed by washing under slight agitation (110 rpm in multiwell plates).

We observed a reduction of 60% in cell adhesion of *E.coli* on unmodified nanostructured PC as compared to flat PC. Modification of the surfaces with a hydrophobic silane or PEI resulted in an increased adhesion on structured versus unstructured surfaces (Fig. 3 left). Interestingly the adhesion reducing effect of the nanostructuration

was not universal but dependent on the type of investigated polymer (Fig. 3 right). These results are in line with a study by Serrano et al. [2], which also reports strong differences in bacterial adhesion ratios of structured versus unstructured medical sutures despite similar micro-/nanostructuration.

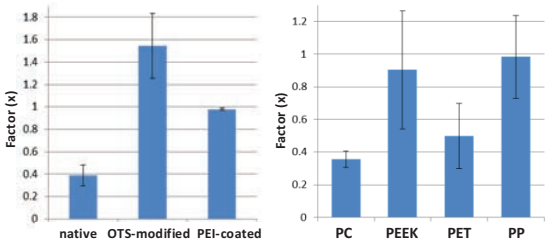

Fig. 3 Ratios of the numbers of adhering live bacteria on structured:unstructured polycarbonate when investigating native and OTS/PEI modified samples (left) and ratios of adhesion of live bacteria on different structured versus unstructured polymers (right).

To compare the adhesion of *E.coli* on different flat and nanostructured polymers adhesion experiments were run in parallel and the results were normalized with reference to unstructured PC (Fig. 4a). The largest extend of adhesion was observed on flat PC, while on structured PC as well as on flat and nanostructured PEEK and PET adhesion is strongly reduced.

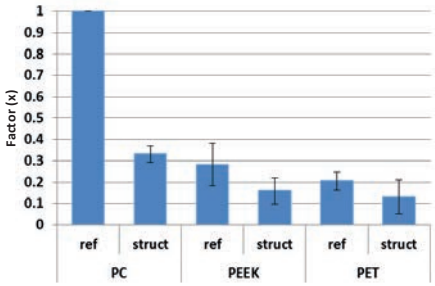

Fig. 4 Relative bacterial adhesion on different structured and unstructured (ref) polymer surfaces in relation to unstructured polycarbonate.

Furthermore, The AFM adhesion measurements (Fig. 5) reported 60% adhesion reduction on structured polycarbonate as compared to flat surface, in agreement with fluorescent microscopy results.

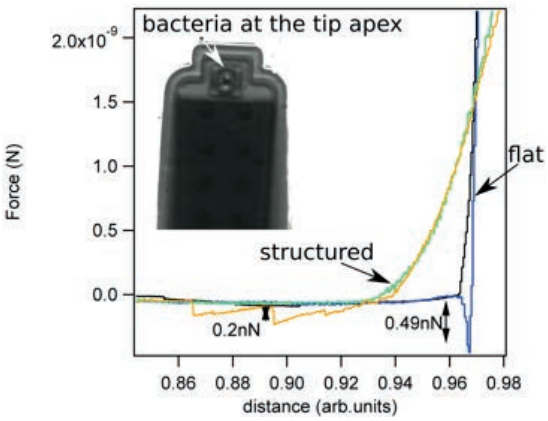

Fig. 5 Adhesion forces for E. coli cell envelope measured on flat and plasma structured polycarbonate surface. Adhesion forces are reduced by factor 2.5 on structured areas.

Titanium surfaces exposed to helium plasma

To proceed on the issue of antibacterial surfaces we nanostructured by means of non-equilibrium helium plasma, a titanium metal surface – a biocompatible material. Plasma exposure and sample annealing to temperature T=300°C results in production of pillars of heights of hundred nanometers (Fig. 6). Their antibacterial properties have to be further investigated.

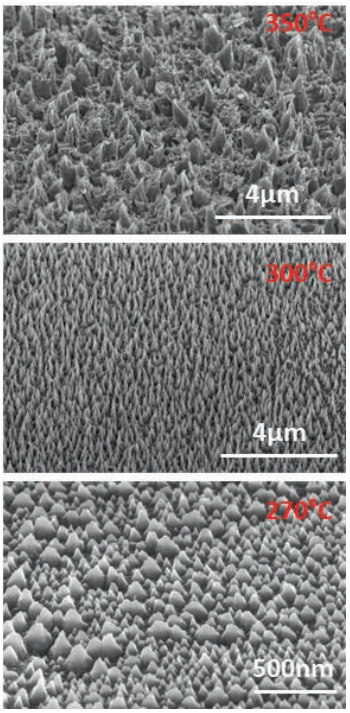

Fig. 6 Effect of helium plasma exposure and sample temperature on titanium surface nanostructuration.

References

[1] E.P. Ivanova, J. Hasan, H.K. Webb, V.K. Truong, G.C. Watson, J.A. Watson, V.A. Baulin, S. Pogodin, J.Y. Wang, M.J. Tobin, C. Löbbe, R.J. Crawford, *Natural bactericidal surfaces: mechanical rupture of Pseudomonas aeruginosa cells by cicada wings*. Small, **8(16)**, 2489-94 (2012)

[2] C. Serrano, L. García-Fernández, J.P. Fernández-Blázquez, M. Barbeck, S. Ghanaati, R. Unger, J. Kirkpatrick, E. Arzt, L. Funk, P. Turón, A. del Campo, *Nanostructured medical sutures with antibacterial properties*. Biomaterials, **52**, 291-300 (2015)

[3] E.P. Ivanova, J. Hasan, H.K. Webb, G. Gervinskas, S. Juodkazis, V.K. Truong, A.H. Wu, R.N. Lamb, V.A. Baulin, G.S. Watson, J.A. Watson, D.E. Mainwaring, R.J. Crawford, *Bactericidal activity of black silicon*. Nat Commun, **4**, 2838 (2013)

[4] J. Althaus, C. Padeste, J. Köser, U. Pieles, K. Peters, B. Müller, *Nanostructuring polyether-etherketone for medical implants*. In European Journal of Nanomedicine; **4(1)**, 7-15 (2012)

CerInk: Biomimetic ceramic scaffolds with density gradient and improved mechanical stability fabricated by Binder-into-Bed 3D-printing and ceramic NanoInk

Project A11.01 CerInk (School of Life Sciences-FHNW, PSI, Medicoat AG Mägenwil)
Project Leader: A. Testino
Collaborators: A. Carino, R. Schumacher, N. Matter, and Ph. Gruner

Introduction

The 3-dimensional printing (3DP) technology has become a convenient tool in different fields. It is defined as flexible solid freeform fabrication technology, with the advantage of versatility with respect to the materials used, such as ceramic, metals and polymers. In the medical field, metal 3D-printed scaffolds are a well-established technology and nowadays used as a routine in orthopaedic surgery. Instead, the production of 3D-printed ceramic scaffolds remains a challenge albeit, in the recent years, relevant improvements have been done. Ceramic scaffolds can be made of hydroxyapatite (HA), the most abundant inorganic compounds of natural bone. Although the excellent biocompatibility, additional properties need to be reproduced in a synthetic bone such as an optimal trade-off between mechanical properties and porosity.

The aim of the two-year CerInk project was ambitious: manufacturing ceramic scaffolds by 3DP mimicking the natural bones in term of biocompatibility, mechanical properties and porosity. In particular, a natural bone is composed of cortical and cancellous/trabecular zones, being the former more porous and the latter characterized by a higher compressive strength. In order to be able to mimic such a complex 3D structure, an ad-hoc 3DP technology was needed.

Since 2008, the Life Science FHNW in Basel established a considerable know-how on the Binder-into-Bed (BiB) 3DP of calcium phosphate bioceramics. In order to improve the mechanical characteristics of the 3D-printed scaffolds, biopolymeric infiltration and nano-HA powder have been used to modify the sintering properties of the bulk material and promoting densification. Figure 1 of the previous report [1] represented the state-of-the-art, before the CerInk project: it was clear that the ceramic-ceramic junction needed to be improved. Thus, a modified BiB 3DP system was conceived. The new technology allows the use of two inks, each of them with a specific composition, in order to promote, upon sintering, a controlled densification only where required, leaving other zones with higher porosity. Consequently, the complexity of the natural bone can be reproduced.

At PSI the appropriate ceramic NanoInk compositions were developed and during the second year, several green bodies with controlled porosity were produced by conventional techniques. The sintering properties of the ceramic bodies were systematically studied by thermomechanical analysis and the composition optimized to promote a good ceramic-ceramic junction between parts, while the different mechanical properties and porosity were preserved.

Results

During the first year, several NanoInks were prepared. The NanoInks were water- and water/organic based and containing micro- and nano-HA and biocompatible sintering aids. The NanoInks were designed based on specific rheological constraints in order to be compatible with low-cost commercial HP print heads. In particular, viscosity and surface tension were kept in the range of 8–100 mPa·s and 46–57 mN·m-1, respectively. Nano-HA was included in the formulation up to 40 wt.% in order to improve deification upon sintering. However, formulations with >≈20 wt.% solid load results to be non-printable or with a too short shelf time even if polymeric additives, such as PAA, and surfactants were used. Some NanoInks containing ≈20 wt.% of nano-HA powders were produced with a shelf life of 48 hours and different green bodies were 3D-printed [2]. It was concluded that solid load limit was a major issue and the maximum allowed nano-HA was not enough to promote the aimed controlled densification. A more efficient strategy was required: a formulation containing an optimal combination of sintering aids and nano-HA.

In the second year of the project, we applied a fast prototyping strategy in order to define the appropriate ceramic NanoInk compositions to achieve the density gradient upon sintering. Several green bodies with a porosity equivalent to that obtained by BiB were prepared using potatoes starch as pore former and binder. In particular, micro-HA powders (50%wt) and the pore former (50wt%) were wet milled in a planetary milling machine for one hour and then dried in the oven at 50°C. Afterwards, defined amounts of nano-HA, bioglass (Schott Vitryxx, MD01), and colloidal silica were added and mixed to the previous formulation to get all compositions reported in Table 1. Nano-HA, bioglass, and colloidal silica act as a sintering aid and bioactivity improver. It has been reported that the addition of such sintering aids promotes the osteoblast differentiation and proliferation compared to pure hydroxyapatite samples. Finally, the

dry powders were uniaxially pressed in a 5 mm die with a pressure of 2 Tons. A first thermal treatment (TT) was then applied to burn out the pore former and achieve the equivalent BiB sample's density (~1 g·cm-3). The porous green bodies undergo sintering treatment (ST). The maximum temperature (hold for 1h) was set to 1450 °C, 1400°C, and 1350°C for ST1, ST2 and ST3, respectively. In such a way, 42 different compositions were prepared and sintered according to three different thermal profiles, generating 142 sintered bodies. Density, compressive strength and sintering properties of each sample were measured. The temperature selected for TT and ST were optimized after thermogravimetry, dilatometry, and XRD diffraction analyses. In fact, if the pore former is not burned out properly, the green bodies collapse or massive cracks occur. Similarly, if the sintering temperature is too low, densification does not occur; if it is too high, the sample might partially melt and vitreous samples were obtained.

Table 1 Compression strength (CS) and density of the samples sintered according to ST2. The blue values correspond to the bi-component samples reported in figure 1.

Colloidal Silica wt.% \ Bioglass wt.%	0.5		1		2		4		8		16	
	CS MPa	d g cm^{-3}	CS MPa	d g cm^{-3}	CS MPa	d g cm^{-3}	CS MPa	d g cm^{-3}	CS MPa	d g cm^{-3}	CS MPa	d g cm^{-3}
0.0	9	1.4	15	1.5	15	1.6	23	1.7	14	1.6	--	1.3
0.5	41	1.7	33	1.7	31	1.7	23	1.6	12	1.5	4	1.5
1.0	33	1.7	29	1.6	37	1.7	37	1.7	4	1.4	--	1.5
2.0	42	1.8	37	1.7	32	1.7	21	1.6	10	1.5	--	1.6
4.0	38	1.6	39	1.9	9	1.5	48	1.8	70	1.8	--	2.1
8.0	88	2.4	91	2.5	93	2.5	78	2.5	33	2.3	6	2.2
16	78	2.4	77	2.5	89	2.6	75	2.3	39	2.1	24	2.2

The so-called diffusion couple technique was applied in order to evaluate the co-firing behaviour at the interface between different formulations. Bi-component samples were prepared by pressing two layers of powders, each of them prepared according to the aforementioned protocol and following the TT and the selected ST profile. Since 42 formulations and three sintering profile were investigated, 5166 couples of the formulation were prepared. Thus, the most promising couple of formulations, with appropriate density, mechanical properties, and sintering behaviour, were studied. For the morphological investigation, the axial cross-section of the co-fired samples was prepared and polished using conventional metallographic techniques and analysed by optical and scanning electronic microscopy (SEM). Figure 1 shows an example where an appropriate ceramic-ceramic junction was obtained upon co-firing. The improvement with respect to Figure 1 of the previous report [1] is clear: after sintering the two ceramic layers show different densifications and porosities and, at the interface, no delamination occurs. The ceramic on the left-hand-side has a density of 1.5 g·cm-3 and a compressive strength of 9 MPa, which corresponds to the properties of cancellous/trabecular bone (2-12 MPa) whereas the layer on the right-hand-side shows a density of 1.8 g·cm-3 and a compressive strength of about 70 MPa, which is approaching the properties of cortical bone (>100 MPa). Thus, ceramic scaffolds can be produced using two ceramic NanoInks: the first ink – for the porous ceramic – is composed by 4wt% of colloidal silica, 10% of nano-HA and 2 wt% of bioglass; the second ink – for the densified ceramic – is composed by 4wt% of colloidal silica, 10% of nano-HA and 8 wt% of bioglass. These NanoInks contain an overall solid load compatible with low-cost print heads.

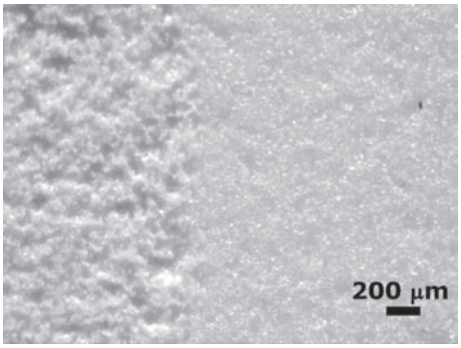

Fig. 1 Example of the interface between porous and densified co-fired ceramic (optical micrograph) sintered according to ST2. On the left-hand side, the ceramic has a density of 1.53 g·cm^{-3} and a compressive strength of 9 MPa, whereas on the right-hand side the ceramic shows a density of 1.76 g·cm^{-3} and a compressive strength of about 70 MPa.

Conclusions

In the CerInk project, we prepared and tested different NanoInks for ceramic 3DP. The inks were evaluated with respect to the rheological parameters reported in the literature. The solid content of the ink, up to a maximum value of ≈20wt%, was identified as a limit for commercial low-cost print heads. In order to achieve the aimed controlled densification gradient, a different approach was followed. We explored several formulations in order to identify couples of materials that can be co-fired without delamination and mimicking porosity and mechanical properties of a natural bone. An extended experimental trial based on 42 different formulations and three sintering profiles was systematically studied. Based on the material characterizations, the appropriate compositions for the ceramic NanoInks were identified. It has been demonstrated that (i) the porosity and the mechanical properties of the co-fired ceramics are appropriate to mimic a natural bone; (ii) the obtained ceramic-ceramic junction does not present delamination and the aimed density gradient is achieved; (iii) NanoInk formulations, within the solid load limitation, for controlled densification is possible; (iv) 3DP using a double-NanoInk BiB technology for ceramic scaffold is feasible.

References

[1] https://nanoscience.ch/en/2017/04/06/annual-report-2016/

[2] N. Matter, A.M. Rohner, A. Carino, P. Gruner, A. Testino, R. Schumacher, *3D printed bone substitutes. Use of Ceramic Nano-Particles as Binder Material to improve Mechanical Stability.* Rapid. Tech – International Trade Show & Conference for Additive Manufacturing. Carl Hanser Verlag GmbH & Co. KG, 38-50, (2017)

Hybrid pixel detectors for electron diffraction of nano-samples

Project A11.04 HPD4FED (University of Basel, PSI, DECTRIS Ltd. Baden-Dättwil)
Project Leader: J.P. Abrahams
Collaborators: T. Gruene, H. Stahlberg, B. Schmitt, and C. Schulze-Briese

The use of light to see the smallest

The use of light and its interaction with matter is one of the best-developed technologies how researchers investigate our environment. One well-known example is the light microscope that shows us the world of things smaller than the eye can see. Another example is the use of X-rays, which are used in medicine to look at our body (e.g. bones and teeth). Most likely the use of light is so widely used because sight is our strongest sense. When it comes to the world of the very small, however, light meets limitations, and at some point even light microscopes cannot be used anymore. Where light meets its limits, one can use electrons to look at a higher level of detail – down to individual atoms. Many of us will be familiar with beautiful images from the world of the small, *e.g.* the close-up view of ants and other insects. Such images have been generated with electron microscopes. The production of such images is much more complicated than taking a picture through the lenses of light microscopes. One of the many reasons: the smaller the objects we look at, the more sensitive they become to the damaging nature of radiation. When we spent too much time in the sun, we burn our skin or in the worst case develop skin cancer. Similarly, small samples get easily destroyed as soon as we use special radiation to look at them – be it with electrons on a microscope, or with the strong X-ray light source, the SwissFEL. At the level of small molecules like proteins, destruction is happening so quickly that we hardly have enough time to take an image of sufficient quality and other tricks are necessary.

A new trick

One of the youngest groups at the PSI, under supervision of group leader Prof. Jan Pieter Abrahams, has recently shown we can overcome this limit. The trick is to take an indirect image of the sample, a so-called diffraction image. This trick gives us more time by a factor of a thousand than with standard imaging to record images. In order to explore this trick, the group is developing an electron diffraction instrument. The Kanton Aargau funds one of its most important components: the construction of a dedicated camera that records the image by selecting exactly that radiation which contains the valuable information. The group has developed two prototypes, based on the Timepix chip (CERN), which are operational and has shown the superiority of this new type of detector technology, a *hybrid pixel detector* [1].

The project

In parallel the PSI detector group has developed a number of hybrid pixel camera chips. They are named after mountain peaks of the Jura. Pilatus has been established for X-ray diffraction about a decade ago. EIGER [2] is the next generation of the PILATUS detector with smaller pixels and higher frame rate. Frame rates up to 2 kHz are possible in continuous data streaming. Last year, the HPD4FED group recorded the very first diffraction pattern with an EIGER camera mounted on an Electron Microscope. We extended this project to see what the new detectors Jungfrau and Moench can do compared to Eiger/Medipix [3, 4]. The aim of this project extension is to see what the most important features are if one would want to build a perfect EM diffraction detector.

Results

Like described in our last report we obtained diffraction patterns of a zeolite. Zeolites are « scaffold » molecules and form a diverse class of microporous minerals. The nanometer sized grains find wide applications in the refinery and chemical industry. The Swiss global player Clariant produces zeolite powder for the reduction of toxic by-products in industrial processes. The powder grains are too small for any other visualizing application than electron diffraction, especially when someone is interested in single grains of the bulk material. Fig. 1 shows a diffraction pattern as well as the structure from the SAPO-34 framework. With T-sites and Oxygen atoms.

After the last report, we were able to characterize the Eiger in parallel with a separate investigation, which was a combined effort of Dectris with the University of Cambridge (UK) [3]. The MTF measured showed that for the EIGER there is a significant broadening of the edge spread function at higher energies, e.g. how sharp is a knife-edge imaged (Fig. 2). Figure 3 shows how close we can get with this detector to the ideal situation. These results are similar to the Medipix detector; the EIGER detector is close to ideal at energies around 100keV (close to the green line).

Currently, we have designed new housing for the upcoming tests with two newly developed detectors from PSI, the Moench and the Jungfrau; both having their own strength and qualities (Fig. 4).

Conclusion

The results indicate that further investigation of these types of detectors is necessary. e.g. If one wants Bragg spots to be closer to each other the MTF needs to be improved, which can be achieved by changing the Si sensor layer to higher Z (atomic number) materials like CdTe and GaAs. Detectors could also be made even faster so quick data collection will the possible by moving quickly from area to area. The first step will be to investigate the Moench and Jungfrau, and together with data collection on other types of detectors these tests will bring fruit to an ideal detector for electron diffraction of (non-) crystalline organic materials.

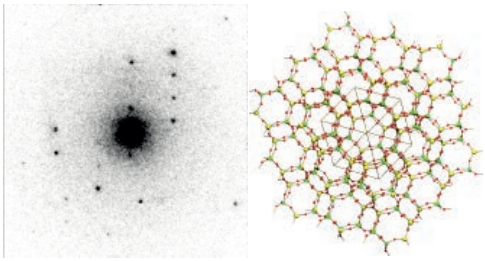

Fig. 1 Left: Electron Diffraction sample (1 frame). Right: Structure of the SAPO-34 framework with T-sides (P and Al) and Oxygen atoms.

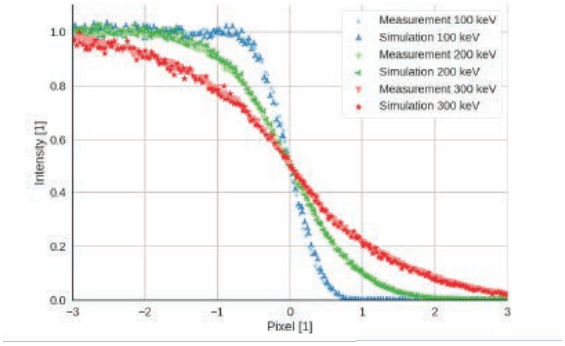

Fig. 2. Comparison between measured and simulated edge for 60 keV energy threshold for different electron energies.

"Unlike monolithic detectors, hybrid pixel detectors are ideally suited for measuring electron diffraction patterns due to their high dynamic range, on-pixel electron counting capabilities, radiation hardness and high frame rate. One can make them viable for imaging above 100 keV by changing the sensor layer to a high Z material, and adapting microscope design." (Abrahams 2017)

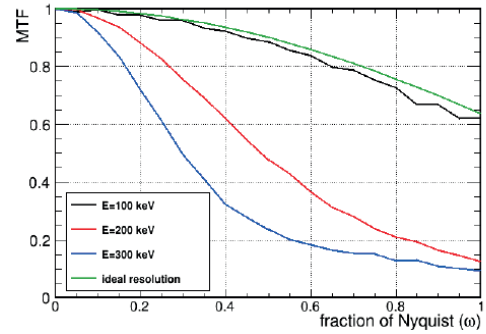

Fig. 3 MTF as a function of Nyquist frequency for 100, 200 and 300 keV electrons.

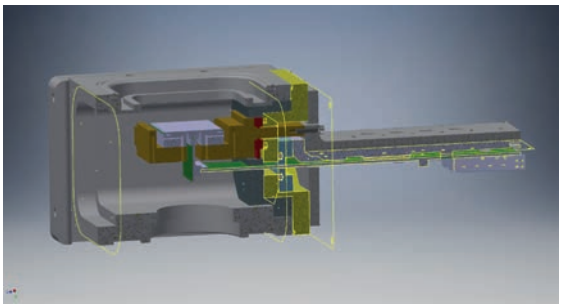

Fig. 4 Design of the new PSI detector for the planned characterization tests of the Moench and Jungfrau.

References

[1] E. van Genderen, M.T.B. Clabbers, P.P. Das, A. Stewart, I. Nederlof, K.C. Barentsen, Q. Portillo, N.S. Pannu, S. Nicolopoulos, T. Gruene, J.P. Abrahams, *Ab initio structure determination of nanocrystals of organic pharmaceutical compounds by electron diffraction at room temperature using a Timepix quantum area direct electron detector*, Acta Crystallogr. A, **72**, 236 (2016)

[2] R. Dinapoli, A. Bergamaschi, B. Henrich, R. Horisberger, I. Johnson, A. Mozzanica, E. Schmid, B. Schmitt, A. Schreiber, XT. Shi, G. Theidel, *EIGER: Next generation single photon counting detector for X-ray applications*, Nuc Instrum Methods Phys Res A. **650**, 79 (2011)

[3] Dectris company (CH), MRC Laboratory for Molecular Biology in Cambridge (UK), *Electrons are the new photons,* https://www.dectris.com/company/news/newsroom/success-story-details/electrons-are-the-new-photons

[4] Paul Scherrer Institut, detector group, *JUNGFRAU: adJUstiNg Gain detector FoR the Aramis User station.* https://www.psi.ch/detectors/jungfrau

[5] Paul Scherrer Institut, detector group, *MOENCH: Micropixel with enhanced pOsition rEsolution usiNg Charge integration.* https://www.psi.ch/detectors/moench

Development of an immunoglobulin detecting biosensor

Project A11.05 IgG Apta NP (FHNW, D-BSSE ETHZ Basel, FGen GmbH Basel)
Project Leader: G. Lipps
Collaborators: M. Held, R. Pellaux, C. Puorger, C. Meyer, and O. Revelles

Sensing particles

Particles with a sensing function are of great interest for bioanalytic and diagnostic applications due to their ease of handling, separation, and immobilization. In this project, we are developing an aptamer based nanosensor to detect human immunoglobulins (IgG). The signal originating from the particles upon activation by the analyte can be directly quantified with any fluorescence-sensitive device including standard microtiter plate readers, microfluidic configurations or flow-cytometry.

IgG binding aptamer

Our nanosensor is based on a mixed RNA/DNA aptamer developed by Nakumara and collegues [1]. The aptamer binds with high specificity and affinity (K_D ~ 100 nM) to human IgG. This aptamer is rather well characterized and the structure of the complex between aptamer and IgG [2] clearly shows the folding of the aptamer into a hairpin and the contribution of eight nucleotides to the binding (Fig. 1). Based on these investigations we could design a series of structure switching aptamers to sense IgG.

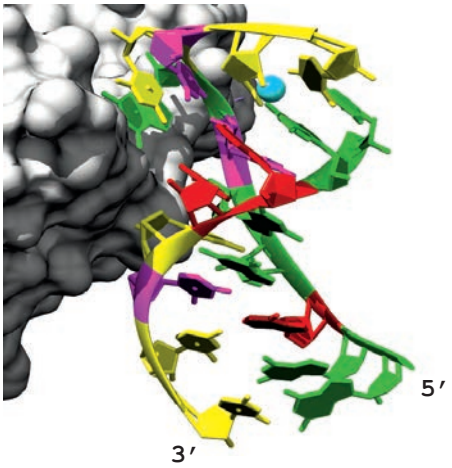

Fig. 1 Complex between human IgG (grey surface) and aptamer Apt8-2 [2]. The aptamer adopts a hairpin conformation. Nucleotides are colored according to base: G (green), A (red), U (magenta) and C (yellow).

Structure switching aptamers

Aptamers may have a high conformational flexibility. This property can be used to engineer aptamers, which specifically undergo a conformational change upon binding to its ligand [3]. These so-called "switching" aptamers can be combined with fluorophore/quencher pairs, which then enable a fluorescent readout of the binding reaction (Fig. 2).

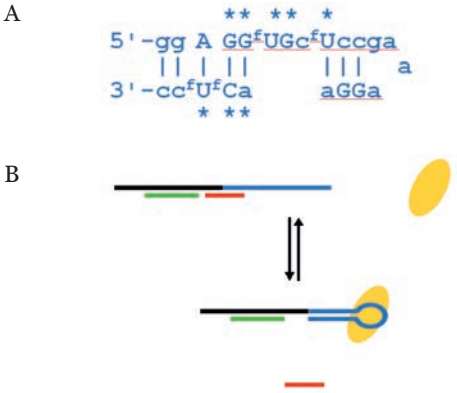

Fig. 2 A: Conformation of the IgG bound aptamer. Asterisks denote nucleotides important for IgG binding. Vertical lines show base pairing between both arms of the hairpin. B: Molecular mechanism of structure switching. The 5' end of the aptamer (blue) is extended by a DNA stretch (black) complementary to short oligonucleotides bearing a fluorophore F1 (green) or a quencher (red), respectively. Upon binding of IgG (orange eclipse), the aptamer adopts the hairpin conformation and displaces the oligonucleotide carrying the quencher. As a result, the fluorescence increases.

We tested a number of different quencher oligonucleotides, which interfere with the hairpin conformation of the aptamer but differ in length and position. As indicated by an increase of the fluorescence of the aptamer in solution, some of these probes (e.g. Q5BH, Q5D and Q1D) were indeed efficiently removed from the aptamer by IgG (Fig. 3).

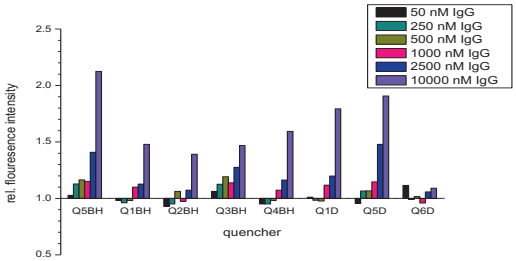

Fig. 3 Comparison of switching aptamers carrying different quenchers. The biosensors were tested between 0 and 10 μM human IgG.

With the best quencher DNA (Q5D) we measured competition kinetics between quencher and IgG. Aptamer complexed with different IgG concentrations was rapidly mixed with quencher DNA. The binding of quencher DNA to the aptamer

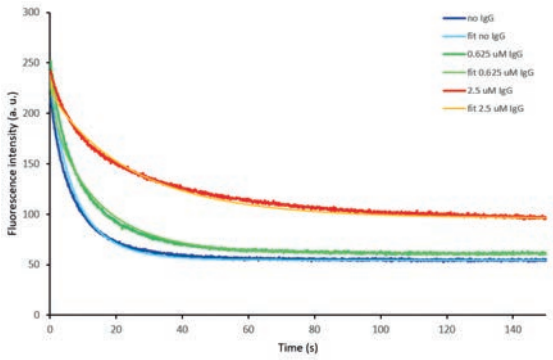

Fig. 4 Competition kinetics of aptamer-IgG complex with quencher Q5D. Kinetics were performed with 50 nM aptamer complexed with the indicated IgG concentrations and with 50, 100 and 150 nM quencher Q5D (kinetics were recorded at 100 nM of the quencher).

was observed via the decrease of the fluorescence signal. Samples with higher IgG concentration showed slower binding of the quencher DNA and a smaller amplitude. Data were globally evaluated according to a three-step reaction:

$$(1)\quad A_{hairpin}\cdot IgG \rightleftharpoons A_{hairpin} + IgG$$
$$(2)\quad A_{hairpin} \rightleftharpoons A_{unfolded}$$
$$(3)\quad A_{unfolded} + Q \rightleftharpoons A_{unfolded}\cdot Q$$

where step (2) is a fast equilibrium between hairpin aptamer and open unfolded aptamer in which the hairpin state is favored (see also Fig. 2B). This allowed us to determine the K_D value for the aptamer-IgG complex (K_D = 1.4 µM) and the apparent K_D value for the aptamer-quencher complex (K_D = 6.5 nM). The apparent K_D for the quencher is in good agreement with values obtained from thermal transition of the aptamer-quencher complex, while the K_D for the aptamer-IgG complex is 10-fold higher than reported.

Next, we immobilized the biosensors onto magnetic beads (diameter 1 µm, ~0.5 Mio biosensors/bead) and monitored the fluorescence using flow cytometry. At cultivation temperature (37 °C) the signal gain was only marginal (10 to 20 % at 10 mM IgG; data not shown). Despite the promising results obtained with the aptamer in solution and on beads at room temperature these results suggest that the QD5/F1 sensor cannot be applicable at standard conditions employed for mammalian cell cultivations. The general poor efficiency of the quencher and perhaps a negative influence of QD5 at elevated temperature on the signal intensity of bead-immobilized aptamers promoted us to exploit an alternative quantification strategy. We decided to test a configuration employing two fluorophores instead of one. The QD5 oligonucleotide was labelled with F2 instead of quencher. We were now able to monitor the IgG binding event via the fluorescence intensity ratio (FIR) of both fluorophores. At a concentration of 10 µM IgG we measured the relative FIR of ~2.8. at 37 °C (data not shown).

Next, we tried to improve the dynamic range of the system by pulling the IgG-replacement reaction further to the right side. For this, we degraded the F2 oligonucleotide after its replacement from the aptamer by IgG with RecJ displaying 5'-exonuclease activity (Fig. 5). The relative FIR saturates at ~5 and the lower limit of quantification is in the range of 100 nM IgG.

Thus, using different configurations of the switching aptamer we are able to measure IgG concentration in various biotechnological settings.

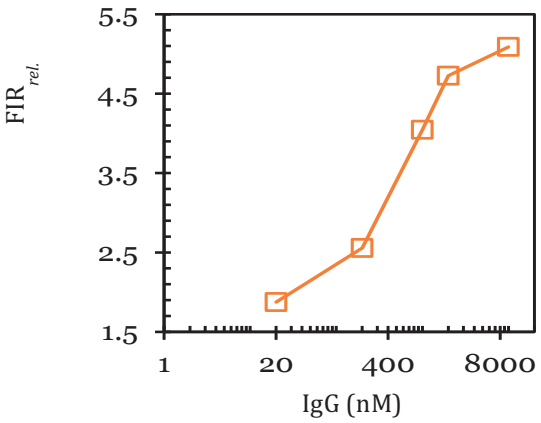

Fig. 5 IgG quantification of the double-labelled immobilized biosensor. Shown is FIR_{rel} which is the ratio of FIR of F1/F2 of biosensor in the presence and absence of IgG. The values have been recorded by flow cytometry at different IgG concentrations (20 min incubation, 37 °C) in the presence of the exonuclease RecJ. Saturation of the biosensor is reached at a concentration of ~2 µM IgG. The lower limit of quantification (defined as signal intensity of 30% above background) was in the order of ~100 nM.

References

[1] S. Miyakawa, Y. Nomura, T. Sakamoto, Y. Yamaguchi, K. Kato, S. Yamazaki, Y. Nakamura, *Structural and molecular basis for hyperspecificity of RNA aptamer to human immunoglobulin G*, RNA, **14(6)**, 1154-1163 (2008)

[2] Y. Nomura et al., *Conformational plasticity of RNA for target recognition as revealed by the 2.15 A crystal structure of a human IgG-aptamer complex*, Nucleic Acids Res. **38(21)**, 7822-7829 (2010)

[3] R. Nutiu and Y. Li, *Structure-switching signalling aptamers*. J. Am. Chem. Soc. **125(16)**, 4771-4778 (2003)

Development of nanostructured silk fibroin-synthetic textile composites

Project A11.10 NanoSilkTex (FHNW, University of Basel, HeiQ Materials AG Schlieren)
Project Leader: O. Germershaus
Collaborators: D. Buser, M. Altin, J. Sahlin, R. Razo, U. Pieles, M. Schönenberger, W. Bender, and M. Height

Introduction

The extraordinary properties of silk have fascinated consumers and have been applied for textiles for centuries. Its luster, wear comfort and exceptional mechanical strength have made silk textiles highly thought-after. However, production of silk garments is labor-intensive and hence expensive and silk textiles lack the durability and versatility of modern synthetic textiles.

The NanoSilkTex project aims at combining the advantageous properties of natural silk with the versatility and robustness of synthetic textiles in the form of composite materials.

Silk fibroin, the main structural protein of the silk brin (Fig. 1), is extracted from cocoons using hydrolysis under alkaline conditions, followed by dissolution of silk fibroin in a chaotropic aqueous medium and subsequent dialysis. After extraction and purification, an aqueous solution of silk fibroin is obtained which can be used for thin-film coating of synthetic fibers.

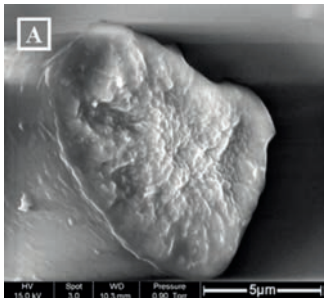

Fig. 1 FESEM micrograph of a single brin from Bombyx mori cocoon [1]. The globular microstructure indicates the presence of silk fibroin nanofibrill bundles. The smooth surface of the brin is coated with silk sericin, which is removed during the extraction process.

Concept

Within NanoSilkTex, synthetic fibers made from polyester are coated with silk fibroin with the aim to impart silks advantageous material properties to synthetic textiles, e.g. improving mechanical strength, wear comfort and hydrophilicity. To achieve this goal, the nanoscale structure of the silk coating as well as its attachment to the polyester surface is optimized. Towards this end, characterization and control over silk fibroin properties after extraction, during coating and after potential curing of the coating as well as proper selection of coating process conditions are crucial. Four coating strategies were investigated. The simplest coating strategy consisted of direct multiple dip coating of polyester fabrics using diluted silk fibroin solution (abbreviated as CN in the following experiments). The second strategy used layer-by-layer coating based on electrostatic interaction between negatively charged silk fibroin and polycations (abbreviated as CP) [2]. In addition to these two strategies which were based on physical interactions between silk fibroin and the fiber surface, two alternative strategies based on chemical conjugation were evaluated (abbreviated as CAP or CAS). The properties of the silk fibroin coated synthetic textile such as mechanical characteristics, feel to the touch, contact angle and UV transmission were evaluated. A special focus was on characterization of the washing fastness of the composite materials with regards to the above-mentioned properties. Finally, a process for the preparation of silk fibroin microcapsules containing limonene was developed.

Coating of synthetic textile samples with silk fibroin

The silk fibroin extraction process was investigated with regards to extraction efficiency and removal of silk sericin. Extraction process conditions were found to significantly affect silk fibroin molecular weight distribution. Extended extraction resulted in more efficient sericin hydrolysis but was also associated with increased formation of low molecular weight fragments of silk fibroin. However, based on FTIR analysis, the capacity to form crystalline beta sheets, which are of special relevance for silk fibroins mechanical properties, was unaffected.

Regenerated silk fibroin solution was used for the coating of polyester fibers. In addition to variation of the coating strategy, silk fibroin concentration as well as the number of dip coating cycles was varied. It was found that high silk fibroin concentrations resulted in inhomogeneous coating and formation of silk fibroin lamellae between individual polyester fiber, negatively affecting mechanical properties. After optimization of the coating process, two coating setups were used for further experiments: 0.1 % or 0.3 % silk fibroin solution was used for 5 dip coating cycles. All experiments were conducted before and after washing of the samples under standardized conditions for 3 or 10 washing cycles.

Microscopic characterization of silk fibroin coatings

Silk fibroin coatings were characterized by SEM and AFM to study the micro- and nanostructure after coating. In the case of CN and CAP strategies, surface

characterization by AFM showed relatively flat surfaces, with few distinct and rather large features. However, in the case of CP and CAS samples, small, globular structures of approximately 50 - 200 nm were observed on the surface. Frequently, these features were found to form larger aggregates of up to 800 – 1000 nm. Hypothetically, these features may represent silk fibroin micelles, which are thought to act as building blocks for silk fibroin nanofibrils [3]. SEM characterization was performed to characterize washing fastness of the coatings (Fig. 2). Interestingly, major changes in the appearance of the coating before and after 10 washing cycles was observed in the case of CAP and CAS samples, while CN and CP showed less pronounced changes of the coating.

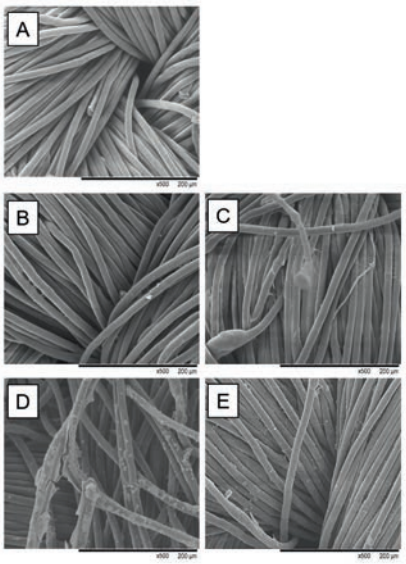

Fig. 2 Scanning electron micrographs showing blank polyester fabric (A), samples coated with CN strategy 0.3 %, 5 cycles before (B) and after 10 washing cycles (C), and samples coated with CAP strategy 0.3 %, 5 cycles before (D) and after 10 washing cycles (E).

Effect of washing on major composite textile properties

Washing fastness was investigated with regards to the amount of silk fibroin deposited on synthetic textile fibers (Fig. 3). Initially, CAP and CAS strategies resulted in higher deposition of silk fibroin on the fiber surface than CN and CP strategies. Washing for 3 and 10 cycles, resulted in pronounced reduction of silk fibroin amount still bound to the textile surface in the case of CAP and CAS strategies, resulting in similar or even lower levels after 10 washing cycles than CN and CP strategies. From this data, it might be concluded that despite the simpler coating strategy, CN and CP appeared to be superior to the more complicated CAP and CAS strategies.

Hydrophilicity of the samples was assessed by contact angle measurements. It was observed that coating with silk fibroin lead to a profound reduction of hydrophobicity, potentially improving wicking properties of composite textiles.

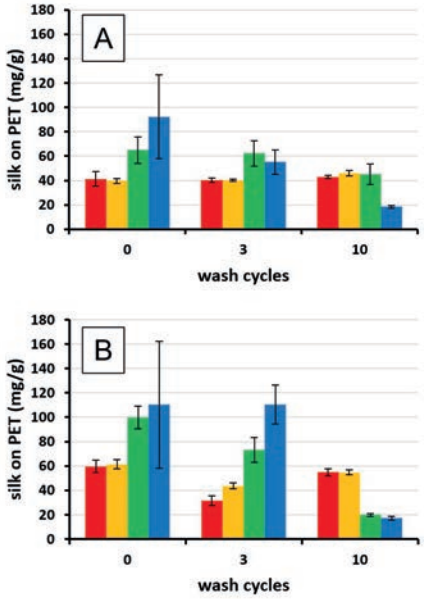

Fig. 3 Evaluation of washing fastness of coated textile samples (coating strategies: red CN; orange CP; green CAP; blue CAS). (A) samples coated using 0.1 % silk fibroin, 5 coating cycles and (B) samples coated with 0.3 % silk fibroin, 5 coating cycles.

This effect was more pronounced with higher silk fibroin concentrations. At high silk fibroin concentrations effects appeared to be more pronounced with CN and CP strategies compared to CAP and CAS strategies. After only 3 washing cycles, contact angles of all samples were virtually identical, most likely due to efficient adsorption of surfactants to the surface.

It was expected that the flexibility of the textiles would be reduced after coating with silk fibroin, which is regarded a disadvantage. CAP and CAS strategies resulted in higher bending stiffness than CN and CP strategies, similar to previous findings. Washing overall reduced bending stiffness, however, the overall trend between strategies remained.

Finally, silk fibroin microcapsules containing limonene and a GC based assay to investigate the release from microcapsules were developed. Further experiments will focus on covalent attachment to silk fibroin coating and limonene release from composite textiles.

References

[1] K. Zhang, F.W. Si, H.L. Duan, J. Wang, *Microstructures and mechanical properties of silks of silkworm and honeybee*, Acta Biomaterialia **6**, 2165 (2010)

[2] L. Li, S. Puhl, L. Meinel, O. Germershaus, *Silk fibroin layer-by-layer microcapsules for localized gene delivery*, Biomaterials **35**, 7929 (2014)

[3] Q. Lu, H. Zhu, C. Zhang, F. Zhang, B. Zhang, D. L. Kaplan, *Silk Self-Assembly Mechanisms and Control-From Thermodynamics to Kinetics*, Biomacromolecules **13**, 826 (2012)

Uniaxially oriented anisotropic electrospun nano-fibrous layers for optical applications

Project A11.12 NF-Optics (CSEM, FHNW, BASF Schweiz AG Basel)
Project Leader: M. Stalder
Collaborators: A. Hafner, R. Oehrlein, C. T. Bormann, Y. Grether, M. Waser, U. Pieles, O. Fernandez, and R. Ferrini

Introduction

Today most optical instrumentation is based on thin optical films, which act as interference filters, color beam splitters etc. The majority of these components are manufactured by vacuum processes like magnetron sputtering or physical vapor deposition. Because of their large technical demand, vacuum free methods are very much appreciated. Electrospinning is a vacuum-free versatile method to deposit nano-fibrous materials, originally used for the production of non-woven fabrics for applications in filtration, textile, and medtech industries. Electrospinning has attracted a lot of interest in the past years, as it is simple and economic [1].

The goal of this project was to use electrospinning for depositing highly oriented nano-fibrous layers of dielectric materials on planar substrates (e.g. glass or thin polymer sheets) to fabricate optical components. In this report, the fabrication and characterization of A) optical retarders based on electrospun nano-fiber layers and B) electrospun nano-fiber layers based on a fluorescence molecule doped polymer are summarized.

A) Fabricated retarders fabricated by uniaxially aligned nano-fibrous layers by electrospinning

The deposition of highly oriented nano-fibrous layers of optical materials is a new approach for the production of optical anisotropic films such as retarders or waveplates. Retarders are used to modify the state of polarization of light e.g. in liquid crystal displays, projectors or novel brand protection devices.

The electrospinning machine for the fabrication of uniaxially oriented nanofibers is based on a rotating cylinder which collects the nanofibers ejected from the motorized syringe holding the polymer solvent solution. The electrospinning set-up is illustrated in figure 1.

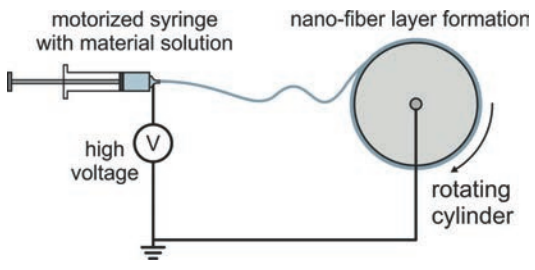

Fig. 1 Electrospinning aligned nanofibers with a rotating cylinder, experimental set-up at the FHNW

For the generation of retarders based on nano-fibers, two concepts were targeted: a) nanofibers with a fiber diameter significantly smaller than 100nm leading to birefringence [2] and b) nano-fibers with intrinsic birefringence.

Commercial polymer materials were used for electrospinning, including: polyimide P84 (PI), polypyrrolidone (PVP), poly(vinyl alcohol) (PVA), polyethylene oxide (PEO), polystyrene (PS). Moreover, high index of refraction polymers synthesized by BASF Schweiz AG were also tested. The experiments showed that the diameter of the electrospun fibers remained larger than approx. 100 nm and are thus generating strong and unwanted scattering light [3].

In order to minimize light scattering, the polymer fibers were encapsulated in a material with a index of refraction close to that of the fibers. Once the light scattering is minimized, the intrinsic birefringence of the nano-fibers can be observed. The analysis of the fabricated samples showed that PS is the polymer with the best parallel aligned nano-fibers and the highest birefringence, thus it was chosen as reference for further studies. Figure 2 shows scanning electron microscopy (SEM) images of perfectly aligned PS nano-fibers from a 6% and a 1.5% solution.

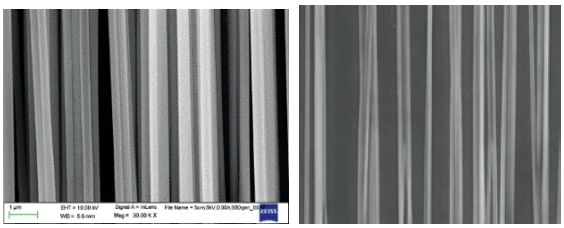

Fig. 2 Perfectly oriented PS nano-fibers generated with a 6% solution (left) and with a 1.5% solution (right)

PS nanofiber based retarders were fabricated, encapsulated and spectroscopically characterized by measuring the transmission spectrum of the devices between crossed polarizers with a diagonal orientation of the nanofibers of 45° with respect to the polarizer. The best nanofiber based retarder (from the 6% solution) showed a retardation of approximatively 1/8 wave for green light (500nm). By placing the retarder on a mirror, the retardation is doubled, thus acting as a quarter wave plate. The measurement set-up is illustrated in figure 3 (left). Figure 3 shows images of the nanofiber retarder between crossed polarizers (retarder area approximatively 8 x 8 mm²).

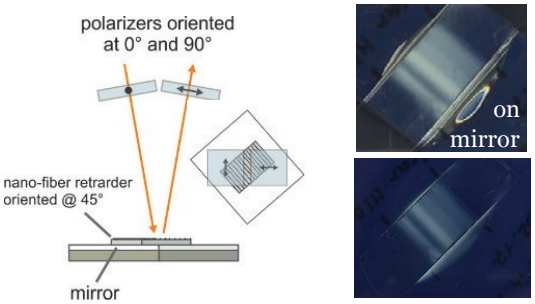

Fig. 3 Optical measurement set-up, side and top view (left) and fiber-based retarder between crossed polarizers (right), retarder on mirror (right top)

In conclusion, the fabrication of a quarter wave plate retarder based on electrospun PS nanofibers was successfully demonstrated. Similar results were published 2016 with PVA as nanofiber material [3].

B) Uniaxially aligned nano-fibrous layers doped with fluorescence dye fabricated by electrospinning

The 6% PS nanofiber were also doped with the red fluorescence dye Lumogen F red 305 from BASF, with a dye concentration of 2%. The electrospun nanofibers had an average diameter of 670 nm. An SEM image of the dye doped PS nanofibers is shown in figure 4.

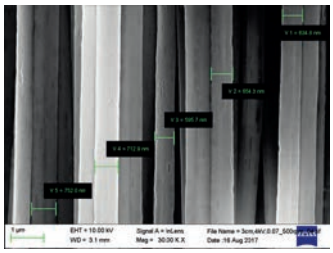

Fig. 4 Highly aligned electrospun PS nanofibers doped with the fluorescent dye Lumogen F red 305 from BASF

Again, highly oriented nanofibers were obtained.

In order to test whether the fluorescence emission of dye doped nanofibers prepared on a glass plate deviates from the emission of a dye doped thin film, the experimental set-up shown in figure 5 was used. The measurements were carried out with green excitation laser light (wavelength 532 nm) horizontally (H) and vertically (V) polarized.

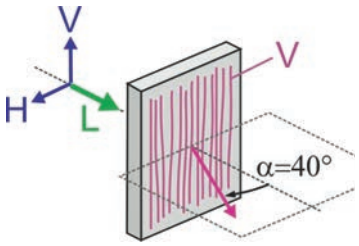

Fig. 5 The optical measurement set-up for the fluorescence (red arrow) studies, with excitation with green polarized (H and V) laser light L for horizontally (H) and vertically (V) oriented nanofibers (only the vertically oriented nanofibers (V) are shown).

The fluorescence emission was measured at an oblique angle of 40° for the laser polarization cases H and V and the fiber orientation H and V as illustrated in figure 5. For comparison with a non-fibrous fluorescence layer a thin film of red fluorescence dye (Lumogen F red 305) doped PS was spin coated on a slab of glass and characterized with the described experimental set-up. The measured fluorescence spectra are shown in figure 6 for the representative cases horizontal polarization and nanofibers horizontally (HH) and vertically (HV) oriented and the thin film sample.

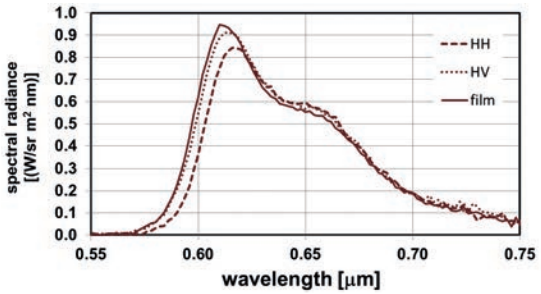

Fig. 6 Measured fluorescence emission from the Lumogen F red 305 doped nanofibers and a thin film (solid line) sample; with the nanofibers oriented vertically (dotted) and horizontally (dashed line)

In conclusion, the fluorescence measurements at the dye doped PS nano-fiber sample showed a minor shift of the main emission peak toward longer wavelength compared to the thin film sample. A similar red shift was recently observed in dye doped PVP nanofiber samples [4]. Additionally, spectroscopic measurements showed that the absorption of the dye doped PS nanofibers are only weakly depending on linearly polarized illumination light (parallel versus perpendicular to the fibers).

References

[1] A. Greiner and J. H. Wendorff, *Elektrospinnen - eine faszinierende Methode zur Präparation ultradünner Fasern*, Angew. Chem. **119** 5770 (2007)

[2] C. Gu and P. Yeh, *Form birefringence dispersion in periodic layered media*, Opt. Let. **21** 504 (1996)

[3] Z. Ma, Z. Hu, H. Zhang, M. Peng, X. He, Y. Li, Z. Yang, J. Qiu, *Flexible and transparent optically anisotropic films based on oriented assembly of nanofibers,* J Mater Chem C **4** 1029 (2016)

[4] M. Enculescu, A. Evanghelidis, I. Enculescu, *Influence of morphology on the emissive properties of dye-doped PVP nanofibers produced by electrospinning,* J Phys Chem of Solids **75** 1365 (2014)

Applicability of 3D electron diffraction in the pharmaceutical industry

Project A12.01 A3EDPI (PSI, University of Basel, DECTRIS Ltd. Baden-Dättwil)
Project Leader: T. Grüne
Collaborators: J. P. Abrahams and S. De Carlo

Crystal Structure – Basis for R&D

The crystal structure of a molecule has become one of the standard analytical tools to Research and Development (R&D) in pharmaceutical academia and industry. A crystal is illuminated with X-rays and reveals a very abstract pattern of spots – the crystal diffracts. From the positions of the spots and their intensities, the structure of the chemical compound can be calculated, *i.e.* the atom types and their arrangement in space.

Fig. 1 Grains of icing sugar are cubes of 10 µm - still 50x larger than the crystals that A3EDPI will look at. The right panel shows an example, about 0.5 µm across.

The structure serves as starting point for modifications that aim at the improvement of the drug: the same effect at lower dose, or the reduction of side effects. The production of large single crystals is a major bottleneck for single crystal structure determination. Pharmaceutical companies like Roche or Novartis may have a selection of 300,000 powder drugs, but "only" one third are available as single crystal X-ray structure determination.

As part of this Nano-Argovia-project A3EDPI, X-rays will be replaced with electrons. For electrons, the individual grains of a powder appear as single crystals, as shown in Fig. 1. Structures can be solved with electrons the same way they can be solved with X-rays [1, 2]. Before the break-through results from Kolb *et al.*, it was believed that the tiny crystals would get destroyed from radiation damage before sufficient data had been recorded.

Dectris – Fast and sensitive Cameras

The detector that records the diffraction data is an important component. The more sensitive the camera, the less radiation damage reduces the quality of the structure. The company DECTRIS, a spin-off company from the detector development group at the Paul Scherrer Institut, is the market leader for photon counting hybrid pixel detectors. These are designed for X-ray crystallography as carried out at the Swiss Light Source and the Swiss Free Electron Laser. Last year, the nanoArgovia Project HPD4FED demonstrated how well they are suited to also detect electrons.

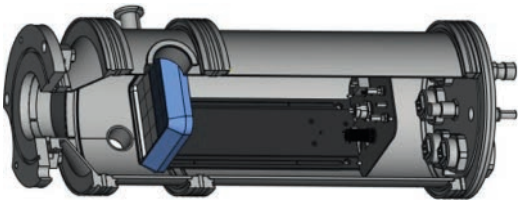

Fig. 2 The EIGER X 1M detector inside its vacuum compatible steel housing. Electrons enter from the left and are detected with the silicon layer framed blue. Image courtesy DECTRIS Ltd.

The flag ship product EIGER is characterised by only 4 µs read-out time, its hardness against damaging radiation, and its reliability that ensures every recording is useable. The latter is an essential property as the detector can generate several thousand images per second.

Combination of high-tech instruments

Electron microscopes are commonly used in Life Sciences (*e.g.* single particle cryoEM). These machines so far are mainly used in Material Science, and single particle EM. Both disciplines have been recognised by Nobel prizes for the discovery of quasicrystals (D. Shechtman, 2011) and for developing cryo-electron microscopy for high-resolution structure determination of biomolecules in solution (J. Dubochet, J. Frank, and R. Henderson, 2017). Combining such instruments with the Dectris EIGER detector will open the world of the smallest also to the field of organic crystallography and hence into the realm of pharmaceutical research.

Fine details

Molecule can be chiral, i.e. there are pairs like our left and right hand (Fig. 3). In many cases, only one version is biologically active. The other hand increases negative side effects. One of the main strengths of X-ray crystallography is the determination of a molecule's chirality and whether or not the pure form is present in the crystal. The technique is based on the »anomalous signal«. This is not available with electrons. However, other options are at least theoretically available. Very recently, the chirality of a certain class of molecules – zeolites - could be determined from electron diffraction [3]. As part of A3EDPI, an exciting challenge will be the determination of the chirality of organic compounds. The effect is much more subtle than for zeolites.

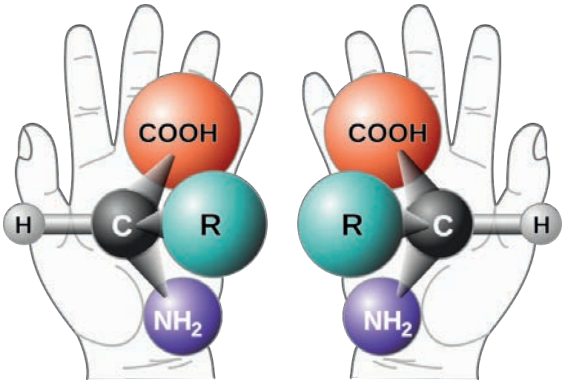

Fig. 3 Left and right-handed molecules look very similar. For our body, the difference can be between healing and bad side effects. Can electrons tell the difference?

Potential for industry and academia

The first phase of A3EDPI could benefit from great expectations to the young field of organic electron crystallography. Two main Swiss centres for electron microscopy, C-CINA in Basel and ScopeM at ETH Zurich, have allocated a total of three weeks of instrument time to this Nano-Argovia-project. The measurements will take place in January and February 2018. The *nano*crystals will be provided through academic collaborations, by the *Argovian* company Crystallise! AG, and by Roche.

References

[1] T.E. Gorelik, J. van de Streek, A.F.M. Kilbinger, G. Brunklaus, U. Kolb, *Ab-initio crystal structure analysis and refinement approaches of oligo p-benzamides based on electron diffraction data*, Acta Cryst. **B68**, 171 (2011)

[2] E. van Genderen, M.T.B. Clabbers, P.P. Das, A. Stewart, I. Nederlof, K.C. Barentsen, Q. Portillo, N.S. Pannu, S. Nicolopoulos, T. Gruene, J.P. Abrahams, *Ab-initio structure determination of nanocrystals of organic pharmaceutical compounds by electron diffraction at room temperature using a Timepix quantum area direct electron detector*, Acta Crys. **A72**, 235 (2016)

[3] Y. Ma, P. Oleynikov, O. Terasaki, *Electron-crystallography for determining the handedness of a chiral zeolite nanocrystal,* Nature Mat. **16**, 755 (2017)

Antibacterial modification of nonwovens using e-grafting and other strategies

Project A12.04 AntibakVlies (FHNW Windisch, INKA, FHNW Muttenz, HLS, Jakob Härdi AG Oberentfelden)
Project Leader: S. Neuhaus
Collaborators: E. Rehmann, S. Wollmann, J. Köser, R. Dubuis, and H. Härdi

Introduction

Nonwoven fabrics are widely used in everyday life ranging from applications in medical areas like gowns, wound dressings or surgical masks to their use as insulation materials and paddings, filters and for consumer goods like diapers or wipes. Their surface properties are frequently tuned via non-covalent surface coatings, e.g. for increased wetting performance. However, certain long-term applications of nonwoven fabrics require a permanent surface modification, which we will for instance try to achieve by electron beam assisted grafting (e-grafting). In this work, we evaluate different strategies for the antimicrobial modification of nonwovens.

Modification strategies

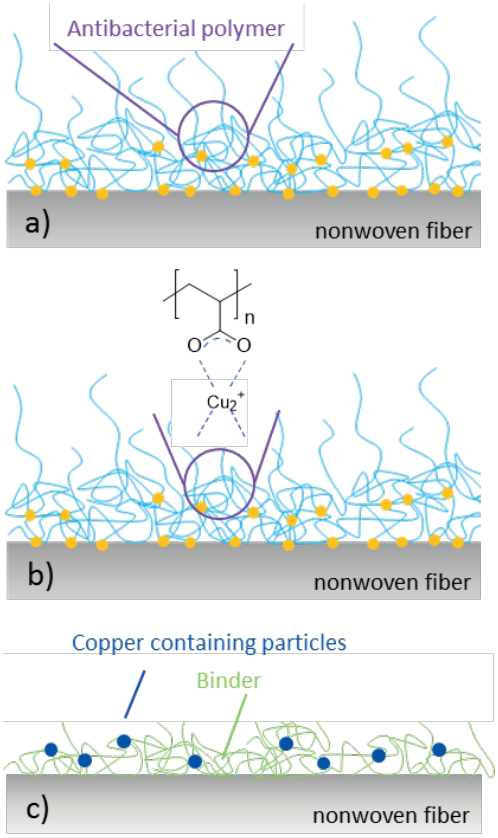

Fig. 1 Modification strategies. a) An inherently antibacterial polymer is covalently attached to the nonwoven by e-grafting; b) a polymer capable of binding Cu^{2+} by complexation is e-grafted on the nonwoven. Yellow dots = crosslinks. c) Copper containing particles are immobilized using a proprietary binder.

Potentially antimicrobial nonwovens were prepared by three strategies relying on either contact killing mechanisms or leaching of bactericidal Cu^{2+} ions.

E-grafting of antimicrobial polymers
Antimicrobial polymers were covalently attached to the nonwoven surface by e-grafting (Fig. 1a). The investigated polymers are known for their contact killing action, i.e. bacteria must be in intimate contact with the surface in order to be killed.

E-grafting of polymers with copper binding affinity
Polymers with repeat units capable of binding copper ions by complexation were grafted on nonwovens (Fig. 1b). Bacteria are killed by release of Cu^{2+} ions from the modified surface.

Immobilization of copper particles using proprietary binders
Copper containing particles were immobilized using proprietary binder materials (Fig. 1c). Slow leaching of Cu^{2+} ions leads to the bactericidal activity of these surfaces.

E-grafting

In electron beam assisted grafting (e-grafting), functional molecules are deposited on the substrate, which is then irradiated with low energy electrons to obtain a multitude of covalent crosslinks between the substrate material and the functional coating. For reliable and reproducible deposition of functional coatings, a dedicated spraystand was designed in the frame of the project.

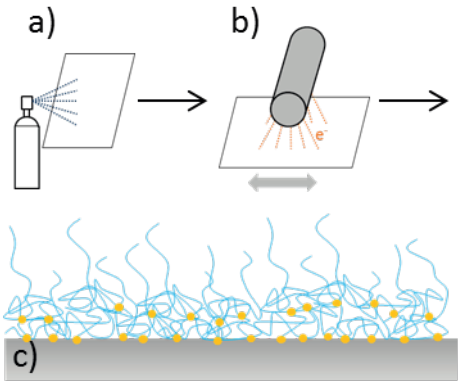

Fig. 2 e-grafting procedure. a) Nonwoven substrates are coated with a functional polymer and then b) irradiated with low energy electrons resulting in c) nonwovens with covalently linked layers of functional polymer (yellow dots = crosslinks).

Antimicrobial Assays

Standard antimicrobial assays according to ISO, ASTM and other norms quantify antimicrobial activity by the number of released surviving bacteria following contact with modified materials for defined periods of time. Thus, adhesion to the modified material cannot be distinguished from killing. To overcome this limitation, we combine these standard assays with methods to determine the metabolic activity of bacteria in contact with the sample. Furthermore, we vary the chemical composition and volume of the bacterial inoculum in order to represent the planned fields of applications.

Results

In nonwovens with covalently bound antibacterial polymers, the amount of eluted live bacteria was reduced by more than 99.9%. However, metabolic assays showed that more than 20% of live bacteria were still attached to the modified nonwovens. Hence, we must assume that e-grafted antimicrobial polymers can immobilize but not sufficiently kill bacteria.

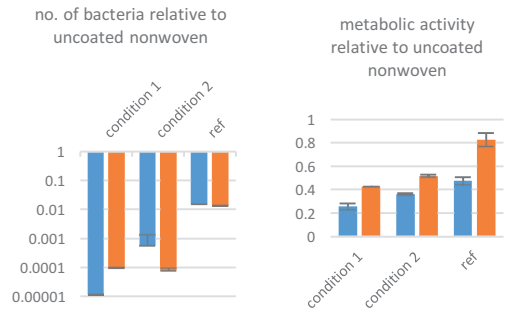

Fig. 3 Comparison of a standard antimicrobial activity assay (left) with a metabolic assay (right) detecting sample adsorbed bacteria. All samples were modified with antibacterial polymers (blue: polymer 1; orange: polymer 2) and extracted for 20 days following coating. The reference samples (coated with polymer but not irradiated) also exhibit a certain activity.

In former work at the HLS, it was demonstrated that the minimum Cu^{2+} concentration to reliably kill bacteria is very low, but depends on the medium composition. We found that untreated e-grafted polymers with copper binding capacity leach high quantities of copper within the first hours after incubation in water. Such a "burst release" is undesirable since it will lead to quick depletion of the copper reservoir in the coating. Still several samples killed >99% of bacteria after washing/extraction for 10/20 days. Further work will focus on adjusting the polymer's copper affinity and therefore optimizing the release profile by pH adjustment.

As another means of establishing continuous, long lasting copper ion release a variety of copper containing particles were incorporated in a proprietary binder system and applied to nonwovens. Certain particles showed prolonged leaching of significant amounts of copper. By adjusting the size/number of applied particles, the Cu^{2+} release rate can be optimized according to the requirement specifications. The observed amounts are deemed sufficient for the desired antibacterial effect, but this has to be proven in antibacterial test.

Conclusion and Outlook

Of the three tested approaches, two are highly promising for the antibacterial modification of nonwovens. It seems that the immobilization of antibacterial polymer rather leads to attachment of live bacteria than to the desired killing action. We will therefore not follow this road. In the remainder of the project, we will focus on adjusting release rates of Cu^{2+} from copper binding polymers (Fig. 1b) and on optimizing the binder/particle mixture, e.g. by varying copper particle size, adjusting particle concentration and by careful selection of additives (Fig. 1c).

On the modified substrates, other properties of high relevance for nonwoven applications such as hydrophilicity and antistatic properties will also be investigated.

Currently we determine the long term Cu^{2+} release rates of the modified fabrics which will continue until the project end.

References

[1] A. Schulze, M.F. Maitz, R. Zimmermann, B. Marquardt, M. Fischer, C. Werner, M. Went, I. Thomas, *Permanent surface modification by electron-beam induced grafting of hydrophilic polymers to PVDF membranes*, RSC Advances **3**, 22518 (2013)

[2] N. Kawabata, M. Nishiguchi, *Antibacterial activity of soluble pyridinium-type polymers*, Appl. Enviro. Microb. **54**, 2532 (1988)

[3] B.L. Rivas, E. Pereira, C. Guzman, A. Maureira, *Complexes of water-soluble polymers with Cu^{2+} and Ag^{+} as antibacterial agents,* Macrom. Symp. **304**, 46 (2011)

Biomimetic microstructures for improved friction and wear behavior

Project A12.09 MicroSlide (FHNW Windisch, PSI, BRUGG AG)
Project Leader: C. Rytka
Collaborators: J. Schmidli, N. Ghielmetti, M. Grob, A. Stumpp, C. Knecht, K. Vogelsang, H. Schift, M. Kristiansen, M. Siegfried, and R. Holtz

Introduction

In the elevator technology, steel wire reinforced thermoplastic elastomer (TPE) belts are used to bear and move the elevator car. Due to high forces, these belts suffer from significant wear. In order to reduce wear, friction reducing slip agents are currently used as master batches. However, these compounds migrate from the thermoplastic material over time, which results in increased friction and wear. This leads to limited lifetime of the belts and therefore a need of more frequent inspections and replacement of the components. Instead of using friction-reducing additives, a modification of the surface structure can lead to sustainably increased friction and wear behavior. In the animal world, a number of species exhibit micro- and nanostructured skin surfaces, which help them to reduce friction in an abrasive environment. In particular, the sandskink (*Scincus albifasciatus*) as well as several kinds of snakes living in sandy deserts have specific structures on their ventral scales, which are in direct contact with the sand soil [1, 2].

In this project, a broad variety of microstructures was replicated with TPEs with two different Shore hardness, followed by measurements of friction and wear. Structured specimens were produced by injection molding of round TPE patches and by hot embossing of structures directly on belts.

Manufacturing of injection mold inserts and TPE Samples

For injection molding, a selection of structures was manufactured in round, 1 mm thick stainless steel inserts, using various fabrication methods, including CNC (micro)milling, pulsed laser ablation, sandblasting and wet etching. Furthermore, stainless steel wire cloth was used as stamp for hot embossing. Figure 1 shows an example of a pyramid structure generated with picosecond pulsed laser ablation.

Samples for friction measurements and wear tests were manufactured in TPEs using Arburg injection molding machines (example shown in Fig. 1).

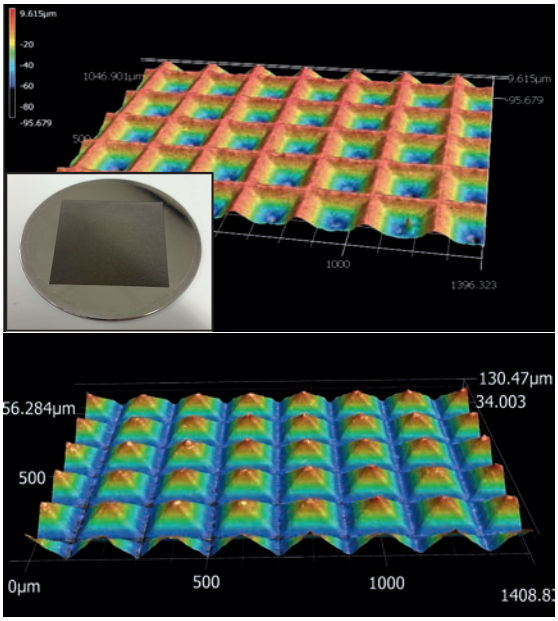

Fig. 1 Top: Photograph and CLSM scan of pyramids laser-ablated in stainless steel insert; bottom: Replicated structures in a TPE

Friction measurements

For measuring the friction of structured samples, two different testing setups were used. For measurements with low surface pressures, a compact construction comprised of a Lego® motor drive system and a Logger Pro® compatible load cell was used. For measurements with higher surface pressure, an NC machine was used as power unit in combination with the same load cell. Figure 2 shows the two friction measuring setups.

The friction measurements showed significant differences among the structures. It could be observed that in the harder tested TPE the structuring potentially led to increased friction coefficients. Conversely, in the softer material, the structuring led to potentially decreased friction coefficients.

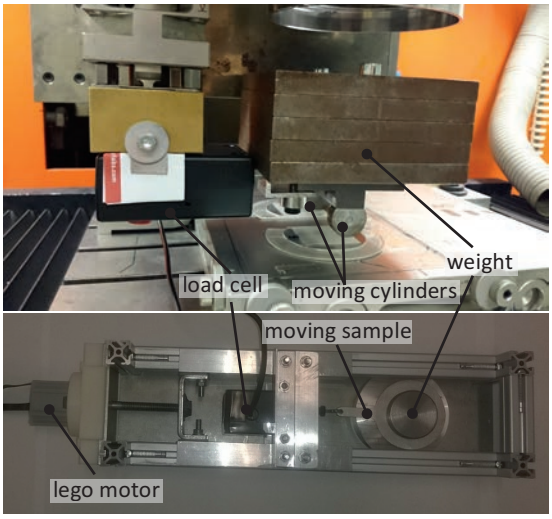

Fig. 2 Two different friction measurement setups. Top: heavy-duty setup with 46.3 N weight force, friction measurements performed by moving cylinder over static sample. Bottom: Light setup with 2N weight force, friction measurement with moving sample over static steel plate.

Wear measurements

Additional to friction, the wear of the structures is also very relevant. First simple trials with a pin-on-disc setup were carried out. In the next step, a setup will be built which will represent the current application more realistically.

Investigation of snake-skin surface structures

Skins of different species of snakes were collected and provided to FHNW by the "*Schlangenzoo Eschlikon*". Sections of the snake skins' dorsal scales were scanned using Confocal Laser Scanning Microscopy (CLSM) and Scanning Electron Microscopy (SEM).

Replication of snake skin structure in Polymers

The replication of snake skin surface structure in PDMS (Sylgard 184, Dow Corning Inc.) was examined. The aim was to create a negative of the snake's surface in a rigid polymer, which would then be used as injection mold insert to produce copies of snake skin structure in TPE materials. Due to the necessity of high curing temperatures, it is not possible to cast structures from snake skin directly into epoxy resins. Therefore, two steps of PDMS casting were carried out, which led to a "positive" copy of the original structure. Due to the good thermal stability of PDMS, it is possible to replicate structures from PDMS into epoxy resin using thermal curing.

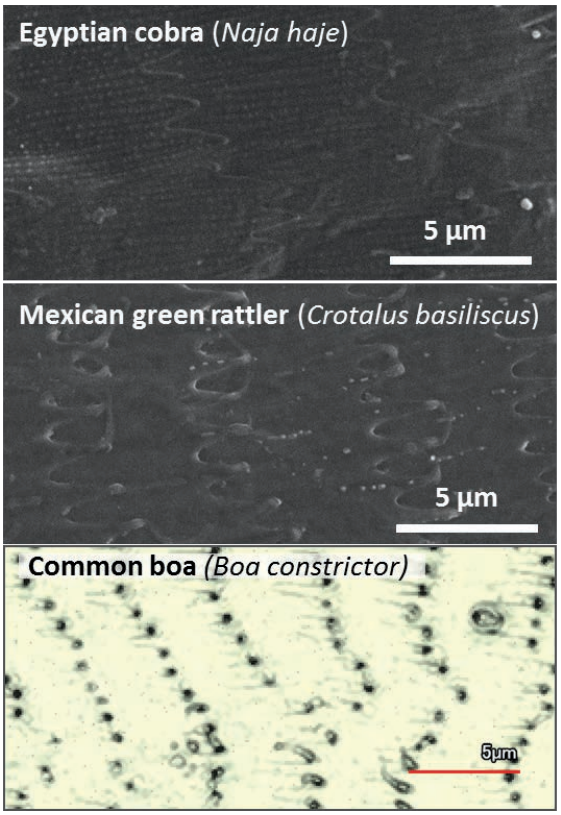

Fig. 3 SEM images of Egyptian cobra and Mexican green rattler and CLSM image of common boa. Direction of snake's movement is to the left.

Outlook

Further measures are still to be taken:

- Generation of Epoxy inserts out of snake skin structure in PDMS for subsequent injection molding
- Structuring of bigger areas on belts using hot embossing or roll to roll embossing
- Wear measurements

References

[1] A. Regabi El Khyari and I. Rechenberg, *Der Sandskink der Sahara – Vorbild für Reibungs- und Verschleißminderung,* Technische Universität Berlin (2005)

[2] M.-C.G. Klein and S.N. Gorb, *Epidermis architecture and material properties of the skin of four snake species*. J R Soc Interface, **9(76)**, 3140–3155 (2012)

Microfluidic protein isolation, stabilization and cryo-EM preparation for high-resolution structural analysis

Project A12.10 MiPIS (University of Basel, FHNW, leadXpro AG Villigen)
Project Leader: T. Braun
Collaborators: M. Hürzeler, M. Chami, M. Hennig, and M. Botte

Introduction

Direct electron detection cameras for electron microscopes (EM) introduced a fast and lasting change to structural biology and are now regarded as a standard method for the structural analysis of protein-complexes to atomic resolution. However, protein isolation techniques and sample preparation methods for cryo-EM remain a bottleneck. Furthermore, classical sample preparation methods often destroy the native conformation of protein complexes by the aggressive filter paper blotting step or the long exposure to the large water surface area. Hence, advanced methods for protein isolation and sample preparation for high-resolution electron microscopy are urgently needed, especially when large (and unstable) protein assemblies are targeted.

For a high-resolution analysis of proteins by the EM single particle approach, only 10'000 to a few million individual protein particles must be analysed. Therefore, microfluidic techniques can provide enough protein complexes for the structural investigation. We developed (i) a microfluidic and paper-blotting free cryo-EM grid preparation method and, (ii), a sample conditioning method for negative stain (Fig. 1). Both methods only require nanoliter-volumes of sample. Additionally, we developed an automated preparation method for negative stain. We also developed methods for the fast isolation of protein-complexes (around 1 hour) from minimal cell amounts (approx. 40'000 cells).

This project aims to develop improved methods for microfluidic protein isolation and electron microscopy (EM)-grid sample preparation towards better protein stability by (i) directly linking protein purification to the microfluidic sample preparation stage; (ii) developing new microfluidic protein cross-linking strategies; (iii) developing new sample conditioning methods to introduce agents protecting proteins from the air-water interface. Final goal will be an integrated microfluidic pipeline for ultra-fast protein isolation and cryo-EM grid preparation requiring less than two hours.

Microfluidic EM sample preparation

Principles of the microfluidic EM grid sample preparation are depicted in figure 1. Both methods can be performed using the same hardware [1, 2]. Importantly, the sample is only in contact with the microcapillary nozzle and does not travel long distances in the microfluidic system, minimizing sample loss by unspecific binding to the microfluidic's wall.

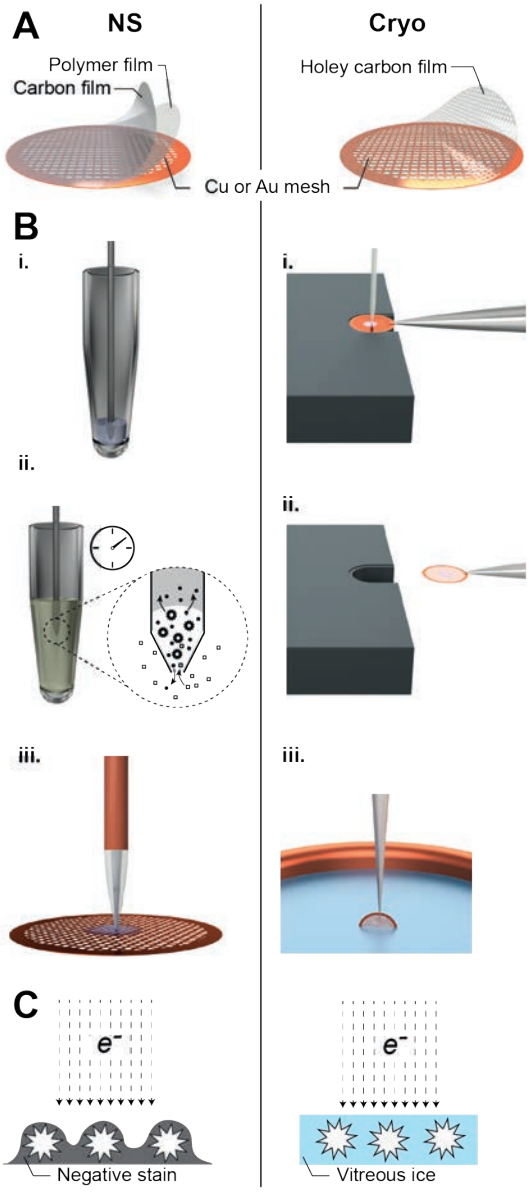

Fig. 1 Microfluidic EM grid sample preparation for negative stain (NS, left column) and cryo-EM (right columns) using the cryoWriter setup. A) Typical EM grid used for negative stain and cryo-EM. For negative stain, a nanometer-thin electron-transparent polymer film, e.g., Parlodion or Formvar, is placed on a copper or gold mesh

of the raw grid and a thin amorphous carbon layer is deposited on top by evaporation. For cryo-EM the raw grid is covered by a perforated (holey) carbon film. B) Microfluidic sample priming, conditioning and EM grid preparation using the cryoWriter setup. Negative stain EM grid preparation: A 5 nl volume is aspirated from the sample stock using a microcapillary (i). For sample conditioning, the microcapillary tip is immersed into the conditioning solution, e.g., 2% ammonium acetate. Ions and small molecules are exchanged by diffusion (ii). Proteins have much lower diffusion constants than salt ions and are not significantly lost. Finally, the sample is dispensed onto the grid and allowed to dry (iii). Cryo-EM grid preparation: A holey carbon film EM grid, held position between the tips of tweezers is placed flat on the surface of a temperature-controlled dew point stage. The stage temperature is set with a defined offset from the dew point temperature. The motorized xy axis of the stage is used to move the grid relative to the microcapillary containing the sample until this is in the correct position. The microcapillary is then lowered until it is a few micrometers above the grid and a few nanoliters of sample are deposited from it while the stage is moved to distribute the sample (i). After sample deposition, the microcapillary is withdrawn and the grid remains on the dew point stage for a short thinning process by controlled sample evaporation. For plunge freezing, the tweezers with grid are rapidly withdrawn from the stage (ii), flipped into the vertical position and plunged into a cryogen (iii). C) In negative stain the specimen on the grid is embedded in a thin layer of amorphous heavy metal salt, which provides structural support for the biological material and imaging contrast in the electron microscope. In cryo-EM, the sample is suspended in a vitreous ice layer and trapped in a close to physiological environment.

Note that these new microfluidic methods have significant advantages compared to classical EM grid preparation approaches: (i) only a minimal total volume of 3 nL is needed (conventional methods: 3 to 5 µL); (ii) the EM grid preparation is basically lossless. In classical sample preparation methods, 99.99% of the sample is lost; (iii) the harsh paper-blotting step is completely eliminated and the exposure time of the protein to the air/water interface is minimized. Furthermore, the new method allows to be directly coupled to protein isolation methods as shown below.

Microfluidic protein isolation

We are using a magnetic trap to immobilize super paramagnetic particles (15 to 1000 nm in diameter, depending of the application) developed before for targeted proteomics and diagnostics. The principles for microfluidic protein purification coupled to EM grid preparation are shown in figure 2A. We are now able to isolate proteins from raw cell lysate (Fig. 2B) in about one hour. Note that the "photo-elution" avoids changing the chemical composition of the buffer for the release of the target protein. Therefore, only minimal amounts of unspecific proteins are eluted, as seen in the clean background of the eluate (Fig. 2C). This system also allows the direct preparation of the protein for cryo-EM.

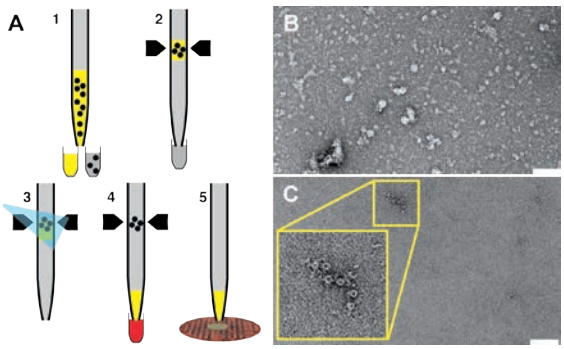

Fig. 2 Integration of protein purification into the cryoWriter set-up. A) Principle of the protein isolation procedure used for this particular experiment. (1) The super-paramagnetic particles functionalized with an antibody against the target protein are mixed with cell lysate. For the functionalization, a photo-cleavable linker is used. (2) The particles are immobilized using the magnetic trap and the beads are washed with buffer. (3) The photo-cleavable linkers are split by UV-light illumination. (4) After photo-elution the sample plug is conditioned with negative stain (tungsten salt) and written onto an EM grid with continuous carbon film (5). All protein isolation steps and EM-grid preparation are now automated. B) Negative stain of raw cell lysate containing the target protein. C) Purified protein (ring like structures), connected by antibodies. Inset shows the indicated region 2.5x enlarged. Note the clean background. Scale bars B&C: 100 nm.

References

[1] S.A. Arnold, S. Albiez, N. Opara, M. Chami, C. Schmidli, A. Bieri, C. Padeste, H. Stahlberg, and T. Braun, *Total Sample Conditioning and Preparation of Nanoliter Volumes for Electron Microscopy*, ACS Nano **10**, 5 (2016)

[2] S.A. Arnold, S. Albiez, A. Bieri, A. Syntychaki, R. Adaixo, R.A. McLeod, K.N. Goldie, H. Stahlberg, and T. Braun, *Blotting-free and lossless cryo-electron microscopy grid preparation from nanoliter-sized protein samples and single-cell extracts*, JSB **197**, 3 (2017)

Plasmonic nanoscale retarder controlled with liquid crystals

Project A12.13 PlasmoRetarder (CSEM Muttenz, PSI, Rolic Technologies Ltd. Allschwil)
Project Leader: B. Gallinet
Collaborators: F. Lütolf, L. Driencourt, M. Schnieper, R. Ferrini, D. Kazazis, Y. Ekinci, F. Federspiel, and M. Ibn-Elhaj

Surface plasmon resonances in metallic nanostructures enable the confinement and manipulation of the electromagnetic field well below the diffraction limit, thus opening new paradigms for optical devices. This project aims for developing an optical retarder and its integration in display devices. This is achieved by design and fabrication of plasmonic nanostructures showing a strong and spectrally narrow birefringence effect, which can be actively controlled by liquid crystals.

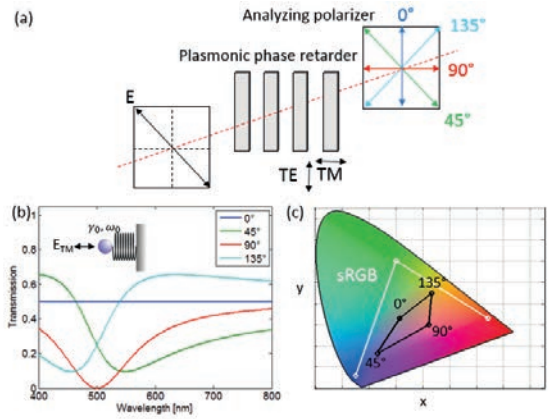

Fig. 1 (a) Plasmonic phase retarder placed between crossed polarizers. (b) Harmonic oscillator model applied as a decrease of TM transmission, while the TE transmission is spectrally flat. Constructive and destructive interferences are observed for cross polarizations. (c) The rotation of the analyzing polarizer yields different colors.

The basic working principle is shown in figure 1a. A plasmonic phase retarder is placed between crossed polarizers to generate different colors in transmission [1]. An analytical model based on harmonic oscillator has been developed by CSEM in order to understand the contribution of plasmon resonances to transmitted light. The total transmission through the device with the analyzing polarizer at 45° or 135° can be computed using Jones' matrices: $T=T_{TM}/4+T_{TE}/4\pm\sqrt{T_{TM}}\sqrt{T_{TE}}\cos(\phi_{TE}-\phi_{TM})/2$, where T_{TM} and T_{TE} are the transmission amplitudes for TM and TE polarizations, respectively, and ϕ_{TM} and ϕ_{TE} their phase. The TM transmission of the plasmonic phase retarder is modelled by a harmonic oscillator model for a given resonance frequency ω_o and bandwidth γ_o: $T_{TM}=1-\gamma_o^2\omega_o^2/[(\omega_o^2-\omega^2)^2+\gamma_o^2\omega^2]$, and $\phi_{TM}=\tan^{-1}[\gamma_o\omega/(\omega_o^2-\omega^2)]$. Introducing this response in the equation for the transmission as a function of the orientation of the analyzing polarizer yields the different spectra in figure 1b. The resonance wavelength of 500nm and bandwidth have been chosen to maximize the color difference. Interestingly, the phase variation of the oscillator around the resonance leads to a sharp constructive or destructive interference for crossed polarizations (45° and 135°), thus generating a low-pass or high-pass optical filter, respectively. The resulting colors are shown in figure 1c.

In a metallic nanostructure, the birefringence is determined by plasmonic and non-resonant contributions (i.e. effective refractive index). Numerical calculations have been performed by CSEM to gain a deep insight in the optical near and far-field, which is necessary to design and optimize the combination of these contributions. The presented silver nanostructure has a deep-subwavelength periodicity (220nm and below) in order to avoid diffraction effects. Constraints from the fabrication process have been included from the scanning electron microscopy (SEM) images of first fabricated structures in order to make a realistic design. The polarization-dependent transmission amplitude and phase have been calculated and used to obtain the transmission for different angles of the analyzing polarizer (Fig. 2a). As predicted by the oscillator model, sharp interference effects occur for crossed polarizations (45° and 135°). Strong purple and yellow colors are observed because of the slope of the combined resonant and non-resonant responses (Fig. 2b).

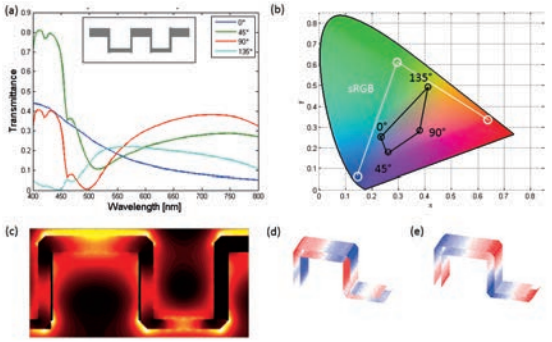

Fig. 2 Numerical analysis of a plasmonic phase retarder using the surface integral method [2]. (a) Transmittance as a function of the angle of the analyzing polarizer. (b) Corresponding colors in CIE space. (c) Electric field intensity at resonance. (d-e) Surface charge distribution (d) below and (e) above resonance. Red: positive. Blue: negative.

Studying the electromagnetic response in the near-field, we can observe a strong intensity on the top and bottom corners of the structure (Fig. 2c). The

distribution of charges below (λ=450nm) and above resonance (λ=550nm) show a change of sign which implies that the sharp phase variation in transmission around the plasmon resonance originates from oscillations of the surface charges (Fig. 2d-e).

We have fabricated high-resolution and large-area (~3×3cm²) plasmonic phase retarder using extreme ultraviolet interference lithography (EUV-IL) tool at PSI. We have adopted Talbot lithography [3] owing to its high resolution and high throughput.

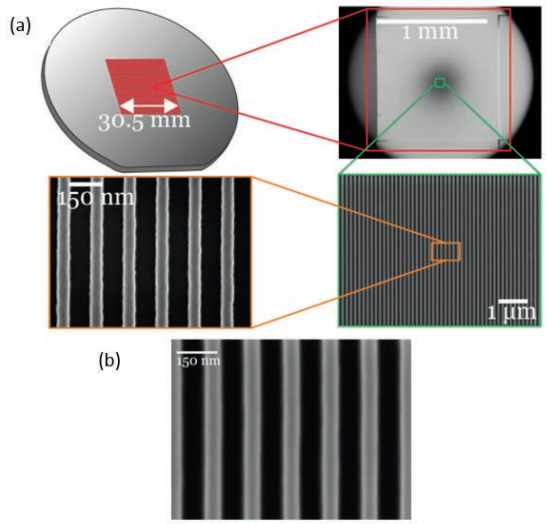

Fig. 3 (a) SEM image of HSQ lines on Si with a period of 150 nm and line width of 60 nm. The left inset shows a low magnification SEM image of a single exposed field and the right inset a low magnification SEM image of the HSQ grating. (b) The grating transferred to the Si wafer with 60-nm-width lines.

A 100 mm Si wafer is spin-coated with a high-resolution resist (hydrogen silsesquioxane or HSQ) with a thickness of ~60 nm. The required pattern (grating with a period of 150 nm and a linewidth of 60nm) is recorded on the photoresist using a specially developed transmission mask (on 100 nm Si3N4 membrane). An area larger than 3×3 cm² is patterned by step-and-repeat. The wafer is subsequently developed in a TMAH solution. Figure 3a shows an SEM image of the nanograting recorded on the HSQ resist. A low magnification image of a single exposed field (~1×1 mm²) is shown together with its adjacent fields, as well as a high magnification image of the 60-nm lines. The HSQ pattern needs to be transferred to the Si substrate with reactive ion etching. The residual HSQ resist is stripped from the wafer by a buffered HF. The resulting pattern transferred into Si is shown in Fig. 3b. The development of the Si grating was the result of a series of tests, required for the development and optimization of the nanofabrication process, including optimal HSQ coating conditions, Talbot lithography dose optimization, stitching minimization, development and optimization of the Si anisotropic etch etc.

A plasmonic phase retarder has been fabricated at CSEM by UV-nanoimprint of a grating master and evaporation of a silver thin film, followed by an encapsulation. The polarization-dependent transmittance is shown in figure 5a, with a plasmon resonance at 480 nm for the TM polarization.

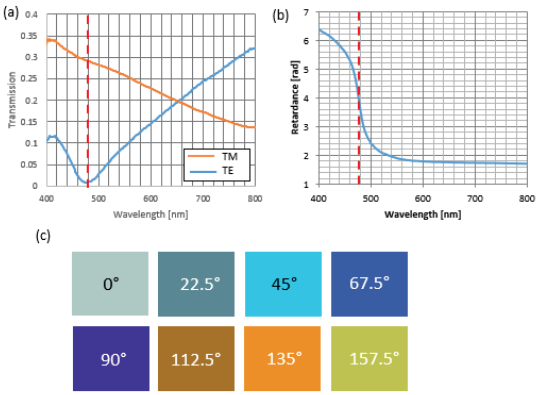

Fig. 4 (a) Transmission for TM (orange) and TE (blue) polarization of a fabricated plasmonic phase retarder. (b) Ellipsometric measurement of retardance, showing a strong phase variation around the plasmonic resonance. (c) Colors under rotation of the analyzing polarizer.

Ellipsometric measurements have been performed by ROLIC to measure the phase retardation between the transmitted TM and TE fields (Fig. 4b). A strong phase variation is observed at the plasmon resonance, in perfect agreement with simulations. This phase behavior for a thickness below 100 nm cannot be obtained from nanostructured phase retarders. A variety of colors, from blue to purple, orange and yellow are generated from the structure (Fig. 4c) in agreement with the theoretical predictions.

In summary, we performed the design, fabrication and characterization of plasmonic phase retarders with spectrally narrow phase variations. We have demonstrated the ability to control the optical phase beyond birefringent materials which paves the way for display applications [4]. In the continuation of the project, the integration with liquid crystal cells as variable optical retarders controlled with a ~60 Hz square voltage from ROLIC will demonstrate their potential to be integrated into display devices. In parallel, further optimization of the design and fabrication will be conducted by the consortium to extend the color palette towards the green and red ranges and to improve their performance.

References

[1] L. Dümpelmann, A. Luu-Dinh, B. Gallinet, L. Novotny, *Four-fold color filter based on plasmonic phase retarder*, ACS Phot. **3**, 190 (2016)

[2] B. Gallinet, T. Siegfried, H. Sigg, P. Nordlander and O.J.F. Martin, *Plasmonic radiance: probing structure at the Ångström scale with visible light*, Nano Lett. **13**, 497 (2013)

[3] W. Karim, S.A. Tschupp, M. Oezaslan, T.J. Schmidt, J. Gobrecht, J.A. van Bokhoven, Y. Ekinci, *High-resolution and large-area nanoparticle arrays using EUV interference lithography*", Nanoscale **7**, 7386 (2015)

[4] L. Shao, X.L. Zhuo, J. Wang, *Advanced Plasmonic Materials for Dynamic Color Display*, Adv. Mater., 1704338 (2017)

3D printable nano porose Cellophil® membranes with nano hydroxyapatite gradient for tissue regeneration applications

Project A12.17 3D Cellophil® membrane (FHNW Muttenz, University of Basel, CIS Pharma AG, Bubendorf)
Project Leader: U. Pieles
Collaborators: S. Stübinger and Ch. Geraths

Introduction

The project aims for the development of a 3D printable membrane composed of the new biocompatible polymer family "Cellophil®" and gradients of hydroxyapatite to be utilized in a 3 D printing process on a RegenHu Bioprinter. The functional membranes are crosslinked during the printing process to achieve a polymer network, with a barrier function on one side and a porous structure on the other side of the membrane allowing cells to grow and the tissue to regenerate. Furthermore the membrane will be functionalized by e.g. growth factors to assist the regeneration process. The immobilization of the selected factors will be accomplished by non- covalent interactions by so called coiled-coil peptides, where one coil is attached to the membrane and the other coil to the factor. These peptides interact with each other by building up a super-coiled conformation. The super-coiled conformation shows strong ionic and hydrophobic affinities (Kd up to 10^{-10}). The peptides will be produced by genetic engineering and expressed in E. Coli, after purification further chemically functionalized allowing the immobilization of growth factor and to the membrane respectively. Because the binding is based on non-covalent interaction the immobilization of the growth factors will take place under very mild conditions and is universally applicable. Furthermore the number of bound molecules can be controlled very precisely.

Synthesis of the Prepolymer

In the first part of the project (month 0-4) a suitable set of different pre-polymers for the 3D printing process was synthetized utilizing RAFT polymerization and a bifunctional RAFT linker which was designed and synthesized in course of the project.
In order to make use of the immobilization strategy based on Coiled-Coil peptides the prepolymers where chemically modified allowing the immobilization process via Click-chemistry.

The synthesized functional prepolymers will be used in the 3D printing process with a RegenHU bioprinter to produce the double sided functional membranes. After the individually printed layers the polymers will be crosslinked by a built in UV source (360 nm) to form a polymeric network. Depending on the composition of the polymers a barrier layer or a layer allowing cell growth is formed.

First successful crosslinking experiments revealed good mechanical properties of the final polymer allowing further experiments to be carried out on the 3D printing system.

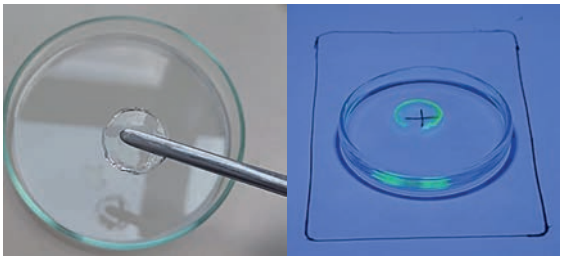

Fig. 1 Left: UV Crosslinked Hydrogel. Right: FITC labelled Polymer

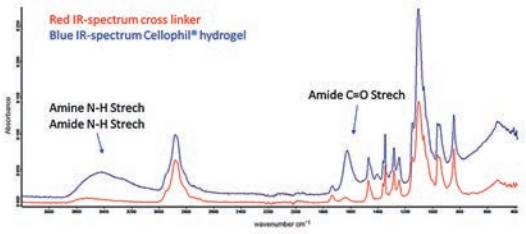

Fig. 2 Infrared analysis of the FITC labelled crosslinked polymer

Further, a part of the amino groups in Cellophil® pre-polymers were functionalized with fluorescine-iso-thiocyanate (FITC) and crosslinked with UV light (365 nm). Subsequently obtained hydrogels were washed extensively with PBS pH 7.4. Most of the fluorescence label remained inside the hydrogel indicating a good cooperation of Cellophil® into the hydrogel network. These results are in line with the IR Analysis.

First trials utilizing the inhouse (FHNW-HLS) RegenHu 3D Cell printer to study the rheological properties of the polymers, the printing stability and the crosslinking efficacy have been performed. The very promising results revealed that the polymers can be successfully crosslinked with the current setup maintaining the printed structure.

Expression of ACID and BASE coiled-coil peptides

The expression "coiled-coil" designates a protein structure motif. Proteins and their functions are

determined by their three-dimensional structure, which occurs by folding processes performed by many natural proteins. The first and simplest form of protein folding is the α-helical coiled coil. Therefore, those interactions are among the best-understood motifs, so such structures are often main objects for protein studies [1, 2]. In coiled-coil proteins, the α-helices are wrapped around each other, forming a supercoil, which can be left- or right-handed. Generally, a coiled-coil sequence consists of seven residue repeats, called heptad. One heptad consists of the aminoacids *a*, *b*, *c*, *d*, *e*, *f* and *g*, whereas *a* and *d* are hydrophobic aminoacids (mainly Leu, Ile and Val), *e* and *g* are charged (often Lys and Glu). This leads to a hydrophobic core (*a* and *d*) and interhelical ionic interactions (*e* and *g*) (Fig.3) [3]. The simplest form of a coiled-coil peptides are two heptads, but can go up to 200 heptads in more complex proteins [4]. form of a coiled-coil peptides are two heptads, but can go up to 200 heptads in more complex proteins [4].

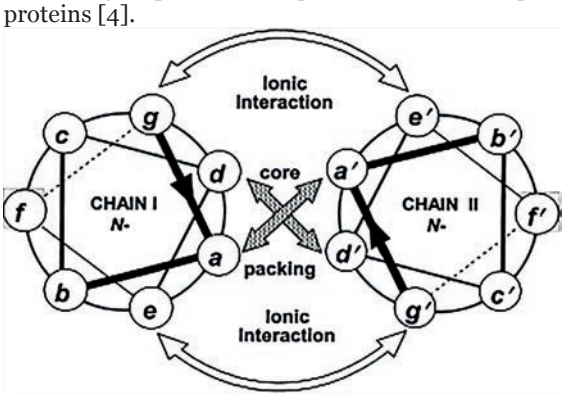

Fig. 3 Scheme of the coil coiled interaction

In the context of the project, coiled-coil peptides are used to stimulate cell growth in an indirect way. Thereby, one coil is bound to a scaffold surface and one coil is connected to a growth factor, such as BMP. The two coils will form a supercoil (coiled-coil) by non-covalent interaction. As the sequences of the coiled-coil peptides contain also a MMP-2 cleavage site, a controlled release of the growth factor from the surface of the scaffold will be ensured.

The plasmid coding for the coiled-coil peptide (ACID) was obtained from CIS Pharma AG. Coil peptide BASE was created by cloning reaction between the synthetically ordered sequence for the coil BASE (Geneart, Thermo Fisher Scientific) and the backbone of the plasmid coding for ACID using the same restriction enzymes *EcoR1* and *Nde1* for both reactions. Ligation was performed over night with T4 DNA Ligase for increased efficiency and maximum yield. Transformation reactions were conducted using heat shock treatment of NEB5α competent *E.coli* to obtain high amount of plasmid DNA. Due to an ampicillin resistance marker on the plasmid, selection of successfully transformed bacteria was possible on ampicillin LB agar plates. The sequence of the plasmids (ACID and BASE) was confirmed by sequencing (Synergene Biotech), the peptide sequence (ACID and BASE) and HisTag (for protein purification) as well as the enzymatic cleavage sites in the fusion protein is necessary, as solely expression of the coiled-coil peptides its due to small size not possible. Finally, Finally, plasmids were transformed into BL21 pLysS *E.coli* strains for expression.

Protein expression could be successfully demonstrated as indicated in figure 4. Expression was performed with the coiled-coil peptide ACID. Therefore, an overnight culture containing ampicillin was inoculated with BL21 pLysS *E.coli* carrying the plasmid ACID. Afterwards, shaking ampicillin over night cultures at 37°C and 18°C, induced with Isopropyl-β-D-thiogalactopyranoside (IPTG), were started. The bacteria in the culture were lysed with Triton X, Lysozym, DNase and ultrasound. After high speed centrifugation, the supernatant, containing the soluble protein fraction, was collected and purified with cobalt-based chromatography package material on Profinia Affinity Chromatography Protein Purification System by Bio-Rad. In course of the project the peptide production process will be further optimized and utilized in the non-covalent modification process of the 3 D printed Cellophil® membranes.

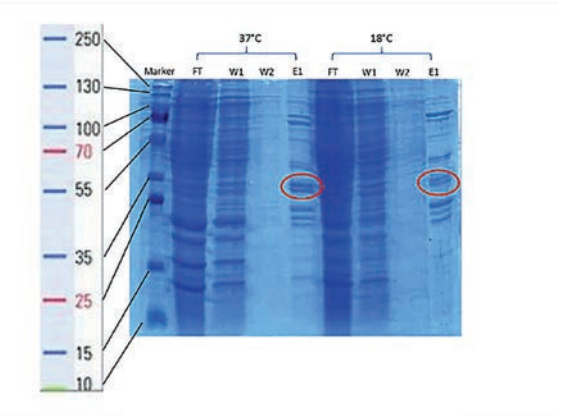

Fig. 4 displays the PAGE gel of the expressed proteins indicated by the red circles

References

[1] A.L. Boyle, and D.N. Woolfson, *De novo designed peptides for biological applications,* Chem. Soc. Rev., 40, 4295–4306 (2011)

[2] D.N. Woolfson, *The design of coiled-coil structures and assemblies*, Adv. Protein Chem., **70**, 79–112 (2005)

[3] Y.B. Yu, *Coiled-coils: stability, specificity, and drug delivery potential*, Adv. Drug Deliv. Rev, **54**, 1113 –1129 (2002)

[4] P. Burkhard, M. Meier, A. Lustig, *Design of a minimal protein oligomerization domain by a structural approach*, Protein Sci., **9(12)**, 2294-2301 (2000)

Swiss Nanoscience Institute
A research initiative of the University of Basel and the Canton of Aargau

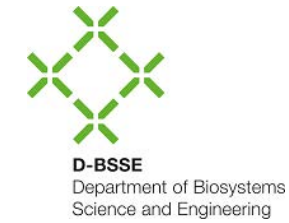

Educating Talents
since 1460.

University of Basel
Petersplatz 1
P.O. Box 2148
4001 Basel
Switzerland

www.unibas.ch

Swiss Nanoscience Institute
University of Basel
Klingelbergstrasse 82
4056 Basel
Switzerland

www.nanoscience.ch